Cranfield University

Mark Manders

Interferometric fibre optic sensors incorporating photonic crystal fibre, for the measurement of strain and load

School of Aerospace, Transport & Manufacturing

Engineering Photonics

MPhil Thesis

Date of Initial Registration; 6th February 2012

Supervisors: Prof. Stephen James, Dr. Matthew Partridge,
& Prof. Ralph Tatam

Date of Submission; 31st March 2016

Contents

Contents **i**

List of figures **v**

List of tables **xviii**

1 Introduction **1**

1.1 Aims 1

1.2 Novelty 2

1.3 Thesis structure and summary 3

2 Background: strain sensors **7**

2.1 Introduction 7

2.2 Fibre grating sensors 8

2.3 Interferometric sensors 11

2.4 Chapter summary 14

3 Theory and applications **25**

3.1 Introduction 25

3.2 Light confinement in optical fibres 26

3.3 Photonic crystal fibres 29

3.4 Chapter summary 34

4 Photonic crystal fibre splicing **37**

4.1 Introduction 37

4.2 Fusion splicing 39

4.3 Hole Collapse 50

4.4 Splicing approach 54

4.5 Reducing loss in splices 56

4.5.1 Arc offset 56

4.5.2 Main arc current 65

4.5.3 Hole collapse and splice loss 73

4.5.4 PCF to PCF splice 74

4.6 Chapter summary 75

5 In-fibre Fabry-Perot microcavities **82**

5.1 Introduction 82

5.2 Microcavity 85

5.2.1 Construction 90

5.2.2 Resin Cube 95

5.3 Interrogating the microcavity 97

5.3.1 Axial strain 99

5.3.2 Transverse load 100

5.3.3 Temperature change 102

5.4 Response of the microcavity 102

5.4.1 Axial strain 103

5.4.2 Transverse load 107

5.4.3 Temperature change 114

5.5 Chapter summary 122

6 Beat frequency interrogation using a short PM-PCF length for strain measurements **127**

6.1 Introduction . . . 127
6.2 Interrogating the birefringent sensor head . . . 129
6.2.1 Constructing the sensor head . . . 129
6.2.2 Beat interference . . . 129
6.2.3 Interrogating beat interference . . . 133
6.2.4 Approach for using the sensor head for strain measurement . . . 139
6.3 Response of the sensor head to strain . . . 144
6.3.1 Single sensor head . . . 146
6.3.2 Two sensor heads . . . 161
6.4 Chapter summary . . . 166

7 Three wavelength interrogation using FBGs written in PMF 171
7.1 Introduction . . . 171
7.2 Phase shifting interferometry . . . 172
7.3 Interrogation of a birefringent fibre using PSI . . . 175
7.4 Phase response of the sensor head . . . 177
7.4.1 Applied axial strain . . . 178
7.4.2 Applied transverse load . . . 178
7.4.3 Temperature change . . . 180
7.4.4 Limitations of the system . . . 181
7.5 Chapter summary . . . 182

8 Summary and recommendations for future work 185
8.1 Introduction . . . 185
8.2 Conclusions . . . 186
8.2.1 Photonic crystal fibre splicing . . . 186
8.2.2 In-fibre Fabry-Perot microcavities . . . 186
8.2.3 Beat frequency interrogation using a short PM-PCF length for strain measurements . . . 188

8.2.4 Three wavelength interrogation using FBGs written in PMF . 190
8.3 Recommendations for future work 191
8.3.1 Chapter 4 191
8.3.2 Chapter 5 192
8.3.3 Chapter 6 193
8.3.4 Chapter 7 194

Chapter references **196**

A Reproduction of NL-1.5-670-02 technical report **199**

B Derivation of equation 6.1 **203**

List of Figures

1.1 Cross-section of mPOF constructed with large air holes for greater fluid volume. Reproduced from Jensen et al. [1] 2

2.1 Schematic representation of the different approaches of interrogating FBGs. The FBGs interrogated in: (a) series, and (b) parallel. Figure reproduced with modifications from Kersey et al. [2]. 10

3.1 Single mode fibre is composed of a smaller core, and an outer cladding. The propagation axis is the direction light propagates through the fibre. . 26

3.2 ω is the angular frequency of the mode propagating through a glass cylinder. β_z is the wave vector of the mode propagating along the axis of the cylinder. $\omega = \frac{c}{n}\beta_z$ is the line for the minimum angular frequency value required for that mode to propagate in a dielectric medium with refractive index n. This region is highlighted in grey. Adapted from Joannopoulos et al. [3]. 27

3.3 ω is the angular frequency of the mode propagating through an optical fibre. β_z is the wave vector of the mode propagating along the axis of the cylinder. n_{co} is greater than n_{cl}. Adapted from Joannopoulos et al. [3]. . . 28

3.4 Three examples of photonic crystal fibres; (a) Bragg fibre, (b) hollow-core fibre, and (c) solid-core fibre. Reproduced from Joannopoulos et al. [3] . . 29

3.5 Image of PM1550, a solid core birefringent PCF produced by NKT photonics. Image taken with an Olympus BX51 microscope. The birefringence is produced by the enlarged holes. 30
3.6 Image of the cross section of a PCF. This fibre is NL-1.5-670-02, a hollow core PCF produced by NKT photonics. Photograph and fibre properties provided by Thor Labs [4]. 32
3.7 Periodic refractive index change in a dielectric, with a periodicity of a. Reproduced from Joannopoulos et al. [3] 33
3.8 The dispersion relationship of PCF that utilises a Bandgap. Reproduced from Joannopoulos et al. [3] 33

4.1 To align optical fibres for splicing, their positions are assessed using a CCD camera. The chucks hold the fibres in place and can rotate them if the fibres are birefringent. Figure reproduced from Yablon [5]. 42
4.2 Description of the profile alignment system (PAS). The stress lobes of the Panda style PMF are shown. As the fibre is rotated the refactive index profile changes and changes the intensity profile incident on the CCD camera. Figure reproduced with additions from Crisp and Elliott [6]. 43
4.3 Comparison of optical axes of PM-PCF to Panda style PMF. 44
4.4 Fibre end of PM1550 taken using the end view scope of the Fujikura 100P+ arc fusion splicer. This is during θ alignment of the PM-PCF to PMF splice. 45
4.5 Illustration of current and energy density distribution in an arc fusion splicer. Current and energy density is rotationally symmetric about the r = 0 axis. Dashed lines represent contours of constant current flux or constant energy density. Curved solid line with arrow illustrates direction of higher or lower current density. Figure reproduced from Yablon [5]. . . 46
4.6 Arc fusion splicing setup. Figure reproduced from Crisp and Elliott [6]. . . 47

4.7 Schematic illustration of the splicing process. (a), (b), and (c) are the conditions that are represented by the images in Figure 4.8. Reproduced from Yablon [5]. 48

4.8 Examples of fibres experiences the arc fusion process. (a) are fibres that have experienced prefusion. (b) are fibres that have been softened and brought together. (c) are when the fibres have finally formed the splice. Figure reproduced from Yablon [5]. 49

4.9 PM1550 (PCF) to SMF-28E (SMF) splice constructed without an arc offset, and a main arc current of 15.3 mA. 51

4.10 Description of an arc offset, it is where the arc points are not directly over the splice joint during construction but are placed preferentially over one fibre. 53

4.11 Three PM1550 to SMF-28E splices constructed with a main arc current of 15.3 mA: (a) without an arc offset, (b) arc offset of 100 μm, and (c) arc offset of 120 μm. Length of the hole collapse region of; (a) $221 \pm 5\mu m$, (b) $129 \pm 5\mu m$, and (c) $100 \pm 5\mu m$. The splice loss of; (a) $3.99 \pm 0.05dB$, (b) $2.52 \pm 0.05dB$, and (c) $0.61 \pm 0.05dB$. The PCF is on the left of each image. The location splice joint is shown in each image. The enlarged holes of the PM1550 are highlighted for (a). The microcavity formed in (c) is highlighted. 58

4.12 Three PM1550 to HB1500T splices constructed with a main arc current of 15.3 mA: (a) without an arc offset, (b) arc offset of 100 μm, and (c) arc offset of 120 μm. Length of the hole collapse region of; (a) $234 \pm 5\mu m$, (b) $147 \pm 5\mu m$, and (c) $102 \pm 5\mu m$. The splice loss of; (a) $0.89 \pm 0.05dB$, (b) $2.27 \pm 0.05dB$, and (c) $1.39 \pm 0.05dB$. The PCF is on the left of each image. 59

4.13 Length of the hole collapse region in comparison to the arc offset distance used in construction of PM-PCF to SMF splices. R-squared of 0.99 for the points to the fitted line (-1.040x + 230.4). 60

4.14 Length of the hole collapse region in comparison to the arc offset distance used in construction of PM-PCF to Panda splices. R-squared of 0.96 for the points to the fitted line (-0.971x + 238.4). 60

4.15 Loss across the splice in comparison to arc offset distance used in construction of PM-PCF to SMF splices. R-squared of 0.82 for the points to the fitted line (-0.023x + 4.202). 62

4.16 Loss across the splice in comparison to arc offset distance used in construction of PM-PCF to PMF splices. R-squared of 0.21 for the points to the fitted line (0.005x + 1.527). 63

4.17 Three PM1550 to SMF-28E splices constructed with a 120 μm arc offset distance and: (a) a main arc current of 16.3 mA, (b) a main arc current of 15.3 mA, and (c) a main arc current of 14.3 mA. Length of the hole collapse region of: (a) $142 \pm 5\mu m$, (b) $100 \pm 5\mu m$, and (c) $76 \pm 5\mu m$. The splice loss of: (a) $1.96 \pm 0.05dB$, (b) $0.61 \pm 0.05dB$, and (c) $0.17 \pm 0.05dB$. The PCF is on the left of each image. 66

4.18 Three PM1550 to HB1500T splices constructed with a 120 μm arc offset distance and: (a) a main arc current of 17.7 mA, (b) a main arc current of 15.3 mA, and (c) a main arc current of 12.9 mA. Length of the hole collapse region of: (a) $203 \pm 5\mu m$, (b) $102 \pm 5\mu m$, and (c) $74 \pm 5\mu m$. The splice loss of: (a) $3.37 \pm 0.05dB$, (b) $1.39 \pm 0.05dB$, and (c) $-0.41 \pm 0.05dB$. The PCF is on the left of each image. 67

4.19 Length of the hole collapse region in comparison to main arc current used in construction of PM1550 to SMF-28E splices. Equation of the line of best fit: y = 40.7x -510.2, R-squared = 0.98. 68

4.20 Length of the hole collapse region in comparison to main arc current used in construction of PM1550 to HB1500T splices. Equation of the line of best fit: y = 31.5x -350.1, R-squared = 0.94. 69

4.21 Loss across the splice in comparison to main arc current used in construction of PM1550 to SMF-28E splices. Equation of the line of best fit: y = 1.46x -21.19, R-squared = 0.94. 70

4.22 Loss across the splice in comparison to main arc current used in construction of PM1550 to HB1500T splices. Equation of the line of best fit: y = 0.92x -12.09, R-squared = 0.93. 71

4.23 Loss across a splice as a function of the length of the hole collapse region in a PM-PCF to SMF splices 73

4.24 Loss across a splice as a function of the length of the hole collapse region in a PM-PCF to PMF splices 74

4.25 PM1550 to PM1550 splice taken with an Olympus BX51 microscope. (a) is magnification 20, (b), (c) and (d) are magnification 50. The length of the hole collapse region of (c) is 170μm, and (d) is 169μm. . 75

5.1 Image of a PCF to SMF splice produced in this work that contains a microcavity. The microcavity is highlighted. 83

5.2 Microcavity formation at the splicing between a SMF (on the left) and a PCF (on the right). The microcavity forms an ellipsoid at the splice joint, with the longest axis perpendicular to the axis of the fibre. The longest axis of this fibre is 43 μm; the shortest axis is 11 μm. 85

5.3 Diagram of a microcavity. S_1 is the first partially reflecting surface adjacent to the SMF core, S_2 is the second partially reflecting surface opposite the SMF core. d is the distance between these two surface. 88

5.4 A typical channelled spectrum of a microcavity. 89

5.5 Description of how the coupler modifies the intensity of the microcavity wavelength spectrum. Left is the spectrum of light before the modulation of the coupler, right is the spectrum of light after the modulation of the coupler. 90

5.6 Microcavities produced with: (a) a main arc current of 16.3 mA, (b) a main arc current of 14.3 mA 93

5.7 Microcavities produced with different overlap distances. (a) had a overlap of 8μm, (b) had a overlap of 10μm 94

5.8 A silicon mould that could be deformed to release the resin cube. Highlighted are the seam that holds the optical fibre, and the chamber that is filled with the resin. 97

5.9 Graph of a microcavity channelled spectrum, before (red solid line) and after 100 $m\epsilon$ (blue dashed line) of axial strain was applied to it. The three intensity peaks used to measure the shift in the spectrum are highlighted within the black rectangle. When strain was applied the peaks shifted to longer wavelengths, highlighted by the black arrow. 98

5.10 Set up to measure axial strain. The microcavity was suspended between two optical mounts, with equal amounts of fibre on each side. The fibre is pinned to the mount using magnets. When the microcavity was coated in a resin cube it was supported by another mount (labeled support mount) to mitigate strain produced by the weight of the resin cube 100

5.11 Press used to apply transverse load to the microcavities[7]. 101

5.12 This is a top down schematic view of the microcavity fibre coated in a resin alongside a dummy fibre with two resin cubes to ensure even pressure across its surface. This includes the bottom glass slide of the pair presented in Figure 5.11. 101

5.13 Setup used to heat the microcavity. The microcavity is surrounded by the thermocoil. 102

5.14 The response of microcavity A to applied axial strain. The equation of the line $y = 0.32x - 0.18$, R-squared = 0.99. The error bars are the standard deviation of the series of three measurements. 104

5.15 The response of microcavity B, to applied axial strain. The equation of the line $y = 0.27x + 0.07$, R-squared = 0.99. The error bars are the standard deviation of the series of three measurements. 105

5.16 The response of microcavity C, to applied axial strain. The equation of the line $y = 0.29x - 0.02$, R-squared = 0.99. The error bars are the standard deviation of the series of three measurements. 106

5.17 A comparison of the response of microcavity F to axial strain when coated ($y = 0.27x - 0.15$, R-squared = 0.99) or not coated ($y = 0.29x + 0.00$, R-squared = 0.99) in a resin cube. The error bars are the standard deviation of the series of three measurements. 108

5.18 A comparison of the response of microcavity G to axial strain when coated ($y = 0.27x - 0.07$, R-squared = 0.99) or not coated ($y = 0.30x + 0.07$, R-squared = 0.99) in a resin cube. The error bars are the standard deviation of the series of three measurements. 109

5.19 The response of microcavity B, to applied transverse load. The equation of the line $y = -0.02x - 0.02$, R-squared = 0.72. The error bars are the standard deviation of the series of three measurements. 110

5.20 The response of microcavity C, to applied axial strain. The equation of the line $y = -0.04x + 0.00$, R-squared = 0.94. The error bars are the standard deviation of the series of three measurements. 111

5.21 Comparison of the sensitivities of the microcavities to both applied axial strain and applied transverse load. The error bars are the standard deviation in the series of measurements taken, divided by strain range experienced by the microcavity. 112

5.22 Response of microcavity E to applied transverse load while it is coated in a resin cube. The equation of the line $y = 0.85x - 0.24$, R-squared = 0.99. The error bars are the standard deviation of the series of three measurements. 114

5.23 Response of microcavity F to applied transverse load while it is coated in a resin cube. The equation of the line $y = 0.59x + 0.31$, R-squared = 0.94. The error bars are the standard deviation of the series of three measurements. 115

5.24 Response of microcavity G to applied transverse load while it is coated in a resin cube. The equation of the line $y = 0.68x + 0.09$, R-squared = 0.98. The error bars are the standard deviation of the series of three measurements. 116

5.25 Response of microcavity E, to applied transverse load while it is uncoated, or coated in a resin cube. The error bars are the standard deviation of the series of three measurements. 117

5.26 Microcavity E when coated in resin took time to respond to the applied transverse load ($2N/mm^2$). The response relieving the load has been vertically inverted such that a comparison between it and applying load can be made. 119

5.27 Response of microcavity A to temperature change from 25 $°C$ to 125 $°C$. The error bars are the standard deviation of the series of three measurements. 119

5.28 Response of microcavity E, to temperature change from 2 $°C$ to 60 $°C$. The error bars are the standard deviation of the series of three measurements. 120

5.29 Response of microcavity F, to temperature change from 25 $°C$ to 60 $°C$. The error bars are the standard deviation of the series of three measurements. 120

5.30 Response of microcavity G, to temperature change from 25 $°C$ to 60 $°C$. The error bars are the standard deviation of the series of three measurements. 121

6.1 Schematic of the sensor head, it is a short length (less than 20 cm) of PM-PCF. Light propagates through the SMF from the source, to enter the PM-PCF (which contains the sensor head). The light propagates through the PM-PCF, is reflected off the cleaved end due to Fresnel reflection, propagates through the PM-PCF again. The light propagates from the PM-PCF into the SMF, and propagates along the SMF to the detector. . . 129

6.2 Representation of the beat interference of two orthogonal polarisation modes of equal intensity to each other, and equal intensity with regards to wavelength, as they interfere after exiting a birefringent optical fibre. . . . 132

6.3 Schematic view of the apparatus used to interrogated the beat interference of the sensor head. The OBR is connected to the SMF with an angle cleaved connector. The SMF ($\approx 3\ m$) is spliced to the PM1550 ($\approx 20\ cm$). The sensor head is the short length of PM1550. The polarisation controller can be placed anywhere along the SMF but for convenience was located near the OBR. It modifies the polarisation of light from the OBR (which is linearly polarised) to a linear polarisation state incident at a 45 degree angle to both orthogonal polarisation axis of the birefringent fibre (PM1550). A schematic of the OBR is presented in Figure 6.4. 135

6.4 Schematic of the OBR optical network [8]. The OBR is used in the setup shown in Figure 6.3. The optical fibre used is PMF. The TLS is a tunable laser source. Light propagates from the TLS through two couplers to the device under test (DUT), which is the interface with the external setup. When light returns from the DUT it propagates through the fibre until is reaches a polarising beam splitter (labelled beam splitter). The two orthogonal polarisation modes propagate to two detectors, each detects the intensity of one of the orthogonal polarisation mode. 136

6.5 Beat interference spectrum of a PM-PCF for one polarisation, before and after axial strain is applied. The direction of the shift of the spectrum is highlighted. 140

6.6 Schematic of the cross section of the birefringent fibre (PM1550), within the transverse load experimental setup. The orthogonal polarisation axes of the fibre are highlighted. Force from the load is applied perpendicular to the glass plates. The angle between the vector of the load and each orthogonal polarisation axis is shown. A schematic of the OBR is shown in Figure 6.4. 141

6.7 Schematic of the two sensor head system. The OBR is connected to the SMF B with an angled cleaved connector. SMF B is spliced to sensor head B. Sensor head B is spliced to SMF A. SMF A is spliced to sensor head A. Both sensor heads are short lengths of PM1550. The two polarisation controllers (PC) can be placed anywhere along the lengths of SMF to which they are attached. Light propagates from the OBR, through the system as is reflected off both the reflecting splice and the cleaved end, to propagate through the system back to the OBR. 144

6.8 The sensitivity of a 20 *cm* sensor head to applied axial strain, as a function of the length of the segment that experienced applied axial strain. The error bars are the mean of standard deviation from the series of three sets of measurements divided by the range of strain it experienced. 146

6.9 The wavelength shift of the beat interference of a 21 *cm* length of PM1550 as axial strain was applied to an 8 *cm* segment of its length. R-squared value of 0.99.The error bars are the standard deviation of the series of three measurement sets. 147

6.10 The wavelength shift of the beat interference of a 18 *cm* length of PM1550 as axial strain was applied to an 8 *cm* segment of its length. The R-squared is 0.99. The error bars are the standard deviation of the series of three measurement sets. 148

6.11 The wavelength shift of the beat interference of a 17 *cm* length of PM1550 as axial strain was applied to an 8 *cm* segment of its length. The R-squared is 0.99. The error bars are the standard deviation of the series of three measurement sets. 149

6.12 The sensitivity of the 15 *cm* sensor head to applied axial strain as a function of the length of the segment to which strain was applied. 150

6.13 The wavelength shift of the beat interference of a 15 *cm* length of PM1550 as axial strain was applied to an 6 *cm* segment of its length. R-squared = 0.99. 151

6.14 The wavelength shift of the beat interference of a 14 *cm* length of PM1550 as axial strain was applied to an 6 *cm* segment of its length. R-squared = 0.99. 151

6.15 Relation between length of the sensor head and its sensitivity to applied axial strain. The error bars are the mean of the standard deviation of three sets of measurements, divided by the strain range the sensor head experienced. R-squared = 0.72. 153

6.16 The wavelength shift as a function of applied transverse load, for different rotational orientations of a PM-PCF 15 *cm* sensor head. 155

6.17 The sensitivity of the 14 *cm* sensor head as function of its rotational orientation. 157

6.18 The sensitivity of the sensor head as function of its length, while load is applied parallel to the fast axis. 158

6.19 The sensitivity of the sensor head as function of its length, while load is applied parallel to the slow axis. 158

6.20 Shows the response of both sensor heads, as axial strain is applied to sensor head A. The error bars are the standard deviation of three sets of measurements. 162

6.21 Shows the response of both sensor heads, as axial strain is applied to sensor head B. The error bars are the standard deviation of three sets of measurements. 162

6.22 Shows the response of both sensor heads, as transverse load is applied to sensor head A. The error bars are the standard deviation of three sets of measurements. 163

6.23 Shows the response of both sensor heads, as transverse load is applied to sensor head B. The error bars are the standard deviation of three sets of measurements. 164

7.1 Beat interference of the birefringent fibre that the FBGs were embedded in. Three FBGs that could be used to determine the phase of the beat interference are shown. 172

7.2 Schematic of a Michelson interferometer. M0 is a partially reflecting mirror. M1 is the reference mirror with an oscillating position [9, 10]. 173

7.3 Schematic of the sensor head. The sensor head is the region of PMF between the splice and the three FBGs. The OBR is composed of a coupler, a tuneable laser source (TLS), a polarising beamsplitter, and two detectors. Light from the TLS leaves the OBR, passes through the polarisation controller (PC), crosses the SMF into the PMF (with the sensor head contained within the PMF), reflects off the three FBGs. It returns to the SMF where the two orthogonal polarisation modes propagate to OBR, and through the coupler in the OBR. The modes interfere with each other at the detector, with the detector measuring the intensity of each polarisation mode. 176

7.4 The OBR wavelength spectrum when interrogating the three FBGs. . . . 177

7.5 The absolute phase of light reflecting at FBGs in the PMF, as axial strain was applied to it. 178

7.6 The absolute phase of the beat interference of the PMF sensor head, as transverse load was applied to it, using four different rotational orientations: (a) 0 degrees, (b) 30 degrees, (c) 60 degrees, (d) 90 degrees. 180

7.7 The absolute phase of light reflecting at FBGs in the PMF, as it was heated. 181

List of Tables

4.1 List of the arc offset distance, length of the hole collapse region, and loss across the splice for PCF to SMF splices. 64

4.2 List of the arc offset distance, length of the hole collapse region, and loss across the splice for PCF to PMF splices. 65

4.3 List of the main arc current, length of the hole collapse region, and loss across the splice for PCF to SMF splices. 72

4.4 List of the main arc current, length of the hole collapse region, and loss across the splice for PCF to PMF splices. 72

5.1 The dimensions of the microcavities produced in this thesis work. The uncertainty in the width was $\pm 1.6 \mu m$ and in length was $\pm 0.7 \mu m$. This was calculated by ten measurements of the same microcavity's dimensions. STD is the standard deviation of the microcavities. . . . 94

5.2 Sensitivity of each uncoated microcavity to applied axial strain, and the precision of the sensitivity. The uncertainity is the mean of the standard deviation of the series of three measurements divided by the strain range. The FBG sensitivity is taken from Roths and Jülich [11] for an FBG centred at 780 nm. STD is the standard deviation of the microcavities, either their sensitivity, or the uncertaintiy in their sensitivity. 107

5.3 Sensitivity of microcavities F and G to applied axial strain, when they are either uncoated or coated in a resin cube. The uncertainty is the mean of standard deviation of the series of three measurements divided by the strain range. 107

5.4 Sensitivity of each uncoated microcavity to applied axial strain, and the precision of the sensitivity. The uncertainty is the mean of the standard deviation of the series of five measurements, divided by the range of strain. The FBG sensitivity is taken from Chehura et al. [7], for an FBG written at 1550nm. STD is the standard deviation of the microcavities. 113

5.5 The sensitivities of microcavities E, F, and G to applied transverse load, before and after they are coated in a resin cube. The uncertainty is the mean of the standard deviation of the series of three measurements, divided by the range of strain. Mean is the mean response of the micrcavities. STD is the standard deviation of the response of the microcavities. 118

5.6 The sensitivities of the microcavities to temperature change from 25°C to 60°C. The uncertainty is the mean of the standard deviation of the series of three measurements, divided by the range of strain. The FBG sensitivity is taken from Chehura et al. [7], for an FBG written at 1550 nm in Panda fibre. Mean is the mean response of the microcavities. STD is the standard deviation of the response of the microcavities. 118

6.1 The sensitivity of different lengths of PM-PCF to applied axial strain. The uncertainty is the standard deviation between the three sets of measurements done on each length. 154

6.2 The sensitivity of PM-PCF sensor heads, of different lengths, at different rotational orientations, to applied transverse load. The uncertainty in the sensitivity is derived from the standard deviation of the three sets of measurements done. 160

6.3 The sensitivity of PM-PCF sensor heads, of different lengths, to applied temperature change. The uncertainty in the sensitivity is derived from the standard deviation of the three sets of measurements done. 161

Chapter 1

Introduction

Strain sensing is important in numerous fields such as: structural health monitoring [1], manufacture of composites [2], and civil engineering [3]. For many of these fields fibre optic based sensors have been utilised due to their numerous advantages, that will be described in Chapter 2.

In this thesis I will described the production of three new fibre optic based strain sensors: a microcavity based in-fibre Fabry-Perot etalon (Chapter 4), a birefringent photonic crystal fibre (PM-PCF) based Michleson-interferometer (Chapter 5), and a polarisation maintaining fibre (PMF) based Michleson-interferometer (Chapter 6).

In this chapter we will describe the aim of this work, the novelty of this work, and how this work is presented in this thesis.

1.1 Aims

The main aim of this work was to design and build fibre optic based strain sensors. This was focused on developing strain sensors that are sensitive to applied axial strain and applied transverse load. There was a secondary aim of incorporating photonic crystal fibre (PCF) into the strain sensors, for reasons detailed in the following section.

1.2 Novelty

PCFs are a type of optical fibre proposed in the early 90's [4], but it took until 1997 for Knight et al. [5] to develop the first PCF. PCF confines light using its cross-section structure of air filled cylinders, that run parallel to the core of the optical fibre, an example is shown in Figure 1.1[1]. This is a fundamentally new way of confining light [6], and sensors incorporating PCF are predicted to have properties such as insensitivity to temperature change. How PCF confines light, and why it is predicted to have such properties is explained in Chapter 2. Chapter 4 and 5 present novel transverse load sensors that incorporate PCF, and possess almost no sensitivity to temperature change (less than 1 $pm/^{\circ}C$). Chapter 5 presents a sensor that can be expanded into a new type of quasi-distributed sensor system.

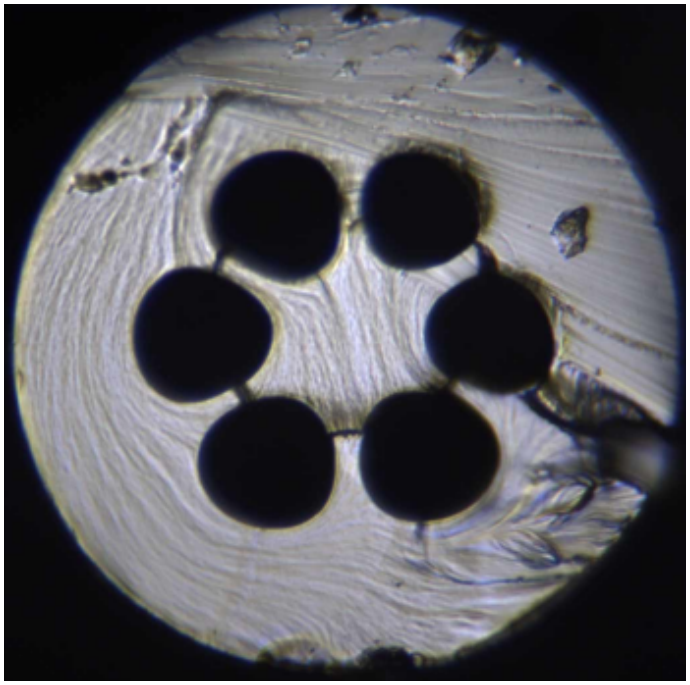

Figure 1.1: Cross-section of mPOF constructed with large air holes for greater fluid volume. Reproduced from Jensen et al. [7]

[1] mPOF is photonic crystal fibre constructed from polymer optical fibre.

1.3 Thesis structure and summary

The thesis is broken down into eight chapters, including the introduction to the thesis in Chapter one.

- **Chapter two**: is a review of the types of sensors used for the measurement of strain. The different types of fibre optic strain sensors will be described, including their advantages and disadvantages. The fibre optic sensor types described in detail will be fibre Bragg gratings (FBGs), interferometric sensors such as Fabry-Perot etalons.

- **Chapter three**: describes light propagation in photonic crystal fibres, and how this impacts their use in strain sensors. A mode theory description will be given of total internal reflection (TIR), and photonic bandgap based light confinement in photonic crystal fibres.

- **Chapter four**: describes the resolution of the difficulties in splicing photonic crystal fibres. Optical fibre splicing is the process of permanently fusing two optical fibres together to allow light to propagate from one fibre into the other. The properties of a good splice will be described, such as having an efficient transfer of light from one fibre to the other across the joint. Splices that are inefficient at transfering light across the joint are lossy, and a source of loss unique to splicing photonic crystal fibre called hole collapse will be described in detail. Finally the chapter will present an approach found to mitigate hole collapse, and reduce the loss across the splice.

- **Chapter five**: describes the production of a microcavity (in-fibre Fabry-Perot) based sensor that was used to measure applied axial strain and applied transverse load. It was produced by a specific method of splicing single mode fibre (SMF) to PCF. The method of construction is described, and how it affects the sensitivity of the sensor to the measurands. A resin cube coating

of the microcavity was used to increase the sensitivity of the sensor to applied transverse load.

- **Chapter six**: described the production of a sensor made from a short length (less than 20 cm) of birefringent PCF (PM-PCF), that was used to measure applied axial strain and applied transverse load. The PM-PCF sensor was spliced to a long length of SMF (greater than 3 m), and interrogated with an optical backscatter reflectometer (OBR). Optical frequency domain-reflectometry was used to observer the change in the beat interference of the PM-PCF as strain was applied to it. Two of these sensors were spliced in series, separated by a long length of SMF (greater than 3 m). This allowed the OBR to interrogate both sensors simultaneously, with the aim to test if this approach is viable to produce a quasi-distributed strain sensor system. The signal of one sensor was found to interfere with the signal from the other, however an approach was found to resolve this, and allow more sensors to be placed in series.

- **Chapter seven**: described the production of a sensor made from polarisation maintaining optical fibre (PMF), that was used to measure applied axial strain and applied transverse load. Phase shifting interferometry was used to observer the change in the beat interference of the PMF as strain was applied to it. It was interrogated with an OBR, with three FBGs used to sample the beat interference intensity at three different wavelengths.

- **Chapter eight**: is a summary of the work presented in this thesis, and details expansions to the three sensors developed.

References

[1] D. Inaudi and B. Glisic. Distributed Fiber optic Strain and Temperature Sensing for Structural Health Monitoring. *IABMAS'06 The Third Int'l Conference on Bridge Maintenance, Safety and Management*, 1(July):16–19, 2006.

[2] A. Bernasconi, M. Kharshiduzzaman, and L. Comolli. Strain Profile Measurement for Structural Health Monitoring of Woven Carbon-fiber Reinforced Polymer Composite Bonded joints by Fiber Optic Sensing Using an Optical Backscatter Reflectometer. *The Journal of Adhesion*, 92(6):440–458, 2016.

[3] Z. Wang. *Intrinsic Fabry-Perot Interferometric Fiber Sensor Based on Ultra-Short Bragg Gratings for Quasi-Distributed Strain and Temperature Measurements*. PhD thesis, Virginia Polytechnic Institute and State Univesity, 2006.

[4] F. Poli, A. Cucinotta, and S. Selleri. *Photonic Crystal Fibers; Properties & Applications*. Springer Series in Material Sciences, 1st edition, 2007.

[5] J. C. Knight, T. A. Birks, P. Russell, and D. M. Atkin. All-silica single-mode optical fiber with photonic crystal cladding. *Optics Letters*, 21:1547–1549, 1996.

[6] A. Massaro, editor. *Photonic Crystals; Introduction, Applications and Theory*. InTech, 1st edition, 2012.

[7] J. Jensen, P. Hoiby, G. Emiliyanov, O. Bang, L. Pedersen, and A. Bjarklev. Selective detection of antibodies in microstructured polymer optical fibers. *Optics Express*, 13(15):5883–5889, 2005.

Chapter 2

Background: strain sensors

2.1 Introduction

Strain sensing is a broad field with many competing approaches with their own advantages and disadvantages [1]. This Chapter is a review of strain sensors relevant to this research. There is a focus on the incorporation of photonic crystal fibre (PCF) into sensors used for the measurement of strain. This is to provide the context of the work in Chapter 4, 5, & 6. The two most common approaches to constructing strain sensors; use a piezoelectric material, or use an optical fibre [2, 3].

When a piezoelectric material is exposed to mechanical stress or strain, it produces a voltage difference across its length [4]. The voltage can be used to gauge the strain the material has been exposed to. The strain-dependent voltage of piezoelectric materials has been used for sensor applications such as accelerometers, microphones, or load cells [5, 6]. Piezoresistive material, materials that change their resistance as strain is applied to them, can also be used as strain sensors [7]. Compared to optical fibre based sensors, piezoelectric materials are sensitive to electromagnetic interference and cannot be used in flammable environments as they can ignite volatiles [8].

Optical fibre based sensors use an optical fibre that has sensitised to a measurand,

such that changes in that measurand modify the light propagating through the fibre [9]. The two most common types of optical fibre based sensors are; fibre gratings, and interferometric sensors [10].

Fibre gratings are broken down into fibre Bragg gratings (FBGs) and long period gratings (LPGs). FBGs reflect light in the core at wavelength specific to the grating [11]. LPGs couple light of a specific wavelength between core and cladding modes [12]. The wavelength for fibre gratings is sensitive to the conditions the grating experiences; i.e. strain or temperature [12, 13].

Interferometric sensors measure the change in phase across a region of an optical fibre [14]. The phase can change due to numerous factors that affect the fibre including strain applied to it [15].

A review of FBG based sensor systems will be presented in Section 2.2, and a review of interferometric sensors will be presented in Section 2.3.

2.2 Fibre grating sensors

Fibre grating sensors are divided into fibre Bragg gratings (FBGs) and long period gratings. FBGs are simple, intrinsic sensing elements that are useful in a variety of applications [16].

The first construction of FBGs was in 1978, however study into them only began when there was controllable and effective construction method devised in 1989 [10]. FBGs are constructed by illuminating a region of optical fibre with a periodic light intensity pattern [17]. The optical fibre is sensitised to UV such that the intensity modulation of the light produces a spatially periodic modulation of the refractive index of the fibre [18, 19, 20, 21]. The fibre can be sensitised by hydrogen loading, where the optical fibre is left in a high pressure and high hydrogen concentration environment so that it absorbs the hydrogen [2, 13].

Hydrogen loading increases the efficiency of the exposure the germanium doping

of the optical fibre's core to the UV light[22]. Telecommunication optical fibre cores are doped with germanium, as this produces the refractive index contrast between the cladding and the core [23]. How this refractive index contrast confines light to the core with be described in greater detail in Chapter 3. Instead of using hydrogen loading, the core of the optical fibre can have a higher concentration of germanium doping. This increases its susceptibility to refractive index modulation caused by the UV light in a similar fashion to hydrogen loading [24].

As light propagating along the fibre encounters the region of periodic refractive index, it partially reflects off each interface of two different refractive indexes. These reflections interfere destructively and constructively. There is a narrow wavelength range where the constructive interference blocks modes with those wavelengths from propagating through the FBG [17]. They are instead reflected off the first interface that marks the beginning of the periodically modulated region. This effectively couples light from the forward propagating core mode into a backwards core for a narrow range of wavelengths [10]. The central wavelength of the range that experience high reflectance, is given by the Bragg condition $\lambda_B = 2n_e\Lambda$ [10, 13, 16]. n_e is the effective refractive index of the fibre, and Λ is the periodicity of the refractive index modulation. Effects that modify the effective refractive index of the fibre or the period of the FBG, such as strain [10, 25], change the wavelength of the reflection peak.

FBGs are used as point sensors, acting in concert to be a distributed sensor system embedded in a range of materials [16]. FBGs can be interrogated simultaneously in series or in parallel using wavelength division multiplexing [10, 13, 16, 21], as shown in Figure 2.1. This is where the FBGs are written to reflect at different wavelengths such that each FBG can be distinguished by its wavelength when the whole system is interrogated [21]. If interrogated in series the FBGs are written into the same optical fibre and separated spatially as well as with regards to wavelength, represented by the schematic in Figure 2.1 (a). This length can be used for

structural health monitoring of large structures such as bridges, or in vehicles such as airplanes [26]. If interrogated in parallel the fibres the FBGs are written in are coupled together like branches of a tree, this can be seen in the schematic in Figure 2.1 (b).

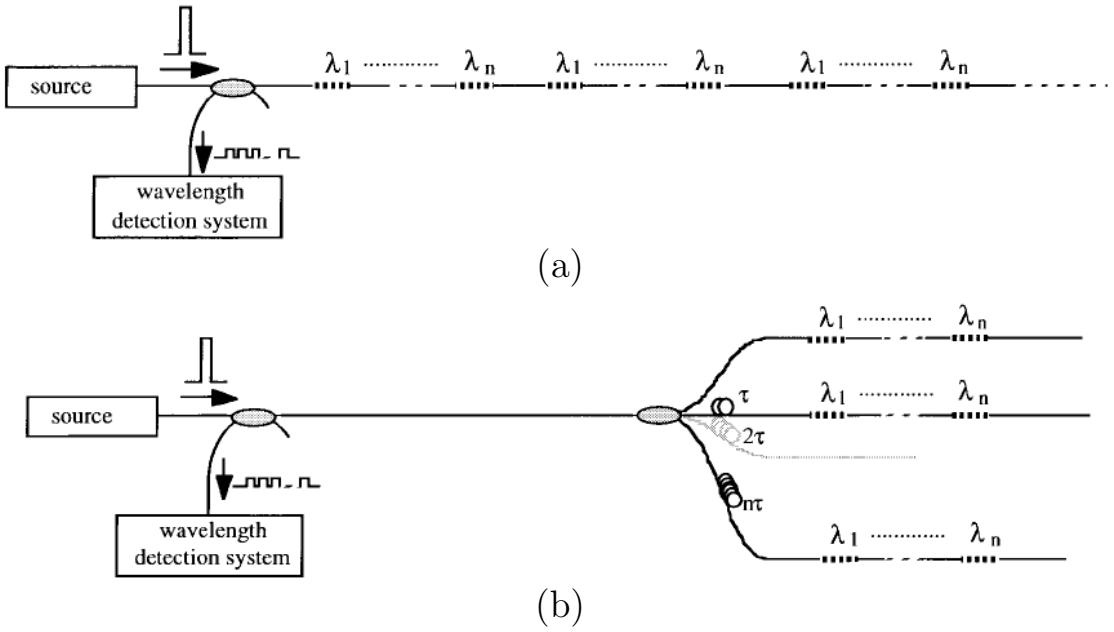

Figure 2.1: Schematic representation of the different approaches of interrogating FBGs. The FBGs interrogated in: (a) series, and (b) parallel. Figure reproduced with modifications from Kersey et al. [16].

The strain applied to an FBG can be along the axis of propagation for the fibre, or perpendicular to it. Roths and Jülich [23] measured the sensitivity of FBGs of $k^{SMF28} = (0.7951 \pm 0.0041)$ to applied axial strain, strain applied along its axis of propagation. k is defined as;

$$\frac{\frac{\Delta\lambda(\epsilon)}{\lambda}}{\epsilon}$$

FBG written in birefringent optical fibre sensitivity to transverse strain was found to be of order $0.14 \pm 0.01 nm/(N/mm)$ [27], however the sensitivity was highly dependent on what type of birefringent fibre and the orientation of the fibre.

The linewidth of the FBG is inversely related to its length, so very short FBG gratings can have a large band of reflectivity making them apropriate for Fabry-Perot

cavities, described in the next section [28].

FBGs have become the industry standard in areas such as embedded strain sensors in carbon fibre resin [29, 30, 31]. Due to their small size, chermical resistance and insensitivity to electromagnetic radiation [29, 30, 31]. A key benefit of FBGs is that they can be interrogated in reflection, which is more convenient for quasi-distributed sensor systems [14].

LPGs formed inside single mode fibre, are constructed in a similar fashion to FBGs, but the period is much longer to allow light in the core to couple to a cladding mode [16, 32]. LPGs can also be produced in PCF, by doing controlled hole collapse using a femto-second laser Qian et al. [33], Kakarantzas et al. [34], Jin et al. [35]. This can produce a periodic modification in the cladding to produce the LPG. This can controlled enough to produce an LPG on only one side of an PCF, allowing a bend sensitive LPG to be produced [35].

2.3 Interferometric sensors

Interferometric sensors work by splitting a beam of coherent light into two or more paths, and then recombining them to interfere [36]. The difference in the path length between those two paths produces the interference effect [36]. Interferometric sensors measure change in the path length difference as a function of strain, to determine the strain the sensor is experiencing [36, 37]. The multiple paths can be produced by several different interferometer designs such as; Michelson, Mach-Zehnder or Sagnac [38]. Each design has its own benefits and disadvantages.

Michelson interferometers split light from a coherent source such as a laser using a beam splitter or 3 dB coupler [39]. The light is sent down both the test arm and the reference arm, then reflected back to the coupler that recombines them [40]. The limitation of this approach for strain sensing is that temperature variations between the reference arm and the test arm can produce a false signal [22, 41]. Michelson

interferometers have been used to produce a strain sensor that can spatially select between multiple strain sensors embedded in one optical fibre, using a white light source and modifying the length of the reference arm [40]. This is a similar capability possessed by the optical backscatter reflectometer used in Chapter 6. Dual Michelson interferometers have been used to measure large ranges of strain ($10^4 \mu\epsilon$) as one interferometer can act as the sensing element, with the other acting as the optical path scanning interferometer [41].

A fibre optic Mach-Zehnder interferometers split lights into two paths using a $3dB$ coupler and then combines them together with a different $3dB$ coupler before it reaches the detector [38]. A Mach-Zehnder approach can be produced by using modal interference, such as a mode confined to a core and a mode that propagates through the cladding using a long period grating (LPG) [16]. If two LPGs are constructed in series in close proximity to each other in an optical fibre, they couple light from the core of the fibre into the cladding and then later back into the core [42]. The difference in path length between the two modes, due to the refractive index difference between the cladding and the core of the fibre, produce an interference that is sensitive to the distance between the two LPGs and the refractive index difference of the cladding and the core [42]. This modal interference can also be produced by a taper, where the fibre is heated and stretched across a small region [43]. This stretching reduces its width, which allows cladding modes and core modes to interfere, acting like a Mach-Zehnder interferometer [43, 44]. This approach has been used to measure strain, but the strain range is limited due to the fragility of the taper [45]. Another approach is to use refractive index difference between the two polarisation modes of birefringent fibre to measure strain across the length of birefringent fibre [46, 47, 48, 49]. Birefringent PCF has been used in this approach to measure strain along its propagation axis [50], a similar approach is used in this work and is presented in Chapter 6.

Sagnac is a common path interferometer, which means that the reference beam

and the test beam propagate along the same path [51]. This is unlike the Michelson or Mach-Zehnder interferometers which use one beam and two paths. The two coherent beams are of slightly different wavelengths, that propagate in opposite direction around a loop to interfere with each other [52]. The disadvantage of this method is that power variations between the two sources used for the two different wavelengths have to be accounted for [53]. This can be used to measure small strains along regions of the optical loop used [54]. Short lengths of birefringent optical fibre, such as birefringent PCF, can be inserted into the Sagnac loop to act as a sensing element [25].

Another interferometric sensor approach uses a Fabry-Perot (FP), which is composed of two parallel partially reflective surfaces in close proximity to each other [2]. Coherent beams of light that propagate through the cavity produced by both surfaces are partially reflected off both [55]. Those reflections interfere with each other producing an interference pattern that can be interrogated in reflection and transmission [56]. Changes in the distance between the surfaces, or in the refractive index of the medium between them, changes the path difference between the reflections.

For optical fibre based strain sensors, FP cavities are described as intrinsic or extrinsic [38]. Intrinsic FP cavities are constructed inside an optical fibre, such as by placing two FBGs in close proximity to each other in an optical fibre [2, 37]. These can be short length FBGs to have high wavelength bandwidth [20]. Intrinsic FP cavities have also been produced by machining the cavity into the core of single mode fibre (SMF), or photonic crystal fibre (PCF) [57]. The Fresnel reflection of the glass air interface cut into the fibre produces the surface with partial reflection. Such cavities can be cut into PCF using a CO_2 laser [34]. A similar cavity is produce by splicing SMF to PCF [58, 59]. When the PCF hole structure, described in Chapter 1, collapses the air can form a microcavity at the splice joint that acts as a FP cavity [60]. This approach was used to produce strain sensors in this work, and is

described in Chapter 5.

Extrinsic FP cavities are constructed such that the light in the core of the fibre is coupled to a cavity external to the optical fibre [16, 61]. This cavity can be constructed by placing two fibre ends in close proximity to each other within a glass cylinder [62, 63]. The space between the two fibres produces the external cavity [64, 65]. Extrinsic FP cavities have been used to develop multiple point sensor systems, equivalent to FBG systems that were described in the previous section [55]. The extrinsic FP cavity point sensors can be used to measure very large range of strain of order $1.2 \times 10^5 \mu\epsilon$ [15]. Due to their construction from silica that allows convenient sterilisation, and small outer diameter (200 μm), they have had medical applications as in vitro sensors [1, 66]. These have been used as point sensors for structural health monitoring like FBGs [29, 56].

2.4 Chapter summary

This chapter covered some of the methods utilizing fibre optics to measure strain. Piezoelectric based strain sensors were briefly discussed, since fibre optics sensors are electromagnetically resistant in comparison, and can be used in environmentally hazard conditions such as an atmosphere of volatile gases. There was a focus in this chapter on fibre optic sensors that incorporate photonic crystal fibres (PCFs), as it provides context for the use of PCFs in Chapter 4, 5, & 6.

Fibre optic sensors were described in two parts; fibre gratings, and interferometric. Fibre gratings can be used as either points sensors, or components of interferometric sensors. It was described how FBG point sensors could be constructed together to produce quasi-distributed sensor systems, which can monitor strain over an extended region. LPG's can be produced from controlled hole collapse of PCFs using a femto-second laser, allowing them to be produced on one side of the PCF and giving it bend sensitivity.

The main types of interferometer configurations were described (Michelson, Mach-Zehnder, Sagnac), and how they have been used in the production of strain sensors. Michelson interferometer's reference arm allows it to spatially separate sources of interference within a long length of fibre optics containing multiple point sensors. Mach-Zehnder is a commonly used configuration since this can utilise modal interference such as; between cladding and core modes, or between two orthogonal polarisation modes. To produce interference between core and cladding modes a taper, or series of LPGs can be used. Sagnac interferometers have been used for strain sensing, but have issues due to the two sources needed to produce the two different wavelengths needed for interference.

Fabry-Perot interferometers were described, and how they are used as point sensors like FBGs. Due to their small size and convenient sterilisation they have medical applications which is a clear advantage over non optical fibre based strain sensors. However the focus on them in this work is on their capability to be point strain sensors for structural health monitoring, which has shown to have precedence in the literature.

An issue that is revealed by research into the subject of PCFs used for strain sensing is that splicing involving PCF is lossy due to a list of factors that will be described in the next chapter.

References

[1] S. Poeggel, D. Tosi, G. Leen, and E. Lewis. Fiber-optic extrinsic FPI/FBG sensor for temperature-compensated pressure measurement in medical applications. *Proceedings of SPIE - The International Society for Optical Engineering*, 8794:1–5, 2013.

[2] Z. Wang. *Intrinsic Fabry-Perot Interferometric Fiber Sensor Based on Ultra-Short Bragg Gratings for Quasi-Distributed Strain and Temperature Measurements*. PhD thesis, Virginia Polytechnic Institute and State Univesity, 2006.

[3] D. Inaudi and B. Glisic. Distributed Fiber optic Strain and Temperature Sensing for Structural Health Monitoring. *IABMAS'06 The Third Int'l Conference on Bridge Maintenance, Safety and Management*, 1(July):16–19, 2006.

[4] J. Sirohi and I. Chopra. Fundamental Understanding of Piezoelectric Strain Sensors. *Journal of Intelligent Materials Systems and Structures*, 11(4):246–257, 2000.

[5] S. R. Anton and H. A. Sodano. A review of power harvesting using piezoelectric materials (2003-2006). *Smart Materials & Structures*, 16(3):R1–R21, 2007.

[6] W. V. Beveren and W. V. Beveren. Lead-free piezoceramics. *Physica Status Solidi B*, 432(November):1–4, 2004.

[7] C. W. Nan, M. I. Bichurin, S. Dong, D. Viehland, and G. Srinivasan. Multi-

ferroic magnetoelectric composites: Historical perspective, status, and future directions. *Journal of Applied Physics*, 103(3):1–36, 2008.

[8] W. J. Westerveld, J. Pozo, P. J. Harmsma, R. Schmits, E. Tabak, T. C. van den Dool, S. M. Leinders, K. W. van Dongen, H. P. Urbach, and M. Yousefi. Characterization of a photonic strain sensor in silicon-on-insulator technology. *Optics Letters*, 37(4):479, 2012.

[9] R. Paschotta. *Field Guide to Optical Fiber Technology*. SPIE Field Guides, 1st edition, 2010.

[10] B. Lee. Review of the present status of optical fiber sensors. *Optical Fiber Technology*, 9(2):57–79, 2003.

[11] T. Erdogan. Fiber Grating Spectra. *Journal of Lightwave Technology*, 15(8): 1277–1294, 1997.

[12] S. W. James and R. P. Tatam. Optical fibre long-period grating sensors: characteristics and application. *Measurement Science and Technology*, 14(5):R49–R61, 2003.

[13] Y.-J. Rao. In-fibre Bragg grating sensors. *Measurement Science and Technology*, 8(4):355, 1997.

[14] Y. Zhao and F. Ansari. Quasi-distributed fiber-optic strain sensor: Principle and experiment. *Applied Optics*, 40(19):3176–3181, 2001.

[15] Y. Huang, T. Wei, Z. Zhou, Y. Zhang, G. Chen, and H. Xiao. An extrinsic Fabry–Perot interferometer-based large strain sensor with high resolution. *Measurement Science and Technology*, 21:105308, 2010.

[16] A. D. Kersey, M. A. Davis, H. J. Patrick, M. LeBlanc, K. P. Koo, C. G. Askins, M. A. Putnam, and E. J. Friebele. Fiber Grating Sensors. *Journal of Lightwave Technology*, 15(8):1442–1463, 1997.

[17] A. Ikhlef, R. Hedara, and M. Chikh-bled. Uniform Fiber Bragg Grating modeling and simulation used matrix transfer method. *Computer Science*, 9:368–374, 2012.

[18] E. Chehura, S. W. James, and R. P. Tatam. Rouard's method as a modelling tool for the sensing characteristics of complex fibre Fabry-Perot interferometers formed between chirped fibre Bragg gratings . *Proc. of SPIE*, 5855:338–341, 2005.

[19] E. Chehura, S. W. James, and R. P. Tatam. A simple and wavelength-flexible procedure for fabricating phase-shifted fibre Bragg gratings. *Measurement Science and Technology*, 094001, 2010.

[20] M.-C. Wu, R. S. Rogowski, and K. K. Tedjojuwono. Fabrication of Extremely Short Length Fiber Bragg Gratings for Sensor Applications. *Sensors, 2002. Proceedings of IEEE*, 2002.

[21] S. Ugale. Fiber Bragg Grating Modeling , Characterization and Optimization with different index profiles. *International journal of Engineering science and technology*, 2(9):4463–4468, 2010.

[22] W. K. S. Chiu, J. M. Maguire, and M. J. Berliner. Phase sensitivity of conventional single-mode and holey optical fibers : a comparison study. *Optical Engineering*, 42:0–6, 2003.

[23] J. Roths and F. Jülich. Determination of strain sensitivity of free fiber Bragg gratings. *Proc. of SPIE*, 7003:700307–700308, 2008.

[24] C. Kerbage, A. Hale, A. Yablon, R. S. Windeler, and B. J. Eggleton. Integrated all-fiber variable attenuator based on hybrid microstructure fiber. *Applied Physics Letters*, 79(19):3191–3193, 2001.

[25] X. Dong, H. Y. Tam, and P. Shum. Temperature-insensitive strain sensor with polarization-maintaining photonic crystal fiber based Sagnac interferometer. *Applied Physics Letters*, 90(15):3–5, 2007.

[26] M. Majumder, T. K. Gangopadhyay, A. K. Chakraborty, K. Dasgupta, and D. K. Bhattacharya. Fibre Bragg gratings in structural health monitoring-Present status and applications. *Sensors and Actuators, A: Physical*, 147(1): 150–164, 2008.

[27] E. Chehura, C.-C. Ye, S. E. Staines, S. W. James, and R. P. Tatam. Characterization of the response of fibre Bragg gratings fabricated in stress and geometrically induced high birefringence fibres to temperature and transverse load. *Smart Mater. Struct.*, 13:888–895, 2004.

[28] M.-C. Wu, R. S. Rogowski, and K. K. Tedjojuwono. Fabrication of Extremely Short Length Fiber Bragg Gratings for Sensor Applications. *Sensors, 2002. Proceedings of IEEE*, 1:49–55, 2002.

[29] J. Leng and A. Asundi. Structural health monitoring of smart composite materials by using EFPI and FBG sensors. *Sensors and Actuators, A: Physical*, 103(3):330–340, 2003.

[30] A. Bernasconi, M. Kharshiduzzaman, and L. Comolli. Strain Profile Measurement for Structural Health Monitoring of Woven Carbon-fiber Reinforced Polymer Composite Bonded joints by Fiber Optic Sensing Using an Optical Backscatter Reflectometer. *The Journal of Adhesion*, 92(6):440–458, 2016.

[31] K. S. C. Kuang, R. Kenny, M. P. Whelan, W. J. Cantwell, and P. R. Chalker. Embedded fibre Bragg grating sensors in advanced composite materials. *Composites Science and Technology*, 61(10):1379–1387, 2001.

[32] X. Shu, L. Zhang, and I. Bennion. Sensitivity characteristics of long-period fiber gratings. *Journal of Lightwave Technology*, 20(2):255–266, 2002.

[33] W. Qian, C.-l. Zhao, X. Dong, J. Kang, J. Guo, and H. Wei. The polarization properties analysis on photonic crystal fibers side-pulsed by CO2 laser. *Optoelectronic Devices and Integration III*, 7847:78471G–78471G–6, 2010.

[34] G. Kakarantzas, T. A. Birks, and P. S. J. Russell. Post-processing of photonic crystal fibres using a CO2 laser beam: a step towards miniature compact fibre devices. In *Information, Communication and Signal Processing, 2003 and Fourth Pacific Rim Conference on Multimedia*, pages 176–177, 2003.

[35] L. Jin, W. Jin, and J. Ju. Directional Bend Sensing With a CO2-Laser-Inscribed Long Period Grating in a Photonic Crystal Fiber. *Journal of Lightwave Technology*, 27(21):4884–4891, 2009.

[36] K. T. V. Grattan and T. Sun. Fiber optic sensor technology: An overview. *Sensors and Actuators, A: Physical*, 82(1):40–61, 2000.

[37] A. Ezbiri. *Passive signal processing techniques for miniature fibre Fabry-Perot interferometric sensors*. PhD thesis, Cranfield, 1996.

[38] B. H. Lee, Y. H. Kim, K. S. Park, J. B. Eom, M. J. Kim, B. S. Rho, and H. Y. Choi. Interferometric fiber optic sensors. *Sensors*, 12(3):2467–2486, 2012.

[39] D. Huang, E. A. Swanson, C. P. Lin, J. S. Schuman, W. G. Stinson, W. Chang, M. R. Hee, T. Flotte, K. Gregory, C. A. Puliafito, A. Et, and E. al. Optical coherence tomography. *Journal of Biomedical Optics*, 254(5035):157–173, 1991.

[40] L. Yuan and F. Ansari. White-light interferometric fiber-optic distributed strain-sensing system. *Sensors and Actuators A: Physical*, 63(3):177–181, 1997.

[41] B. T. Meggitt, C. J. Hall, and K. Weir. All fibre white light interferometric strain measurement system. *Sensors and Actuators, A: Physical*, 79(1):1–7, 2000.

[42] S. W. James and R. P. Tatam. Optical fibre long-period grating sensors: characteristics and application. *Measurement Science and Technology*, 14(5):R49–R61, 2003.

[43] A. Martin, R. Badcock, C. Nightingale, and G. F. Fernando. A novel optical fiber-based strain sensor. *IEEE Photonics Technology Letters*, 9(7):982–984, 1997.

[44] B. S. Wang, J. Stathis, V. Llc, and C. Drive. Technologies of Fiber Fusion and Fused Device Fabrication for Sensing Applications. *Proc. of SPIE*, 7677(2):2–7, 2010.

[45] Z. Tian and S. S. H. Yam. In-line abrupt taper optical fiber Mach-Zehnder interferometric strain sensor. *IEEE Photonics Technology Letters*, 21(3):161–163, 2009.

[46] B. Huttner, J. Reecht, N. Gisin, R. Passy, and J. P. Von Der Weid. Local birefringence measurements in single-mode fibers with coherent optical frequency-domain reflectometry. *IEEE Photonics Technology Letters*, 10(10):1458–1460, 1998.

[47] W. Bock, J. C. J. Chen, T. Eftimov, and W. Urbanczyk. A photonic crystal fiber sensor for pressure measurements. *IEEE Transactions on Instrumentation and Measurement*, 55(4):1119–1123, 2006.

[48] F. C. Fávero, S. M. M. Quintero, C. Martelli, A. M. B. Braga, V. V. Silva, I. C. S. Carvalho, R. W. A. Llerena, and L. C. G. Valente. Hydrostatic pressure sensing with high birefringence photonic crystal fibers. *Sensors (Basel, Switzerland)*, 10(11):9698–711, 2010.

[49] R. Calvani, R. Caponi, and F. Cisternin. Polarization Measurements on Single-Mode Fibers. *Journal of Lightwave Technology*, 7:1187–1196, 1989.

[50] S. Rota-Rodrigo, M. Bravo, a. M. R. Pinto, and M. López-Amo. High-sensitivity PCF sensing head for strain measurement. *Proc. of SPIE*, 8421:842136–842136–4, 2012.

[51] A. B. Vakhtin, D. J. Kane, W. R. Wood, and K. A. Peterson. Common-path interferometer for frequency-domain optical coherence tomography. *Applied Optics*, 42(34):6953–6958, 2003.

[52] R. Anderson, H. R. Bilger, and G. E. Stedman. "Sagnac" effect: A century of Earth-rotated interferometers. *American Journal of Physics*, 62(11):975–985, 1994.

[53] Y. Yang, M. Ye, W. Duan, W. Jin, C. Liu, and S. Ruan. Polarization maintaining photonic crystal fiber IFOG. *Proc. of SPIE*, 8421(c):84210D–84210D–4, 2012.

[54] S. J. Spammer, P. L. Swart, and A. A. Chtcherbakov. Merged Sagnac-Michelson interferometer for distributed disturbance detection. *Journal of Lightwave Technology*, 15(6):972–976, 1997.

[55] Y.-J. Rao. Recent progress in fiber-optic extrinsic Fabry-Perot interferometric sensors. *Optical Fiber Technology*, 12:227–237, 2006.

[56] M. Jiang and E. Gerhard. Simple strain sensor using a thin film as a low-finesse fiber-optic Fabry-Perot interferometer. *Sensors and Actuators, A: Physical*, 88 (1):41–46, 2001.

[57] Y.-J. Rao, M. Deng, D.-W. Duan, X.-C. Yang, T. Zhu, and G.-H. Cheng. Micro Fabry-Perot interferometers in silica fibers machined by femtosecond laser. *Optics Express*, 15(21):14123–14128, 2007.

[58] F. C. Favero, G. Bouwmans, V. Finazzi, J. Villatoro, and V. Pruneri. Fabry

Perot interferometers built by photonic crystal fiber pressurization during fusion splicing. *Optics Letters*, 36:4191–4193, 2011.

[59] C. Xiaopei, S. Fabin, W. Zhuang, H. Zhenyu, and A. Wang. Micro-air-gap based intrinsic Fabry-Perot interferometric fiber-optic sensor. *Applied Optics*, 45:7760–7766, 2006.

[60] F. C. Favero, L. Araujo, G. Bouwmans, V. Finazzi, J. Villatoro, and V. Pruneri. Spheroidal Fabry-Perot microcavities in optical fibers for high-sensitivity sensing. *Optics Express*, 20(7):7112, 2012.

[61] L.-C. Xu, M. Deng, D.-W. Duan, W.-P. Wen, and M. Han. High-temperature measurement by using a PCF-based Fabry Perot interferometer. *Optics and Lasers in Engineering*, 50:1391–1396, 2012.

[62] Q. Yu and X. Zhou. Pressure sensor based on the fiber-optic extrinsic fabry-perot interferometer. *Photonic Sensors*, 1(1):72–83, 2011.

[63] J. S. Leng and A. Asundi. Real-time cure monitoring of smart composite materials using extrinsic Fabry-Perot interferometer and fiber Bragg grating sensors. *Smart Materials and Structures*, 11(2):249–255, 2002.

[64] M. Schmidt, B. Werther, N. Fuerstenau, M. Matthias, and T. Melz. Fiber-optic extrinsic Fabry-Perot interferometer strain sensor with less than 50 pm displacement resolution using three-wavelength digital phase demodulation. *Optics Express*, 8(8):475–480, 2001.

[65] W.-C. Du, X.-M. Tao, and H.-Y. Tam. Fiber Bragg grating cavity sensor for simultaneous measurement of strain and temperature. *IEEE Photonics Technology Letters*, 11(1):105–107, 1999.

[66] S. Poeggel, D. Tosi, G. Leen, and E. Lewis. Low-cost miniature fiber-optic ex-

trinsic Fabry-Perot interferometric pressure sensor for biomedical applications. *Advanced Microscopy Techniques III*, 8797:1–6, 2013.

Chapter 3

Theory and applications

3.1 Introduction

Photonic crystal fibres (PCFs) confine light in their core using a hole structure, a distribution of air filled cylinders of small diameter that run parallel to the propagation axis of the fibre [1]. This is fundamentally different to light confinement in traditional optical fibres, which use a refractive index contrast between a the core and the cladding of the fibre [2].

To understand how the light guiding properties PCFs diverge from traditional optical fibres like single mode fibre (SMF) or polarisation maintaining fibre (PMF), their method of propagation needs to be well understood. This chapter presents the theory that describes light propagation in both traditional optical fibres and PCFs. Section 3.2 provides a mode theory description of light confinement in traditional optical fibres such as single mode fibre. Section 3.3 extends the mode theory description of light confinement in PCFs to include their unusual properties such as endlessly single mode and photonic bandgap.

3.2 Light confinement in optical fibres

Single mode fibre is composed of two layers of glass with different refractive indexes. as shown in Figure 3.1. The refractive index of core is greater than the refractive index of the cladding. The refractive index difference is achieved by doping the core with elements such as germanium which increases its refractive index [3]. Light is confined to the core due to total internal reflection, and propagates along the propagation axis of the fibre [3].

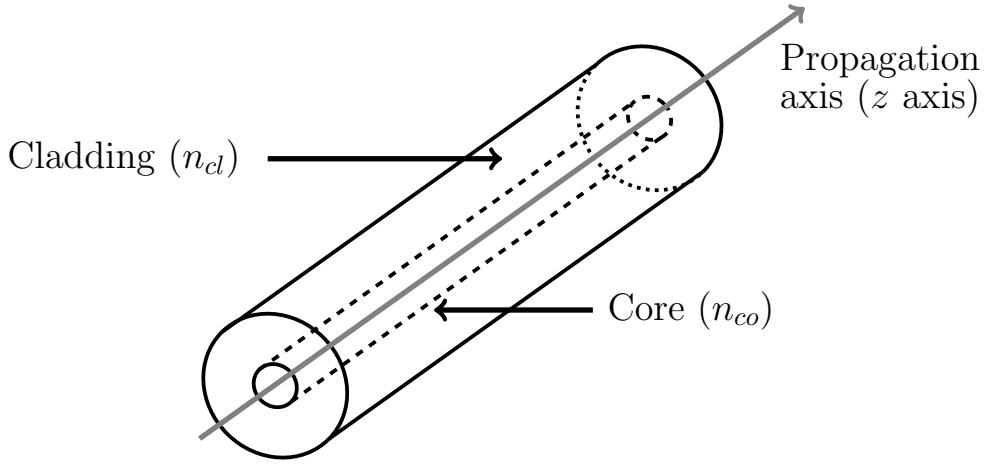

Figure 3.1: Single mode fibre is composed of a smaller core, and an outer cladding. The propagation axis is the direction light propagates through the fibre.

A simplistic description of total internal reflection uses Snell's law; $n_1 Sin(\theta_1) = n_2 Sin(\theta_2)$. Snell's law relates the deflection of a light ray as it passes through the interface of two dielectric mediums [3]. The angle of deflection is related to the difference in refractive index between the two mediums. When light propagates from a medium with a higher refractive index into a medium with a lower refractive index, there is a critical angle where the light is deflected to propagating along the interface. Light cannot propagate like this but is instead reflected at the interface back into the medium with the higher refractive index. This source of reflection is referred to as total internal reflection.

This is described as the ray model of light propagation in optical fibres. It is insufficient to describe light propagation in photonic crystal fibres. A more advanced

model uses mode coupling to described confinement in an optical fibre. This approach is described here as it is better understood initially when applied to single mode fibre. Starting at the dispersion relationship: $\omega = \frac{c}{n}\beta$ [4]. ω is the angular frequency of the wave that is propagating through a dielectric medium with refractive index n, wave speed c in vacuum, and wave vector β. β can be broken into three components aligned with each of the cardinal directions; β_x, β_y, and β_z, where $\beta = \sqrt{\beta_x^2 + \beta_y^2 + \beta_z^2}$. In an optical fibre, such as the one shown in Figure 3.1, symmetry means that β_x and β_y are the same. They are described by β_r, where r is the direction perpendicular to the main axis of the fibre. The β_z component is taken to be parallel to the axis of the optical fibre.

You can state that all modes propagating through a dielectric medium in the z-direction have to possess the relationship $\omega \geq \frac{c}{n}\beta_z$ by definition. The dispersion relationship for a glass cylinder, such as the core of an optical fibre, is shown in Figure 3.2. For light of a specific mode to propagate along the cylinder, that mode must have an ω and β_z that satisfies the relationship $\omega \geq \frac{c}{n}\beta_z$. In Figure 3.2 this is the grey area above the $\omega = \frac{c}{n}\beta_z$ line.

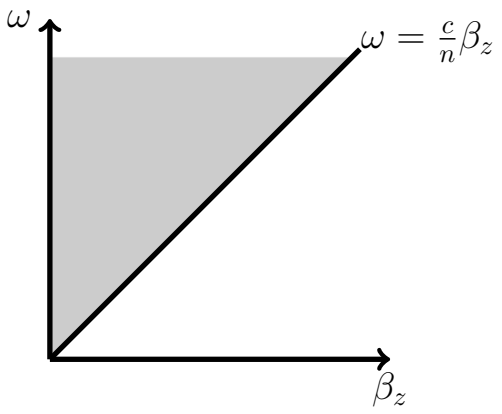

Figure 3.2: ω is the angular frequency of the mode propagating through a glass cylinder. β_z is the wave vector of the mode propagating along the axis of the cylinder. $\omega = \frac{c}{n}\beta_z$ is the line for the minimum angular frequency value required for that mode to propagate in a dielectric medium with refractive index n. This region is highlighted in grey. Adapted from Joannopoulos et al. [5].

An optical fibre, such as the one shown in Figure 3.1, is composed of two glass

cylinders, one nestled at the centre of the other. The core cylinder has a refractive index larger than the surrounding cladding. The dispersion relationship for the fibre is shown in Figure 3.3. Modes that have $\beta_z \leq \frac{n_{co}}{c}\omega$ can propagate in the core, and modes that have $\beta_z \leq \frac{n_{cl}}{c}\omega$ can propagate in both the core and the cladding of the fibre. Modes that satisfy the condition $\frac{n_{cl}}{c}\omega \leq \beta_z \leq \frac{n_{co}}{c}\omega$ can only propagate through the core of the fibre, and not into the cladding. These modes are confined to the core of the fibre, and remain guided by the fibre.

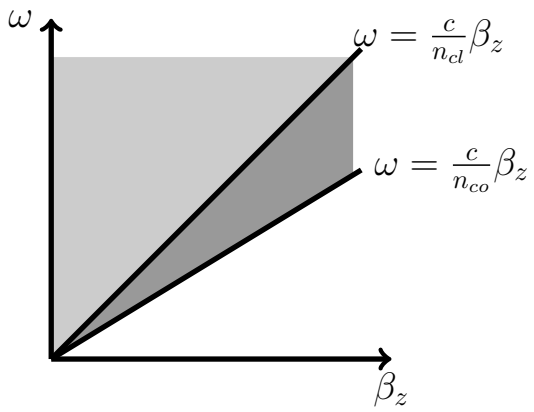

Figure 3.3: ω is the angular frequency of the mode propagating through an optical fibre. β_z is the wave vector of the mode propagating along the axis of the cylinder. n_{co} is greater than n_{cl}. Adapted from Joannopoulos et al. [5].

Anything that changes the refractive index of the core or cladding, can allow modes that had initially been confined to the core to propagate in the cladding as well. It was described in Chapter 2 that long period gratings (LPG) can couple light between the core and the cladding for a specific wavelength. The LPG can be considered to weaken the wave guiding properties of the fibre for a specific wavelength, that wavelength is no longer confined to the core but propagates in the cladding as well [6].

In the next section this description of light confinement in traditional fibres will be extended to describe how light is confined in the core of PCF, even when the refractive index of the core is lower than that of the cladding.

3.3 Photonic crystal fibres

There are numerous designs that allow photonic crystal fibre to confine light to its core. Figure 3.4 shows the three design classes of PCF; (a) Bragg fibre, (b) hollow core fibre, and (c) solid core fibre [5, 2]. PCF is constructed of two materials with different refractive indexes, arranged in a periodic structure [1]. Bragg fibres are built from concentric layers, and act like fibre Bragg gratings (FBGs), reflecting light back into the core [5, 2, 7]. Hollow core fibres are built from a periodic lattice of holes in the cladding that run parallel to the propagation axis of the fibre, with a large hole at their centre [5, 2, 7]. Both Bragg fibres and hollow core fibres utilise a photonic bandgap to confine light to their core [5, 2, 7], this will be described in greater detail later in this section. Solid core fibres have a periodic lattice of holes like hollow cores, but have a silica core which the light propagates down.

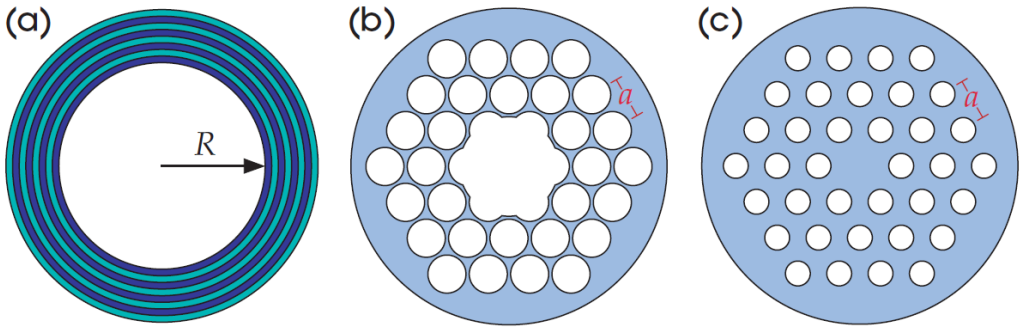

Figure 3.4: Three examples of photonic crystal fibres; (a) Bragg fibre, (b) hollow-core fibre, and (c) solid-core fibre. Reproduced from Joannopoulos et al. [5]

Like SMF, solid core fibres use total internal reflection to confine light to their cores. SMF uses the refractive index contrast between its higher refractive index core and its lower refractive index cladding. Solid core fibre can provide this contrast by reducing the refractive index of its cladding by inserting the air holes as a periodic lattice around the core. Figure 3.5 shows a commercially available PCF, the core and the cladding have been highlighted. The birefringence of this PCF is produced by the two enlarged air holes adjacent to its core, this reduces the refractive index of this axis of the cross section of the PCF. As the refractive index contrast between

the cladding and the core of the PCF is produced by the air hole structure, the fibre doesn't need to be doped to guide light [8].

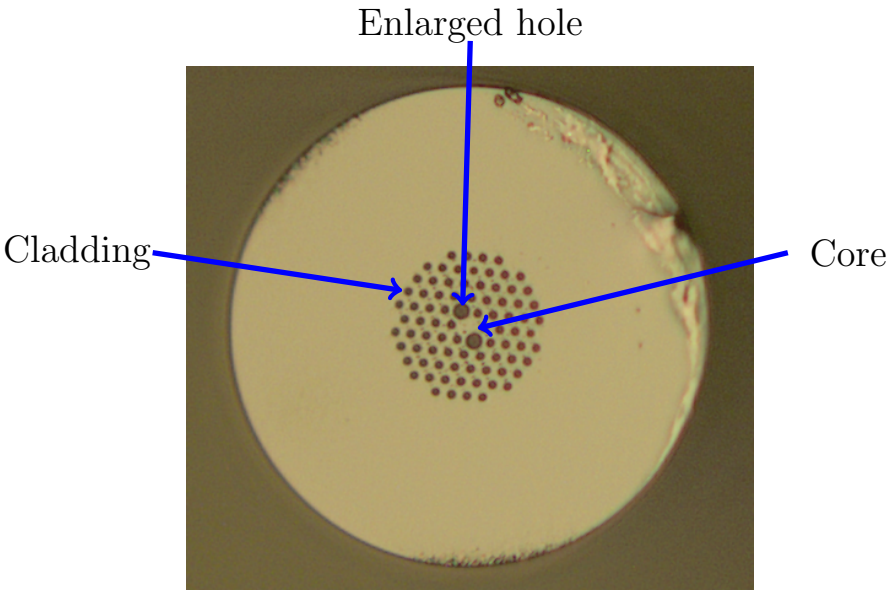

Figure 3.5: Image of PM1550, a solid core birefringent PCF produced by NKT photonics. Image taken with an Olympus BX51 microscope. The birefringence is produced by the enlarged holes.

A benefit of this structure is that solid core fibre can be constructed that is endlessly single mode [2]. Single mode fibre is constructed to have a small core, that can only guide one fundamental mode above a cut-off wavelength [3]. For wavelengths below this cut-off the core is large in comparison, and can support multiple modes. Endlessly single mode fibre doesn't possess a cut-off wavelength, and only guides the fundamental mode regardless of wavelength [5, 2, 7]. There are two descriptions of the causes of this endlessly single mode property. Joannopoulos et al. [5] state that shorter wavelengths penetrate less into the PCF cladding from their core, and therefore experience a higher refractive index of the cladding than for longer wavelengths. As a consequence of this they experience a lower effective refractive index difference between the cladding and the core. This reduces the confinement for shorter wavelengths such that higher order modes are not confined to the core of the PCF. Poli et al. [2] states that endlessly single mode property

is due to the different intensity profiles of higher order modes when compared to the fundemental mode. Light is evanescent in air [2], and provides a strong barrier for light. The air hole structure can be imagined as a "sieve", with the air holes the "wire mesh". The fundamental mode is a lobe that acts like a "grain of rice", trapped in the mesh. Higher order modes have finer lobes that can escape through the gaps in the mesh. The endlessly single mode property of the PCFs has been experimentally verified [2], and has provided benefits in high power delivery [8].

Hollow core PCF is also capable of high power delivery since the high power doesn't damage the air in the core of the fibre [8]. An example of hollow core fibre is shown in Figure 3.6. The fibre is NL-1.5-670-02, a commercially available PCF produced by NKT photonics. PCF can be designed for specific non-linear properties as well as dispersion profiles [2]. NL-1.5-670-02 is designed to be highly non-linear for supercontiniumm generation [9] (this reference is reproduced in Appendix A). Hollow core and Bragg fibres require the photonic bandgap to confine light to their core. This effect is similar to the reflection properties of fibre Bragg gratings (FBGs). When light crosses an interface between two dielectric mediums with different refractive indexes, some of the light propagates across the interface and some is reflected [3, 4].

If the light is propagating through a dielectric medium with a periodic change in refractive index, as shown in Figure 3.7, the reflections from each interface can destructively interfere with the light propagating through the medium [4, 10]. This occurs only for modes with specific wavelengths where the Bragg condition is met, $\lambda_B = 2n\Lambda$, in Figure 3.7 $\Lambda = a$. A mode with this value of λ cannot exist inside the medium, and therefore cannot propagate through it. Since it cannot propagate through it, it reflects off the first interface.

The hole structure of the PCF produces regions where modes of specific propagation constants cannot exist in the cladding, and therefore light of those modes remains confined to the core. Following the formalism used to produce Figures 3.2

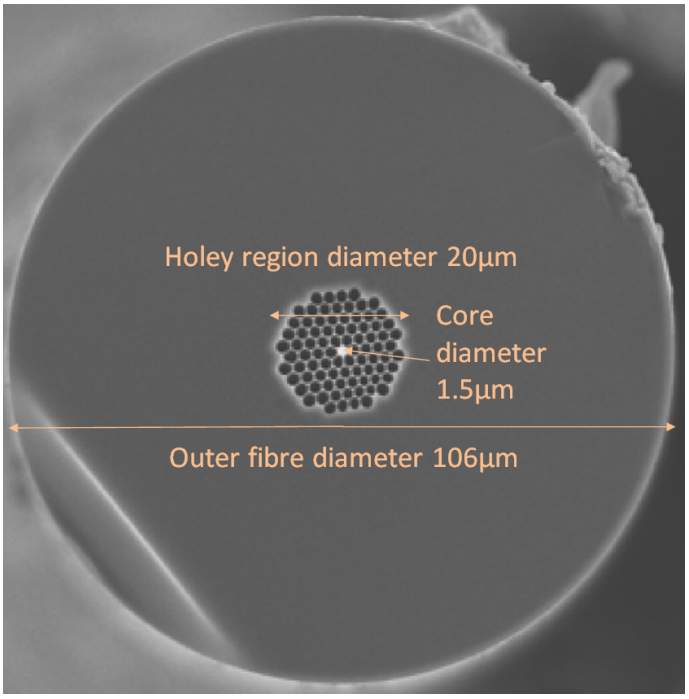

Figure 3.6: Image of the cross section of a PCF. This fibre is NL-1.5-670-02, a hollow core PCF produced by NKT photonics. Photograph and fibre properties provided by Thor Labs [9].

and 3.3, the dispersion relation of a PCF that uses bandgaps is shown in Figure 3.8. Modes from the region above the vacuum dispersion relation, $\omega = ck_z$, can propagate in air. Modes in the blue region can propagate in the cladding of the fibre. However there is a region highlighted where a mode can propagate in air, but not in the cladding of the fibre. This is a bandgap, and that mode is confined to propagating through the air in the hollow core fibre.

The bandgap means that the fibre can be filled with air, or other fluids with a refractive index lower than the cladding [8]. This is a very versatile property and has been used for high non-linearity for supercontinuum generation [2], and even transportation of polystyrene spheres along their length [11].

In the next section the guiding principles for both traditional fibres and PCFs will be summarised.

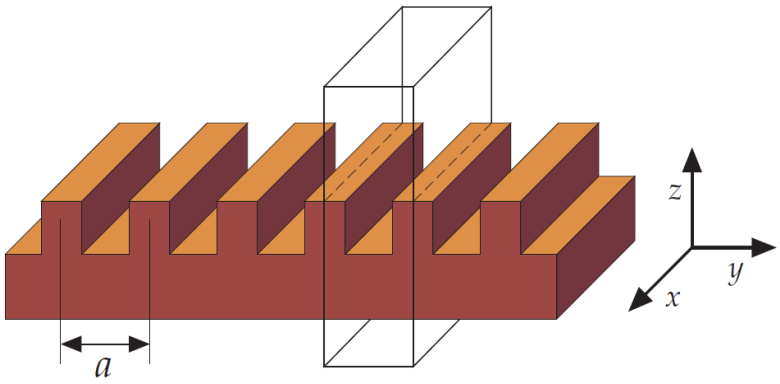

Figure 3.7: Periodic refractive index change in a dielectric, with a periodicity of a. Reproduced from Joannopoulos et al. [5]

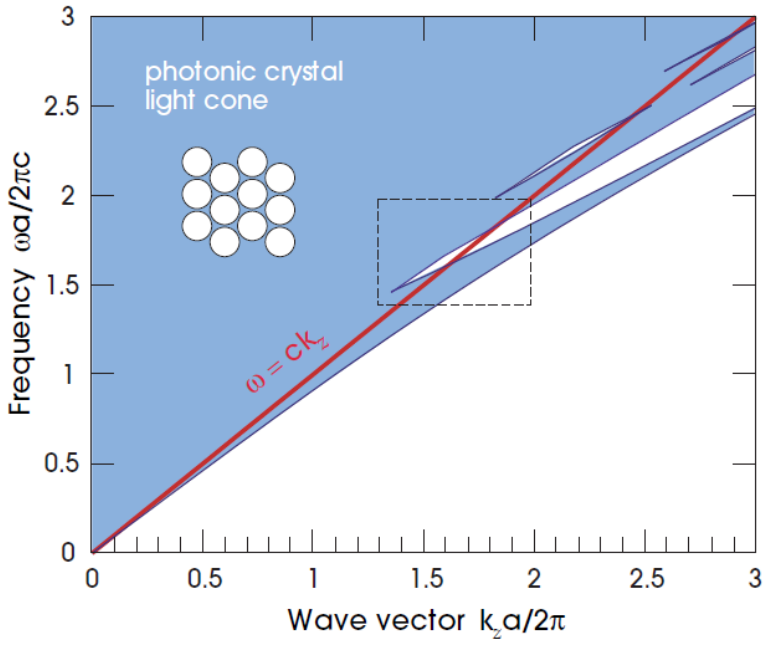

Figure 3.8: The dispersion relationship of PCF that utilises a Bandgap. Reproduced from Joannopoulos et al. [5]

3.4 Chapter summary

Light confinement was discussed throughout this chapter. For both traditional fibres and PCFs, for a given angular frequency there is a range of propagation vectors where the mode is confined to the core of the fibre. This is due to the refractive index difference between the core and cladding of the fibre.

PCFs can confine light with a refractive index difference between the core and cladding like a traditional fibre. It can also confine light with a photonic bandgap. Solid core PCF can be structured to be endlessly single mode, which allows it to be single mode for all wavelengths. Hollow core fibre uses the photonic bandgap to confine light of specific wavelengths to its core, making it more resistant to damage and allowing high power delivery.

Due to the line confining structure of PCF, it has different difficulties when being spliced to other optical fibres, or other PCF. These difficulties are described in the following chapter, and their implications in this work.

References

[1] A. Massaro, editor. *Photonic Crystals; Introduction, Applications and Theory.* InTech, 1st edition, 2012.

[2] F. Poli, A. Cucinotta, and S. Selleri. *Photonic Crystal Fibers; Properties & Applications.* Springer Series in Material Sciences, 1st edition, 2007.

[3] J. Crisp and B. Elliott. *Introduction to Fiber Optics.* Elsevier, third edition, 2005.

[4] D. L. Lee. *Electromagnetic principles of integrated optics.* John Wiley and Sons, second edition, 1986.

[5] J. J. D. Joannopoulos, S. Johnson, J. N. J. Winn, and R. R. D. Meade. *Photonic crystals: molding the flow of light.* Princeton University Press, 2nd edition, 2008.

[6] S. W. James and R. P. Tatam. Optical fibre long-period grating sensors: characteristics and application. *Measurement Science and Technology*, 14(5):R49–R61, 2003.

[7] F. Poletti. *Direct and inverse design of microstructured optical fibres.* PhD thesis, Southampton, 2007.

[8] R. Paschotta. *Field Guide to Optical Fiber Technology.* SPIE Field Guides, 1st edition, 2010.

[9] B. Photonics. NL-1.5-670-02. Technical report, Blaze Photonics, 2003.

[10] A. Ikhlef, R. Hedara, and M. Chikh-bled. Uniform Fiber Bragg Grating modeling and simulation used matrix transfer method. *Computer Science*, 9:368–374, 2012.

[11] F. Benabid, J. Knight, and P. Russell. Particle levitation and guidance in hollow-core photonic crystal fiber. *Optics Express*, 10(21):1195–1203, 2002.

Chapter 4

Photonic crystal fibre splicing

4.1 Introduction

Yablon [1] defines optical fibre fusion splicing as "the process by which a permanent, low-loss, high-strength, welded joint is formed between two optical fibers". Other approaches to connect two optical fibres include connectorization, mechanical splicing, or free-space optical coupling [1]. Connectorized fibres have a special device that covers the fibre end, which allows it to be coupled and uncoupled to other connectors or devices [1]. Connectors typically exhibit higher reflectance and loss than either fusion splices or mechanical splices [1]. These methods of splicing require bulky components to couple the light from one fibre to the other [2]. Mechanical splices use a special housing to hold two cleaved fibre tips close to each other, usually with index matching gel between the fibre tips to maximise coupling and minimise reflection [1]. As the refractive index of most compounds used as index matching gel varies with temperature, the optical performance of mechanical splices using the gel is dependent on the ambient temperature [1]. Free space coupling uses bulky glass lenses and mirrors to focus light into the core of an optical fibre, or focus light from the core into other optics [1]. Free space coupling exhibits relatively high reflectivity and is sensitive to dust and other contaminants entering the optical path

[1]. In comparison to the other approaches optical fibre fusion splice joints are compact, with a thickness equivalent to the fibre diameter before splicing [1]. Fusion splicing typically produces lower loss and reflectance at the splice than alternative optical fibre connecting technologies [1]. Fusion splices are permanent, and block contaminants from entering the optical path [1].

Photonic crystal fibres present specific challenges with regard to optical fibre fusion splicing. A factor that increases loss in these connections, unique to PCF, is physical damage to the hole structure of the PCF, referred to as hole collapse [3]. Hole collapse is described in greater detail later in this chapter. This increased loss has been found to negate the potential benefits of using PCF in applications that already use optical fibre such as interferometric fibre optic gyroscopes (IFOGs) [4]. PCF based IFOGs have low thermal sensitivity, low bending losses, and low cross talk between the two orthogonal polarisation modes, which can provide greater sensitivity to rotation if the loss across the splice from non-PCF to PCF can be mitigated [5].

The work in this research to mitigate loss across splices between photonic crystal fibre, and either single mode fibre (SMF) or polarisation maintaining fibre (PMF) is presented in this Chapter. This supports the experimental work discussed in Chapters 5 and 6.

As detectors have a limit on the lowest power of light incident on them, this creates a requirement for the minimum required power of light initially injected into the optical system. This power requirement is the minimum power required for detection, and the summation of all the losses across the system. As the systems presented in Chapters 5 and 6 interrogated fibres in reflection, the loss across a PCF to non-PCF is effectively doubled. To minimise this requires low loss robust splices.

Chapter 5 has a sensor design that utilises an effect noticed during the construction of this work. Chapter 6 uses short lengths of PCF as a sensor for strain. The PCF is spliced to SMF, and reducing the loss across the splice was found to be

advantageous for multiple sensors in series.

Since the first reported experimental work splicing PCF to SMF by Bennett et al. [6] in 1999, several approaches have been suggested to splice PCF to SMF. PCFs can be designed to have mode field diameters (MFDs) that match the SMF to which they will be spliced [7, 8, 9]. If two fibres that are spliced together possess different mode field diameters, this causes loss when light from the fibre with the larger MFD propagates into the fibre with the smaller MFD [10], which will be described in greater detail in this Chapter. Low-loss splices of solid-core PCF to SMF have been produced by using fusion splicers [6, 11, 12] or CO2 lasers [13, 14]. Fusion splicers have also been used to produce low-loss splices between hollow-core PCFs and SMFs which possess similar MFDs [15, 16, 17].

Zuoming et al. [10] presented a detailed description of a method of using arc fusion to splice PM1550, a commercially available birefringent PCF, to SMF. This was the basis of the work in this research to develop an approach to forming consistent and robust low-loss splices between PCF and PCF, or PCF and non-PCF. Low-loss in this case means loss lower than $0.1dB$, in comparison to a normal SMF to SMF splice which has loss of order $0.01dB$. Robust in this case means able to survive handling in the setup. Reducing loss for PCF to SMF splices will make it easier and more convenient to incorporate PCF into fibre optic sensor arrangements. While this will not change other issues such as the cost of PCF, it will allow short lengths to be used such as in the setups shown in Chapters 5 and 6.

In the following section fusion splicing is described in greater detail and how it relates to producing PCF splices.

4.2 Fusion splicing

Fusion splicing can be broken down into a series of steps, as described by Yablon [1]. The optical fibres have their protective polymer coating removed, referred to

as stripping [18], which allows access to the glass fibre. The fibres are cleaved, to produce flat fibre end faces. The fibre ends are laterally aligned with each other; if the fibres are birefringent their rotational axes are aligned. The fibre tips are heated to their softening point, so that when they are pressed together they form a joint. The splice is often proof tested to determine its long term mechanical reliability.

The first step, stripping the optical fibre's polymer coating, is important since it can damage the optical fibre and weaken its long term mechanical reliability [1]. The polymer coating needs to be stripped since the high temperatures used to form the joint can damage the coating, and damage the heated glass in contact with the coating. These polymer coatings often have shape memory, known as curl, which can interfere with aligning the fibre ends [1]. Stripping can be done with solvents such as methyl chloride, or hot acids, which leave defect free glass. More convenient approaches are mechanical stripping, which can weaken the fibre when compared to solvent stripping [1].

The second step is cleaving the optical fibres, this is because flat fibre end faces are required for the minimum deformation of the fibres when the end faces are brought together [1]. Flat in this case means no notches or bumps in the fibre's end face greater than a few percent from the surface [1]. An optical fibre can be cleaved by placing it under sufficiently high tensile stress, around a sufficiently large surface crack [1]. This crack then propagates across the fibre cross section until the fracture crosses to encompass the whole fibre cross section, and the fibre is detached into two parts [1]. Cleaving is a violent and difficult to control process, and cleavers will periodically produce defective cleaves [1]. Defective cleaves, such as large chips or angled end faces, will produce misshapen splices, and require the fibre end to be recleaved before the splice is produced [1].

The third step is to align the fibre end faces before splicing. The fusion splicer, the device that splices the fibres, needs to position the end faces relative to each other. The two fibres are held in chucks, or v-grooves, that can move the fibre ends

with four degrees of motion; x, y, z and θ. These are two transverse directions, one direction that brings the faces together, and one rotational orientation around the propagation axis of the fibre. The next component of the splicing process is the method of verifying the position of the fibre ends for splicing. There are three approaches for alignment; passive alignment, active alignment, and light injection and detection (LID) [1].

Passive alignment is where the fusion splicer uses the known positions of the v-grooves that grip the fibres, to move the fibres into alignment [1]. Passive alignment is fast and simple compared to the other approaches of fibre alignment [1]. This approach is less effective for fibres with smaller diameter cores such as SMF, since such fibres are more sensitive to core misalignment. If dirt is on the fibre or in the v-groove, it interferes with the correct position of the fibres and passive alignment will not function properly [1]. Due to the limitations of passive alignment, Yablon [1] states that "nearly all contemporary optical fibre fusion splicers employ some form of active alignment".

The most common active alignment approach is to use an imaging system to measure the position of the fibre ends, and then a microprocessor to activate the motors attached to the v-grooves to manoeuvre the fibre ends [1]. This is achieved with a light source that illuminates the fibre ends to be imaged by a CCD camera as shown in Figure 4.1 [1]. The microprocessor calculates the position of the fibre ends relative to each other, by measuring their apparent size with regards to each other, and the separation between the fibre ends [1, 19]. This approach is capable of compensating for small amounts of fibre curl, core eccentricity, dirty fibres or v-grooves, and cladding diameter variations [1].

Image-based active fibre alignment systems can align the fibre ends using either their cladding position, or the image of their cores. Aligning using the cores is termed a profile alignment system (PAS), as it aligns the fibre ends based on their refractive index profile [1, 19]. Figure 4.2 is a diagram of how the PAS measures the

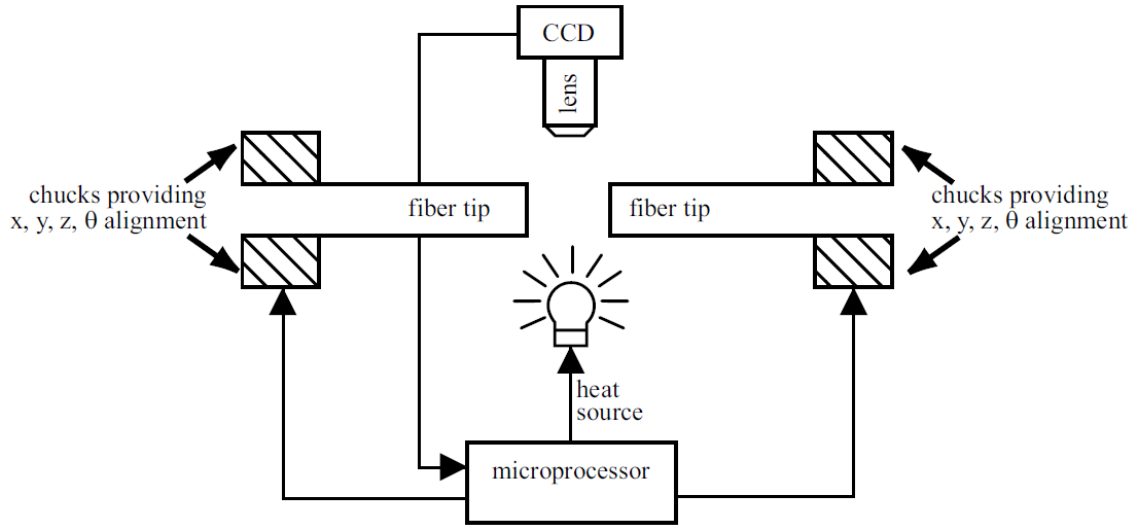

Figure 4.1: To align optical fibres for splicing, their positions are assessed using a CCD camera. The chucks hold the fibres in place and can rotate them if the fibres are birefringent. Figure reproduced from Yablon [1].

position of the optical fibre. Light hitting the fibre is refracted due to the angle of incidence on the fibre, and the refractive index profile of the fibre along the path the light takes through the fibre. The core of the fibre, for SMF and PMF, has a larger refractive index than the surrounding cladding. Light that travels through the core is deflected more than light that only travelled through the cladding. This allows the PAS to measure the position of the core. For birefringent fibre the refractive index profile is different depending on the angular orientation of the fibre. In Figure 4.2 this is shown by the position of the stress lobes. Panda style PMF has two stress lobes that induce its birefringence [18], these create the two orthogonal polarisation axes of the fibre. They increase the refractive index of the fibre along a line that bisects the fibre and is parallel to the stress lobes [18]. This means as the fibre is rotated the refractive index profile changes [18]. This can be detected by the CCD camera, and allows the PAS to align the fibre by a polarisation axis.

Light injection and detection (LID) systems monitor the optical power that transmits through the small gap between fibres before they are spliced [1]. Light is coupled into the free end of one fibre, while a power meter is attached to the free end of the other fibre [1]. A microprocessor uses an algorithm to move the fibres to maximise

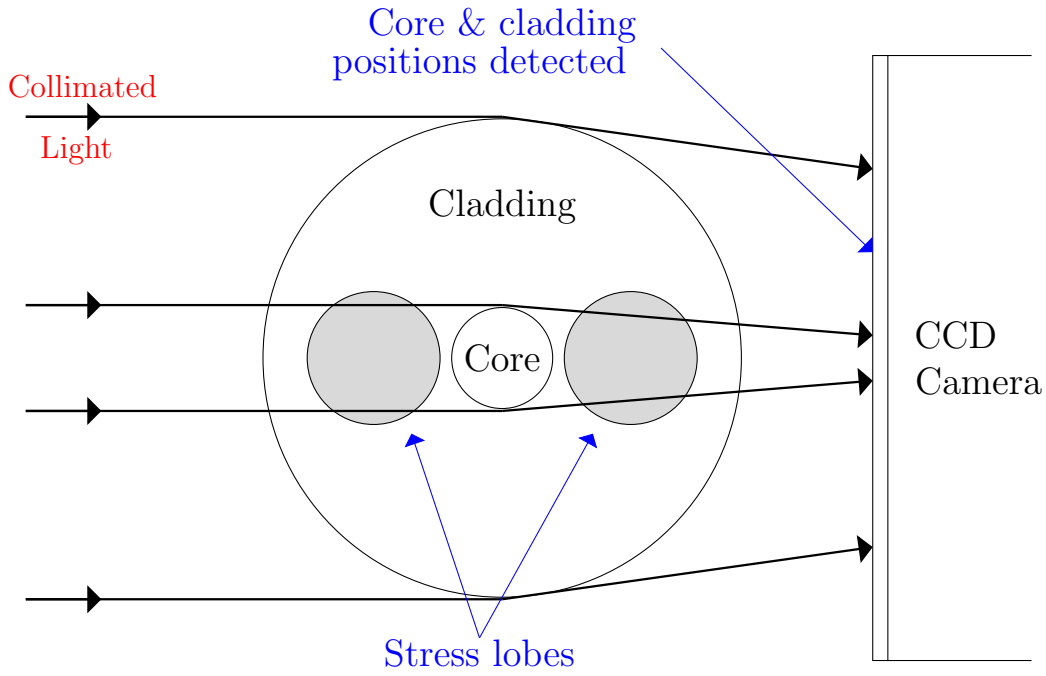

Figure 4.2: Description of the profile alignment system (PAS). The stress lobes of the Panda style PMF are shown. As the fibre is rotated the refactive index profile changes and changes the intensity profile incident on the CCD camera. Figure reproduced with additions from Crisp and Elliott [18].

the transmitted light. This is taken to be the optimal position of the fibres [1]. This alignment approach is sensitive to imperfect cleave angles, which shifts the position of maximum transmitted light away from the optimum position for fibre splicing [1].

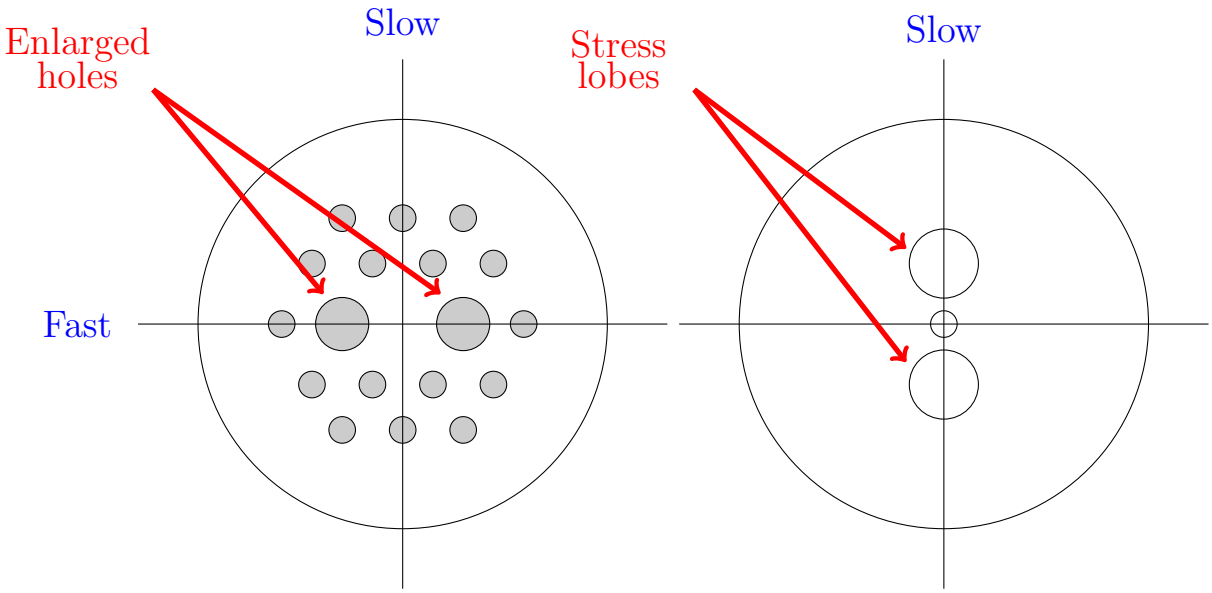

(a) PM-PCF (b) PANDA

Figure 4.3: Comparison of optical axes of PM-PCF to Panda style PMF.

It was described in Chapter 1 that PCF is composed of a hole structure that guides the light within it. This structure can be modified to produce birefringent photonic crystal fibre (PM-PCF), a diagram of PM-PCF is shown in Figure 4.3 (a). The fast and slow axes of the PM-PCF are shown, the enlarged holes reduce the refractive index along a line that bisects them and the core of the PCF. This produces a fast axis, which is differentiated from the slow axis which does not possesses the enlarged holes. Figure 4.3 (b) shows a Panda style PMF as a comparison to the PM-PCF. The PCF's hole structure obscures the side view of the core of the PCF, which means that side illumination cannot reveal the orientation of the polarisation axes of the PM-PCF. To align the fibre by those, the fibre end face must be observed.

Some arc fusion splicers, such as the Fujikura 100P+ possess an end view capability. This is a mirror that allows the CCD camera to observe the end face of the PM-PCF. Figure 4.4 is an image taken by this end view system of PM1550. Light is coupled into the PM-PCF from LEDs inside the splicer, which illuminates the core and allows it to be positioned by the splicer. The light also allows the enlarged holes to be observed, which allows the splicer to orientate the orthogonal polarisation axis

of the PM-PCF when splicing it to other birefringent fibre.

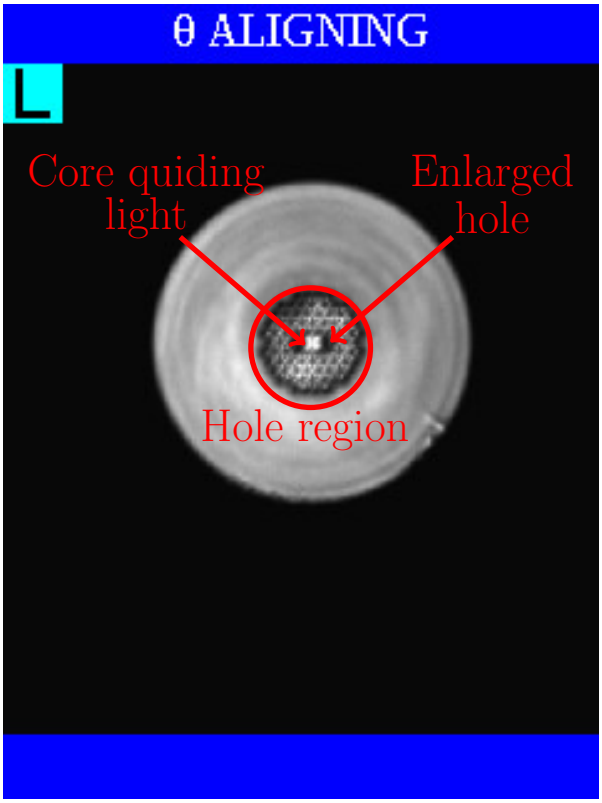

Figure 4.4: Fibre end of PM1550 taken using the end view scope of the Fujikura 100P+ arc fusion splicer. This is during θ alignment of the PM-PCF to PMF splice.

After the fibre end faces have been aligned, they need to be heated to their softening point and brought together. To weld two silica fibres together requires the fibre ends to be at 2000 $^{\circ}C$ [18]. The heat sources that can be employed in fusion splicing are; an electric arc, a heated metal filament, a flame, or a laser [1]. Almost all commercial fusion splicers use an electric arc as a heat source, with the majority of the rest using a heated metal filament [1]. The most commonly used laser is a CO_2 system, as silica strongly absorbs at 10.6 μm. Laser heating can focus on a small region of the fibre tip, whereas the other approaches heat an extended area [1, 13].

Heat transfer in fusion splicing is a complex time-dependent process [1]. It is impractical to know the actual temperature of the fibre ends as they are being heated [1]. Proxies are used, and in the case of electical arc heating, the main arc current is

used [1, 19, 10]. The electrical arc approach is composed of two pointed electrodes, shown in Figure 4.5, with the heating provide by an electical discharge between the electrodes. This creates a heating profile with the hottest temperatures close to the electrodes. Figure 4.5 shows this heating profile, which is rotationally symmetric around the axis between the two electrodes. Distance from this axis is represented by r, and is the vertical axis on Figure 4.5. The distance along the axis between the electrodes is z, and is the horizontal axis. When splicing optical fibres, the end faces will meet at $r = 0$ and $z = 0$. This heating profile is a component in hole collapse in PCFs, described in Section 4.3.

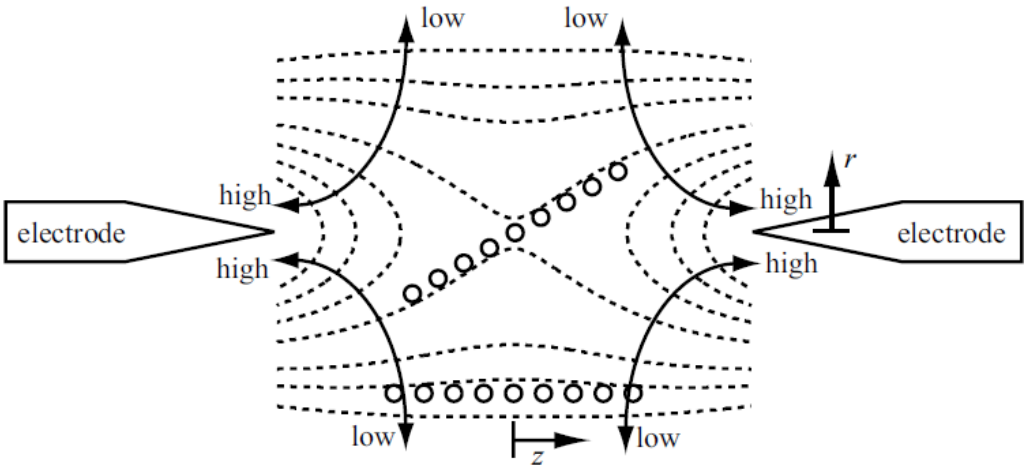

Figure 4.5: Illustration of current and energy density distribution in an arc fusion splicer. Current and energy density is rotationally symmetric about the r = 0 axis. Dashed lines represent contours of constant current flux or constant energy density. Curved solid line with arrow illustrates direction of higher or lower current density. Figure reproduced from Yablon [1].

When the fibre end faces are aligned, they have to be brought together to be heated. Figure 4.6 is a diagram that relates the position of the fibres with regards to the arc points for an electrical arc fusion splicer. The heating cycle is illustrated in Figure 4.7. The fibre first experiences prefusion, which uses a short duration electrical discharge to clean the fibre end surfaces of particles such as dust. This is done when the fibre ends are a fixed distance apart, and the temperature of the electrical arc is less than the melting point of the silica. An example of the fibres

that have just experienced prefusion cleaning is shown in Figure 4.8 (a).

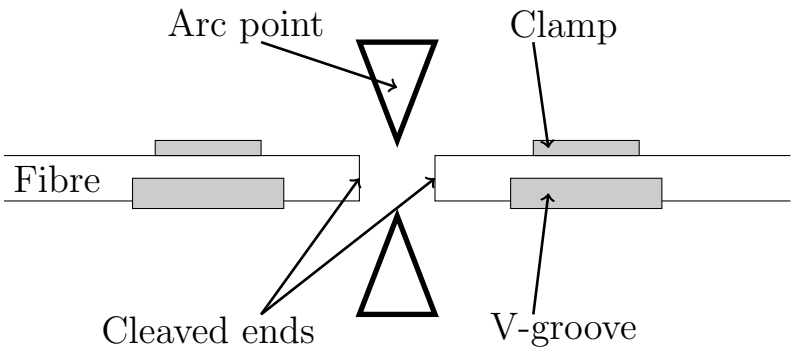

Figure 4.6: Arc fusion splicing setup. Figure reproduced from Crisp and Elliott [18].

After the fibres' end faces have been cleaned, there is a brief pause to allow the dust to escape. Then the two fibre ends are heated to their softening point and brought together, as shown in Figure 4.7. This is done by moving the V-grooves which the fibres are attached. The fibres are pushed together so that they partially overlap, this overlap puts pressure on the forming joint between the two fibres. This pressure allows the surface tension of the hot silica to adhere the two fibre ends together, to form one fibre. An example of two fibres at this point is shown in Figure 4.8 (b).

The two fibre ends are kept with a fixed overlap, and heated until surface tension and the viscosity of the silica merge the fibres together into a seamless joint. An example of this joint can be seen in Figure 4.8 (c).

The heating process required for splicing damages the hole structure of PCF [10]. To understand why, an effect called hole collapse will be explained.

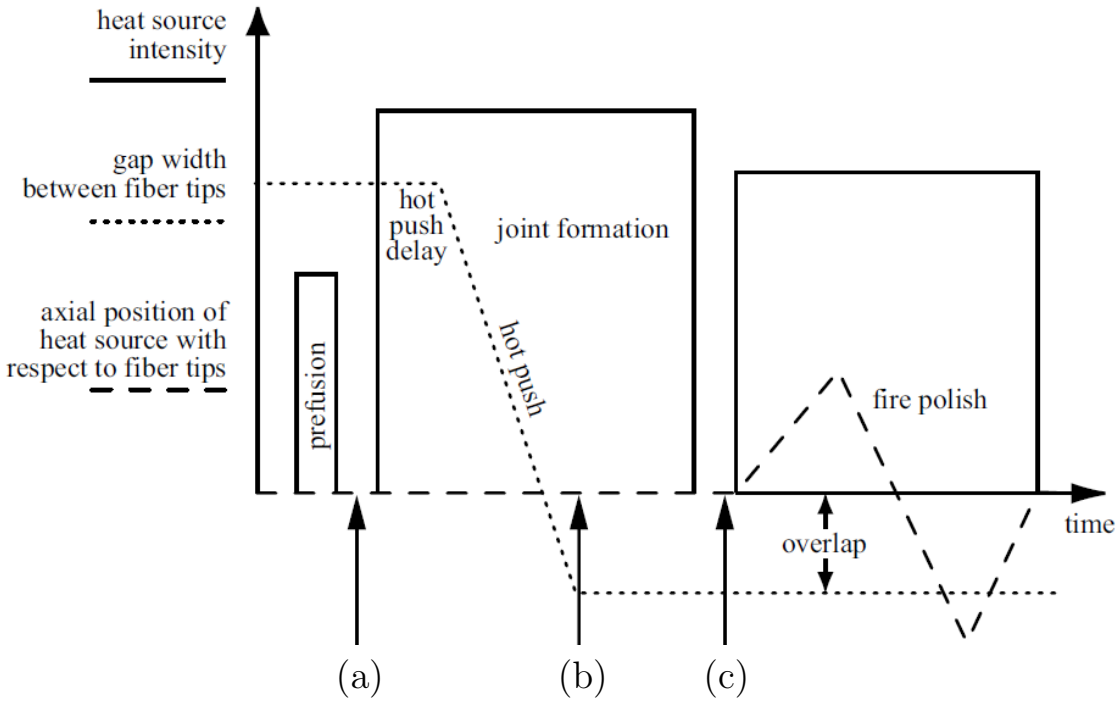

Figure 4.7: Schematic illustration of the splicing process. (a), (b), and (c) are the conditions that are represented by the images in Figure 4.8. Reproduced from Yablon [1].

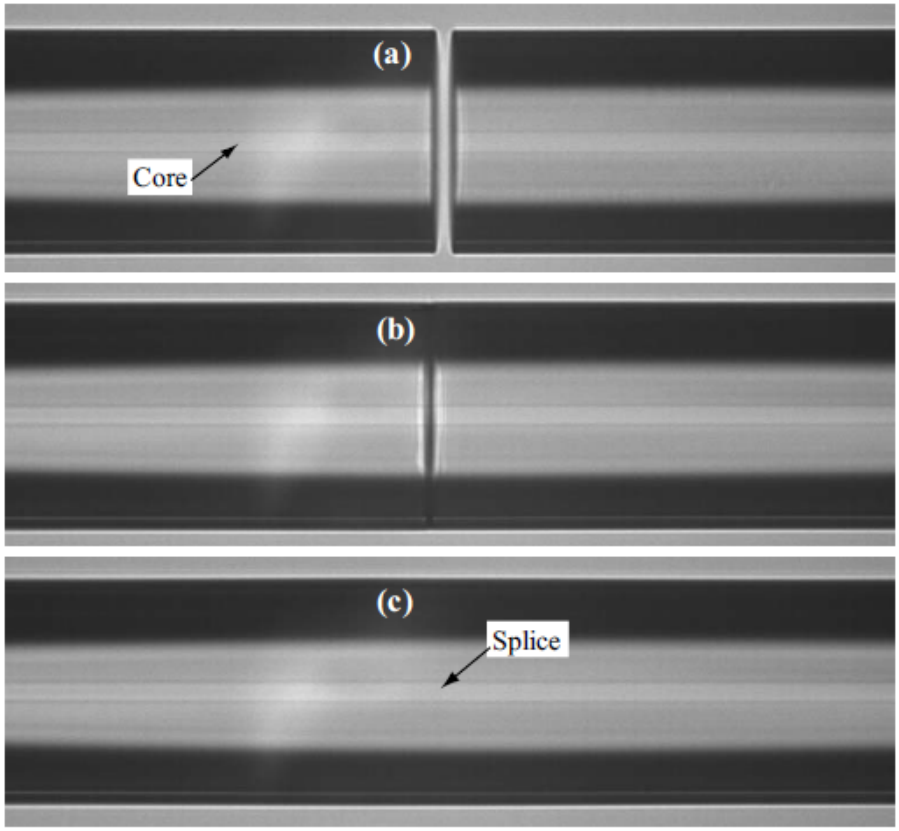

Figure 4.8: Examples of fibres experiences the arc fusion process. (a) are fibres that have experienced prefusion. (b) are fibres that have been softened and brought together. (c) are when the fibres have finally formed the splice. Figure reproduced from Yablon [1].

4.3 Hole Collapse

As discussed above when forming a splice the two fibres are heated. The heat causes hole collapse, which is where the light guiding structure of the PCF collapses [2, 3, 10]. Regions of PCF where the hole structure has collapsed no longer guide light, which allows light to escape the core of the fibre and is a source of loss [2]. For PM-PCF fibres, the hole collapse region is not birefringent and the fibre loses its polarisation maintaining property across that region [10]. To reduce the length of the hole collapse region, and reduce loss caused by it, the heat applied to the PCF needs to be reduced. This can be achieved by reducing the main arc current or applying an arc offset. The process of hole collapse will be described in detail, and how reducing the main arc current and applying an arc offset reduces the length of the hole collapse region.

Figure 4.9 shows one of the splices produced during this research. The splice was produced without an arc offset, and a main arc current of 15.3 mA. These are the parameters used to produce SMF to SMF splices. The PCF is PM1550, which is a birefringent polarisation maintaining fibre. The birefringence is produced by two enlarged holes adjacent to the fibre core. These are more resistant to hole collapse, and are highlighted in Figure 4.9. The hole collapse is composed of two regions, where there is complete hole collapse, and where there is partial hole collapse. Complete hole collapse is where the hole structure has collapsed completely, and the fibre no longers confines light to the core. The holes in the partial collapse region have shrunk in diameter, causing light confinement to be weakened but still present [2].

When the PCF is heated during splicing, two forces determine if the holes will collapse and the rate of their collapse; the surface tension of the silica, and the viscosity of the silica. The surface tension of the silica acts to collapse the holes. This is the same force that draws the fibre ends together into a splice. The viscosity of the silica resists the surface tension [2]. When the fibre is not being heated, the

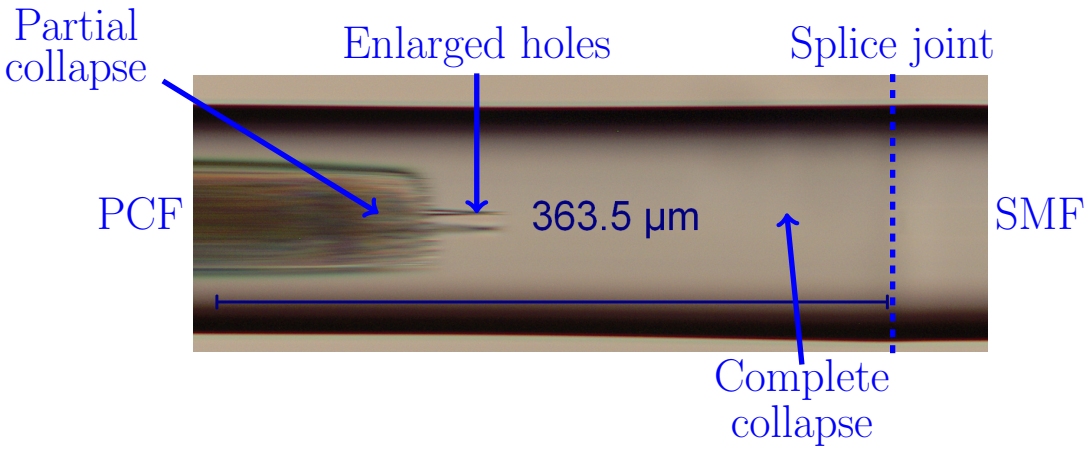

Figure 4.9: PM1550 (PCF) to SMF-28E (SMF) splice constructed without an arc offset, and a main arc current of 15.3 mA.

viscosity of the silica is high enough that the diameters of the holes remain constant. As the fibre is heated towards the melting point of silica (2000°C) the viscosity of the silica reduces [2]. There is a threshold point close to 2000°C where the surface tension of the silica overcomes its viscosity, and the holes begin to collapse [1]. The speed of this collapse is given by equation 4.1, where γ is the surface tension of the silica, and η is the viscosity of the silica [2, 20].

$$V_{collapse} = \frac{\gamma}{2\eta} \tag{4.1}$$

The temperature a region of the PCF experiences, decreases as a function of distance of that region from the arc points. This means that while the electrical arc is on, the viscosity of the silica of a region increases the further away from the arc points that region is. This reduces the speed of the collapse, for holes of regions further away from the arc points. The time it takes for a hole to collapse is given by $\frac{D_{hole}}{V_{collapse}}$, where D_{hole} is the diameter of the hole. As the speed of collapse reduces, it takes longer for the hole structure to collapse. For some of the fibre far enough away from the arc points, this time is longer than the duration of the electrical arc. This region of the PCF only experiences partial collapse. There is a point along the fibre far enough away from the arc points that the temperature does not reach the

threshold value for collapse to begin, which represents the boundary between partial collapse and no collapse.

As the speed of the collapse is based on two factors of silica, and not on the dimensions of the hole, $V_{collapse}$ is the same for all hole diameters [2]. Due to their larger diamaters, the enlarged holes of the PM1550 take longer to collapse than the smaller holes. This extends the region of partial collapse for those holes closer to the splice joint, and is why they can be seen in Figure 4.9.

Reducing the main arc current, reduces the heat experienced by all of the PCF [10]. This will reduce the length of the PCF that experiences a temperature above the threshold temperature for hole collapse to begin. This also shifts the region that experiences partial hole collapse closer to the splice joint. The limit for reducing the main arc current is that the two fibre end faces still need to be hot enough for a splice to form. The main arc current needs to be large enough for this condition.

An arc offset is where the two fibre end faces are not brought together directly between the arc points, but are brought together a distance offset along the length of the fibres. Figure 4.10 shows a diagram of arc offset. Moving the PCF away from the arc points shifts more of the PCF into regions around the arc points where the temperature is below the threshold for hole collapse to begin. This reduces the length of the hole collapse region. The limit on the arc offset distance, how far the fibres are moved, is that the fibre ends still need to be hot enough to form a splice. Applying an arc offset also interferes with aligning the two fibre end faces with each other. The splicer used determines which one of these two limits is the major limiter [10].

The advantage of reducing the main arc current over applying an arc offset is that it does not interfere with alignment of the two fibre ends. The advantage of applying the arc offset over reducing the main arc current is that it preferentially heats the SMF. This keeps the SMF fibre end hot enough for splicing [10].

Another consequence of hole collapse on the loss across the splice is that the

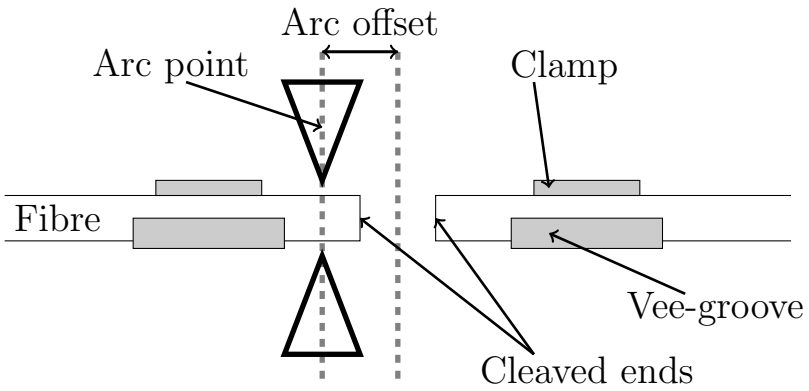

Figure 4.10: Description of an arc offset, it is where the arc points are not directly over the splice joint during construction but are placed preferentially over one fibre.

mode field diameter (MFD) increases across the hole collapse region [5]. This can cause a mismatch between the mode field diameter of the PCF and the fibre to which it is being spliced. If the MFD of the PCF is greater than the fibre to which it is spliced, only the intensity of light within the area of the MFD of the other fibre will be transmitted into its core. The greater the mismatch, the lower the fraction of light that will transmit from the core of the PCF into the core of the other fibre [1]. If the MFD of the PCF is smaller than of the fibre to which it is spliced, all of the light that transmits across the splice will be guided by the core of the other fibre [3].

This means that loss across the splice is described as non-symmetrical, or non-reciprocal [3, 4]. The MFD of both fibres can be chosen to match, but as the MFD of the PCF depends on the length of the hole collapse region, the mismatch is dependent on the nature of the splice [3, 4, 10]. In this work, the fibres were not chosen for matching MFDs, as the preference was for the other properties of the fibres.

The approaches described above were used to reduce the length of the hole collapse region. How they were used is described in Section 4.4.

4.4 Splicing approach

Two arc fusion splicers were used to produce either PCF to SMF splices or PCF to PMF splices. A Fujikura 100P arc fusion splicer was used to produce PCF to SMF splices. The Fujikura 100P is a versatile splicer capable of PMF to PMF splices using the PAS[19]. The Fujikura 100P+ arc fusion splicer was used to produce PCF to PMF splices. The 100P+ possesses an End View system [19], which is designed to allow any type of polarisation maintaining fibre to be spliced, including PM-PCF. The software of both the 100P and 100P+ allows a program to be written that contains the specific parameters for a splice. Modifications to these parameters were explored, to observe how they influenced splice formation for both PCF to SMF splices and PCF to PMF splices. These parameters were; arc offset, and main arc current.

Five different arc offset distances were used to observe the influence of arc offset on the length of the hole collapse region, thus reducing the loss across the splice. The distances chosen were; no offset, 50 μm, 100 μm, 110 μm, and 120 μm. It was found that for offset distances greater than 120 μm, splices would consistently fail to form for both PCF to SMF splices using the 100P, and for PCF to PMF splices using the 100P+. Three splices were produced for each offset distance, their loss was measured, and the length of the hole collapse region at the splice was measured. This was done for both PCF to SMF splices and PCF to PMF splices. The same main arc current of 15.3 mA was used for each of the splices constructed using different arc offset distances.

To explore how varying main arc current could reduce the length of the hole collapse region at a splice, thus reducing loss across the splice, five different main arc currents were used. Each of these main currents was used with a 120 μm arc offset. It will be shown in Section 4.5 that 120 μm arc offset distance is the optimum offset, proceeding from there it was used as the offset for the range of main arc currents. The main arc currents chosen for PCF to SMF splices using the

100P were; 14.3 mA, 14.8 mA, 15.3 mA, 15.8 mA, and 16.3 mA. Currents below 14.3 mA were not used since they failed to consistently produce splices. The rest were chosen to be symmetrical around 15.3 mA which was the main arc current used for standard SMF to SMF splices. The main arc currents chosen for PCF to PMF splices using the 100P+ were; 12.9 mA, 14.1 ma, 15.3 mA, 16.5 mA, and 17.7 mA. It was observed that main arc currents below 12.9 mA, consistently failed to produce splices. This provided the minimum main arc current used. The rest were chosen to be symmetrical around 15.3 mA which was the main arc current used for standard SMF to SMF splices. For each main arc current three splices were constructed, their loss was measured, and the length of the hole collapse region at the splice was measured. This was done for both PCF to SMF splices and PCF to PMF splices. One PCF to PCF splice was constructed. It was impractical to measure its loss but the length of the hole collapse region was measured.

The length of the hole collapse region for every splice was measured using an Olympus BX51 microscope. The loss across the splice, for each splice was measured with a Luna Technologies 4400 optical backscatter reflectometer (OBR). The OBR will be described in greater detail in Chapter 6. A brief description is given here. The OBR acts as a laser light source at 1550 nm, and a detector [21, 22, 23]. The OBR is coupled to the distal end of the SMF. Light from the OBR experiences Rayleigh scattering along the length of the fibre [21, 22, 23]. The light scattered backwards is detected by the OBR [21, 22, 23]. The OBR uses interferometry to measure the intensity of the backscatter as a function of distance from the port where it is coupled to the fibre [21, 22, 23]. Breaks in the fibre are detected as sources of reflection. The OBR observes a splice as a partial break in the fibre [24]. The OBR can measure the intensity of the Rayleigh scattering before and after the splice, and use this to measure the loss across the splice [1, 21, 22, 23]. Light that is scattered after the splice towards the OBR, crosses the splice twice in its path from and to the OBR. The OBR halves the loss it detects to produce the actual

loss across the splice [21, 22, 23]. As discussed in Section 4.3, loss is non-symmetric across a splice of PCF to SMF, or PCF to PMF. Due to this the OBR measures the average loss across the splice. The loss of each splice, the length of the hole collapse region, and the parameters to produce it were recorded. These are presented in the following Section.

4.5 Reducing loss in splices

This section covers the effect of applying an arc offset, and changing the main arc current on the length of the hole collapsed region in the splice. This was explored for both PCF to SMF, and PCF to PMF splices.

As described in Section 4.4, the OBR measures the intensity of Rayleigh backscatter from the regions surrounding the splice. Comparing the change in intensity of backscatter after the splice allows the OBR to measure the loss across the splice. It was observed that the backscatter coefficient of the PM1550 was greater than both the SMF and PMF used. This effect has never been reported in the literature. The consequence of this was that when the loss across the splice was low, the difference in backscatter coefficient gave a negative loss across the splice. This is not due to the mode gaining power as it crosses the splice, but to a difference in the backscatter coefficient of the different fibres. We were unable to measure the backscatter coefficient for PM1550, because of this negative loss reported for some of the splices. This is just an artefact of the difference in coefficient, and can be ignored when measuring the relative difference in loss between splices.

4.5.1 Arc offset

The parameter modification investigated was applying an arc offset. In the following section the effect of an arc offset during splice formation for PCF to SMF, and PCF to PMF will be presented.

PCF to SMF splices

Now we will present the images relative to the PCF to SMF splices. Figure 4.11 shows three example PCF to SMF splices formed with the same main arc current (15.3 mA), but with different arc offset: (a) without an arc offset, (b) arc offset of 100 μm, and (c) arc offset of 120 μm. In each image we only show the PCF side of the splice, since in this project we were only interested in the performance of the PCF component.

The parameters used to construct the splice presented in Figure 4.11 (a) are the same for classical SMF to SMF splices (main arc current 15.3 mA and no arc offset). There is a long hole collapsed region ($221 \pm 5\mu m$). When a 100 μm arc offset is used during construction the length of the hole collapsed region is observed to be reduced ($129 \pm 5\mu m$), an example splice is shown in Figure 4.11 (b). While the length of the hole collapsed region is reduced compared to splices without an arc offset, the shape of the hole collapsed region remains roughly the same. This is because the arc offset displaces the hole collapsed region along the fibre towards the splice. It does not change the length of the transition region where the temperature is high enough to shrink the holes, but not to completely collapse them.

Increasing the arc offset further reduces the length of the hole collapsed region, shown in Figure 4.11 (c). The example splice presented in Figure 4.11 (b) was produced with an arc offset of 120 μm. This hole collapsed length ($100 \pm 5\mu m$) is less than half the one for the splice with no arc offset. This splice was formed with the maximum arc offset distance that was found to successfully produce splices. Longer arc offset distances were found not to produce splices that survived the mechanical testing of the splicer. Before a splice can be removed from the splicer, it applies slight tension to the splice to test its mechanical strength. If the splice breaks it would not have survived most conditions it would have encountered outside the splicer. This weakness of the mechanical strength of splices with an arc offset applied can be seen in the interface of the two fibres.

The PCF had two enlarged holes close to its core, these are highlighted in (a). They are more resistant to collapse, and therefore persist closer to the splice joint, as their larger diameters increase the time taken for them to collapse (Section 4.3).

Small air filled voids, or microcavities, occasionally form in the interface between the core of the PCF and the SMF. A microcavity is highlighted in Figure 4.11 (c). They are formed as the air from the air holes that collapsed is pushed towards the splice joint and becomes trapped. These microcavities can be used as an axial strain and transverse load sensor, and they will be described in greater detail in Chapter 5.

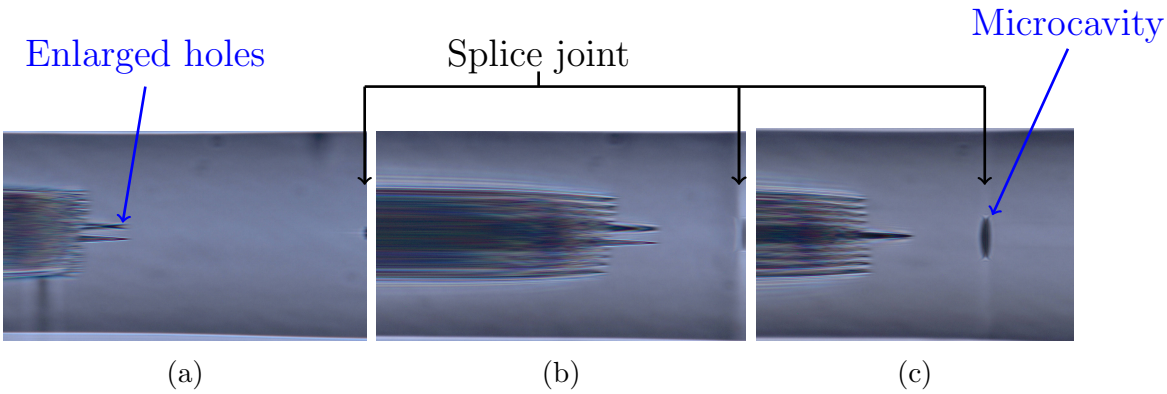

Figure 4.11: Three PM1550 to SMF-28E splices constructed with a main arc current of 15.3 mA: (a) without an arc offset, (b) arc offset of 100 μm, and (c) arc offset of 120 μm. Length of the hole collapse region of; (a) $221 \pm 5\mu m$, (b) $129 \pm 5\mu m$, and (c) $100 \pm 5\mu m$. The splice loss of; (a) $3.99 \pm 0.05dB$, (b) $2.52 \pm 0.05dB$, and (c) $0.61 \pm 0.05dB$. The PCF is on the left of each image. The location splice joint is shown in each image. The enlarged holes of the PM1550 are highlighted for (a). The microcavity formed in (c) is highlighted.

PCF to PMF splices

In this subsection we present the images for PCF to PMF splices. Figure 4.12 shows three example PCF to PMF splices formed with the same main arc current (15.3 mA), but with different arc offset (same as the PCF to SMF splices): (a) without an arc offset, (b) arc offset of 100 μm, and (c) arc offset of 120 μm.

In Figure 4.12 (c) the core of the PMF has been highlighted. The Panda style PMF produces its birefringence with two stress lobes, that applies stress along a

line that bisects the core of the PMF. This refractive index change due to the stress lobes can be seen around the core of the PMF.

As was the case with the PCF to SMF splices, applying the arc offset reduced the length of the hole collapse region, but did not change the shape of the transition region from complete hole collapse to an unaffected hole structure.

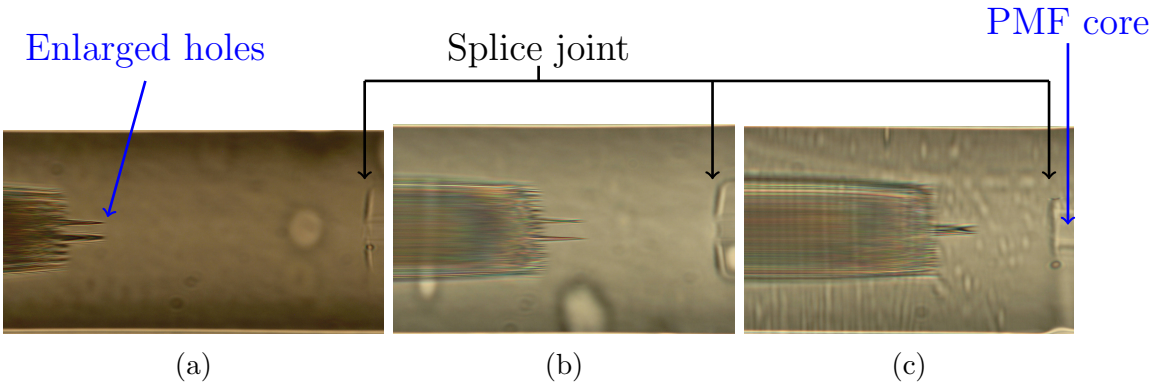

Figure 4.12: Three PM1550 to HB1500T splices constructed with a main arc current of 15.3 mA: (a) without an arc offset, (b) arc offset of 100 μm, and (c) arc offset of 120 μm. Length of the hole collapse region of; (a) $234 \pm 5\mu m$, (b) $147 \pm 5\mu m$, and (c) $102 \pm 5\mu m$. The splice loss of; (a) $0.89 \pm 0.05dB$, (b) $2.27 \pm 0.05dB$, and (c) $1.39 \pm 0.05dB$. The PCF is on the left of each image.

Summary of arc offset

Increasing the arc offset was found to reduce the length of the hole collapse region in splices. The optimum arc offset distance was found to be 120 μm. Arc offset distances larger than this were found to be detrimental to splice formation, successful splices were less frequent, and the formed splices were mechanically weaker. Zuoming et al. [10] found the optimum arc offset distance was 220 μm, however they used a VYTRAN GPX-3000 splicer which was able to still form splices at larger arc offset with respect to this project. The optimum arc offset distance found in this work was used for all of the splices constructed using different main arc currents.

Figures 4.13 and 4.14 are a comparison of length of arc offset used during splice construction and the resultant length of the hole collapse region in the splice. Figure

4.13 was for PCF to SMF splices, and Figure 4.14 was for PCF to PMF splices. The errorbars are the standard deviation of the measurements of the three splices made for each arc offset.

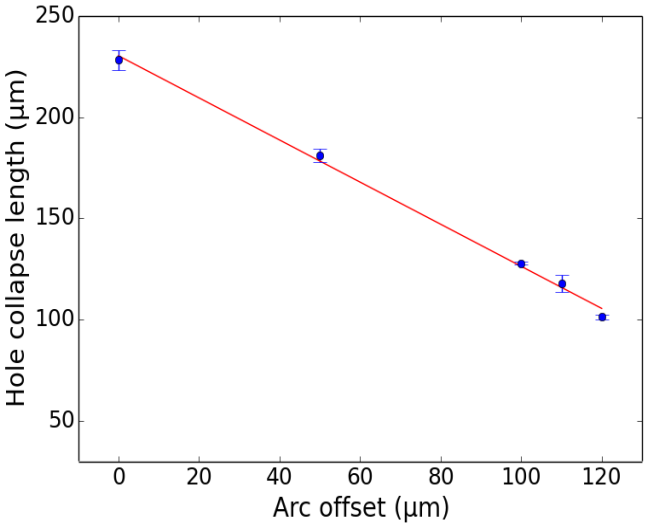

Figure 4.13: Length of the hole collapse region in comparison to the arc offset distance used in construction of PM-PCF to SMF splices. R-squared of 0.99 for the points to the fitted line (-1.040x + 230.4).

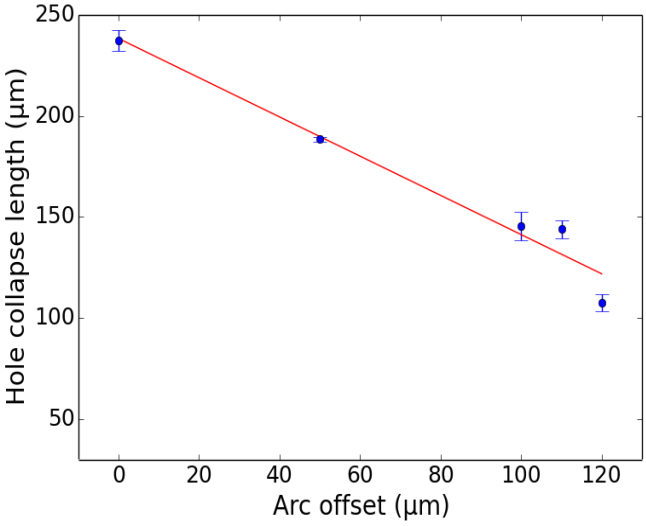

Figure 4.14: Length of the hole collapse region in comparison to the arc offset distance used in construction of PM-PCF to Panda splices. R-squared of 0.96 for the points to the fitted line (-0.971x + 238.4).

For both PCF to SMF, and PCF to PMF splices there was a strong correlation between longer arc offset, and shorter length of the hole collapse region in the splice. The correlation of the line of best fit in Figure 4.13 with the data points had a R-squared of 0.99 [1], and the correlation of the line of best fit in Figure 4.14 with the data points had a R-squared of 0.96. This gives a high confidence in a negative proportional relationship between the arc offset used, and the length of the hole collapse region. As explained in Section 4.3, hole collapse is caused by heat applied to the PCF. There is a threshold temperature when the surface tension of the holes overcomes resistance and the holes begin to collapse. The temperature distribution around the arc points used to heat both fibres, also heats the part of the fibre that is not directly involved in the splicing process. Using the arc offset moves more of the PCF away from the arc points to reduce the amount of the PCF heated, thus reducing the length of hole collapse in the fibre. The implication is that the arc offset used should be proportional to the reduction in the length of the hole collapse region of the splice. This is confirmed by the large R-squared values of the data points with regards to the linear fit for both Figures 4.13 and 4.14. Comparing the two linear fits, we observe that there is no significant difference. It did not matter whether the splice was between PCF and SMF (gradient -1.040 ± 0.024), or PCF and PMF (gradient -0.971 ± 0.037), the splices had the same reduction in length of the hole collapse region for the same arc offset distance used.

After having measured the hole collapsed length as a function of the arc offset, we measured the loss of the splice as a function of the arc offset, in order to understand the dependence of the quality of the final splice on the arc offset parameter.

Figure 4.15 and Figure 4.16 show the loss for splices as a function of the arc offset used during construction, linear for PCF to SMF splices, and for PCF to PMF splices respectively. The linear fit in Figure 4.15 (-1.040x + 230.4) had an R-squared of 0.82, this implies that for PCF to SMF splices increasing the arc offset

[1] R-squared is $1 - \frac{SS_{res}}{SS_{tot}}$, where SS_{tot} is the residual sum of squares, and SS_{tot} is the total sum of squares[25].

reduces loss. This was expected from the reduction in the length of the hole collapse region of the splices with an arc offset applied during construction. By contrast, on a careful inspection of Figure 4.16, we notice that the line fitted to the data shows an R-squared of 0.21. This is a low R-squared value, which implies that while the linear fit (0.005x + 1.527) describes an increase in the loss across the splice as a larger distance is used for the arc offset, this relationship is weak ($|gradient| << 1$). Therefore for PCF to PMF, there is not a strong correlation between loss and arc offset, even though a strong correlation between hole collapsed length and arc offset still remains. This can be explained, bearing in mind that the hole collapse is not the only factor determining the loss across the splice (see Section 4.3).

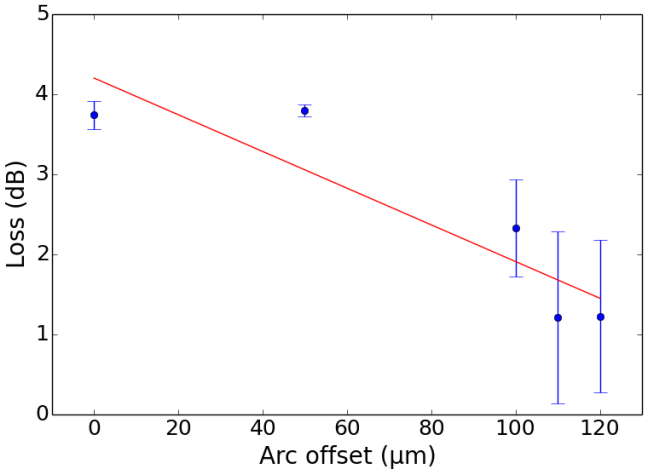

Figure 4.15: Loss across the splice in comparison to arc offset distance used in construction of PM-PCF to SMF splices. R-squared of 0.82 for the points to the fitted line (-0.023x + 4.202).

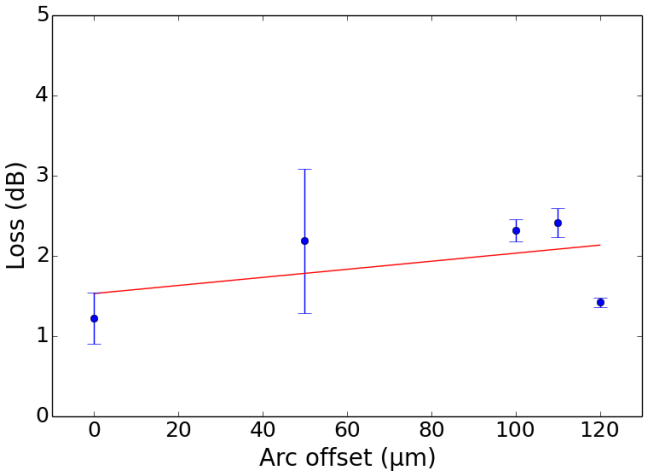

Figure 4.16: Loss across the splice in comparison to arc offset distance used in construction of PM-PCF to PMF splices. R-squared of 0.21 for the points to the fitted line (0.005x + 1.527).

Applying an arc offset reduces the length of the hole collapse region, however it also reduces the quality of the splice. Large arc offsets interfere with the alignment of the two fibre end faces [1]. The cores of the two fibres being misaligned, due to the end faces being misaligned as the splice was formed, is a source of loss[1], however this source of loss is masked by the loss caused by a long region of hole collapse [10]. As the length of the hole collapse region is reduced, it no longer masks the loss caused by the cores of the two fibres being misaligned.

An alternative hypothesis is that most of the loss is dominated by the collapse of the PCF hole structure close to the splice joint. Applying an arc offset modifies the length of hole but does not change the features of the region close to the splice joint, and therefore does not have an impact on splice loss. While this might be true for the PCF to PMF splices, the results shown in Figure 4.15 imply that applying an arc offset reduces loss overall for PCF to SMF splices. This might be because the arc offset modifies the features of the structure of the hole collapse close to the splice joint, however this is unlikely. This implies the length of the hole collapse region has an impact on overall splice loss, even if it is less dominant in PCF to PMF splices.

The only difference between the PCF to SMF, and PCF to PMF splices, was in the splicer used to produce the splice. The PCF to PMF splices were produced with a different splicer to the PCF to SMF splices, and this splicer may be less effective at aligning the fibres at larger arc offset distances when compared to the splicer used for PCF to SMF splices.

Tables 4.1 and 4.2 shows the arc offset distance used for each splice, the length of the hole collapse region, and the loss across the splice. Example splices produced with different arc offset distances are presented in this section, to show how the hole collapse region and quality of the splices varied between different arc offset distances.

Table 4.1: List of the arc offset distance, length of the hole collapse region, and loss across the splice for PCF to SMF splices.

Arc offset	Length of the hole collapse region	Splice loss
No arc offset	$230 \pm 5\mu m$	$3.59 \pm 0.05dB$
No arc offset	$221 \pm 5\mu m$	$3.99 \pm 0.05dB$
No arc offset	$233 \pm 5\mu m$	$3.64 \pm 0.05dB$
50 μm	$183 \pm 5\mu m$	$3.82 \pm 0.05dB$
50 μm	$184 \pm 5\mu m$	$3.69 \pm 0.05dB$
50 μm	$177 \pm 5\mu m$	$3.87 \pm 0.05dB$
100 μm	$127 \pm 5\mu m$	$2.95 \pm 0.05dB$
100 μm	$128 \pm 5\mu m$	$1.51 \pm 0.05dB$
100 μm	$129 \pm 5\mu m$	$2.52 \pm 0.05dB$
110 μm	$119 \pm 5\mu m$	$2.73 \pm 0.05dB$
110 μm	$112 \pm 5\mu m$	$0.38 \pm 0.05dB$
110 μm	$122 \pm 5\mu m$	$0.51 \pm 0.05dB$
120 μm	$100 \pm 5\mu m$	$0.61 \pm 0.05dB$
120 μm	$101 \pm 5\mu m$	$0.49 \pm 0.05dB$
120 μm	$103 \pm 5\mu m$	$2.57 \pm 0.05dB$

Table 4.2: List of the arc offset distance, length of the hole collapse region, and loss across the splice for PCF to PMF splices.

Arc offset	Length of the hole collapse region	Splice loss
No arc offset	$234 \pm 5\mu m$	$1.11 \pm 0.05dB$
No arc offset	$245 \pm 5\mu m$	$1.65 \pm 0.05dB$
No arc offset	$234 \pm 5\mu m$	$0.89 \pm 0.05dB$
50 μm	$190 \pm 5\mu m$	$1.64 \pm 0.05dB$
50 μm	$187 \pm 5\mu m$	$1.46 \pm 0.05dB$
50 μm	$189 \pm 5\mu m$	$3.45 \pm 0.05dB$
100 μm	$136 \pm 5\mu m$	$2.17 \pm 0.05dB$
100 μm	$153 \pm 5\mu m$	$2.50 \pm 0.05dB$
100 μm	$147 \pm 5\mu m$	$2.27 \pm 0.05dB$
110 μm	$147 \pm 5\mu m$	$2.60 \pm 0.05dB$
110 μm	$138 \pm 5\mu m$	$2.17 \pm 0.05dB$
110 μm	$147 \pm 5\mu m$	$2.48 \pm 0.05dB$
120 μm	$102 \pm 5\mu m$	$1.39 \pm 0.05dB$
120 μm	$112 \pm 5\mu m$	$1.37 \pm 0.05dB$
120 μm	$109 \pm 5\mu m$	$1.50 \pm 0.05dB$

4.5.2 Main arc current

After having investigated the effect of the arc offset, we proceeded to observe the effect of modifying the main arc current used during construction of the splice. In the following section the affect of main arc current on splice formation for PCF to SMF, and PCF to PMF will be presented.

PCF to SMF splices

Figure 4.11 shows three example PCF to SMF splices formed with the same arc offset (120 μm) but with different main arc currents: (a) main arc current of 16.3 mA, (b) main arc current of 15.3 mA, and (c) main arc current of 14.3 mA.

As the main arc current was reduced the length of the hole collapsed region was reduced. The shape of the hole collapsed region is roughly the same for every main arc current used. This shape is produced by the transition region where the temperatures from the splice process were hot enough for the holes to begin to collapse, but not hot enough for them to completely collapse during the arc's duration. The

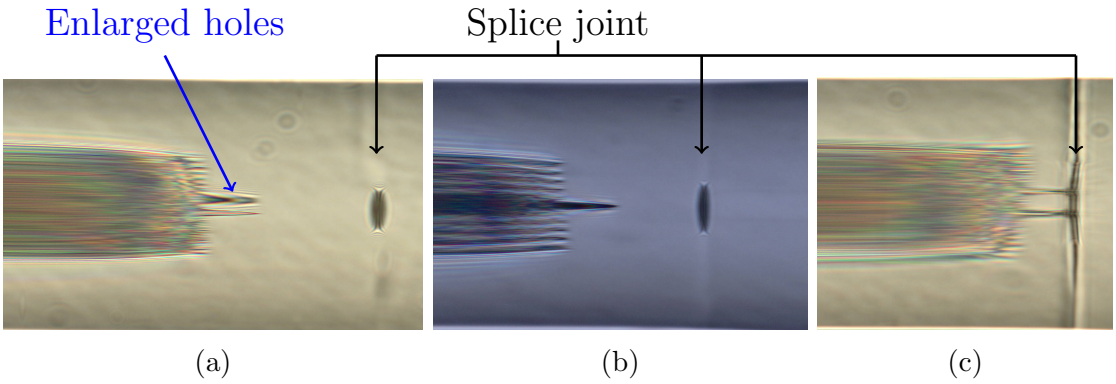

Figure 4.17: Three PM1550 to SMF-28E splices constructed with a 120 μm arc offset distance and: (a) a main arc current of 16.3 mA, (b) a main arc current of 15.3 mA, and (c) a main arc current of 14.3 mA. Length of the hole collapse region of: (a) $142 \pm 5\mu m$, (b) $100 \pm 5\mu m$, and (c) $76 \pm 5\mu m$. The splice loss of: (a) $1.96 \pm 0.05dB$, (b) $0.61 \pm 0.05dB$, and (c) $0.17 \pm 0.05dB$. The PCF is on the left of each image.

length of the transition region is a function of the gradient of temperature change with respect to distance r from the arc points. It can be deduced that as the shape of the transition region is not observed to change between different main arc currents, the gradient of temperature change is constant for the range of main arc currents used.

When the main arc current was reduced to 14.3 mA, example shown in Figure 4.11 (c), the length of the hole collapsed region was reduced until the enlarged central holes survived at the splice joint. The splice joint is visible, this was not observed for splices constructed with larger main arc currents such as those in Figure 4.11 (a) and (b). Due to the lower temperature used to construct the splices, the two fibre end faces did not bond smoothly to each other, making the splice mechanically weak. Splices constructed with a lower main arc current were too mechanically weak to survive the testing conducted by the splicer of their robustness.

It can be observed in Figure 4.11 (a) and (b), that there is a small air filled void at the splice joint, or microcavity . The microcavity was not found to have an influence on the splice loss at 1550 nm, as there was not a correlation between greater loss and presence of a microcavity at the splice joint.

PCF to PMF splices

Figure 4.11 shows three example PCF to PMF splices formed with the same arc offset (120 μm) but with different main arc currents: (a) main arc current of 17.7 mA, (b) main arc current of 15.3 mA, and (c) main arc current of 12.9 mA.

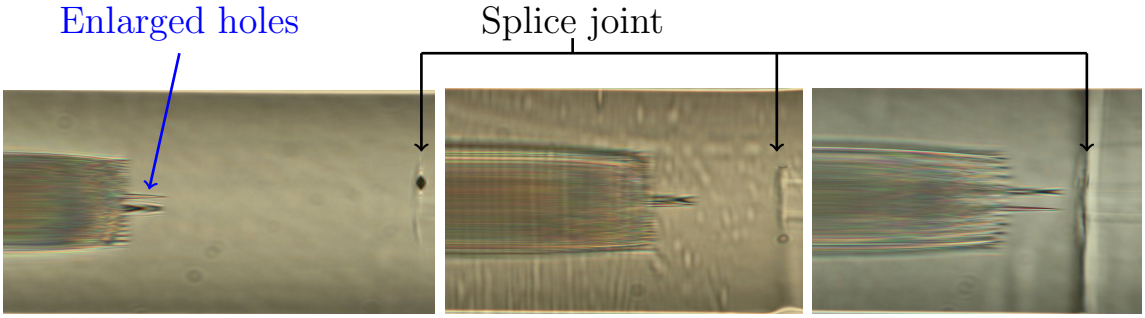

(a) (b) (c)

Figure 4.18: Three PM1550 to HB1500T splices constructed with a 120 μm arc offset distance and: (a) a main arc current of 17.7 mA, (b) a main arc current of 15.3 mA, and (c) a main arc current of 12.9 mA. Length of the hole collapse region of: (a) $203 \pm 5\mu m$, (b) $102 \pm 5\mu m$, and (c) $74 \pm 5\mu m$. The splice loss of: (a) $3.37 \pm 0.05dB$, (b) $1.39 \pm 0.05dB$, and (c) $-0.41 \pm 0.05dB$. The PCF is on the left of each image.

It was described earlier how larger main arc currents increased the length of the hole collapse region, and the loss across the splice. In the case of the splices using a main arc current greater than 15.3 mA, example in Figure 4.18 (a), the reduction in the length of the hole collapsed region from applying an arc offset was negated.

Reducing the main arc current to 12.9 mA, reduced the hole collapsed region length until the enlarged holes survived at the splice junction, equivalent to the 14.3 mA used with PCF to SMF splices. Reducing the main arc current also greatly reduced the quality of the splices. The interface of the two fibres is visible in Figure 4.18 (c). The quality of the splice is reduced due to the lower heat at the splice joint during construction, if a main arc current lower than 12.9 mA is used the splice fails to form.

Summary of main arc current

For both PCF to SMF, and PCF and PMF splices there was a strong correlation between reducing the main arc current during splice formation, and a shorter length of the hole collapse region. Figures 4.19 and 4.20 are a comparison of main arc current used during splice construction and the resultant length of the hole collapse region in the splice. Figure 4.19 was for PCF to SMF splices, and Figure 4.20 was for PCF to PMF splices.

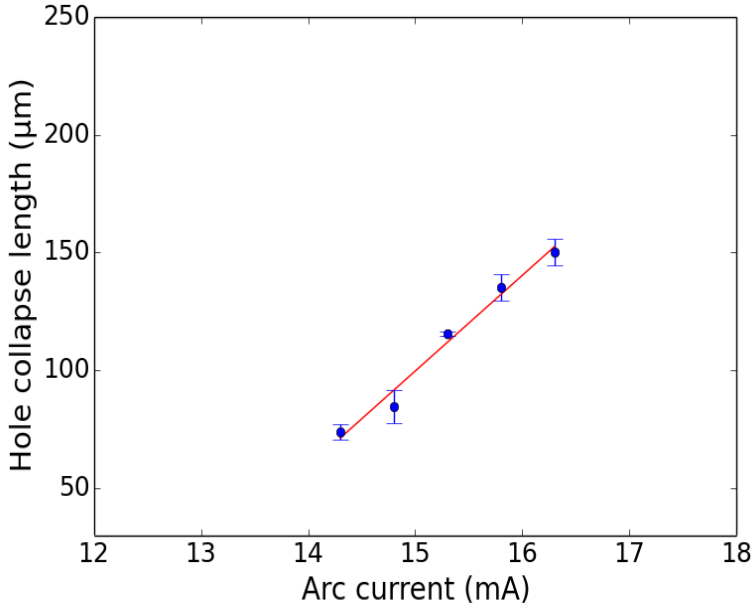

Figure 4.19: Length of the hole collapse region in comparison to main arc current used in construction of PM1550 to SMF-28E splices. Equation of the line of best fit: y = 40.7x -510.2, R-squared = 0.98.

The correlation of the data points with the fitted line (gradient 40.7 ± 0.3) in Figure 4.19 (PCF to SMF splices) had an R-squared of 0.98. There was a similar correlation of data points to the fitted line (gradient 31.5 ± 0.7) in Figure 4.20, with an R-squared of 0.94. These high R-squared values give a high confidence in the observation that reducing the main arc current reduces the length of the hole collapse linearly.

Heat applied to the PCF during the splicing process causes the hole structure

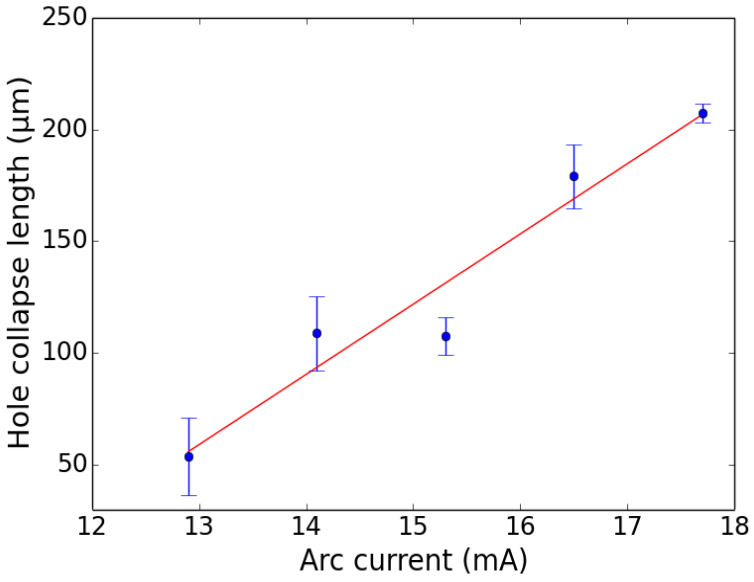

Figure 4.20: Length of the hole collapse region in comparison to main arc current used in construction of PM1550 to HB1500T splices. Equation of the line of best fit: y = 31.5x -350.1, R-squared = 0.94.

to collapse. The main arc current is a proxy for the amount of heat applied by the electrical arc to the fibre ends. As described in Section 4.2, there is a heat distribution around arc points, temperature reduces with distance r from the arc points linearly. Reducing the main arc current linearly, reduces the maximum temperature between the arc points linearly, and reduces the temperature for each point along r linearly. The temperature needs to be above a threshold value for the hole structure to begin to collapse. Reducing the main arc current decreases the length of the region exposed to a temperature above that threshold.

Unlike applying an arc offset, reducing the main arc current does not interfere with aligning the fibre end faces during the splice formation. This means reducing the main arc current does not increase loss from fibre misalignment. This can be observed in Figures 4.21 and 4.22, where there is a strong correlation between reducing the main arc current and reducing the loss across the splice for both PCF to SMF, and PCF to PMF spices. The R-squared was 0.94 for the fitted line of Figure 4.21 (PCF to SMF splices). The R-squared was 0.93 for the fitted line of

Figure 4.22 (PCF to PMF splices). Although the length of the hole collapsed region is not the only factor in the loss across the splice, reducing the main arc current reduces both loss and the length of the hole collapse region.

A different range of main arc currents were used for the PCF to SMF splices, and the PCF to PMF splices. This is due to a different minimum main arc currents of the two different splicers. The minimum main arc current was determined by an initial investigation that addressed the minimum required current, between the PCF to SMF, and PCF to PMF splices, before the splice was no longer formed.

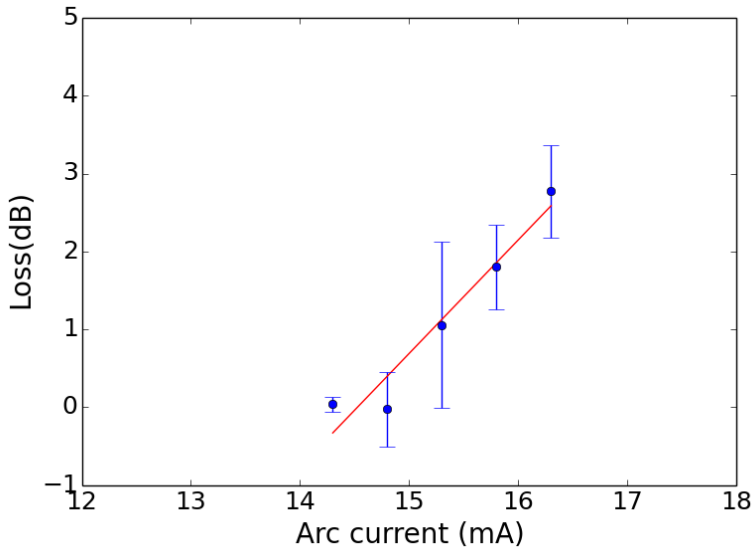

Figure 4.21: Loss across the splice in comparison to main arc current used in construction of PM1550 to SMF-28E splices. Equation of the line of best fit: y = 1.46x -21.19, R-squared = 0.94.

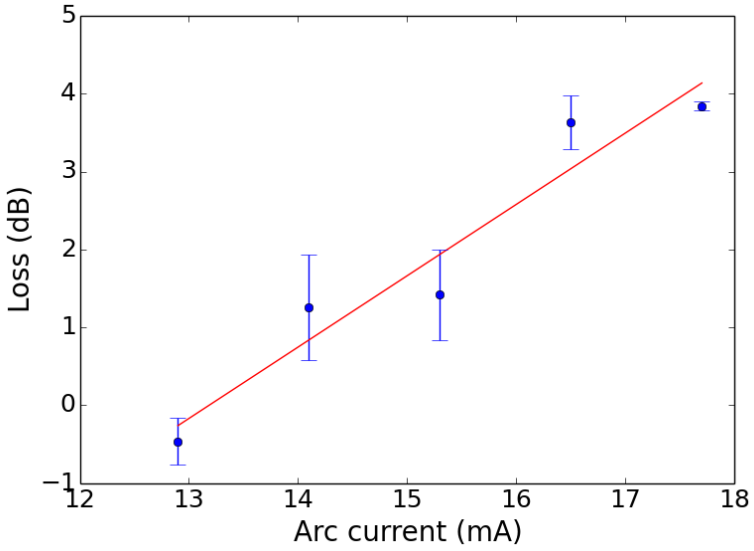

Figure 4.22: Loss across the splice in comparison to main arc current used in construction of PM1550 to HB1500T splices. Equation of the line of best fit: y = 0.92x -12.09, R-squared = 0.93.

Tables 4.3 and 4.4 shows the arc offset used for each splice, the length of the hole collapse region, and the loss across the splice. Example splices produced with different main arc currents are presented in this section, to show how the hole collapse region and quality of the splices varied between different arc offsets.

Table 4.3: List of the main arc current, length of the hole collapse region, and loss across the splice for PCF to SMF splices.

Main arc current	Length of the hole collapse region	Splice loss
$16.3mA$	$154 \pm 5\mu m$	$3.34 \pm 0.05dB$
$16.3mA$	$154 \pm 5\mu m$	$3.01 \pm 0.05dB$
$16.3mA$	$142 \pm 5\mu m$	$1.96 \pm 0.05dB$
$15.8mA$	$140 \pm 5\mu m$	$1.86 \pm 0.05dB$
$15.8mA$	$127 \pm 5\mu m$	$2.43 \pm 0.05dB$
$15.8mA$	$138 \pm 5\mu m$	$1.11 \pm 0.05dB$
$15.3mA$	$117 \pm 5\mu m$	$2.57 \pm 0.05dB$
$15.3mA$	$115 \pm 5\mu m$	$0.36 \pm 0.05dB$
$15.3mA$	$115 \pm 5\mu m$	$0.24 \pm 0.05dB$
$14.8mA$	$94 \pm 5\mu m$	$0.40 \pm 0.05dB$
$14.8mA$	$83 \pm 5\mu m$	$0.21 \pm 0.05dB$
$14.8mA$	$77 \pm 5\mu m$	$-0.69 \pm 0.05dB$
$14.3mA$	$69 \pm 5\mu m$	$0.01 \pm 0.05dB$
$14.3mA$	$76 \pm 5\mu m$	$0.17 \pm 0.05dB$
$14.3mA$	$76 \pm 5\mu m$	$-0.07 \pm 0.05dB$

Table 4.4: List of the main arc current, length of the hole collapse region, and loss across the splice for PCF to PMF splices.

Main arc current	Length of the hole collapse region	Splice loss
$17.7mA$	$203 \pm 5\mu m$	$3.37 \pm 0.05dB$
$17.7mA$	$226 \pm 5\mu m$	$4.20 \pm 0.05dB$
$17.7mA$	$192 \pm 5\mu m$	$3.96 \pm 0.05dB$
$16.5mA$	$177 \pm 5\mu m$	$3.09 \pm 0.05dB$
$16.5mA$	$190 \pm 5\mu m$	$3.37 \pm 0.05dB$
$16.5mA$	$170 \pm 5\mu m$	$4.44 \pm 0.05dB$
$15.3mA$	$102 \pm 5\mu m$	$1.39 \pm 0.05dB$
$15.3mA$	$112 \pm 5\mu m$	$1.37 \pm 0.05dB$
$15.3mA$	$109 \pm 5\mu m$	$1.50 \pm 0.05dB$
$14.1mA$	$102 \pm 5\mu m$	$0.70 \pm 0.05dB$
$14.1mA$	$132 \pm 5\mu m$	$2.21 \pm 0.05dB$
$14.1mA$	$93 \pm 5\mu m$	$0.85 \pm 0.05dB$
$12.9mA$	$31 \pm 5\mu m$	$-0.86 \pm 0.05dB$
$12.9mA$	$56 \pm 5\mu m$	$-0.13 \pm 0.05dB$
$12.9mA$	$74 \pm 5\mu m$	$-0.41 \pm 0.05dB$

4.5.3 Hole collapse and splice loss

It was discussed above that applying an arc offset reduced the length of the hole collapse region, but did not necessarily reduce the loss across the splice, whereas reducing the main arc current reduced both the length of the hole collapse region, and the loss across the splice. Figures 4.23 and 4.24 show the loss across a splice as a function of the length of the hole collapse region, for PCF to SMF and PCF to PMF splices respectively. Both figures are composed of the data for splices constructed with different arc offset distances applied, and different main arc currents. The figures are confirmation that the length of hole collapse region has a strong influence on the loss across the splice, and reducing it reduces the loss across the splice. While the length of the hole collapse region is not the only influence on the loss across the splice, it is a dominant influence. This validates the approach to reduce the length of the hole collapse region, to reduce the loss in PCF to SMF splices, and PCF to PMF splices.

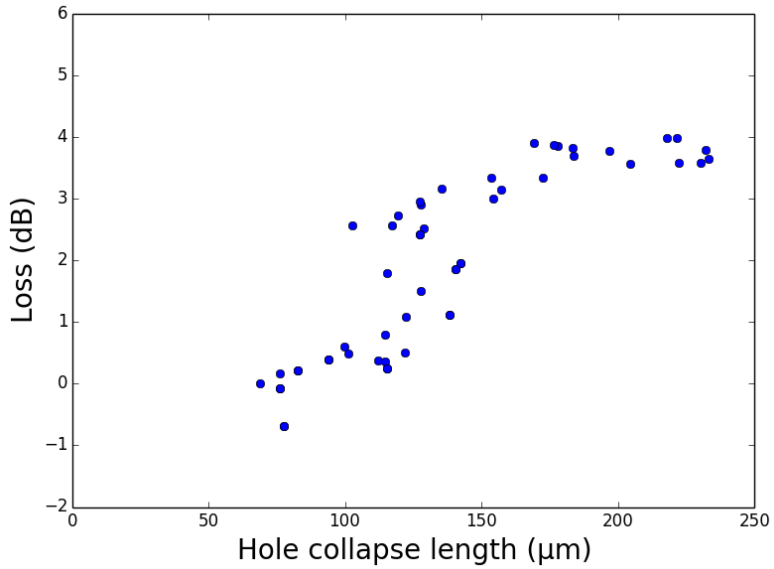

Figure 4.23: Loss across a splice as a function of the length of the hole collapse region in a PM-PCF to SMF splices

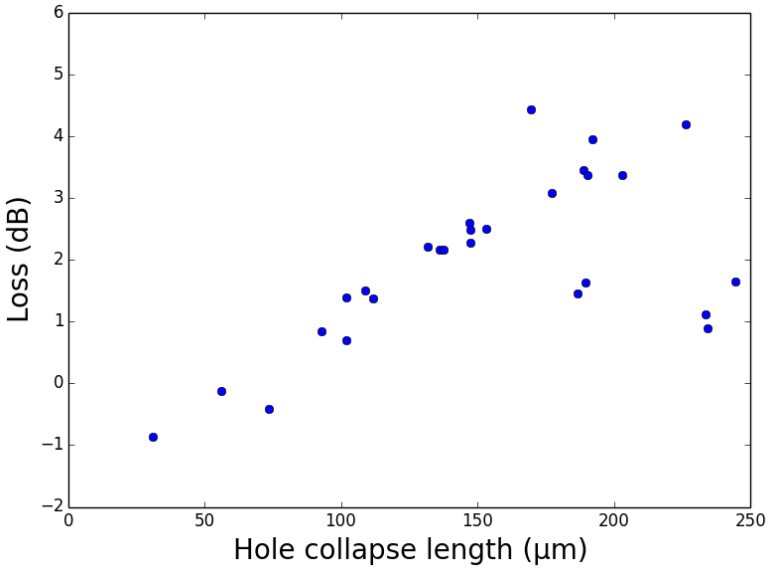

Figure 4.24: Loss across a splice as a function of the length of the hole collapse region in a PM-PCF to PMF splices

4.5.4 PCF to PCF splice

Figure 4.25 shows a PM1550 to PM1550 splice. This splice was constructed to observe a PCF to PCF splice, since it was unknown how it would affect hole collapse, or if it would produce a microcavity. This was constructed with no arc offset and with a main arc current of 13.7 mA, by the Fujijura 100P+ arc fusion splicer. No arc offset was used, as it would not reduce the overall length of hole collapsed region of both fibres. This is because it would have reduced the length of the hole collapsed region for one fibre, but increase it for the other fibre.

A main arc current of 13.7 mA was used rather than 15.3 mA, as lower main arc currents have been shown in this work to reduce the length of the hole collapse region, and reduce loss across the splice. It was observed that hole collapse was symmetrical on either side of the splice, which is expected if the heat distribution around the arc points is symmetrical. A microcavity formed from the combined hole collapse of both fibres; it is highlighted in Figure 4.25 (b). It was impractical to measure the loss across the splice, as neither fibre could be directly coupled to the

OBR.

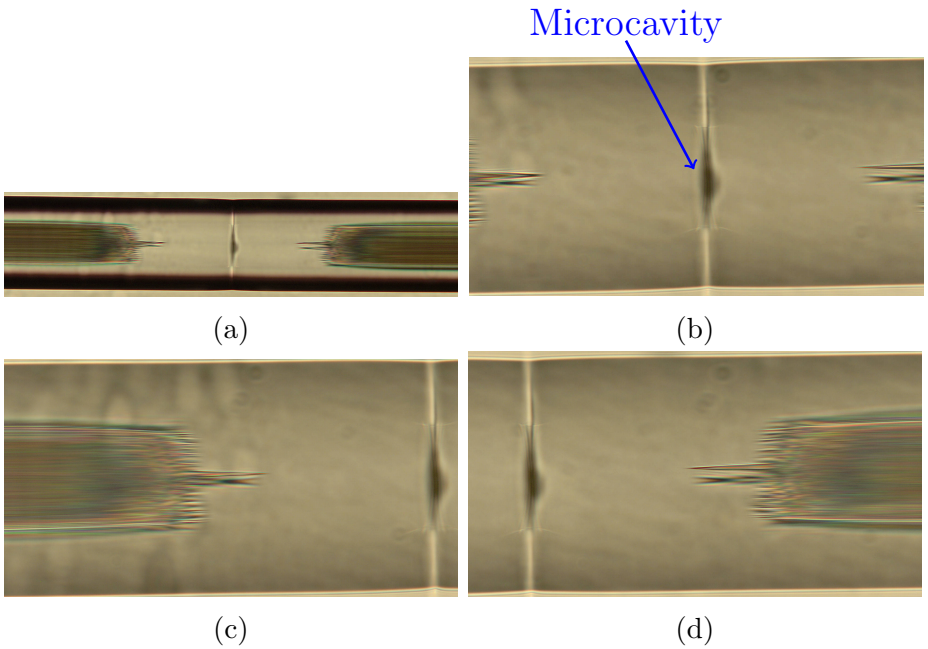

Figure 4.25: PM1550 to PM1550 splice taken with an Olympus BX51 microscope. (a) is magnification 20, (b), (c) and (d) are magnification 50. The length of the hole collapse region of (c) is 170μm, and (d) is 169μm.

4.6 Chapter summary

The aim was to produce PCF to SMF splices and PCF to PMF splices with lower loss by reducing the length of the hole collapse region. These splices were robust low loss connections. Two approaches were taken to reduce the length of the hole collapse region for both types of splices; applying an arc offset, and modifying the main arc current.

It was found that applying an arc offset reduced the length of the hole collapse, but did not necessarily reduce the loss across the splice. There was a reduction in the loss for PCF to SMF splices. The loss effectively remained the same for PCF to PMF splices. Applying the arc offset interfered with the alignment of the two cores of the fibres during splicing, which could increase loss across the splice. The reduction in the length of the hole collapse region was proportional to the arc offset

distance. This was expected as the arc offset moved the PCF away from the heat source that caused hole collapse, effectively shifting the heated regions that would cause hole collapse in the PCF, to heat the SMF or PMF instead. The maximum arc offset distance that could be applied to both PCF to SMF, and PCF to PMF splices was 120 μm. Arc offset distances greater than this would fail to produce splices.

Splices produced with lower main arc currents were observed to have shorter hole collapse regions. The reduction in the length of the hole collapse region for the splices was proportional to the reduction in the main arc current. This was expected as the PCF needed to be heated above a threshold temperature for its hole structure to collapse. Reducing the main arc current, reduces the temperature between the arc points, and reduces the temperature for all the regions around the arc points. This reduces the amount of fibre that experiences a temperature above the threshold temperature for hole collapse.

It was observed that lower main arc currents produce mechanically weaker splices. This is because heat is required to melt the two fibre ends together. Forming physically robust splices requires conditions in opposition to those required to reduce the length of the hole collapse region. The minimum arc current used before the splice would no longer form was 14.3 mA for PCF to SMF splices, and 12.9 mA for PCF to PMF splices. These observations were also made by Zuoming et al. [10], who found an arc offset distance of 220 μm was the optimum arc offset distance. They also found that the optimum main arc current was a reduction of 25% when compared to the main arc current of PMF to PMF splices.

This work found that the central issue is limiting the length of the PCF that is heated to only the region required for forming a splice. An arc fusion splicer was used as it is a commonly used splicer type, and therefore this work can be more readily utilised by others. A laser based splicer has the potential to focus heating on a smaller region of the fibre, when compared to arc fusion splicing [13]. An

expansion of this work would be to utilise a laser splicer, to produce PCF to PCF splices with low loss. Mode field diameter (MFD) mismatch was not focused on in this work, but others have taken steps to reduce this [7, 8, 9]. In most cases this is achieved by modelling the mode field diameter of the PCF after it has experienced complete or partial hole collapse. If such a model is combined with using a laser splicer, it might allow the splicing process to be tailored to control the change in the MFD. If not, then the PCF and, SMF or PMF, can be chosen such that there is little or no MFD mismatch. This would further reduce loss across the splice. Finally the backscatter constant of the PCF in this work was not calculated due to time constraints. An investigation into this would improve the measure of the actual loss across the splice joint. While change in relative loss was sufficient in this work, further extension would benefit from a more precise and absolute measure.

References

[1] A. D. Yablon. *Optical Fiber Fusion Splicing*. Springer Series in Optical Sciences, 1st edition, 2005.

[2] A. D. Yablon and R. T. Bise. Low-loss high-strength microstructured fiber fusion splices using GRIN fiber lenses. *IEEE Photonics Technology Letters*, 17: 118–120, 2005.

[3] L. Xiao, M. S. Demokan, W. Jin, Y. Wang, and C.-L. Zhao. Fusion Splicing Photonic Crystal Fibers and Conventional Single-Mode Fibers: Microhole Collapse Effect. *Journal of Lightwave Technology*, 25:3563–3574, 2007.

[4] O. De-qin, G. Chun-yu, R. Shuang-chen, W. Yi-ming, Y. Jin-hui, L. Huai-qin, and W. Hui-feng. Theoretical and experimental analysis of splicing between the photonic crystal fiber and the conventional fiber using grin fibers. *Applied Optics*, 51:8516–8520, 2012.

[5] Y. Yang, M. Ye, W. Duan, W. Jin, C. Liu, and S. Ruan. Polarization maintaining photonic crystal fiber IFOG. *Proc. of SPIE*, 8421(c):84210D–84210D–4, 2012.

[6] P. J. Bennett, T. M. Monro, and D. J. Richardson. Toward practical holey fiber technology: Fabrication, splicing, modeling, and characterization. *Optics Letters*, 24(17):1203–120, 1999.

[7] J. T. Lizier and G. E. Town. Splice losses in holey optical fibers. *IEEE Photonics Technology Letters*, 13(8):794–796, 2001.

[8] Y. L. Hoo, W. Jin, J. Ju, and H. L. Ho. Loss analysis of single-mode fiber/photonic-crystal fiber splice. *Microwave and Optical Technology Letters*, 40(5):378–380, 2004.

[9] K. Nakajima, K. Hogari, J. Zhou, K. Tajima, and I. Sankawa. Hole-Assisted Fiber Design for Small Bending and Splice Losses. *IEEE Photonics Technology Letters*, 15(12):1737–1739, 2003.

[10] S. Zuoming, S. Ningfang, J. Jing, S. Jingming, and M. Pan. Low loss fusion splicing polarization-maintaining photonic crystal fiber and conventional polarization-maintaining fiber. *Optical Fiber Technology*, 18:452–456, 2012.

[11] B. Bourliaguet, C. Paré, F. Emond, A. Croteau, A. Proulx, and R. Vallée. Microstructured fiber splicing. *Optics Express*, 11(25):3412–3417, 2003.

[12] B. H. Park, J. Kim, U. C. Paek, and B. H. Lee. The optimum fusion splicing conditions for a large mode area photonic crystal fiber. *IEICE Trans. Electron.*, E88-C(5):883–888, 2005.

[13] J. H. Chong, M. K. Rao, Y. Zhu, and P. Shum. An effective splicing method on photonic crystal fiber using CO2 laser. *IEEE Photonics Technology Letters*, 15(7):942–944, 2003.

[14] J. H. Chong and M. Rao. Development of a system for laser splicing photonic crystal fiber. *Optics Express*, 11(12):1365–1370, 2003.

[15] T. P. Hansen, J. Broeng, C. Jakobsen, G. Vienne, H. R. Simonsen, M. D. Nielsen, P. M. W. Skovgaard, J. R. Folkenberg, and A. Bjarklev. Air-Guiding Photonic Bandgap Fibers: Spectral Properties, Macrobending Loss, and Practical Handling. *Journal of Lightwave Technology*, 22(1):11–15, 2004.

[16] F. Benabid, F. Couny, J. C. Knight, T. a. Birks, and P. S. J. Russell. Compact, stable and efficient all-fibre gas cells using hollow-core photonic crystal fibres. *Nature*, 434(7032):488–491, 2005.

[17] R. Thapa, K. Knabe, K. L. Corwin, and B. R. Washburn. Arc fusion splicing of hollow-core photonic bandgap fibers for gas-filled fiber cells. *Optics Express*, 14(21):9576–9583, 2006.

[18] J. Crisp and B. Elliott. *Introduction to Fiber Optics*. Elsevier, third edition, 2005.

[19] Fujikura. Technical Datasheet: Fujikura 100P Specialty Arc Fusion Splicer Manual. Technical report, Fujikura Corporation, 2012.

[20] J. K. Mackenzie and R. Shuttleworth. A Phenomenological Theory of Sintering. *Proceedings of the Physical Society. Section B*, 62:833–852, 1949.

[21] *Optical Backscatter Reflectometer 4400 User Guide*. Luna Technologies, 2009.

[22] A. J. Rogers, S. V. Shatalin, and S. E. Kanellopoulos. Optical-fibre Backscatter Polarimetry for the Distributed Measurement of Full Strain Fields. *Proc. of SPIE*, 6004:1–14, 2005.

[23] S. Poeggel, D. Tosi, G. Leen, and E. Lewis. Fiber-optic extrinsic FPI/FBG sensor for temperature-compensated pressure measurement in medical applications. *Proceedings of SPIE - The International Society for Optical Engineering*, 8794:1–5, 2013.

[24] R. R. J. Maier, W. N. MacPherson, J. S. Barton, S. McCulloch, and B. J. S. Jones. Distributed sensing using Rayleigh scatter in polarization-maintaining fibres for transverse load sensing. *Measurement Science and Technology*, 21: 094019, 2010.

[25] N. R. Draper and H. Smith. *Applied Regression Analysis.* Wiley Series in Probability and Statistics, 3rd edition, 1998.

Chapter 5

In-fibre Fabry-Perot microcavities

5.1 Introduction

It was discussed in Chapter 4, that when splicing photonic crystal fibre (PCF) to a single mode fibre (SMF), a microcavity would occasionally form in the interface of the PCF and SMF splice near the fibre cores. An example of such a mircocavity is shown in Figure 5.1. The microcavity acts as a Fabry-Perot etalon [1], with the glass/silica interface at the SMF acting as the first partially reflecting surface due to Fresnel reflection, and the glass/silica interface at the PCF acting as the second partially reflecting surface.

In this chapter, work is presented on the use of the microcavity as an intrinsic Fabry-Perot interferometer. An intrinsic Fabry-Perot interferometer (IFPI) consists of two in-fibre partial reflectors, with the region of fibre between them acting as the sensor[2]. In this work the microcavity's two surfaces parallel to each other, and perpedicular to the cores of the fibres composing the splice, are the partial reflectors, using the Fresnel reflection from the air/silica interface. The etalon formed by the microcavity acts as the sensor.

[1] A Fabry-Perot etalon is composed of two partially reflecting surfaces parallel to each other [1]. A beam that perpendicularly intersects both surfaces experiences partial reflection, with reflected beams also experiencing partial reflection. The multiple beams interfere with each other, producing a reflection spectrum dependent on the spacing between the partially reflecting surfaces.

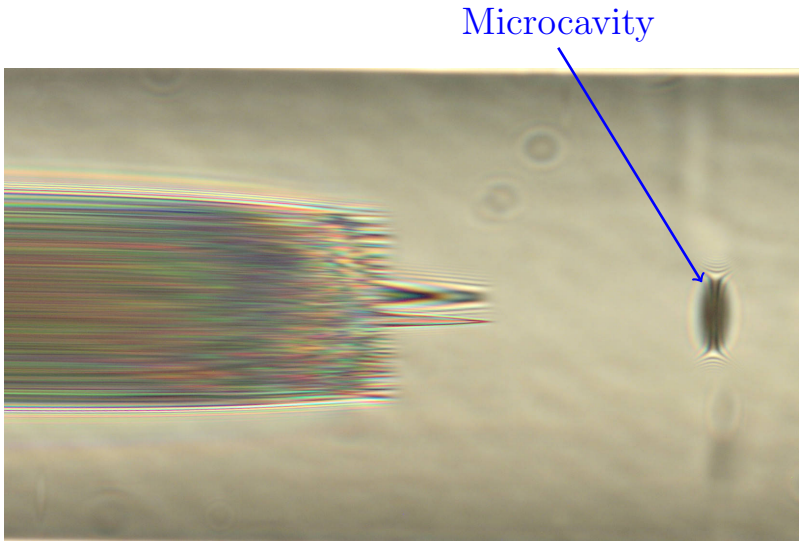

Figure 5.1: Image of a PCF to SMF splice produced in this work that contains a microcavity. The microcavity is highlighted.

As discussed in Chapter 2, extrinsic Fabry-Perot interferometers (EFPI) have been used in a large range of sensor applications such as structural health monitoring of dams, bridges and airplanes [3]. EFPIs are normally constructed of a cavity external to the optical fibre, for which the fibre is coupled [4]. EFPIs can be constructed by placing the end faces of two optical fibres in close proximity to each other, held in place with a cylinder. Conditions changing the distance between the fibre ends change the spectrum of the etalon, allowing it to be used as a strain sensor [1]. IFPIs in comparison to EFPIs, can be embedded more easily in composites or used in harsh environments[2]. This is because they are constructed within the optical fibre, such as with a cavity produced by the spacing between two broadband fibre Bragg gratings (FBGs) in close proximity to each other [5], or can be machined into the fibre to produce an air filled cavity inside the fibre core [6].

The microcavity based IFPIs produced in this work, used the novel construction approach of forming them from a splice of SMF to PCF, which allowed them to be the approximate size of a fibre Bragg grating (FBG), and to be used in roles currently occupied by EFPI while being more easily embedded or used in harsh environments. A detailed description of the construction of the microcavities is in

Section 5.2.

This type of microcavity IFPI has been used as an axial strain sensor with a linear response in the range $0\mu\epsilon$ to $1000\mu\epsilon$ [7]. Favero et al. [8] only used it as an axial strain sensor. Starting from this approach, this will be extended for the first time to applied transverse load. A comparison was done between individual microcavities to both applied transverse load and applied axial strain [9], to assess if there was a correlation in their sensitivity to both measurands. The response of the microcavities to the measurands is reported in Section 5.4.

Further, a comparison of the microcavities' sensitivity to applied axial strain and transverse load, when either coated in a resin cube or uncoated, was undertaken. The resin cube was intended to transduce applied transverse load into applied axial strain. This is based on the work of Correia [10], who used the resin cube to enhance the sensitivity of FBGs to transverse load. The properties of the resin is described in Section 5.2.2, while its effect on the sensitivity of the microcavities to measurands is reported in Section 5.4.

A number of microcavities were produced in this work, and variation in their sensitivity to all measurands, and their dimensions, was used to assess the consistency of the fabrication process. The consistency of the construction is described in the following section, which details the construction of the microcavities.

In summary, the aim of the work in this chapter was to produce a microcavity based strain sensor. The focus was to use them to measure transverse load, but as they have previously been used to measure axial strain their sensitivity to both was measured. This allowed a comparison to see if their sensitivity to one measurand correlated with their sensitivity with the other measurand. A further aim was to enhance their sensitivity to transverse load, by use a resin coating (in the shape of a cube centred on the microcavity).

The aim of this work is to develop a sensor with similar capabilities to an FBG, but not requiring the complicated and delicate setups used to produce FBGs [11]. As

will be described later, the microcavities are produced in a commerically available arc-fusion splicer, a more convenient construction method. As such the microcavities possess the potential to be a cheaper alternative to commonly available FBGs.

5.2 Microcavity

This section describes the approaches used to construct microcavities, and their resultant properties due to the specific parameters used during construction. These parameters are similar to the parameters in Chapter 4 for modifying the quality of PCF splices. These parameters are; main arc current, overlap distance, and internal pressure of the PCF.

An example of a microcavity produced in this work is shown in Figure 5.2. The optical fibre on the left is the SMF with a visible core, the optical fibre on the right is PCF with the partially collapsed hole structure visible. The microcavity in Figure 5.2 presents an ellipsoidal shape with its shortest axis parallel to the cores of the fibres that compose the splice.

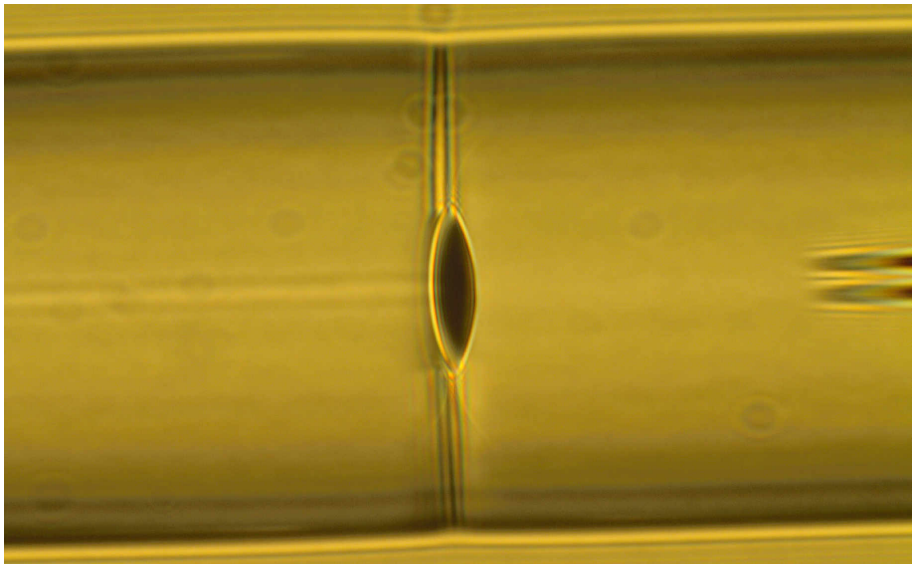

Figure 5.2: Microcavity formation at the splicing between a SMF (on the left) and a PCF (on the right). The microcavity forms an ellipsoid at the splice joint, with the longest axis perpendicular to the axis of the fibre. The longest axis of this fibre is 43 μm; the shortest axis is 11 μm.

As discussed in Chapter 4, when splicing a PCF, the hole structure near the splice joint collapses due to the heating process used during splicing. The air that occupies the hole structure is pushed in two opposite directions, towards the splice joint, and away from the splice joint. The air pushed into the splice joint becomes trapped and forms the microcavity. Favero et al. [7] found that when a small amount of air is trapped, this forms a spherical microcavity at the splice joint. During splicing, the viscosity of the silica drops and air is able to displace it to form a sphere[7]. If the distal end of the PCF is pressurised, this forces more air towards the splice joint during splicing, and the resulting microcavites are ellipsoidal [7], like the microcavity in Figure 5.2. In this work the PCF was pressurised by resin sealing a rubber hose (internal diameter 4 mm) on to the distal end of the PCF. The hose was connected to a Druck pump and digital pressure indicator (DPI 601(IS)), which was used to pump air into the PCF. It is unknown how Favero et al. [7] pressurised the PCF in their work. When pressurising the PCF, the air moved to the splice joint due to hole collapse, has more force to displace silica of the fibres at the interface between the SMF and PCF. The silica resists displacement, with the resistance weaker along the interface of the splice joint. The excess air moves along this interface, producing an ellipsoidal microcavity. The splicing parameters used by Favero et al. [7] to produce ellipsoidal microcavities was: prefusion time $0.3s$, prefusion arc $13mA$, overlap $5\mu m$, and the main fusion current was $12mA$. These parameters are described in greater detail in Chapter 4, however a brief description is given here. The prefusion arc current is used to clean the fibre ends of dirt during splicing. The prefusion time refers to the duration of the prefusion arc current, which needs to be short to avoid unduly heating the optical fibre ends. The prefusion arc current is at a value required to vaporise any dirt residing on the optical fibre end faces. The main arc current is used to heat the fibre ends so they can be melted together, it will be described later in this section how larger main arc currents reduce the viscosity of the silica during splice formation, and how this affects the shape of the microcavity. The overlap

refers to the length of the region of the fibres forced to overlap each other. Favero et al. [7] used an 5 μm overlap during the construction of the microcavity, this is much shorter than the normal 15 μm. Using a shorter overlap weakens the interface of the PCF to SMF, which reduces the resistance against air displacing the silica along the interface, resulting in more ellipsoid microcavities. How these parameters affected the shape of the microcavity will be described in greater detail later in this section.

In this work the microcavity etalon was interrogated in reflection with a broadband light source and detector, with the centre of the light spectrum at 780 nm. The microcavity was not interrogated from the PCF end as the distal end of the PCF was attached to the pump used to pressurise it [7]. When interrogating the microcavity in reflection, light propagates from the core of the SMF into the microcavity, as shown in Figure 5.3. The channelled spectrum of the microcavity in Figure 5.3 consisted of a sinusoidal intensity pattern with a fringe visibility of 0.95. A description of this spectrum is given later in this section.

This channelled spectrum is produced from the etalon formed by the microcavity, described in Figure 5.3. When light propagating along the core of the SMF encounters the first silica/air interface, S_1, it experiences Fresnel reflection at the interface. The light that transmits through the first interface propagates through the air filled microcavity until it encounters the second interface, S_2, and is partially reflected ($\approx 4\%$) back to S_1. This defines the Fabry-Perot etalon produced by a microcavity, with d the distance between the parallel partially reflecting surfaces. Light reflects between these two surfaces, with the intensity of the light as a function of wavelength given by; $I = I_1 + I_2 + 2\sqrt{I_1 I_2} cos(\Delta\phi)$ [8], where I_1 is the intensity of reflection of S_1, I_2 is the intensity of reflection of S_2, and $\Delta\phi$ is the phase difference of the light reflected by the two different surfaces [7]. $\Delta\phi$ can be taken as $4\pi nd/\lambda$ [2], where n is the refractive index of air in the microcavity ($n \approx 1$), and λ is the

[2]This is a summation of the phase of the beam propagating from the SMF to PCF, and the phase of the beam reflected at the PCF and propagating from the PCF to SMF. d/λ is the number

wavelength of light [7].

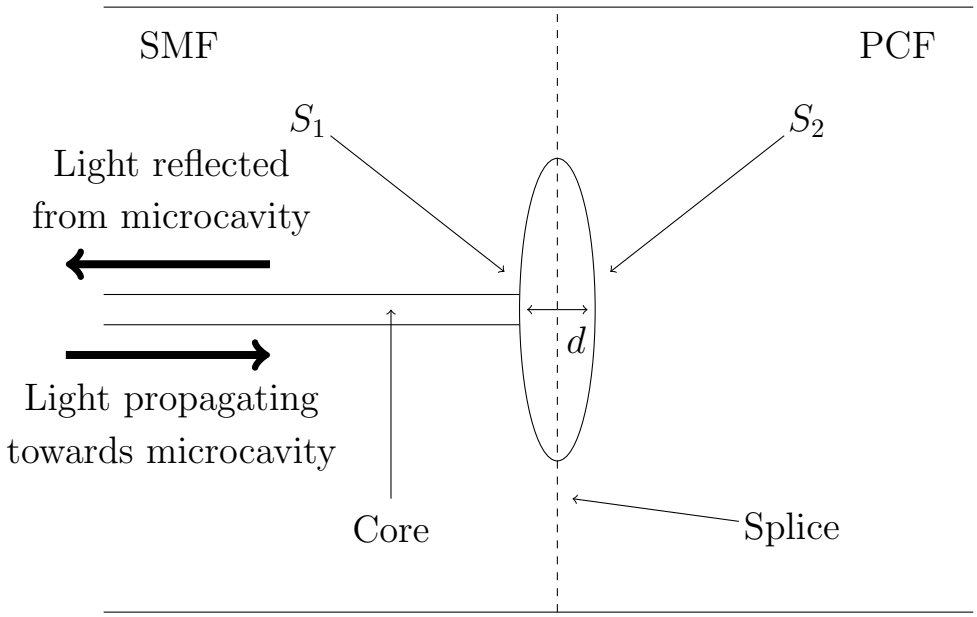

Figure 5.3: Diagram of a microcavity. S_1 is the first partially reflecting surface adjacent to the SMF core, S_2 is the second partially reflecting surface opposite the SMF core. d is the distance between these two surface.

The periodicity of the channelled spectrum is given by equation 5.1 [7];

$$P = \frac{\lambda^2}{2nd} \tag{5.1}$$

where λ is the central wavelength of the light illuminating the cavity, n is the refractive index of the air in the microcavity ($n \approx 1$), and d is the distance between the two partially reflecting surfaces of the microcavity. This equation reveals that the periodicity of the microcavity is inversely proportional to the length of the microcavity (d). Here it will be related how the length of the microcavity can affect its sensitivity to applied axial strain, or applied transverse load.

Figure 5.4 gives an example of a channelled spectrum of a microcavity produced during the work for this chapter. The spectrum of the microcavity consisted of an oscillating intensity pattern with a fringe visibility of 0.95, where the intensity

of wavelength periods across the distance d, multiplying this by 2π gives the phase increase across d.

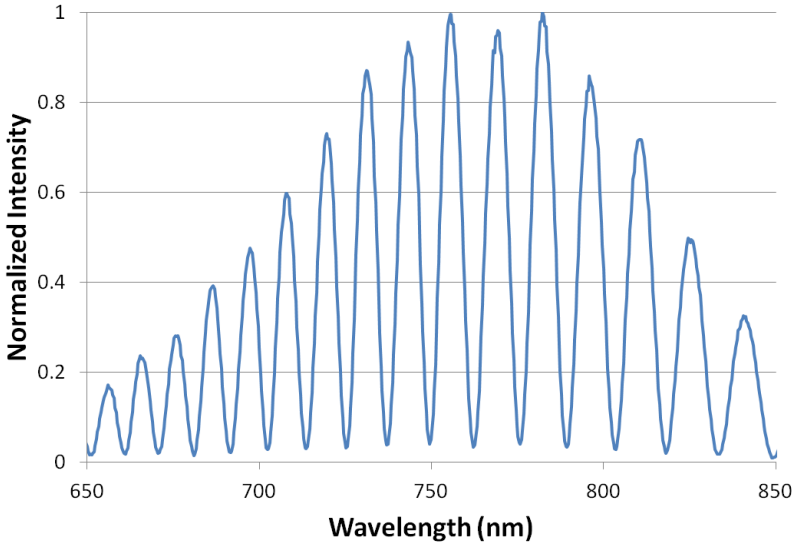

Figure 5.4: A typical channelled spectrum of a microcavity.

envelope is due to the light spectrum used to interrogate the microcavity. This is due to the 780 nm coupler. The coupler has maximum efficiency at coupling light at 780 nm, the efficiency reduces the further the wavelength is from 780 nm. A diagram of this is shown in Figure 5.5. Assuming a uniform intensity spectrum across wavelengths, the coupler only couples light to the other fibre as a function of wavelength, reducing the intensity of light in the other fibre for wavelengths further from 780 nm.

Conditions that modify the dimensions of the cavity after its production, such as applied strain, change the phase differences between the two reflections and therefore the channelled spectrum observed. This shifts the position of the spectrum. Favero et al. [7] analysed the position of this spectrum for their microcavities, as axial strain was applied to the cavity in the range of $0\mu\epsilon$ to $1000\mu\epsilon$. They found that the spectrum shifted to longer wavelengths linearly, as axial strain was applied to the microcavity.

From the work of Favero et al. [8] it was known that the preferred shape for the microcavities to sense strain was an ellipsoid. The partially reflecting surfaces of the microcavity have a larger region parallel with each other, improving the finesse of the mircocavity. This work aimed to replicate such microcavities, since they were

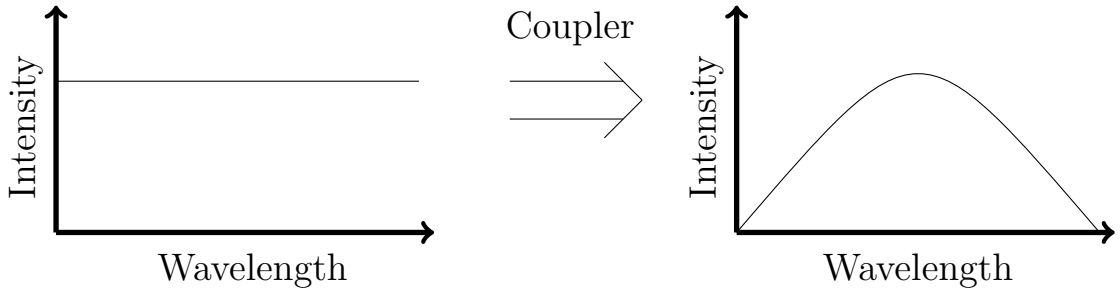

Figure 5.5: Description of how the coupler modifies the intensity of the microcavity wavelength spectrum. Left is the spectrum of light before the modulation of the coupler, right is the spectrum of light after the modulation of the coupler.

most likely to produce better sensors of applied transverse load.

5.2.1 Construction

The Fabry-Perot microcavities were fabricated using a Fujikura 100P fusion splicer. The SMF fibre used was Fibercore SM750 and the polarisation maintaining photonic crystal fibre was NKT Photonics PM1550. The SM750 was chosen so that its cut-off wavelength allowed the microcavities to have a periodicity of $20nm$. This provides the possibility to observe multiple periods in the spectrum (see equation 5.1).

In this work the PM1550 was internally pressurised by a Druck pump and digital pressure indicator (DPI 601(IS)) to the proximal end [3] of the fibre from the splicing end. It was observed that pressurizing the PCF favours the formation of a microcavity. However, increasing the applied pressure reduces the quality of the splicing, and decreased the likelihood of the splice forming. Favero et al. [7] found that increasing the pressure inside the PCF during construction of the splice increased the size of the resultant microcavities.

In this work it was found that increasing the pressure gave a small improvement on fringe visibility, but that the main arc current dominated the shape of the microcavity. The optimum pressure was found to be $7.50 \pm 0.005bar$, this was much greater than the maximum pressure used by Favero et al. [7] of $4.0bar$. Favero

[3] The proximal end of the fibre is the opposite end to the one that is spliced.

et al. [7] found increasing the pressure made the microcavities more ellipsoid, and improved their fringe visibility. This difference is most likely due to the different PCF used in this work, in comparison to the PCF used in [7].

It was thought that the length of the PCF between the distal end and the proximal end could influence the effective pressure at the proximal end of the fibre. Longer fibres could have lower pressures at the proximal end, and inhibit the formation of microcavities. This would be due to the ratio of the volume within PCF, and the volume within the reservoir. The Druck pump has a reservoir of air it pressurises to exert pressure on anything attached to it. Regardless of the size of the reservoir within the Druck pump, the volume of air within the PCF is very small. The volume of air the PCF can hold per metre is low. The air holes have diameters of order $1\mu m$, and with approximately 100 holes in the structure, $1m$ of fibre would have $0.1mm^3$ of air inside its hole structure. The length of the fibre would have little effect on reducing the volume of air from the reservoir inside the pump used to pressurise the fibre.

The small cross-section of a hole could inhibit the rate of flow of air through it, such that when the distal end of the fibre is pressurised there is a significant time delay until the proximal end of the fibre reaches equilibrium pressure with the distal end. With a waiting period of a few minutes between pressurising the distal end of the fibre and splicing, length did not have an effect on the formation of the microcavity.

The main arc current was found to change the shape of the microcavity, and increasing the main arc current during construction of the splice, produced more spherical microcavities. Figure 5.6 shows examples of two microcavities constructed with all other parameters the same such as overlap, or pressure, but with different main arc currents. As described in Chapter 4, the main arc current heats the fibre to allow the two cleaved fibre ends to adhere to each other. Heating silica reduces its viscosity, and reduces the resistance against air escaping the hole collapse displacing

the silica.

The silica in Figure 5.6a was hotter [4] due to the greater main arc current, and was more easily displaced by air to form a more spherical microcavity. Ellipsoid microcavities are preferred over spherical microcavities, as they have larger regions of partially reflecting surfaces parallel to each other, and possess a better finesse [8]. Lower main arc currents reduce the quality of the splices formed, and in some cases even the splice formation. The sharp line down the fibre, that bisects the microcavity in Figure 5.6b is an example of an inferior splice forming. That line is the interface between the two fibres, which should be smoother with regards to the rest of the fibre. A main arc current of $15.3mA$ (duration $1700ms$) was used, it was found to reliably produce splices, and the microcavities that formed were ellipsoid rather than spherical. This was used in conjunction with a different overlap which will be discussed later in this section. This is a larger main arc current than the $12mA$ used by Favero et al. [7]. The difference in main arc current is most likely due to the different splicers used in this work and Favero et al. [7], for the construction of the microcavities.

As discussed in Chapter 4, when splicing fibres the overlap parameter is used to bring the two cleaved fibre ends together. The overlap is the length of each fibre which is forced to overlap the other. The larger the overlap, the greater the force of the two fibres pushed together. This force can be enough to allow the hole structure to avoid collapsing at the fibre end. Figure 5.7 shows two splices with the same parameters except that (a) had an overlap of 8 μm and (b) had an overlap of 10 μm. The force of the two fibres meeting increases the air pressure at the splice joint, in (a) this was enough to preserve some of the hole structure at the splice joint. The greater force from the larger overlap for (b) increased the air pressure at the splice joint, preserving more of the hole structure.

As explained in Chapter 4, the hole collapse is caused by heating the PCF, the

[4]The main arc current is used as a proxy for the heat of the optical fibre. It was not possible to know the fibre's actual temperature, for reasons described in Chapter 4.

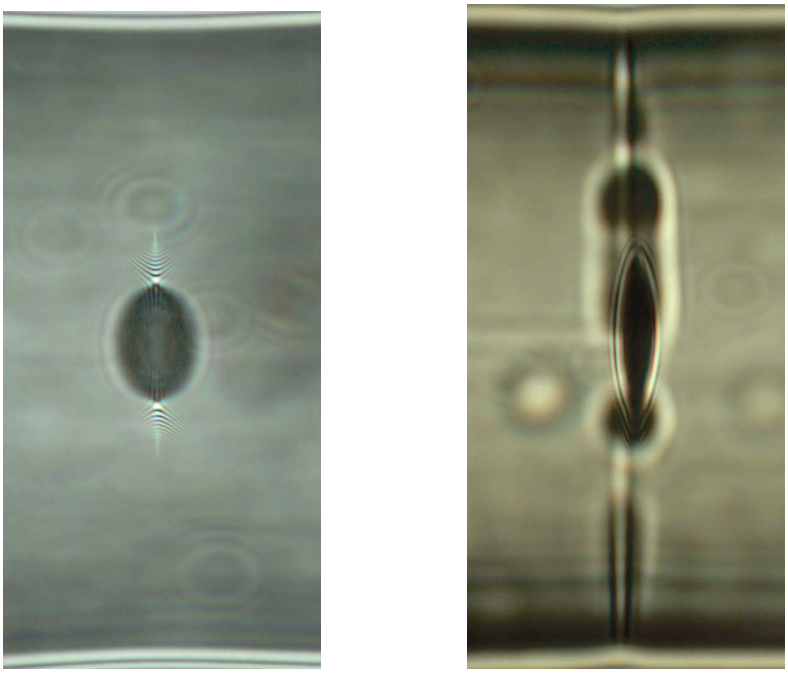

(a) (b)

Figure 5.6: Microcavities produced with: (a) a main arc current of 16.3 mA, (b) a main arc current of 14.3 mA

speed of this collapse is given by equation 4.1, which is reproduced here;

$$V_{collapse} = \frac{\gamma}{2\eta} \tag{5.2}$$

In equation 5.2, $V_{collapse}$ is the collapse velocity, γ is the surface tension of silica, and η is the viscosity of silica. This equation is true for all sized holes [12][13].

The surface tension of silica can be taken as a constant over the range of temperatures used during splicing [13]. What changes is the viscosity of the silica, as that reduces as the fibre heats up, the holes begin to collapse, and the hotter the temperature, the quicker the collapse. Greater air pressure in the hole structure can provide a force to counteract the surface tension of the silica, and reduce the speed of hole collapse. Larger overlap values provide this increased air pressure at the splice joint, slowing the rate of hole collapse such that the two enlarged holes of the PM1550 do not collapse before the end of the splicing process. As discussed in Chapter 4, the enlarged holes of the PM1550 collapse at the same speed as the

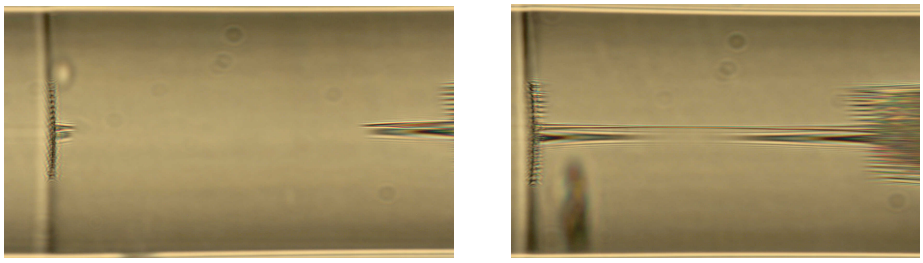

(a) (b)

Figure 5.7: Microcavities produced with different overlap distances. (a) had a overlap of $8\mu m$, (b) had a overlap of $10\mu m$

smaller holes, but their larger diameters give them more time before they collapse.

It was found that increasing the overlap from 5 μm [5] produced larger microcavities as more air was trapped at the splice joint. To avoid the preservation of the hole structure at the splice, which inhibits the formation of a microcavity, the duration and value of the main arc current was increased, to the value of 15.3 mA (duration 1700 ms) as stated earlier. The optimum overlap was found to be $8\mu m$, which is larger than the overlap of $5\mu m$ used by Favero et al. [7]. Increasing the overlap increased the air pressure within the PCF at the splice joint, and with the greater air pressure used during splice construction, was most likely due to the different PCF used in this work in comparison to Favero et al. [7].

Table 5.1: The dimensions of the microcavities produced in this thesis work. The uncertainty in the width was $\pm 1.6\mu m$ and in length was $\pm 0.7\mu m$. This was calculated by ten measurements of the same microcavity's dimensions. STD is the standard deviation of the microcavities.

Microcavity	Width (μm)	Length (μm)
A	40	13
B	43	13
C	54	16
D	44	12
E	47	12
F	47	11
G	46	11
Mean	46	13
STD	4.4	1.7

[5] The overlap distance used by Favero et al. [7].

The microcavities in this work were photographed with an Olympus BX51 microscope. The dimensions of the microcavities are presented in table 5.1, the microcavities were not selected for their dimensions directly but for the resulting spectrum. Due to the variability in construction specific dimensions could not be selected. The width of the microcavity is the axis of the ellipsoid perpendicular to the core of the fibre. The length of the microcavity is parallel to the propagation axis of the fibre, and is described as the diameter by Favero et al. [7]. The length of the microcavites are in the range of $10\mu m$ to $20\mu m$, much smaller than the range of $25\mu m$ to $60\mu m$ produced by Favero et al. [7]. This is most likely due to reduced volume of air at the splice joint in the microcavities produced in this work, in comparison to the microcavities produced in Favero et al. [7]. The microcavity formation was found to be very sensitive to the internal conditions of the splicer, and thus using a different splicer can have a significant effect on the properties of the microcavities produced. Favero et al. [7] also used different PCF to produce their microcavities, the use of different PCF was not explored in this work, but is a clear next step in improving the construction of microcavity based in-fibre IFPI.

5.2.2 Resin Cube

It was observed in this work that the sensitivity of the microcavity to applied transverse load was much weaker than its sensitivity to applied axial strain. This is discussed in greater detail in section 5.4. To improve the sensitivity of the microcavity to applied transverse load, it was coated in a resin cube. This was to transduce applied transverse load experienced by the resin cube into applied axial strain experienced by the microcavity.

How it modifies the microcavities' response to applied axial strain, applied transverse load, and to changes in temperature will be discussed in section 5.4. To coat the microcavity, the fibre splice was placed into a silicon mould [6], shown in Figure

[6]Dimensions: 4.0 ± 0.2 *cm* long, 4.0 ± 0.2 *cm* wide, 1.0 ± 0.2 *cm* deep. The seam is 0.3 ± 0.05 *cm*

5.8. The fibre was placed in the seam, the mould was deformed along the seam to ease the placement of the optical fibre within it. To centre the microcavity in the mould's chamber, shown in Figure 5.8, a USB microscope was used to view the fibre and microcavity. When the microcavity was at the centre of the chamber, an epoxy [7] was poured in to produce a slight meniscus. The resin was cured using UV light, then the resin cube was filed down until flush with the mould. Finally the resin cube encased microcavity was removed from the mould, by deforming the mould to release the resin cube. Initially a Teflon mould was used, to form 3 mm resin cubes, but the resin adhered to it too strongly and the microcavity could not be removed undamaged from the mould. A second silicon mould that could deform was used, shown in Figure 5.8, that produced 6 mm resin cubes. Smaller resin cubes (such as the 3 mm) were preferred, as they weigh less, and have a smaller surface area. Reducing the surface area increases the effective pressure experienced by the microcavity, this will be discussed later in this section.

The weight had to be accommodated in the setup used to apply axial strain to the microcavity, which is described in greater detail in section 5.3. The larger surface area of the resin cubes produced by the second mould, reduced the effective transverse load experienced by the microcavity in the transverse load setup, which is described in greater detail in section 5.3. The silica of the microcavity had a much smaller thermal expansion constant than the resin cube. A smaller resin cube would have experienced less expansion, and applied less strain to the microcavity due to temperature changes. This is described in greater detail in section 5.4. The resin cube work was based on an approach reported by Correia [10], who had applied it to fibre Bragg gratings (FBGs) to improve their sensitivity to applied transverse load.

deep.

[7] EPO-TEK og134; a UV curable epoxy adhesive used for fibre optic and opto-electronic device packaging [14]. It was used because it adheres strongly to the optical fibre, and its hardness limits its deformation under load [10].

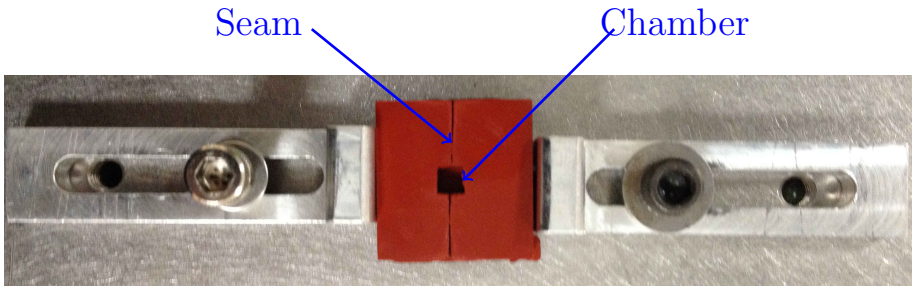

Figure 5.8: A silicon mould that could be deformed to release the resin cube. Highlighted are the seam that holds the optical fibre, and the chamber that is filled with the resin.

5.3 Interrogating the microcavity

The channelled spectrum produced by the microcavities was interrogated in reflection using an Ocean Optics S2000 spectrometer, coupling the output from an Ocean Optics SL-1 light source and a 50/50 coupler at $780nm$. An example spectrum is showed in Figure 5.9, it shows the spectrum of the microcavity before and after 100 $m\epsilon$ of axial strain is applied to it. As strain is applied the position of the spectrum shifts, in Figure 5.9 shown by the arrow.

The spectrometer had a resolution of $0.3nm$, the peak position was resolved to less than this limit ($0.1nm$) using a spectrum interrogation routine (SIR) developed in house by Dr Matthew Partridge. SIR is a Labview based peak fitting algorithm, that measures the shift of the peaks with changing measurands. Its default peak tracking uses the position of previous peaks to predict the position of the next [15]. It takes a series of files, and compares the position of the peaks between files. It can measure the mean shift between files, and uses this to estimate the shift of the peaks between files.

As described in the previous section, the main factor in producing the intensity envelope is the 780 nm coupler used, this was shown in Figure 5.5. The peak with the highest intensity is expected to be close to 780 nm, Figure 5.9 shows the difference is less than 40 nm. The three highest intensity peaks are used to measure the peak shift of the whole spectrum, these are highlighted in Figure 5.9 with a black

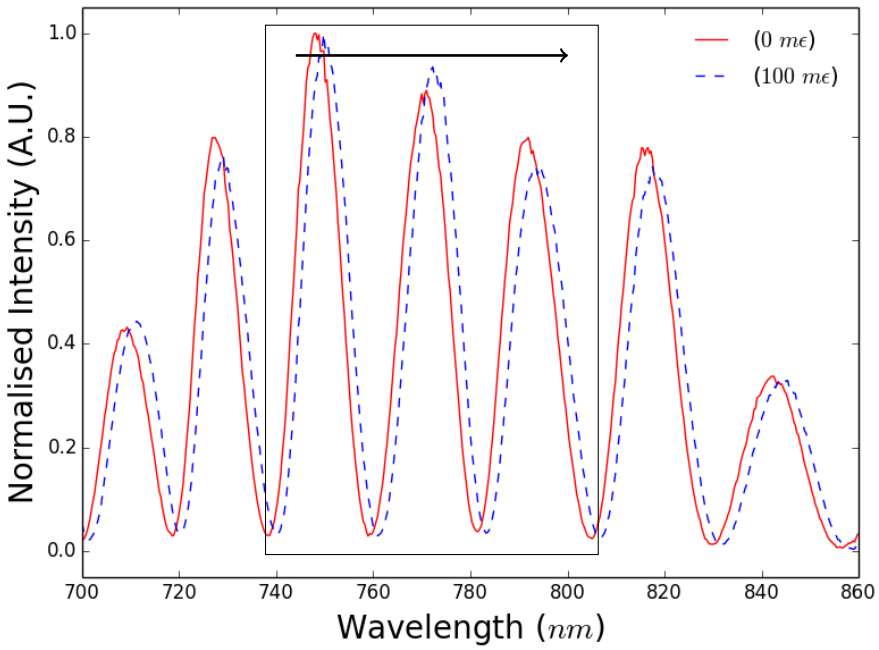

Figure 5.9: Graph of a microcavity channelled spectrum, before (red solid line) and after 100 $m\epsilon$ (blue dashed line) of axial strain was applied to it. The three intensity peaks used to measure the shift in the spectrum are highlighted within the black rectangle. When strain was applied the peaks shifted to longer wavelengths, highlighted by the black arrow.

rectangle. The mean wavelength shift of these peaks is taken as the wavelength shift of the whole spectrum.

Favero et al. [7] also interrogated the microcavity in reflection, however their broad band light source was centred at wavelength of 1550 nm. The light source and the detector (an optical spectrum analyser (OSA)), were coupled to the fibre containing the microcavity with a fibre optic circulator (FOC). This approach was not used in this work since the period of the microcavity scaled with the wavelengths used to interroagate it, and it was convenient to interrogate it at 780 nm since it did not require the use of an OSA.

The measurands of the experiments were; applied axial strain, applied transverse load, and change in temperature. The setup used to measure the microcavities' response to each of these factors is described in this section.

To observe how a resin coating on the microcavity would modify its response to the measurands, three microcavities were produced in addition to the ones used

to measure the microcavities response to the measurands. The response of these microcavities' (microcavity E, microcavity F, and microcavity G), before and after they were coated in a resin cube, to the measurands was recorded and is presented in the next section.

5.3.1 Axial strain

The setup used to apply axial strain to the microcavity is shown in Figure 5.10. The fibre containing the microcavity is held between two fibre mounts. The mounts have a v-groove fibre holder, whose position can be changed by three controllers with micrometer precision. The fibre is held to the v-groove fibre holder with a magnet. To apply axial strain to the microcavity, the fibre is elongated by repositioning the v-groove fibre holder of one of the mounts, using a controller. The v-groove fibre holder is translated along an axis parallel to the fibre length, away from the other v-groove fibre holder. The elongation, in increments of $20 \pm 1 \mu m$, is much smaller than the distance between the mounts, 15.3 cm, so that it produced linear increments of strain. The strain range was 0 $\mu\epsilon$ to 1300 $\mu\epsilon$, in ten 130 ± 6 $\mu\epsilon$ increments.

When the response to the maximum extension was made the fibre was allowed to relax to the minimum extension and the process of incrementally stretching the fibre was repeated for a series of three measurement sets.

When the microcavity was encased in a resin cube, the weight of the cube provided a source of strain on the fibre. To support this weight a third mount was used, as shown in Figure 5.10 and labelled as the support mount. Without this support the fibre broke when measuring the response of a microcavity E from the increased strain. The dimensions of microcavity E are described in table 5.1, and its response is described in the next section. After applied axial strain was applied to each microcavity, their response to applied transverse load was measured.

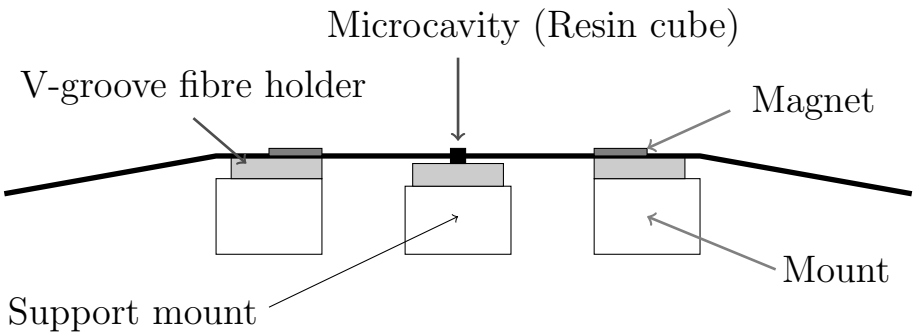

Figure 5.10: Set up to measure axial strain. The microcavity was suspended between two optical mounts, with equal amounts of fibre on each side. The fibre is pinned to the mount using magnets. When the microcavity was coated in a resin cube it was supported by another mount (labeled support mount) to mitigate strain produced by the weight of the resin cube

5.3.2 Transverse load

Transverse load was applied to the microcavity by placing it in a press as shown in Figure 5.11. A lever applied load to a load button, which depressed an upper glass plate onto a lower glass plate. The upper glass plate moved on four rungs, so that it pressed evenly across the surface of the fibre or resin cubes.

The fibre containing the microcavity was inserted between the two glass plates, with a dummy fibre. This, as well as the rungs, was to produce even pressure across the microcavity. The fibre and the dummy fibre were stripped so that there was no coating on either for the region inside the press. The force exerted by the upper glass plate was divided by the area of both fibres to calculate the transverse load per millimetre squared that the microcavity experienced. The transverse load range was 0.32 N/mm^2 to 10.90 N/mm^2. A series of five measurements were taken for each data point, repeating from minimum transverse load to maximum transverse load.

When the microcavity was coated in a resin cube, the dummy plug included two resin cubes as shown in Figure 5.12. The dummy resin cubes were to even the pressure exerted on the resin cube containing the microcavity across its surface. The force exerted by the upper glass plate was divided by the total area of all three resin

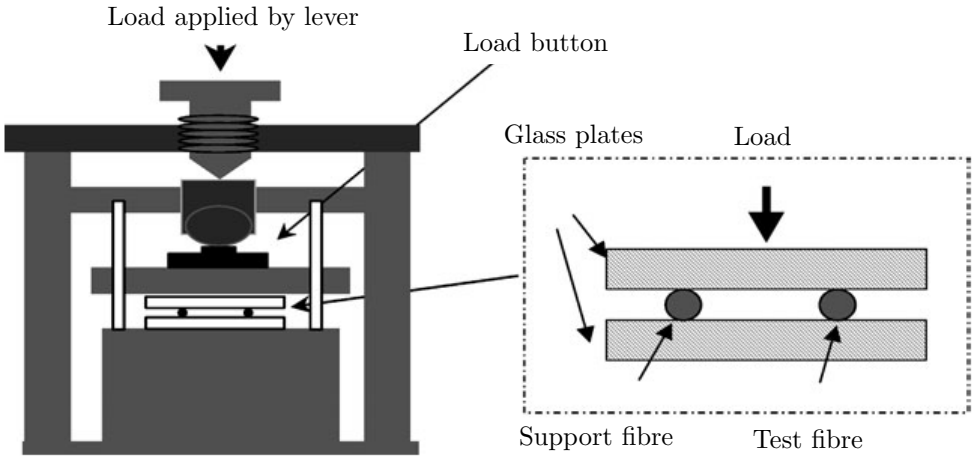

Figure 5.11: Press used to apply transverse load to the microcavities[16].

cubes, to calculate the transverse load per millimetre squared that the microcavity experienced. The transverse load ranges between 0.17 N/mm^2 and 5.68 N/mm^2. It was found that when load was applied to the resin cube, it took 30 seconds for the resin cube to settle and the position of the wavelength spectrum to stabilise. This stabilisation is described in greater detail in the next section. It is mentioned here as this time delay between application of weight and measurement of the spectrum of the microcavity was not required for microcavities without a resin coating, and is an additional component of the method.

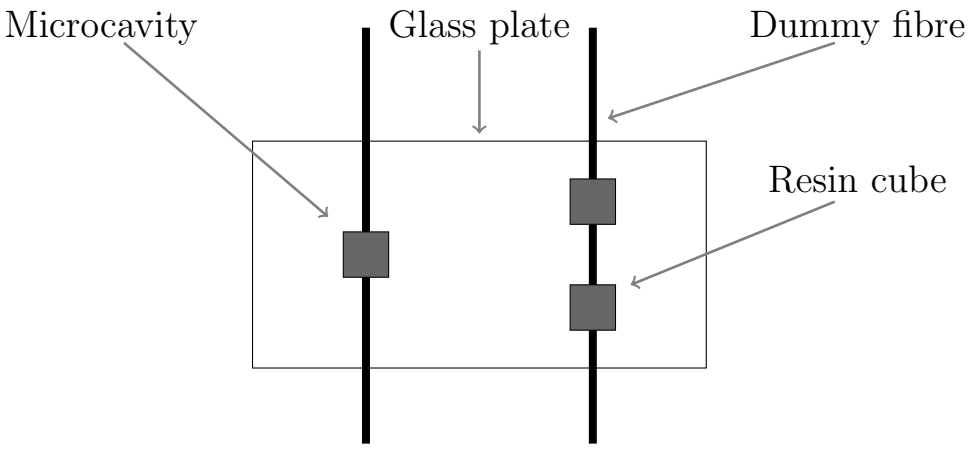

Figure 5.12: This is a top down schematic view of the microcavity fibre coated in a resin alongside a dummy fibre with two resin cubes to ensure even pressure across its surface. This includes the bottom glass slide of the pair presented in Figure 5.11.

5.3.3 Temperature change

A thermocoil was used to heat a two centimetre segment of the fibre containing the microcavity, with the microcavity at the centre of thermocoil, as shown in Figure 5.13. The response of the microcavity was monitored in a temperature range of $25 \pm 1\ ^{\circ}C$ to $60 \pm 1\ ^{\circ}C$, in $5 \pm 1\ ^{\circ}C$ increments. $25\ ^{\circ}C$ was chosen as it is was at least $5^{O}C$ above lab temperature to control for temperature fluctuations in the lab.

The operating temperature of the resin is $-55^{\circ}C$ to $100^{\circ}C$[14], so the $25^{\circ}C$ to $60^{\circ}C$ range was included. A series of three measurement sets were taken, running from the lowest temperature of the range to the highest, and then repeating.

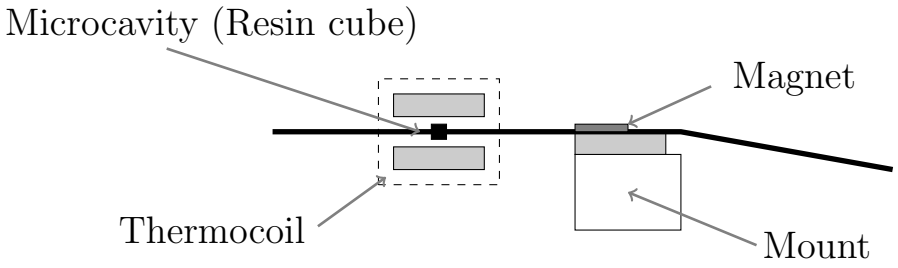

Figure 5.13: Setup used to heat the microcavity. The microcavity is surrounded by the thermocoil.

5.4 Response of the microcavity

Using the set up presented in the previous section, we measured the change in the channelled spectrum of microcavities A to G, as a function of axial strain, transverse load and temperature. First the response of the microcavities to applied axial strain will be described. Example responses of three of the microcavities will be presented, then the responses of the microcavities F and G, before and after they are coated in a resin cube.

Second the response of the microcavities to applied transverse load will be described, with example microcavities, and the microcavities encapsulated in resin cubes. Third the response of the microcavities to temperature change will be de-

scribed using the same approach that described the applied axial strain response and the applied transverse load response.

5.4.1 Axial strain

The mean shift in the peaks of the channelled spectrum of the microcavities were proportional to applied axial strain in the strain range 0 $m\epsilon$ to 13 $m\epsilon$. Figure 5.14 shows the response of microcavity A to applied axial strain, the equation of the line of best fit is $y = 0.32x - 0.18$ (R-squared = 0.99). This line was calculated using the Python function scipy.stats.linregress, which was used to calculate all the lines of best fit in this chapter. The response of microcavity A was reproducible, shown by the small error bars. The error bars are the standard deviation of the three sets of measurements taken. As described in section 5.2 the phase difference between the two reflections that compose the Fabry-Perot etalon is given by $4\pi nd/\lambda$. Linear changes in the phase difference results in linear shifts in position of the peaks of the channelled spectrum of the microcavity. This implies that d, the length of the microcavity, is changing linearly across the range of strain applied to the microcavity.

The linear response of microcavity A is matched by that of microcavity B (equation $y = 0.27x + 0.07$), shown in Figure 5.15. The response of microcavity B was less reproducible than for microcavity A, shown be larger error bars than microcavity A, however microcavity B holds close to the line of best fit (R-squared = 0.99). Microcavity C (equation $y = 0.29x - 0.02$), shown in Figure 5.16 fits the same response as microcavities A and B. This implies it was consistent behaviour for the microcavities' length to change linearly with applied axial strain in the range 0 $m\epsilon$ to 13 $m\epsilon$. As the peaks shifted to longer wavelengths, this implies that the microcavity had a slight decrease in its length, a change in length much less than its unstrained length. The response of microcavities D, E, F, and G also had linear sensitivity to applied axial strain.

Table 5.2 shows the sensitivities of the microcavities used in this work to applied

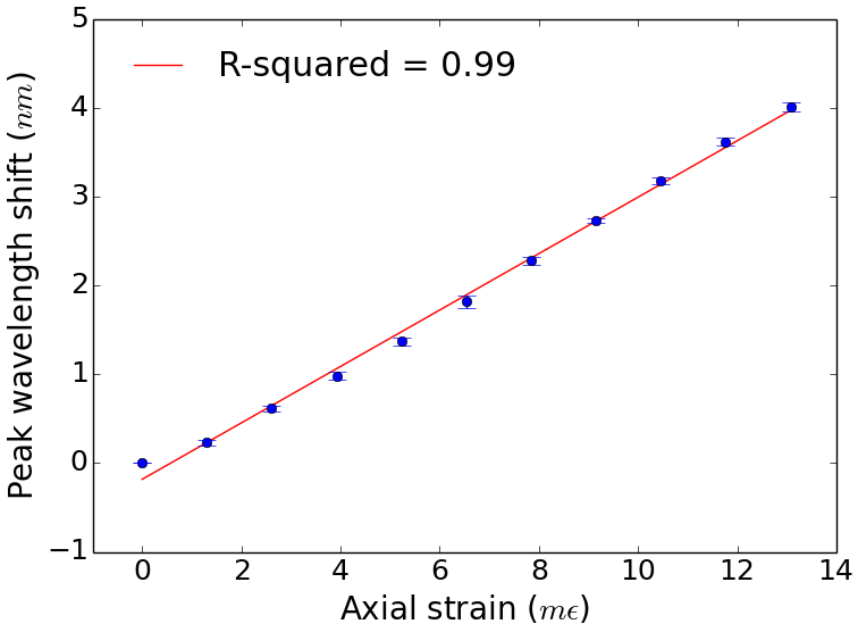

Figure 5.14: The response of microcavity A to applied axial strain. The equation of the line $y = 0.32x - 0.18$, R-squared $= 0.99$. The error bars are the standard deviation of the series of three measurements.

axial strain. This is calculated from the gradient of the lines of best fit for each microcavity. The uncertainty is the mean of standard deviation of the series of three measurement sets taken for each microcavity, divided by the range of axial strain to which the microcavities were subjected. The mean sensitivity of the microcavities is 0.286 ± 0.005 $/m\epsilon$, this is half the sensitivity of a fibre Bragg grating (FBG) written at 780 nm in single mode fibre (SMF).

For microcavity based axial strain sensors to be commercially competitive with FBG based sensors, their sensitivity needs to be comparable, or the microcavity must possess a property not possessed by FBGs. The standard deviation in the sensitivities of the microcavities was 0.021 ± 0.005 $nm/m\epsilon$, this is a variation of 10% between the microcavities. Before microcavities can reliably be used as an axial strain sensor their construction needs to become more reproducible. The construction is sensitive to the internal conditions of the splicer, which can not be easily determined using a commercial splicer. An expansion of this work would be the

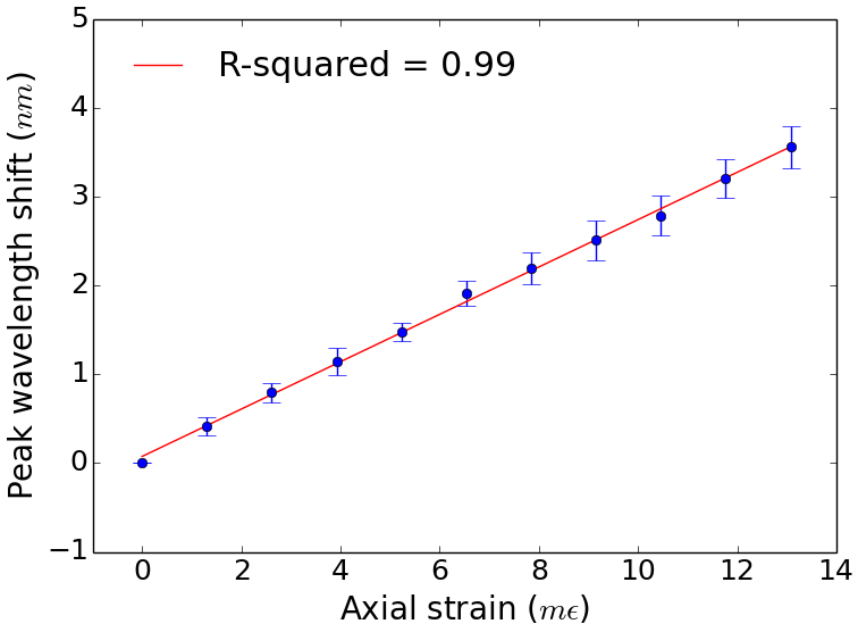

Figure 5.15: The response of microcavity B, to applied axial strain. The equation of the line $y = 0.27x + 0.07$, R-squared = 0.99. The error bars are the standard deviation of the series of three measurements.

development of a device custom built to produce microcavities. More precise control over microcavity formation would allow the properties of the microcavity to be better tailored to improve their use as a sensor.

Coating the microcavity in a resin cube slightly reduced its sensitivity to applied axial strain. Figure 5.17 shows the response of microcavity F to applied axial strain, before and after it was coated in a resin cube. The response of the uncoated microcavity to applied axial strain was linear, with a line equation $y = 0.29x + 0.00$ (R-squared = 0.99). This is close to the line of the coated microcavity, with a line equation $y = 0.27x - 0.15$ (R-squared = 0.99). This is a reduction in the sensitivity of 7% after the microcavity is coated. The reproducibility of the response of the microcavity did not change between being uncoated and coated; this is shown by similar sized error bars for both the uncoated and coated fibre.

Microcavity G also experienced a slight reduction in sensitivity when the microcavity was coated in a resin cube. The response of the uncoated microcavity to

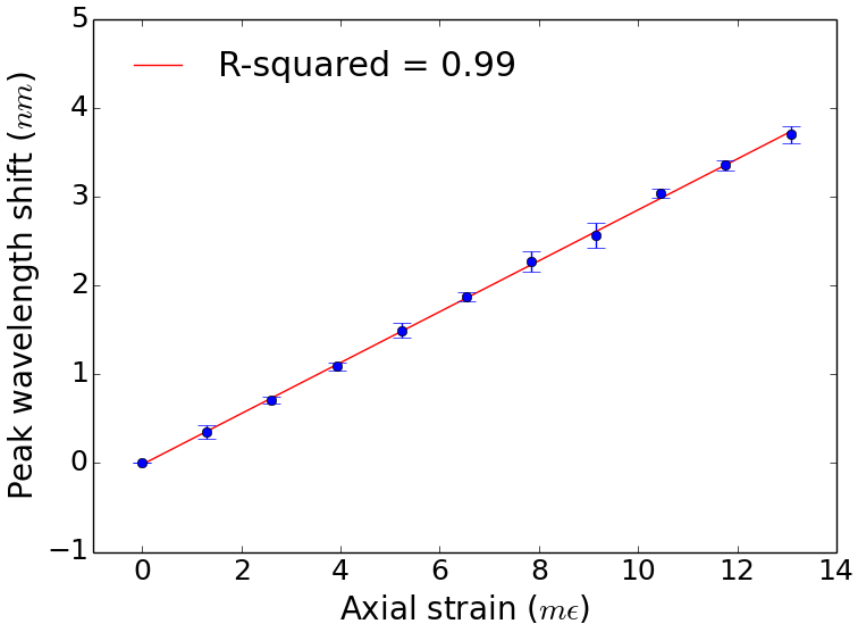

Figure 5.16: The response of microcavity C, to applied axial strain. The equation of the line $y = 0.29x - 0.02$, R-squared = 0.99. The error bars are the standard deviation of the series of three measurements.

applied axial strain was linear, with a line equation $y = 0.30x + 0.07$ (R-squared = 0.99). This is close to the line of the coated microcavity, with a line equation $y = 0.27x - 0.07$ (R-squared = 0.99). As already discussed the shift in the wavelength spectrum is caused be a change in the phase difference between the two reflections that compose the Fabry-Perot etalon. This phase difference changes when the length of the microcavity changes, when the distance between the two partially reflecting surfaces changes. The reduction in sensitivity implies that the rate of change of this distance with respect to applied axial strain, decreases when the microcavity is coated in a resin cube. This is most likely caused by counter tension provided by the resin cube, reducing the axial strain experienced by the microcavity.

Table 5.3 shows the sensitivity of microcavities F and G to applied axial strain, before and after they were coated in a resin cube. The table shows that the reduction in sensitivity was around 10% for both microcavities. This reduction in sensitivity could be partially mitigated if the stiffness of the resin cube was reduced, however

Table 5.2: Sensitivity of each uncoated microcavity to applied axial strain, and the precision of the sensitivity. The uncertainity is the mean of the standard deviation of the series of three measurements divided by the strain range. The FBG sensitivity is taken from Roths and Jülich [17] for an FBG centred at 780 nm. STD is the standard deviation of the microcavities, either their sensitivity, or the uncertaintiy in their sensitivity.

Microcavity	Sensitivity ($nm/m\epsilon$)	Uncertainty ($nm/m\epsilon$)
A	0.318	0.003
B	0.267	0.012
C	0.287	0.005
D	0.255	0.006
E	0.283	0.004
F	0.289	0.001
G	0.301	0.004
Mean	0.286	0.005
STD	0.021	0.003
FBG	0.620	0.003

that would reduce its effectiveness in transducing transverse load to applied axial strain. When primarily using the microcavity to sense applied axial strain, it should not be coated in a resin cube.

Table 5.3: Sensitivity of microcavities F and G to applied axial strain, when they are either uncoated or coated in a resin cube. The uncertainty is the mean of standard deviation of the series of three measurements divided by the strain range.

Microcavity	Without coating		With coating	
	Sensitivity ($nm/m\epsilon$)	Uncertainty ($nm/m\epsilon$)	Sensitivity ($nm/m\epsilon$)	Uncertainty ($nm/m\epsilon$)
F	0.289	0.001	0.266	0.003
G	0.301	0.004	0.265	0.005

5.4.2 Transverse load

When compared to their sensitivity to applied axial strain, the microcavities showed a weak sensitivity to applied transverse load. Figure 5.19 shows the response of microcavity B to applied transverse load, equation of the line $y = -0.02x - 0.02$, R-squared = 0.72. The small gradient, lower R-squared value, and larger error bars when compared to the microcavity's response to applied axial strain implies the microcavity is only weakly sensitive to applied transverse load. The applied

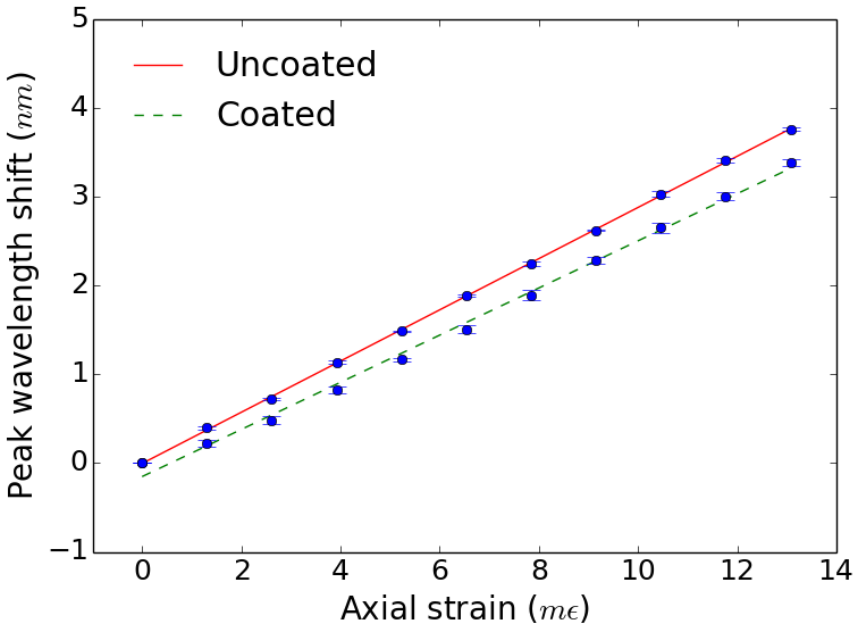

Figure 5.17: A comparison of the response of microcavity F to axial strain when coated ($y = 0.27x - 0.15$, R-squared = 0.99) or not coated ($y = 0.29x + 0.00$, R-squared = 0.99) in a resin cube. The error bars are the standard deviation of the series of three measurements.

load is given in units of N/mm^2, so that a comparison can be made between the microcavities uncoated and then coated in a resin cube. This is to evaluate the benefits of coating the microcavity in a resin cube.

Microcavity C had a higher sensitivity to applied transverse load when compared to microcavity B. As already stated in section 5.4.1, microcavity C had a higher sensitivity to applied axial strain than microcavity B. Figure 5.20 shows the response of microcavity C to applied transverse load. The equation of the line $y = -0.04x + 0.00$, R-squared = 0.94. While the R-squared for microcavity C is higher than for microcavity B, the small gradient shows it is still only weakly sensitivity to applied transverse load. The microcavities' wavelength shift in response to applied transverse load is to shorter wavelengths, this is the opposite direction to the peak shift in response to applied axial strain. The periodicity of the wavelength spectrum is given by $\lambda^2/2nd$, described in Section 5.2. As d increases, the periodicity decreases, this implies that the wavelength spectrum shifting to shorter wavelengths is due to

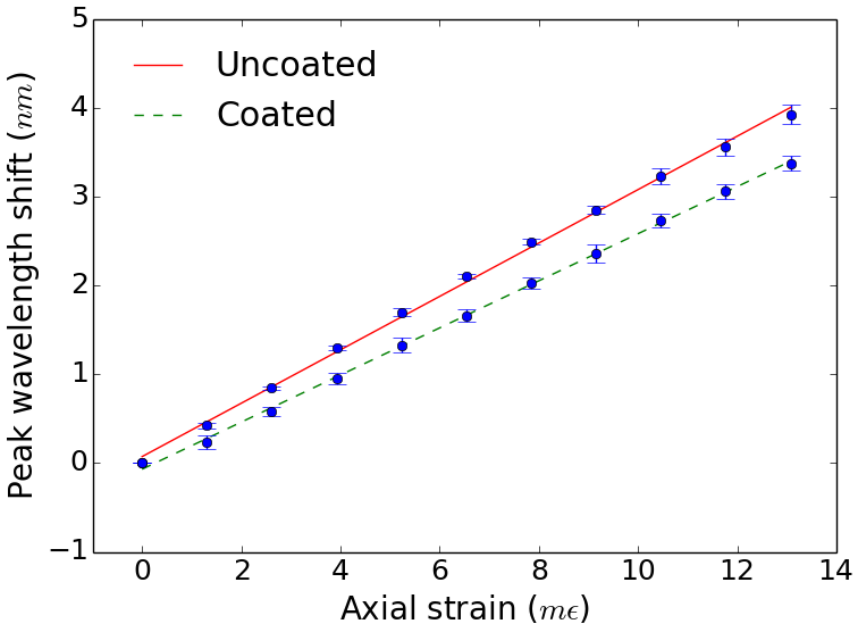

Figure 5.18: A comparison of the response of microcavity G to axial strain when coated ($y = 0.27x - 0.07$, R-squared = 0.99) or not coated ($y = 0.30x + 0.07$, R-squared = 0.99) in a resin cube. The error bars are the standard deviation of the series of three measurements.

the length of the microcavity increasing. This increase in length is much less than the length, as the periodicity was not seen to change.

There was a correlation of microcavities' sensitivity to both applied axial strain, and applied transverse load. Figure 5.21 plots the sensitivity of the microcavities with respect to each other. The trend was for microcavities' sensitivity to apply to both, however the order of the relationship could not be inferred due to the large uncertainty in the sensitivity of the microcavities to either measurand. This trend implies that modifications to the microcavity can improve its sensitivity to both applied axial strain and applied transverse load. The uncertainity of the sensitivity of the microcavity is the mean of the standard deviation between the series of measurements, divided by the strain range experienced by the microcavity.

The sensitivities of the microcavites produced during this study and used to measure applied transverse load is reported in table 5.4. The uncertainty is the mean of the standard deviation of the series of five measurement sets taken, divided

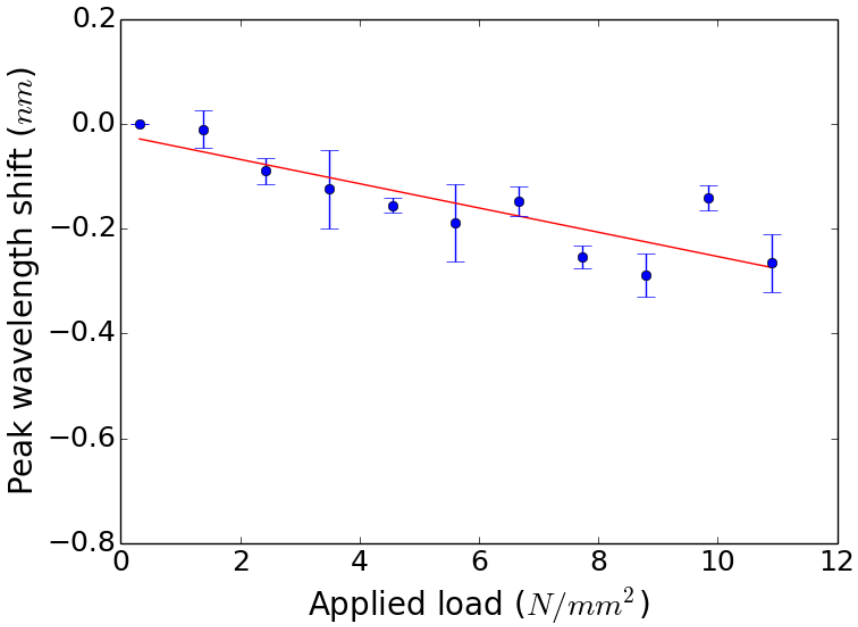

Figure 5.19: The response of microcavity B, to applied transverse load. The equation of the line $y = -0.02x - 0.02$, R-squared = 0.72. The error bars are the standard deviation of the series of three measurements.

by the range of strain (0.32 N/mm^2 to 0.013 N/mm^2). The mean sensitivity of the microcavity was -0.018 $nm/(N/mm^2)$, this is much less than the sensitivity of an FBG (0.15 $nm/(N/mm^2)$) written in polarising maintaining fibre (PMF) at 1550 nm [16].

The standard deviation in sensitivity is 0.013 $nm/(N/mm^2)$, this is of the order of the mean sensitivity of the microcavities, -0.018 $nm/(N/mm^2)$. The next step in this work is to improve the consistency in construction of the microcavities, to improve the consistency of the sensitivity of the microcavities to applied transverse load. As shown in Figure 5.21, there is correlation between the microcavities' sensitivity to both measurands, it is unlikely for a microcavity to be sensitive to one and not the other. Therefore improving the consistency of construction will improve the consistency of the microcavities' response to both applied axial strain and applied transverse load. Some of the microcavities in this chapter were coated in resin cubes to improve their sensitivity to applied transverse load, by transducing it into

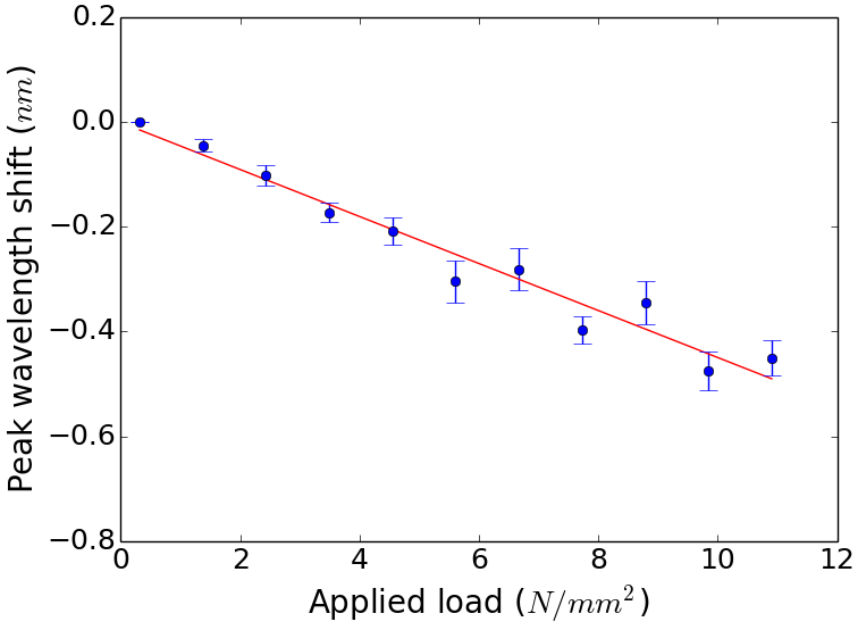

Figure 5.20: The response of microcavity C, to applied axial strain. The equation of the line $y = -0.04x + 0.00$, R-squared = 0.94. The error bars are the standard deviation of the series of three measurements.

applied axial strain. The resin cube adheres to the outside of the fibre, such that when the resin cube is compressed, it places force on the optical fibre perpendicular to the direction of compression, and parallel to the length of the optical fibre. The microcavity experiences this force as tension, or applied axial strain. Microcavity E's response to applied transverse load, shown in Figure 5.22, shows the success of this method. After it was coated in a resin cube, the wavelength shift was to longer wavelengths, unlike before they were coated where the wavelength shift was to shorter wavelengths. This shows that the length of the microcavities increased, like when axial strain is applied to them, and unlike when transverse load is applied to them.

The response of resin coated microcavity F to applied transverse load is shown in Figure 5.23. While a line of best fit is used (equation $y = 0.59x + 0.31$) with a good fit (R-squared = 0.94), there is a curve that implies for applied loads greater than 3 N/mm^2 the sensitivity of the microcavity begins to reduce.

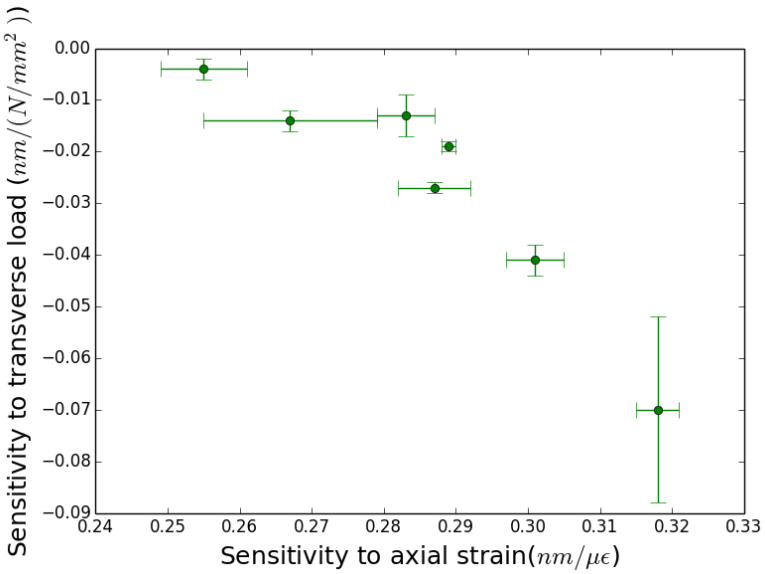

Figure 5.21: Comparison of the sensitivities of the microcavities to both applied axial strain and applied transverse load. The error bars are the standard deviation in the series of measurements taken, divided by strain range experienced by the microcavity.

The microcavities deformed slightly when load was applied, and it was found that the resin cube required 30 seconds to settle to the new load applied before the peak wavelength shift stabilised. This is described in greater detail at the end of this section. With regards to the response of microcavity, the deformation of the resin cube alters its efficiency in transducing applied transverse load into applied axial strain. The microcavities have been shown to have a linear response to applied axial strain, so the curve observed in Figure 5.23 suggests the resin cube becomes less efficient at converting to applied axial strain.

Figure 5.24 shows the response of microcavity G, while coated in a resin cube, to applied transverse load. It also had an inflection around 3 N/mm^2, where the sensitivity starts to reduce as the resin cube deformed. For this resin cube the resin was exposed for a longer period of time to the UV light source, ten minutes compared to five minutes, however this did not successfully improve its stiffness. Despite the inflection, the data points are close enough to the line of best fit (R-squared = 0.98), that its gradient ($y = 0.68x + 0.09$) can be taken as the sensitivity of the microcavity

Table 5.4: Sensitivity of each uncoated microcavity to applied axial strain, and the precision of the sensitivity. The uncertainty is the mean of the standard deviation of the series of five measurements, divided by the range of strain. The FBG sensitivity is taken from Chehura et al. [16], for an FBG written at $1550nm$. STD is the standard deviation of the microcavities.

Microcavity	Sensitivity $(nm/(N/mm^2))$	Uncertainty $(nm/(N/mm^2))$
A	-0.007	0.018
B	-0.014	0.002
C	-0.027	0.001
D	-0.004	0.002
E	-0.013	0.004
F	-0.019	0.001
G	-0.041	0.003
Mean	-0.018	0.004
STD	0.013	0.006
FBG	0.15	

(shown in Table 5.5).

Figure 5.25 shows a comparison of microcavity E before and after it was coated in a resin cube. As already stated there was a greater sensitivity to applied transverse load after the microcavity was coated in a resin cube. This was a clear success in improving the sensitivity of the microcavity to applied transverse load. The sensitivities of microcavities E, F, and G before and after coating in a resin cube is given in table 5.5. The sensitivities after coating are much greater than a birefringent FBG $(0.15nm/(N/mm^2))$ written in polarising maintaining fibre (PMF) at $1550nm$ [16].

As discussed above, the resin cube experienced deformation when load was applied to it. When load was applied it took time for the resin cube to reach its new shape. The channelled spectrum of the microcavity keeps shifting until the resin cube reaches its new shape. To measure the time delay for the channelled spectrum to reach its final position, transverse load was repeatedly applied and removed from resin coated microcavity E.

To observe the change in the channelled spectrum, the intensity of a wavelength was measured as the load was applied and removed. This wavelength was chosen to

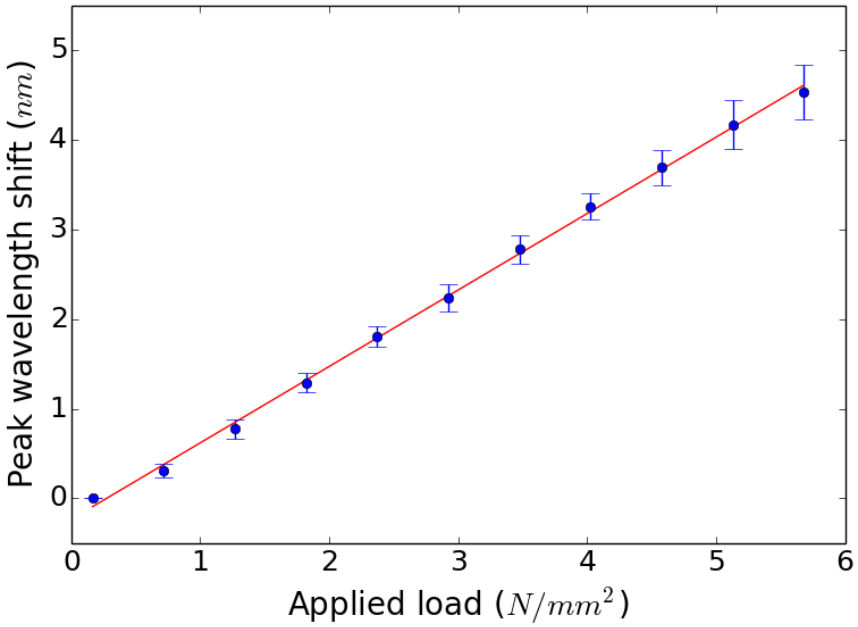

Figure 5.22: Response of microcavity E to applied transverse load while it is coated in a resin cube. The equation of the line $y = 0.85x - 0.24$, R-squared = 0.99. The error bars are the standard deviation of the series of three measurements.

be halfway between a maximum and a minimum of the oscillating channelled spectrum, such that linear wavelength shifts in the channelled spectrum would produce linear changes in the intensity of that wavelength.

Figure 5.26 shows the change in intensity of this wavelength as a function of time, for ten repetitions as 2 N/mm^2 of transverse load is applied or relieved. It was found it took 25 s for the resin cube to reach its new shape, for both when transverse load was applied or relieved, and for the channelled spectrum to stop shifting. The deformation of the resin cube appears to be reversible, as the channelled spectrum returned to its original position after the transverse load is relieved.

5.4.3 Temperature change

The microcavities had a weak response to temperature change across the range 25 $°C$ to 60 $°C$. Favero et al. [7] found a sensitivity of order $1pm/°C$, this matches the mean sensitivity of microcavites in this work ($1pm/°C$). The sensitivity of the

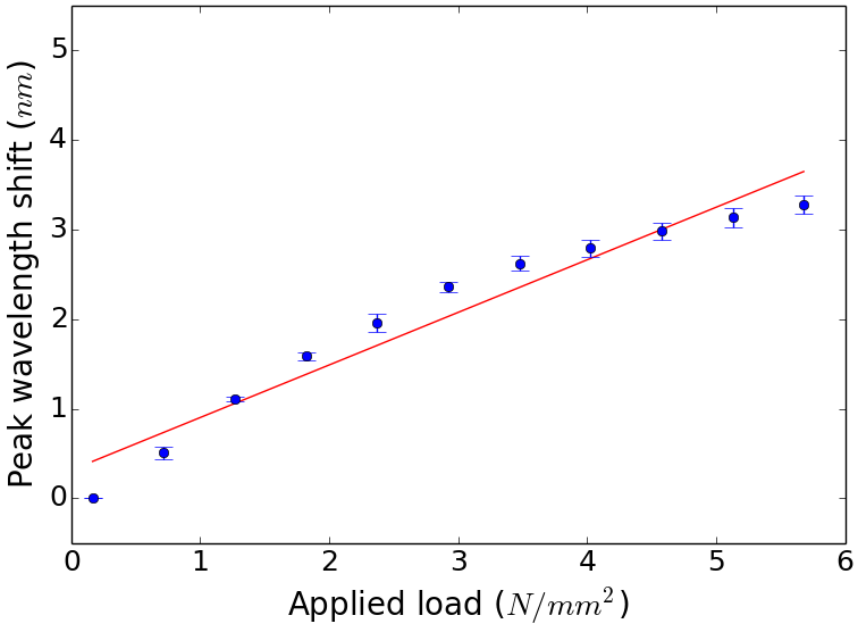

Figure 5.23: Response of microcavity F to applied transverse load while it is coated in a resin cube. The equation of the line $y = 0.59x + 0.31$, R-squared = 0.94. The error bars are the standard deviation of the series of three measurements.

microcavities is most likely lower than this, however it is below the detector limits of the spectrometer (0.3 nm). Figure 5.27 shows that the weak sensitivity for the microcavity holds for a larger temperature range of 25 $°C$ to 125 $°C$. Microcavity A was subject to a larger temperature range to verify the results of Favero et al. [7].

As discussed in this section, the peak shift is caused by a change in the phase difference between reflections from the two partially reflecting surfaces of the microcavity. This phase changes as the distance between these surfaces changes. The thermal expansion coefficient of silica glass is $10^{-}6/°C$ [18], which means that the distance between the surfaces experiences slight change with regards to temperature change. This is why the microcavity has such a low sensitivity to temperature change.

This weak sensitivity to temperature change is advantageous when compared to a FBG written in Panda fibre at 1550 nm, which would have a sensitivity to temperature change of order 15 $pm/°C$ [16]. Sensing roles currently utilising FBGs,

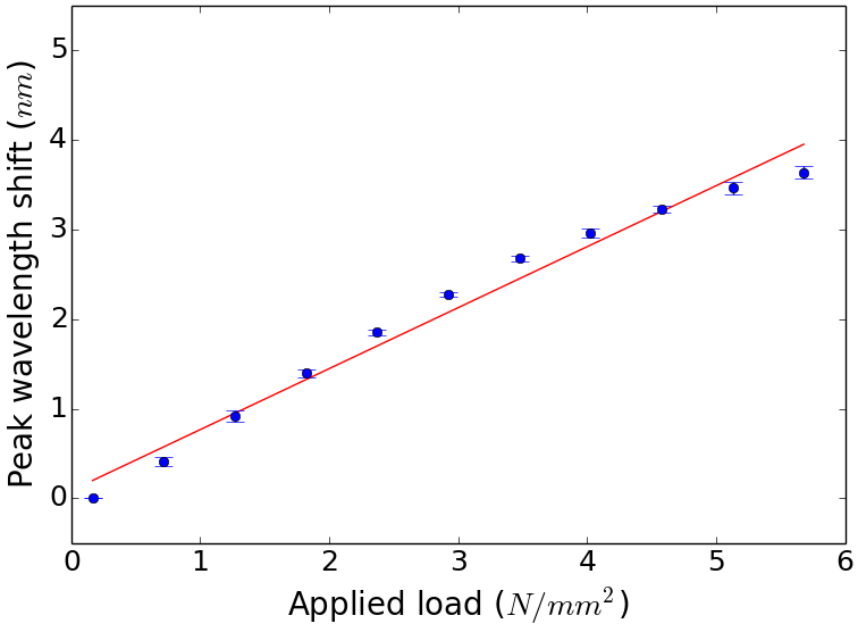

Figure 5.24: Response of microcavity G to applied transverse load while it is coated in a resin cube. The equation of the line $y = 0.68x + 0.09$, R-squared = 0.98. The error bars are the standard deviation of the series of three measurements.

where temperature fluctuations are an issue, could be replaced with a microcavity based sensor system.

The microcavities were coated in a resin cube to enhance their sensitivities to applied transverse strain, by transducing it into applied axial strain. While the microcavities have a low sensitivity to thermal change due to the fibre's low thermal expansion coefficient ($10^{-6}/^{O}C$ [18]), the thermal expansion coefficient of the resin cube is much larger ($208 \times 10^{-6}/^{O}C$ [14]). As the resin cube expands or contracts, it applies strain to the fibre it coats, this induces strain in the microcavity. Figure 5.28 shows the response of microcavity E before and after it has been coated in a resin cube to a temperature change of $25^{O}C$ to $60^{O}C$. The lines of best fit were used to measure the sensitivity of the microcavity to temperature change, however the error bars are too large to assume the response was linear. This increase in sensitivity to temperature was experienced by all the microcavities coated in resin cubes. Figures 5.29 and 5.30 show the response of microcavities F and G to temperature change

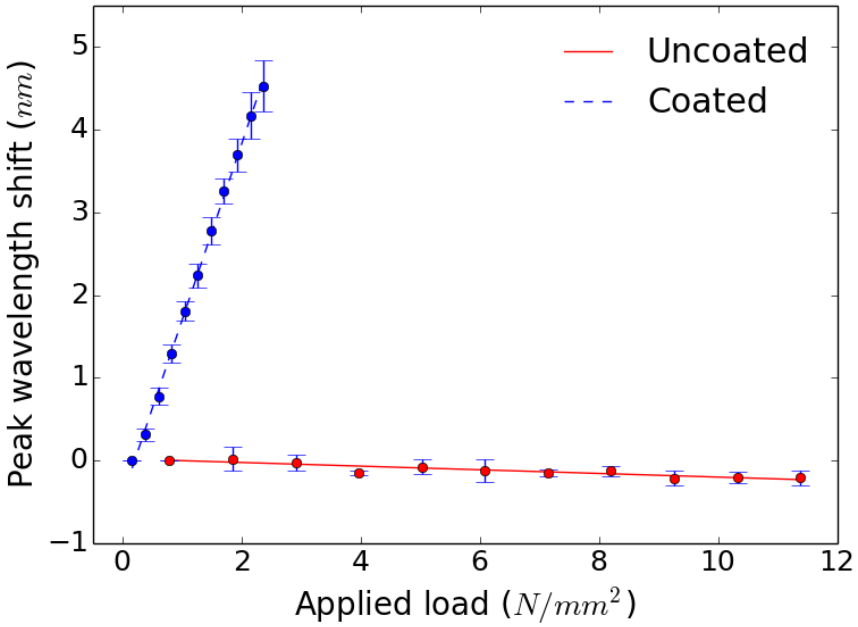

Figure 5.25: Response of microcavity E, to applied transverse load while it is uncoated, or coated in a resin cube. The error bars are the standard deviation of the series of three measurements.

before and after being coated in a resin cube. Only these three microcavities were coated in resin cubes due to time constraints. An expansion to this work would be to measure the response of ten microcavities to temperature change before and after coating in a resin cube. This would be enough to reveal if there is a relationship between the microcavities' sensitivity to applied axial strain and temperature change when coated in a resin cube.

Table 5.6 shows the sensitivity of the microcavities to change in temperature before and after being coated in a resin cube. The uncertainty in the sensitivity is the mean of the standard deviation of the series of three measurement sets taken, divided by the temperature range the microcavities experienced. The mean response of the microcavities to temperature change after coating in a resin cube was $12.6pm/^0C$. This is an order of magnitude greater than the sensitivity of a FBG written in Panda fibre at $1550nm$ to temperature change $1.5pm/^0C$. This means that while coating the microcavity in a resin cube greatly enhances its sensitivity to

Table 5.5: The sensitivities of microcavities E, F, and G to applied transverse load, before and after they are coated in a resin cube. The uncertainty is the mean of the standard deviation of the series of three measurements, divided by the range of strain. Mean is the mean response of the micrcavities. STD is the standard deviation of the response of the microcavities.

Microcavity	Without coating		With coating	
	Sensitivity $(nm/(N/mm^2))$	Uncertainty $(nm/(N/mm^2))$	Sensitivity $(nm/(N/mm^2))$	Uncertainty $(nm/(N/mm^2))$
E	-0.013	0.004	0.854	0.026
F	-0.019	0.001	0.587	0.013
G	-0.041	0.003	0.681	0.008
Mean	-0.024	0.003	0.707	0.016
STD	0.015	0.002	0.135	0.009

applied transverse load, the trade-off is a greater sensitivity to temperature change, an order of magnitude greater than an FBG based system. Coating the resin cube removes one of its advantages over an FBG, having a lower sensitivity to temperature change. As discussed in section 5.2.2, initially smaller resin cubes were to be used, however they could not be extracted from the Teflon mould without damaging the microcavity. Smaller resin cubes may apply smaller amounts of strain to the microcavity due to changes in temperature. The next step in this work would be to explore this, by using a mould that can produce smaller resin cubes without damaging the microcavity.

Table 5.6: The sensitivities of the microcavities to temperature change from $25°C$ to $60°C$. The uncertainty is the mean of the standard deviation of the series of three measurements, divided by the range of strain. The FBG sensitivity is taken from Chehura et al. [16], for an FBG written at 1550 nm in Panda fibre. Mean is the mean response of the microcavities. STD is the standard deviation of the response of the microcavities.

Micro Cavity	Without coating		With coating	
	Sensitivity $(nm/°C)$	Uncertainty $(nm/°C)$	Sensitivity $(nm/°C)$	Uncertainty $(nm/°C)$
E	0.0006	0.0016	0.0165	0.0023
F	0.0010	0.0004	0.0104	0.0012
G	0.0010	0.0004	0.0108	0.0010
Mean	0.0009	0.0008	0.0126	0.0015
STD	0.0002	0.0007	0.0034	0.0007
FBG	0.0015	0.0001		

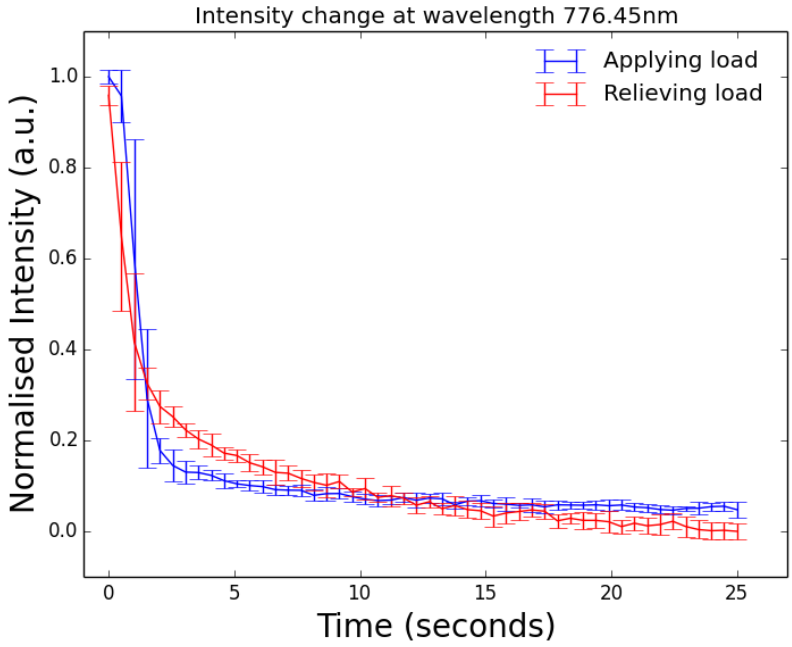

Figure 5.26: Microcavity E when coated in resin took time to respond to the applied transverse load ($2N/mm^2$). The response relieving the load has been vertically inverted such that a comparison between it and applying load can be made.

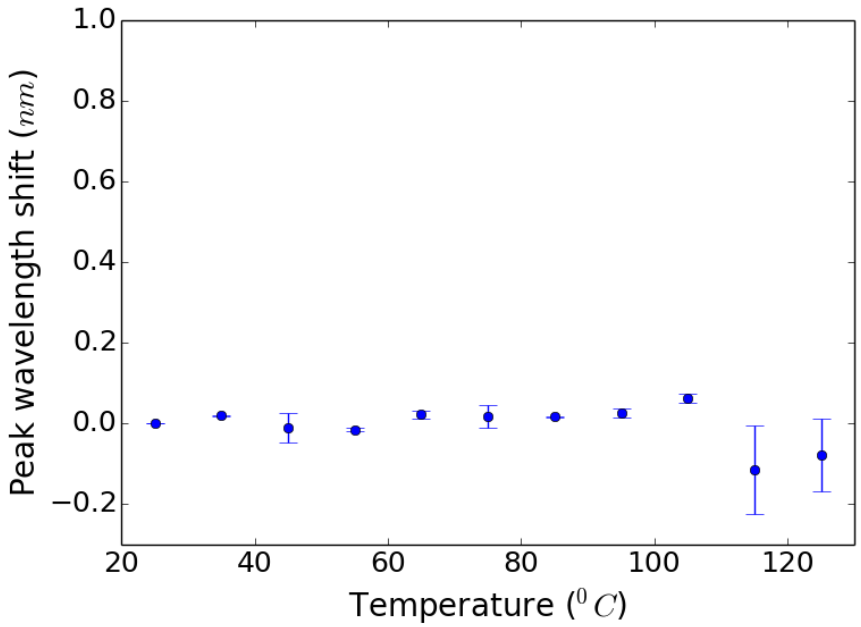

Figure 5.27: Response of microcavity A to temperature change from 25 $^\circ C$ to 125 $^\circ C$. The error bars are the standard deviation of the series of three measurements.

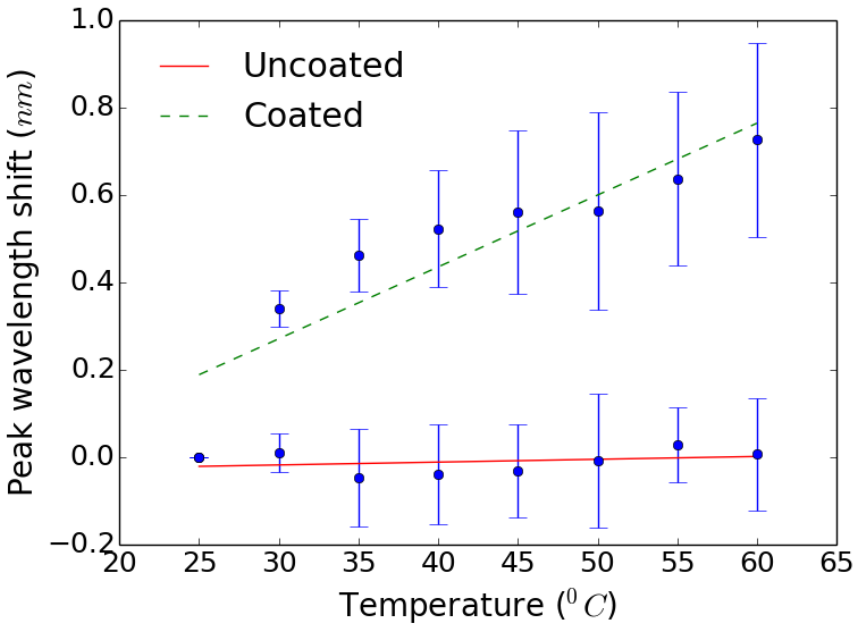

Figure 5.28: Response of microcavity E, to temperature change from 2 $^\circ C$ to 60 $^\circ C$. The error bars are the standard deviation of the series of three measurements.

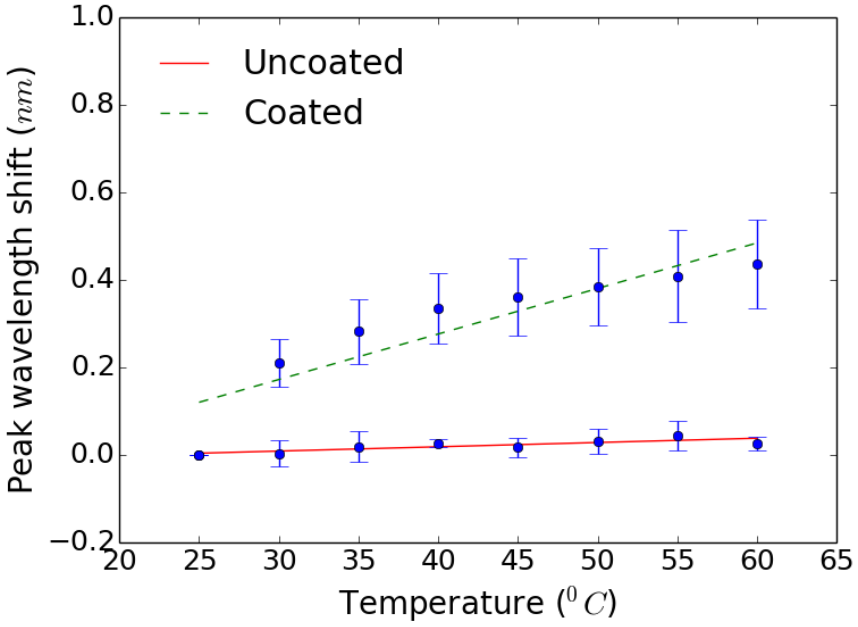

Figure 5.29: Response of microcavity F, to temperature change from 25 $^\circ C$ to 60 $^\circ C$. The error bars are the standard deviation of the series of three measurements.

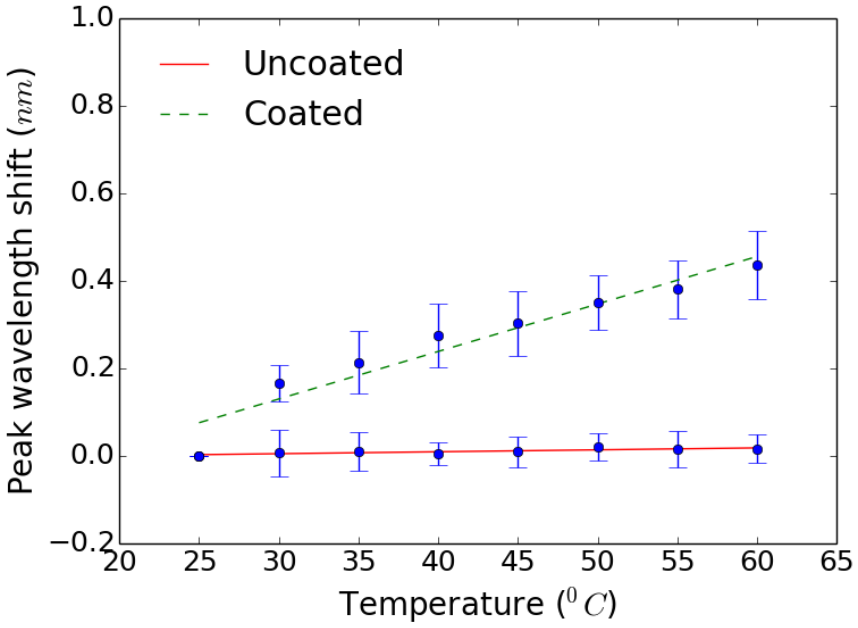

Figure 5.30: Response of microcavity G, to temperature change from 25 $^\circ C$ to 60 $^\circ C$. The error bars are the standard deviation of the series of three measurements.

5.5 Chapter summary

The aim of the work in this chapter was to expand the microcavity based axial strain sensors developed by Favero et al. [7] to include the sensing of applied transverse load. The mean microcavity sensitivity to applied transverse load was $-0.018\ nm/(N/mm^2)$, much lower than an FBG [8] written in Panda fibre at 1550 nm ($0.15nm/(N/mm^2)$ [16]). To enhance the sensitivity of the microcavities, some of them were coated in a resin cube to transduce transverse load into axial strain, to which the microcavities were more sensitive (mean sensitivity 0.286 $nm/m\epsilon$). This increased the mean sensitivity of the microcavities to 0.700 $nm/(N/mm^2)$, however it also increased their sensitivity to changes in temperature.

Uncoated microcavities were found to have a sensitivity to temperature change of order $1pm/^{\circ}C$, which is a match for the sensitivity found by Favero et al. [7]. This is lower than the sensitivity of an FBG, which would be of order 1.5 $pm/^{\circ}C$ [16]. However the mean sensitivity of resin coated microcavities to changes in temperature is $12.6 \pm 1.5pm/^{\circ}C$, an order of magnitude larger than an FBG sensitivity to temperature change. Without the resin coating the microcavity has its lower sensitivity to temperature change as an advantage over FBG based fibre sensor systems, however its sensitivity to transverse load is an order of magnitude smaller, and its sensitivity to applied axial strain is half the sensitivity of an FBG based system (mean sensitivity 0.286 $nm/m\epsilon$ compared to 0.620 $nm/m\epsilon$ for a FBG written at 780 nm in SMF [17]).

The next step in this work would be to improve the consistency in the construction of the microcavities. The microcavities were constructed using a fusion splicer, a device shared in the lab and subject to change in its internal conditions. The construction of the microcavities is highly sensitive to these changes, so would require a dedicated machine. It was discussed in section 5.2 that the formation of the microcavity was dependent on the main arc current of the splicer, the overlap

[8] Correia [10] used the resin cube to enhance the sensitivity of FBGs to applied transverse load.

distance of the two fibres constructing the splice, and the pressure inside the hole structure of the photonic crystal fibre (PCF). Another type of splicing, such as using a laser system, could have advantages over the arc fusion system used. If it provided better temperature control, and more localised heating, the microcavities would have greater reproducibility. The downside of this is that it would make them more complicated and difficult to produce, removing part of their competitive edge over FBGs.

These more reproducible microcavities, coating in smaller resin cubes should be explored. Smaller resin cubes could produce less strain on the microcavities due to changes in temperature, which would decrease the large sensitivity of the microcavity to temperature change when coated. The relationship between the microcavities' sensitivity to axial strain, and sensitivity to temperature change when coated in a resin cube could be explored and determined.

The wavelength resolution of the detector used for the work in this chapter was $0.3nm$. While software was used to extend to a greater resolution, this resolution is still of the order of the sensitivity of the microcavity. As such a scanning laser system that could possess narrower resolution would improve the sensitivity of the microcavity system [19].

An uncoated microcavity has much lower sensitivity to temperature change, but also a lower sensitivity to transverse load. However in a system that utilises a microcavity and an FBG, the microcavity could be used to compensate for temperature change. As such microcavities could be used in hybrid system to correct for temperature change, not just those using FBGs.

Overall a limit of these approaches is that unlike FBGs, a microcavity cannot be put in series. A system that uses multiple microcavities would have to interrogate them in parallel. Chapter 6 explores the use of a system that possesses sensors that can be interrogated in series like FBGs.

References

[1] Y. Huang, T. Wei, Z. Zhou, Y. Zhang, G. Chen, and H. Xiao. An extrinsic Fabry–Perot interferometer-based large strain sensor with high resolution. *Measurement Science and Technology*, 21:105308, 2010.

[2] C. Xiaopei, S. Fabin, W. Zhuang, H. Zhenyu, and A. Wang. Micro-air-gap based intrinsic Fabry-Perot interferometric fiber-optic sensor. *Applied Optics*, 45:7760–7766, 2006.

[3] Y.-J. Rao. Recent progress in fiber-optic extrinsic Fabry-Perot interferometric sensors. *Optical Fiber Technology*, 12:227–237, 2006.

[4] S. Poeggel, D. Tosi, G. Leen, and E. Lewis. Low-cost miniature fiber-optic extrinsic Fabry-Perot interferometric pressure sensor for biomedical applications. *Advanced Microscopy Techniques III*, 8797:1–6, 2013.

[5] Z. Wang. *Intrinsic Fabry-Perot Interferometric Fiber Sensor Based on Ultra-Short Bragg Gratings for Quasi-Distributed Strain and Temperature Measurements*. PhD thesis, Virginia Polytechnic Institute and State Univesity, 2006.

[6] Y.-J. Rao, M. Deng, D.-W. Duan, X.-C. Yang, T. Zhu, and G.-H. Cheng. Micro Fabry-Perot interferometers in silica fibers machined by femtosecond laser. *Optics Express*, 15(21):14123–14128, 2007.

[7] F. C. Favero, G. Bouwmans, V. Finazzi, J. Villatoro, and V. Pruneri. Fabry

Perot interferometers built by photonic crystal fiber pressurization during fusion splicing. *Optics Letters*, 36:4191–4193, 2011.

[8] F. C. Favero, L. Araujo, G. Bouwmans, V. Finazzi, J. Villatoro, and V. Pruneri. Spheroidal Fabry-Perot microcavities in optical fibers for high-sensitivity sensing. *Optics Express*, 20(7):7112, 2012.

[9] M. Manders, M. Partridge, R. N. Correia, S. W. James, and R. P. Tatam. Transverse strain response of in-fibre Fabry-Perot microcavities. *Proc. of SPIE*, 9157:91571O, 2014.

[10] R. N. Correia. *Development of a pore pressure sensor employing fibre bragg gratings*. PhD thesis, Cranfield University, 2008.

[11] Y.-J. Rao. In-fibre Bragg grating sensors. *Measurement Science and Technology*, 8(4):355, 1997.

[12] A. D. Yablon and R. T. Bise. Low-loss high-strength microstructured fiber fusion splices using GRIN fiber lenses. *IEEE Photonics Technology Letters*, 17: 118–120, 2005.

[13] L. Xiao, M. S. Demokan, W. Jin, Y. Wang, and C.-L. Zhao. Fusion Splicing Photonic Crystal Fibers and Conventional Single-Mode Fibers: Microhole Collapse Effect. *Journal of Lightwave Technology*, 25:3563–3574, 2007.

[14] E. Technologies. EPO-TEK OG134 Technical Data Sheet, 2007.

[15] M. Partridge. *Cranfield University*. PhD thesis, Cranfield University, 2012.

[16] E. Chehura, C.-C. Ye, S. E. Staines, S. W. James, and R. P. Tatam. Characterization of the response of fibre Bragg gratings fabricated in stress and geometrically induced high birefringence fibres to temperature and transverse load. *Smart Mater. Struct.*, 13:888–895, 2004.

[17] J. Roths and F. Jülich. Determination of strain sensitivity of free fiber Bragg gratings. *Proc. of SPIE*, 7003:700307–700308, 2008.

[18] Accuratus. www.accuratus.com/fused.html, 2015.

[19] S. Poeggel, D. Tosi, G. Leen, and E. Lewis. Fiber-optic extrinsic FPI/FBG sensor for temperature-compensated pressure measurement in medical applications. *Proceedings of SPIE - The International Society for Optical Engineering*, 8794:1–5, 2013.

Chapter 6

Beat frequency interrogation using a short PM-PCF length for strain measurements

6.1 Introduction

In this Chapter, a sensing system developed to measure axial strain and transverse load across an extended region is presented. This sensor was a short length (less than 20 cm) of birefringent photonic crystal fibre (PM-PCF). The PM-PCF was spliced to a long length of SMF (greater than 3 m), with the SMF connected to an optical backscatter reflectometer (OBR). The length of birefringent fibre was interrogated with the OBR as strain was applied along its axis. This technique is described in greater detail in Section 6.2.

Birefringent photonic crystal fibres are fibres where the birefringent behaviour is induced by the hole structure that is radially distributed in the fibre core (see Chapter 3). Compared to traditional birefringent fibres (see for instance Panda fibres) that are produced by applying stress to the fibre core, PM-PCF have the advantage of showing a linear response to applied stress and no sensitivity to temperature

changes. The linear behaviour is due to the fact that no strain is applied during the construction process.

The effect of the length of the birefringent fibre, on its sensitivity to applied axial strain, and transverse load was explored. It will be explained in a later section the mechanism that relates the sensitivity of the PM-PCF sensor head to its length.

To explore if the system could be expanded to be a quasi-distributed strain sensor system, two sensor heads were placed in series, and interrogated simultaneously with an OBR. A quasi-distributed sensor system is: a series of multiple point sensors that are interrogated simultaneously, and monitor an extended region [1], e.g. strain experienced by a railway track. Quasi-distributed sensor systems have been used in structural health monitoring [2], e.g. to measure strain across a plane wing. There is an issue of cross-talk, where the signals from multiple point sensors interfere with each other. The two sensor head system was used to evaluate methods of mitigating cross-talk.

In summary, the aim of the work presented in this chapter is: to produce a strain sensor based on changes in the phase between two orthogonal polarisation modes propagating through a birefringent PCF. A further aim was, after using this sensor as a point sensor, measuring strain at a local region, to test using this point sensor in a chain of point sensors to measure strain across an extended region.

The intention of this work was to incorporate PCF into approaches that use orthogonal polarisation relative phase changes to measure strain, such as those presented by Rogers et al. [3] or Wang [4]. This builds on the work of Rota-Rodrigo et al. [5], and expands it to measure a different type of strain. This expands the possible uses of the sensor, and would allow a quasi-distributed strain sensor system to measure multiple types of strain across multiple locations.

6.2 Interrogating the birefringent sensor head

A method to measure the strain experienced by a short length (less than 20 cm) of birefringent optical fibre is to analyse the beat interference, as strain is applied to the fibre [6, 5]. This section describes the construction of a birefringent sensor head, the process it is interrogated with, and how it will be used as a strain sensor.

6.2.1 Constructing the sensor head

The sensor head is formed of a short length (less than 20 cm) of birefringent photonic crystal fibre (PM-PCF), a schematic of it is shown in Figure 6.1. The sensing region is a subsection of the PM-PCF, this is highlighted in the Figure as a dashed rectangle. How the PM-PCF senses strain to this region will be described in the following sub section.

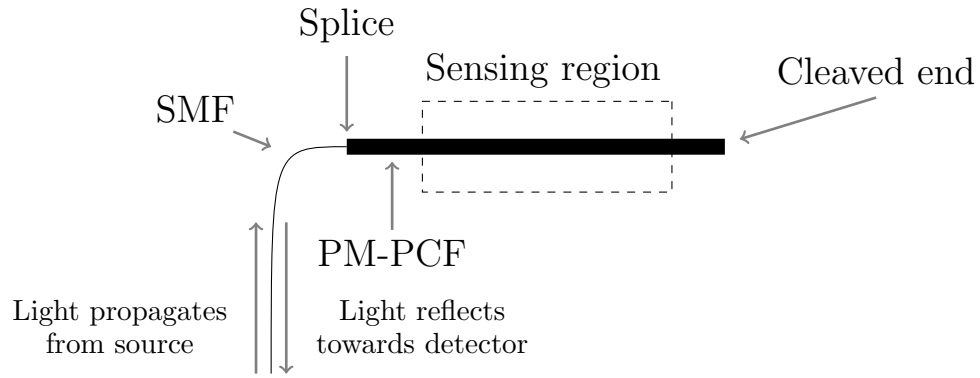

Figure 6.1: Schematic of the sensor head, it is a short length (less than 20 cm) of PM-PCF. Light propagates through the SMF from the source, to enter the PM-PCF (which contains the sensor head). The light propagates through the PM-PCF, is reflected off the cleaved end due to Fresnel reflection, propagates through the PM-PCF again. The light propagates from the PM-PCF into the SMF, and propagates along the SMF to the detector.

6.2.2 Beat interference

The sensing property of the sensor head is produced by its beat interference. The beat interference is created when two orthogonal polarisation modes propagate through a birefringent fibre mix and interfere with each other [7]. When light is

inserted into a birefringent fibre, with the polarisation at an angle to populate both orthogonal polarisation modes, an interference pattern will emerge in the wavelength spectrum after the two orthogonal polarisation modes interfere with each other, after leaving the fibre. Inside the birefringent fibre these modes are decoupled from each other due to the birefringence. When the two modes reach a detector they interfere with each other.

In order to understand the interference behaviour we start from the phase difference between the two orthogonal polarization modes which experience two different refractive indices due to the birefringence of the fibre. We can write the phase difference as: $\phi = L\Delta\beta$, where L is the length of the birefringent fibre, and $\Delta\beta$ is the difference between the propagation values of the two orthogonal polarisation modes while within the birefringent fibre. When this phase relationship is differentiated with respect to wavelength, it gives the change in the phase difference between the orthogonal polarisation modes ($\Delta\phi$), as a function of wavelength. This is given by Equation 6.1, which has been derived in Appendix B.

$$\Delta\phi = -(\Delta\lambda/\lambda)(4\pi L_A/L_B) \tag{6.1}$$

where λ is the central wavelength of the wavelength range $\Delta\lambda$. $\Delta\lambda$ is the wavelength range that produces the change in the phase difference between the two orthogonal polarisation modes of the fibre. L_B is the beat length of the birefringent fibre, this can be taken to be a constant as long as the wavelength range is small ($\Delta\lambda << \lambda$). L_A is the actual length of the birefringent fibre.

As the birefringent fibre is being viewed in reflection, the effective length of the fibre for the beat interference is twice the actual length of the birefringent fibre. The relationship in Equation 6.1 holds true while the refractive index remains invariant of wavelength, this also requires $\Delta\lambda << \lambda$.

It is convenient to focus on the beat frequency. This is the wavelength range

between two adjacent maxima of the beat interference. This is a wavelength separation that produces a change in the phase difference ($\Delta\phi$) of the two orthogonal modes by $|2\pi|$. This is substituted into Equation 6.1, though it is convenient to substitute in -2π since it will cancel out the negative sign in the Equation. The magnitude is what is important, as such the negative sign has no other impact than simplifying the Equation. This leads to this expression;

$$1 = (\Delta\lambda_B/\lambda)(2L_A/L_B)$$

where $\Delta\lambda_B$ is the wavelength range that corresponds to one beat of the beat interference, and shall be referred to as the beat frequency. This can be rearranged to make the wavelength range the subject of the Equation, which reveals the wavelength range that corresponds to one period of the beat interference [1] between the two orthogonal polarisation modes propagating through the birefringent fibre.

$$\Delta\lambda_B = \lambda\frac{L_B}{2L_A} \tag{6.2}$$

Equation 6.2 describes how the wavelength separation of the peaks of the beat interference is a function of the length of birefringent fibre, through which the two orthogonal polarisation modes propagate. Figure 6.2 shows a modelled spectrum of when two orthogonal polarisation modes of equal intensity to each other, and equal intensity across wavelengths, interfere with each other when they leave the birefringent optical fibre, and enter a device that removes the orthogonality of the polarisation modes. The orthogonality is removed in this experiment using the polarisation controller, which is part of the setup which will be described later. It has long been established that an interference signal can be detected by optical backscatter reflectometry [6].

The beat frequency ($\Delta\lambda_B$) is shown in Figure 6.2 as the wavelength separation

[1] one period is the wavelength range between two maxima or two minima

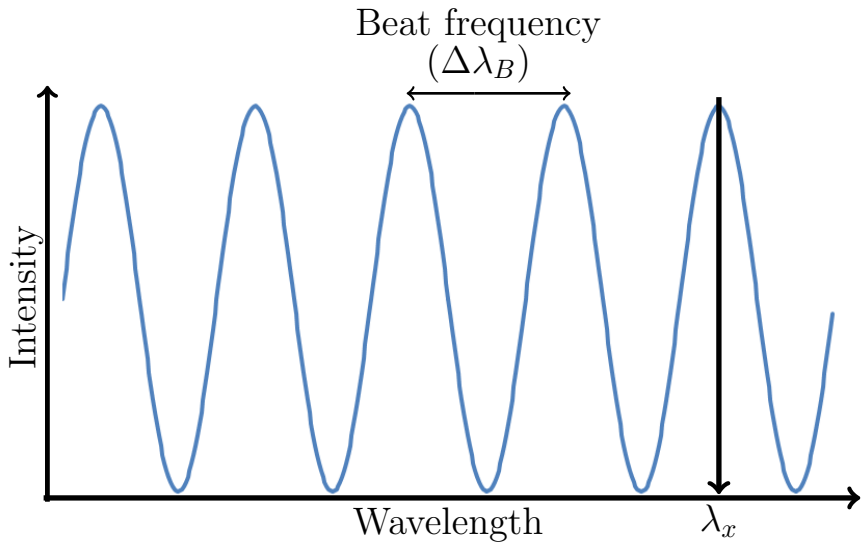

Figure 6.2: Representation of the beat interference of two orthogonal polarisation modes of equal intensity to each other, and equal intensity with regards to wavelength, as they interfere after exiting a birefringent optical fibre.

between the peaks [2]. While the separation between the peaks is a fixed property of the fibre, as long as its length and beat length remain constant, the position of the peaks can move. In Figure 6.2 the position of a peak is taken to be λ_x.

The intensity of the interference at a specific wavelength[8] is given by Equation 6.3;

$$I(\lambda) = I_1(\lambda) + I_2(\lambda) + 2\sqrt{I_1(\lambda)I_2(\lambda)}Cos[\phi(\lambda)] \tag{6.3}$$

where $I_1(\lambda)$ and $I_2(\lambda)$ are the intensities of the two orthogonal polarisation modes at a specific wavelength, and $\phi(\lambda)$ is the phase difference between those two modes. Equation 6.3 shows that the intensity of the beat interference at a specific wavelength is a function of the phase difference between the two orthogonal polarisation modes at that wavelength. This difference changes when either or both the phase of the two orthogonal polarisation modes change for that wavelength. Conditions that change the phase difference between the two orthogonal polarisation modes can be detected as a change in intensity at that wavelength, which results in a shift of the

[2]The wavelength range between two maxima.

beat interference peaks. How this is interrogated will be described in the following subsection.

6.2.3 Interrogating beat interference

Analysing the beat interference allows the change in relative phase between the two orthogonal polarisation modes to be observed. As the phase difference between the two orthogonal polarisation modes change, the position of the peaks will move to either longer or shorter wavelengths, while the beat frequency ($\Delta\lambda_B$) will remain constant. It is the change in the position of the peaks, such as λ_x that reveals the change in the phase difference between the two orthogonal polarisation modes propagating through the birefringent fibre.

As described in section 6.2.1, to analyse the beat interference of a short length of birefringent photonic crystal fibre (PM-PCF), a sensor head was constructed and interrogated with an optical backscatter reflectometer (OBR). In this context the OBR is used as a narrow linewidth scanning laser and detector, that interrogates the fibre in reflection. Figure 6.3 shows the setup used to interrogate the beat interference of the sensor head. The sensor head was constructed from a short length of PM1550 ($< 22cm$), an off the shelf PM-PCF produced by NKT Photonics, spliced to a much longer length of SMF ($> 3m$). PM1550 was chosen because it is a commonly used birefringent photonic crystal fibre that can be purchased from Thor Labs. The OBR was connected to the long length of SMF, with the SMF spliced to the PM1550. The SMF chosen was SMF28E, a standard and easily available telecommunications fibre. Both the SMF28E and PM1550 are designed for propagation of light at 1550 nm. The limit on SMF will be described in detail later. The minimum length of the SMF is limited by convenience, $3m$ was chosen since it is much longer than the length of the sensor head.

The maximum length of the PM1550 is limited by the wavelength resolution of the detector in the OBR. This limit was not reached in this experiment, as this

limit is much greater than the minimum length required for the setups to apply strain to the sensor heads. As shown in Equation 6.2, the longer the length of birefringent fibre, the shorter the wavelength range of the beat frequency. Lengths longer than $22cm$ are possible with the wavelength resolution of the detector, but became inconvenient to place into the strain setups. The minimum length of the PM1550 is limited by the scanning range of the laser within the OBR, however it could interrogate lengths too short to use in the strain setups ($\approx 10\ cm$).

The OBR[3] acts as a narrow linewidth scanning laser, sending light down the SMF to the PM1550. When the light reaches the PM1550 it populates the two orthogonal polarisation modes that can propagate down the birefringent fibre (PM1550). Before it reaches the PM1550 it goes through a polarisation controller, as shown in Figure 6.3. The polarisation controller is used to rotate the angular orientation polarisation of the light leaving the OBR, which is linearly polarised [9], to control the relative intensities of the two orthogonal polarisation modes that propagate through the PM1550.

From Equation 6.3, the fringe visibility [4] is maximised if I_1 is equal to I_2. The two orthogonal polarisation modes reflect off the cleaved end of the PM1550, and when they return to the SMF, which has a polarisation controller, where the two modes interfere with each other. The light then continues to the OBR, where the detector determines the intensity of the light as a function of wavelength. The polarisation controller is composed of three aluminium rings in an aluminium mount, with the SMF wrapped round them to induce weak birefringence in the SMF. The ring sequence acts as a quarter waveplate, followed by a half waveplate, followed by a quarter waveplate. This allows the polarisation controller to modify light propagating through it from polarisation state to any other polarisation state.

[3]Specifications of the OBR [9]: spatial resolution over 2 km is 3 mm, wavelength range 1525–1610 nm, wavelength resolution 0.02 pm, wavelength accuracy ± 1.5 pm.

[4]The intensity separation between the maxima and minima of the beat interference.

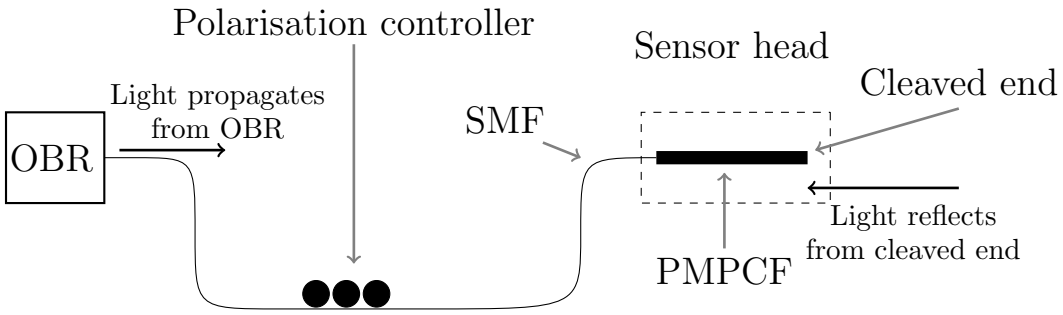

Figure 6.3: Schematic view of the apparatus used to interrogated the beat interference of the sensor head. The OBR is connected to the SMF with an angle cleaved connector. The SMF ($\approx 3\ m$) is spliced to the PM1550 ($\approx 20\ cm$). The sensor head is the short length of PM1550. The polarisation controller can be placed anywhere along the SMF but for convenience was located near the OBR. It modifies the polarisation of light from the OBR (which is linearly polarised) to a linear polarisation state incident at a 45 degree angle to both orthogonal polarisation axis of the birefringent fibre (PM1550). A schematic of the OBR is presented in Figure 6.4.

The Luna technologies OBR is more advanced than just a scanning laser and a detector. "The OBR uses swept-wavelength coherent interferometry to measure minute reflections (< 0.0003 parts per billion) in an optical system as a function of length. This technique measures the full scalar response of the device under test (DUT), including both phase and amplitude information" [9]. This can be used to detect damage to a fibre, since the OBR can locate within millimetres breaks along the fibre [9].

The optical network description of the OBR is given in Figure 6.4. The device under test (DUT) is in one arm of a Mach-Zehnder interferometer, this interferometer is between couplers 2 and 3. This is the port of the OBR to which a fibre can be connected, such as the SMF spliced to the birefringent sensor head. Light from the tunable laser source (TLS) in Figure 6.4, reaches the $3dB$ (50/50) coupler (coupler 1). This splits the light into two paths of equal intensity. One path heads towards the DUT, encountering another coupler (coupler 2). This is the beginning of the Mach-Zehnder interferometer. Coupler 2 splits the light into two paths, one directly towards the next coupler (coupler 3), the other towards the DUT. The light heading towards the DUT goes through the fibre port on the outside of the OBR,

and into the fibre connected to the OBR. Light returns from the fibre after it reflects along sources of reflection in the fibre (DUT), in this case the cleaved end of the birefringent sensor head. The returning light leaves the DUT, reaches the coupler that begins the Mach-Zehnder interferometer (coupler 2), and splits into two paths. The path that leads to the DUT is longer than the path that avoids it. This is to make sure that the time delay between the DUT path and the non-DUT path can be clearly detected, which will be described in detail later in this section. At the end coupler (coupler 3) the two paths interfere; the path that went via the DUT, and the path that avoided it. The light resulting from the interference of the two paths reaches a polarising beam splitter, shown in Figure 6.4 [9]. The intensity of both orthogonal polarisation modes is detected.

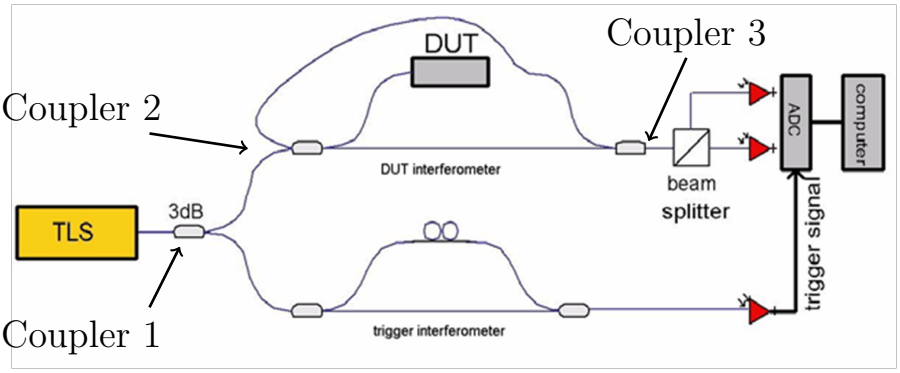

Figure 6.4: Schematic of the OBR optical network [9]. The OBR is used in the setup shown in Figure 6.3. The optical fibre used is PMF. The TLS is a tunable laser source. Light propagates from the TLS through two couplers to the device under test (DUT), which is the interface with the external setup. When light returns from the DUT it propagates through the fibre until is reaches a polarising beam splitter (labelled beam splitter). The two orthogonal polarisation modes propagate to two detectors, each detects the intensity of one of the orthogonal polarisation mode.

The long coherence length of the Tunable Laser Source (TLS) allows sources of reflection in the DUT with a large distance between them to interfere with the reference arm of the Mach-Zehnder interferometer. The TLS's coherence length is long enough that the OBR can resolve sources of reflection in a fibre 100 km long [9]. A TLS can sweep a long range of wavelengths, in this case it was used to sweep a 85 nm range from 1525 nm to 1610 nm. The OBR software Fourier transforms the

wavelength spectrum of the signal that returns from the DUT, for both orthogonal polarisation modes from the polarising beam splitter. This can be described by starting at the instantaneous amplitude of an electric field $E = E_0(t)e^{-i\omega(t)t}$ [10]. The electric field amplitude is given by a magnitude $E_0(t)$ that can vary with time, and a phase component is $e^{-i\omega(t)t}$. ω is angular optical frequency, and $\omega(t)$ describes the instantaneous frequency of the tunable laser source used to produce the electric field [9]. When two fields of equal amplitude interfere, in this case when the two paths through the Mach-Zehnder interferometer meet, they are described by Equation 6.4 [9].

$$E_{out} = E_0(t+\tau_1)e^{-i\omega(t+\tau_1)t} + E_0(t+\tau_2)e^{-i\omega(t+\tau_2)t} \tag{6.4}$$

E_{out} is the resultant field amplitude after the two fields interfere with each other. τ_1 and τ_2 are the respective time delays experienced by the light propagating through either path of the interferometer. What is of importance is the relative time delay between the two paths; $\tau = \tau_1 - \tau_2$, since this will give the phase difference between light propagating through either path. What can be detected is the intensity, which is the square of the amplitude of the electric field, which is described by Equation 6.5 [9].

$$I(\omega) = |E_0(t)|^2 + |E_0(t-\tau)|^2 + 2E_0(t)E_0(t-\tau)cos[\omega(t)\tau] \tag{6.5}$$

When Equation 6.5 is Fourier transformed, the first and second terms, which are non-oscillating, become the intensity at a angular frequency equal to zero. The third term produces the time delay (τ) between the two paths, as an intensity at a position in the frequency domain proportional to that time delay [10]. This is why there is a long delay for the signal returning from the DUT within the Mach-Zehnder interferometer, so that the time delay (τ) will be much greater than zero, so that it is distinct from the intensity from the first two terms of Equation 6.5 which are at angular frequency equal to zero.

The $3dB$ coupler proximal to the TLS also splits light towards the triggering

interferometer. As stated already, to measure the distance from the OBR to the sources of reflection along the DUT, the OBR software Fourier transforms the angular frequency spectrum of the returning signal from the DUT. For the OBR software to perform a fast Fourier transform of the signal, it needs to sample it at equal increments of optical frequency [9]. To provide this sampling the OBR uses a second triggering interferometer. The difference in length of the two arms of this interferometer needs to be twice as long as the difference in length of the two arms of the interferometer that includes the DUT. This sets the limit on the length of the DUT, and therefore sensor head system, as fibres which are too long cause undersampling. Since the sensor heads are short in comparison, this sets the limit on the total length of SMF. This limit is of the order of 100 km, far greater than the total length of SMF used in the sensor head system.

The spatial resolution of the OBR is determined by the wavelength range of the TLS, given by the formula $\delta z = \frac{\lambda_1 \lambda_2}{n_{eff} \delta \lambda}$ [9]. δz is the spatial resolution, n_{eff} is the effective refractive index of the fibre, λ_1 and λ_2 are the start and end wavelengths of the scan, and $\delta\lambda$ is the magnitude of the wavelength range ($\delta\lambda = |\lambda_1 - \lambda_2|$) [9]. A larger wavelength range gives a greater spatial resolution. This is a similar principle to optical coherence tomography (OCT), except that it is one dimensional information extracted from an effectively two dimensional object [11].

The OBR software allows the frequency domain information of a specific source of reflection to be viewed. The OBR gains its initial information of sources of reflection along the fibre by Fourier transforming the wavelength spectrum of the signal. This gives the time delay to and from sources of reflection, to the OBR.

The OBR software inverse Fourier transforms the time delay information for a specific source of reflection, to give the frequency domain (wavelength spectrum intensity) of a specific source of reflection. When the software is used to analyse the reflection from the cleaved end of the birefringent fibre, the distal end of the fibre to the OBR, it gives the beat interference of the birefringent fibre. It was also

found that the reflection from a good splice, those produced using the approach from Chapter 4, was sufficient to give the beat interference of the birefringent fibre. It will be described later how this allowed two sensor heads to be connected by SMF in series. The loss across the splices of PM1550 to SMF, was not different for the two orthogonal polarisation modes, as described in Chapter 4.

The software displays the beat interference in the frequency domain window, as a wavelength spectrum of the returning signal. Figure 6.5 shows an example of the beat frequency observed using the OBR. As strain is applied to the sensor head, the beat interference spectrum shifts to longer wavelengths in the case of applied axial strain. The direction and magnitude of the shift will be described in greater detail in Section 6.3. The shift in the position of the wavelength spectrum was measured using peak tracking software developed in house by Dr Matthew Partridge. It measured the change in position of the minima of the wavelength spectrum, between recorded traces of the wavelength spectrum for each point of strain applied. The minima were tracked as the OBR presents the wavelength spectrum of the returning signal on a logarithmic scale, making measuring the position of the minima easier.

In the following subsection how strain was applied to the sensor head will be described.

6.2.4 Approach for using the sensor head for strain measurement

Figure 6.3 shows the setup used to analyse the beat interference of the birefringent fibre (PM1550). The sensor head was placed in the strain setups and temperature setup used in Chapter 5, to measure the response of the beat interference as strain was applied to the PM1550 sensor head, or when it experienced a temperature change. To evaluate the consistency of each sensor head to applied strain, either axial or transverse load, a series of three measurements were taken for each data point. A measurement set was recording the response of a sensor head as equal

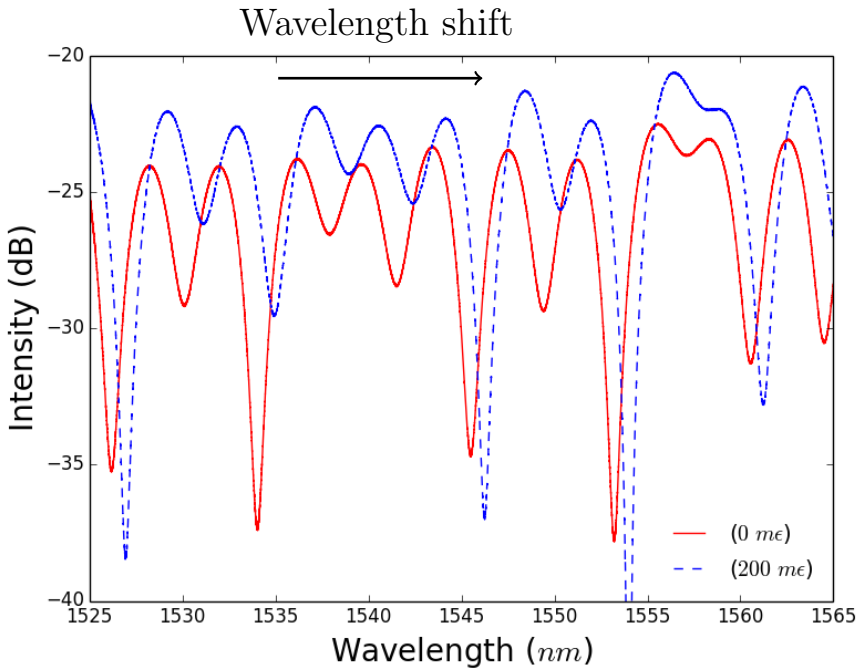

Figure 6.5: Beat interference spectrum of a PM-PCF for one polarisation, before and after axial strain is applied. The direction of the shift of the spectrum is highlighted.

increments of strain were applied across the range of strain applied. This was then repeated to produce the series of three measurement steps. To assess the optimum length of the sensor head, the sensitivity of different lengths was calculated to each of applied axial strain, transverse load, and change in temperature. The lengths used were; 14.0 ± 0.05 cm (14 cm), 15.4 ± 0.05 cm (15 cm), 16.7 ± 0.05 cm (17 cm), 18.1 ± 0.05 cm (18 cm), and 20.9 ± 0.05 cm (21 cm).

As the sensor head was birefringent, the orientation of the cross section of the fibre in the transverse load setup can affect its sensitivity to applied transverse load. Figure 6.6 shows a schematic of the fibre cross section in the transverse load setup. To control the rotational orientation, or angle θ between the fast axis and the vector the load is applied, the fibre was held in two rotating holders while the load was applied between them. The angular position was marked on the holders with an accuracy of 5°. To measure the influence of angular orientation, the sensitivity of the sensor head to transverse load at four different orientations was measured for each fibre length; $\theta = 0$ degrees, $\theta = 30$ degrees, $\theta = 60$ degrees, and $\theta = 90$ degrees.

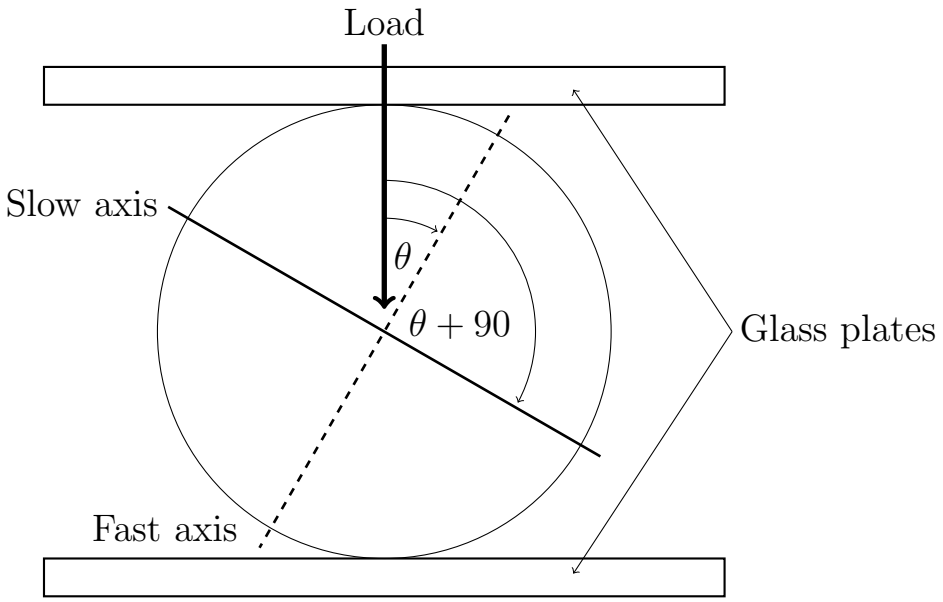

Figure 6.6: Schematic of the cross section of the birefringent fibre (PM1550), within the transverse load experimental setup. The orthogonal polarisation axes of the fibre are highlighted. Force from the load is applied perpendicular to the glass plates. The angle between the vector of the load and each orthogonal polarisation axis is shown. A schematic of the OBR is shown in Figure 6.4.

The sensor head was constructed from a 21 *cm* length of PM1550, which was spliced to the SMF. To produce the shorter lengths of PM1550, the 21 *cm* sensor head was cleaved to a shorter length. This meant the splice between the PM1550 and the SMF was the same for every length of sensor head, however the steps in reducing the PM1550 to the new length were not consistent. This was inconvenient as it reduced the length of the sensor head beyond what was expected initially. This will be discussed in greater detail later in this section. This approach also meant that new lengths had a good cleave. A good cleave was when the fibre end was flat, and perpendicular to the fibre axis. It had been found that bad cleaves produced a noisy beat interference.

Noise in the beat interference made it difficult to track the shift in the spectrum as strain was applied to the sensor head. Due to a miscalculation, the approach to measure the response of the 14 *cm* and 15 *cm* sensor heads to applied axial strain had to be modified, as described below. The three other lengths had axial strain

applied to a 8.0 ± 0.05 *cm* segment. 14 *cm* and 15 *cm* sensor heads were insufficiently long in the applied axial strain setup to have strain applied to a 8 *cm* segment.

The length of the region to which strain is applied affects its sensitivity to applied axial strain. When strain is applied to a fibre it modifies the phase of the light propagating through it [12]. When strain is applied to a longer region of a fibre, the light propagating through the fibre experiences a greater modification to its phase. Doubling the length of the region to which strain is applied, doubles the length of the region light propagates through experiencing a modification to its phase, when compared to travelling through a region of fibre without strain applied to it. To confirm this, a new sensor head of length 20.4 ± 0.05 *cm* was constructed, and its sensitivity to applied axial strain as a function of the length of the segment that had axial strain applied to it was tested. The results of this are described in Section 6.3 and were consistent with the sensitivity of the sensor head being proportional to the length of the segment to which strain is applied.

Since the modification of phase is proportional to the length of the region that strain is applied to, using a segment shorter than 8 *cm* would artificially reduce the sensitivity of the 14 *cm* and 15 *cm* sensor heads. To compensate for this, multiple measurements of the sensitivity of the 14 *cm* and 15 *cm* sensor head to applied axial strain was conducted, applying the strain to different length segments.

For 15 *cm* sensor head the three segment lengths were; 7.0 ± 0.05 *cm*, 6.0 ± 0.05 *cm*, and 5.0 ± 0.05 *cm*. For 14 *cm* sensor head the three segment lengths were; 6.0 ± 0.05 *cm*, 5.0 ± 0.05 *cm*, and 4.0 ± 0.05 *cm*. The sensitivity to applied axial strain for each segment length, for both sensor heads, was calculated and then plotted. This was used to work out the sensitivity to applied axial strain for both the 14 *cm* and 15 *cm* sensor heads, as if strain had been applied to an 8 *cm* segment within them.

After the sensitivity of a sensor head to strain as a function of its length had been analysed, a two sensor head system was constructed. The two sensor head system

was used to explore the extension of the sensor head system to a quasi-distributed sensor system. A natural expansion from a one sensor head is to set up a two sensor head system, to evaluate the difficulties from each sensor head interfering with each other due to cross-talk. The sensitivity of the sensor head as a function of its length will be discussed in Section 6.3.1, however it was found that the practical limits for constructing the sensor head and placing it in the strain setups were more important than the changes in sensitivity of the sensor head due to its length.

A difficulty was that to protect the splice between the SMF and the PM1550, it was placed in a plastic sleeve which glues to the fibre stopping motion around the splice. This sleeve is 2 cm long and when placed well had the splice at its centre. This meant that 1 cm of the length of the sensor head was taken by the splice protector, and it could not fit into the setups used to apply strain to the sensor heads. With a sensor head that was spliced to two lengths of SMF, it had two splice protectors and lost 2 cm. A second difficulty is that cleaving can be unsuccessful in producing a clean cleave for splicing. This meant that sensor heads needed enough length to fit in the strain setups, and then excess material to account for the length lost in the splice protectors, and excess material in case of bad cleaves.

Figure 6.7 shows the setup of the two sensor heads in series. Sensor head A was a PM1550 fibre of length 17 cm, spliced to SMF of length ≈ 3 m (SMF A). Sensor head B was a PM1550 fibre of length 20 cm, spliced to both SMF A and SMF B. SMF B (≈ 3 m) was connected to the OBR with an angled connector. Sensor head A and sensor head B had been intended to be the same length, however a series of bad cleaves meant that sensor head A was shortened. They were intended to be the same length so that they would have the same sensitivity to strain. Given the relatively long lengths involved in both sensor heads A and B, these differences were not material to the outcome in practice

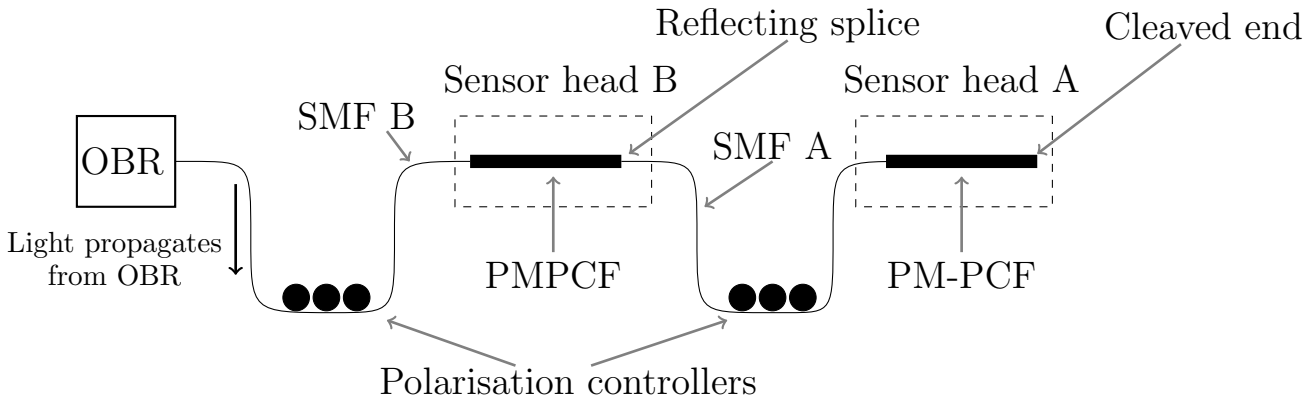

Figure 6.7: Schematic of the two sensor head system. The OBR is connected to the SMF B with an angled cleaved connector. SMF B is spliced to sensor head B. Sensor head B is spliced to SMF A. SMF A is spliced to sensor head A. Both sensor heads are short lengths of PM1550. The two polarisation controllers (PC) can be placed anywhere along the lengths of SMF to which they are attached. Light propagates from the OBR, through the system as is reflected off both the reflecting splice and the cleaved end, to propagate through the system back to the OBR.

The reflecting splice in Figure 6.7 refers to the splice the OBR software focused on to determine the beat interference of sensor head B. Two polarisation controllers were used to separately maximise the fringe visibility for sensor head A and sensor head B. The strain setups were used on either sensor head A, or sensor head B, while the beat interference of both sensor heads was monitored by the OBR. The OBR software records a trace of the response of the device under test connected to the OBR [9]. This allows the response of the beat interference of both sensor heads, as strain is applied to one, to be analysed.

6.3 Response of the sensor head to strain

As stated in Section 6.2, to measure the sensitivity of 14 *cm* and 15 *cm* sensor heads to applied axial strain, their effective sensitivity when strain was applied to an 8 *cm* segment had to be calculated. This was done by measuring the sensitivity of three shorter segments, and extrapolating. To confirm this approach was appropriate, the sensitivity of a sensor head of fixed length (20.4 ± 0.05 *cm*) was measured for five

different length segments. Figure 6.8 shows that the sensitivity of the sensor head to applied axial strain, as a function of the length of the segment of the sensor head to which axial strain is applied. The uncertainty of the sensitivities is the mean of the standard deviation for the series of three measurements taken, divided by the range of axial strain used. The sensitivities for each different length segment hold close to the proportional relationship between sensitivity of the sensor head to applied axial strain, and the length to which segment axial strain is applied, that was described in Section 6.2. The line of best fit was calculated using the python function scipy.stats.linregress, this function was used to produce all the lines of best fit shown later in this chapter. This computes a least-squares regression for two sets of arrays. In this case the two arrays were the length of the segment, and the sensitivity to applied axial strain. This validated the approach used to measure the sensitivity of the 14 cm and 15 cm sensor heads to applied axial strain. This is separate to how the length of the PM-PCF sensor head affects its sensitivity to applied axial strain, that was not found to be linearly proportional to length, and will be discussed later.

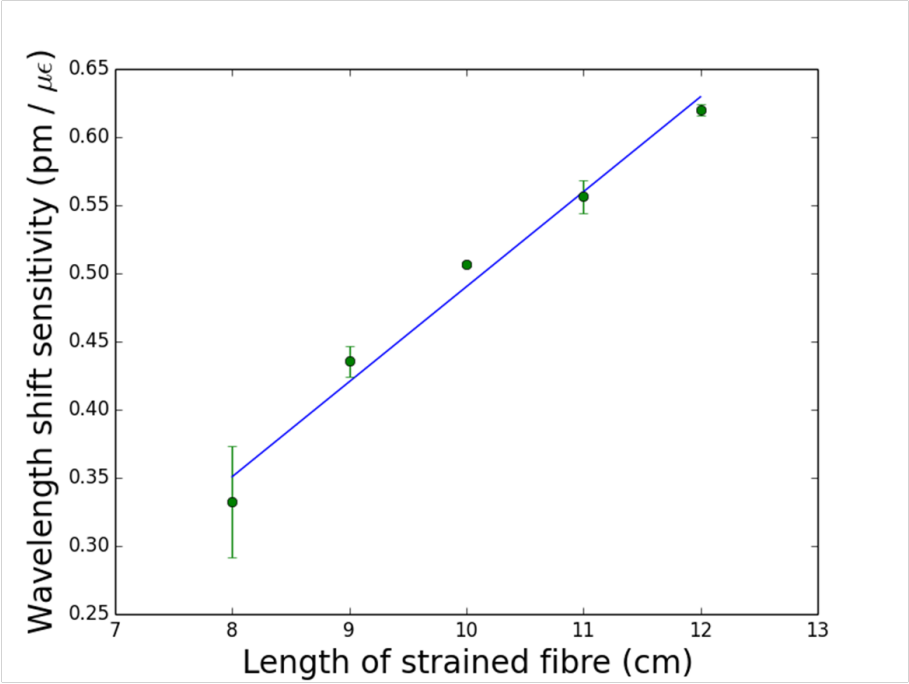

Figure 6.8: The sensitivity of a 20 *cm* sensor head to applied axial strain, as a function of the length of the segment that experienced applied axial strain. The error bars are the mean of standard deviation from the series of three sets of measurements divided by the range of strain it experienced.

6.3.1 Single sensor head

Applied axial strain

Regardless of length, the sensor heads were found to have a linear sensitivity to applied axial strain. Figure 6.9 shows the wavelength shift of the beat interference of the 21 *cm* PM1550 sensor head as axial strain was applied to it. There is a high correlation with the data points at the line of best fit, with an R-squared value of 0.99. Its response to applied axial strain became less consistent as the amount of strain applied increased. These error bars are much larger than those for any of the other sensor heads, it is unclear why the response of this sensor head was so inconsistent. It is possible that twists in the fibre had occurred between sets of measurements, changing the effective strain experienced by that sensor head. When applying the magnets to pin the sensor heads to the mounts, the sensor head may have had tension pre applied to it before measurements began. However this

source of error does not seem to have been repeated with the other sensor heads. The linear response of the sensor heads became clearer as the experiment progressed. The error bars are the standard deviation for the series of three measurements taken for each increment of applied axial strain. As with Figure 6.8, the line of best fit was produced using the python function scipy.stats.linregress. The gradient of this line of best fit was taken as the sensitivity of the 21 *cm* sensor head to applied axial strain. That sensitivity is reported in table 6.1 at the end of this section, along with the sensitivity to applied axial strain for all the other sensor heads of different lengths.

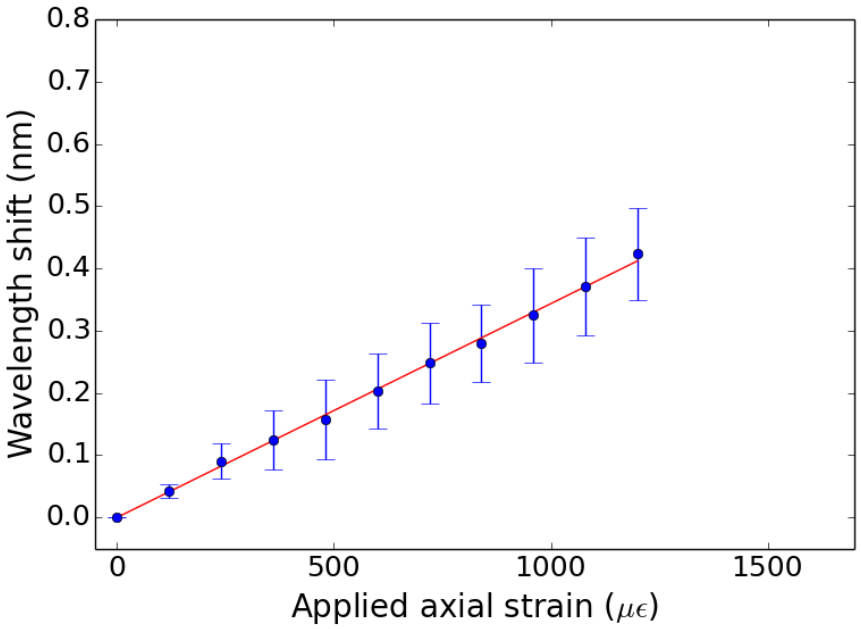

Figure 6.9: The wavelength shift of the beat interference of a 21 *cm* length of PM1550 as axial strain was applied to an 8 *cm* segment of its length. R-squared value of 0.99.The error bars are the standard deviation of the series of three measurement sets.

The wavelength shift of the beat interference of a 18 *cm* length of PM1550 as axial strain was applied to an 8 *cm* segment of its length, was far more consistent in its response to applied axial strain, shown by the reduced error bars in Figure 6.10. They are reduced enough to show that not all the points hold to the line of best fit, though there is a still a strong correlation (R-squared = 0.99), with one

point between 700 $\mu\epsilon$ and 800 $\mu\epsilon$ breaking from the line. This point corresponds to an extension of the fibre by 60 μm, this may have been caused by a consistent over turning of the control for the mount position. As described in Chapter 5, axial strain is applied to the fibre by pinning both ends to separate optical mounts. The distance between them is increased by turning a control on one of the mounts. This control has micrometer precision, but is turned by hand and could suffer from imprecision in being turned. This source of error should reduce as the amount of applied axial strain is increased, since the amount the control over or under turned will become a smaller fraction of the amount the fibre is stretched.

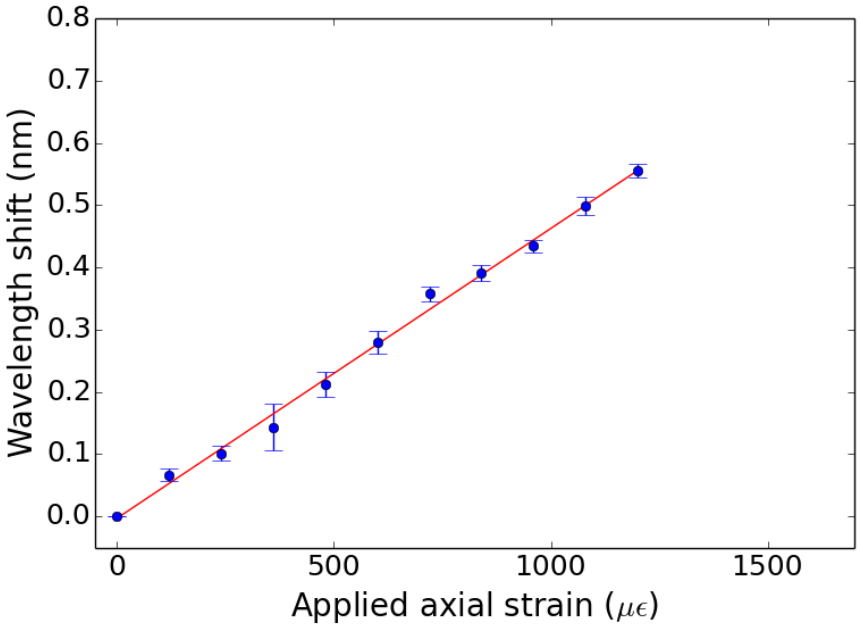

Figure 6.10: The wavelength shift of the beat interference of a 18 *cm* length of PM1550 as axial strain was applied to an 8 *cm* segment of its length. The R-squared is 0.99. The error bars are the standard deviation of the series of three measurement sets.

Like the 21 *cm* sensor head, the inconsistency of the 17 *cm* sensor head's sensitivity to applied axial strain increased as the strain was increased. This is far less pronounced for the 17 *cm* sensor head, and may be due to twist in the fibre as it was placed in the setup, as described for the 21 *cm* sensor head. This source of error cannot be from over or under turning, which should decrease as the applied axial

strain is increased.

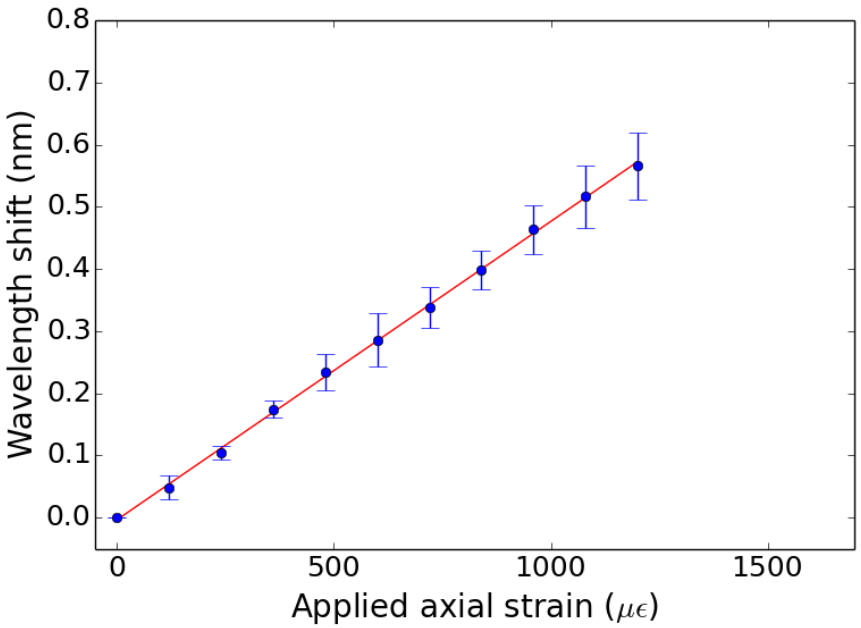

Figure 6.11: The wavelength shift of the beat interference of a 17 *cm* length of PM1550 as axial strain was applied to an 8 *cm* segment of its length. The R-squared is 0.99. The error bars are the standard deviation of the series of three measurement sets.

As stated above the 15 *cm* and 14 *cm* sensor heads were too short for the axial strain setup to apply strain to an 8 *cm* segment, so strain was applied to three different length shorter segments. Figure 6.12 shows the sensitivity of the 15 *cm* sensor head, as a function of the length of the segment to which axial strain was applied. The error bars are the uncertainty of the sensitivity of the sensor head, for that segment length. This was calculated in the same way as for the longer lengths; the mean of the standard deviation of the series of three measurement sets divided by the strain range. The line of best fit was used to calculate the 15 *cm* sensor head sensitivity as if strain was applied to an 8 *cm* segment, in Figure 6.12 by the intersect between the line of best fit and the dashed line for the 8 *cm* point on the x-axis.

The response of the 15 *cm* sensor head to applied axial strain is shown in Figure 6.13, this is for strain applied to a 6 *cm* segment of the sensor head. The distance the

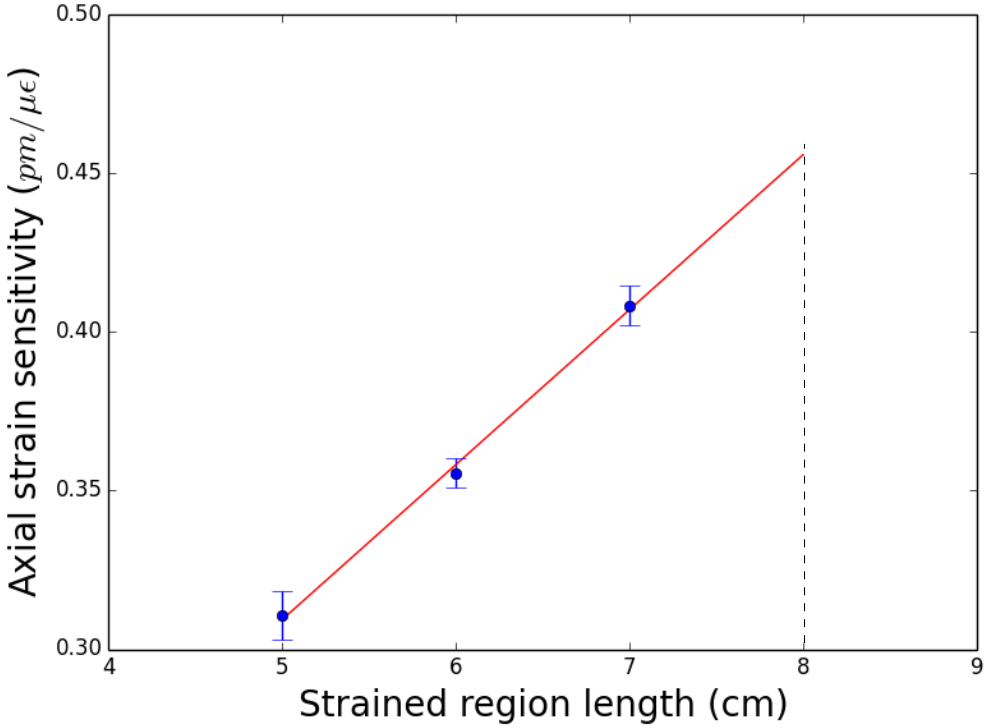

Figure 6.12: The sensitivity of the 15 *cm* sensor head to applied axial strain as a function of the length of the segment to which strain was applied.

fibre was stretched for the 6 *cm* segment was the same as the 8 *cm* segments of the other length sensor heads, and is why the range of strain applied to this sensor head is greater than that of the previous sensor heads. The linear relationship between wavelength shift of the beat interference and applied axial strain seen in the other sensor heads is also demonstrated with the 15 *cm* sensor head.

The final length sensor head, the 14 *cm* sensor head, shows the same linear response to applied axial strain. As with the 15 *cm* sensor head, Figure 6.14 shows a greater range of applied axial strain. This is the strain applied to the 6 *cm* segment of the sensor head. The response of the 14 *cm* sensor head holds tightly to the line of best fit, being the strongest indicator of the linear response out of all the sensor heads.

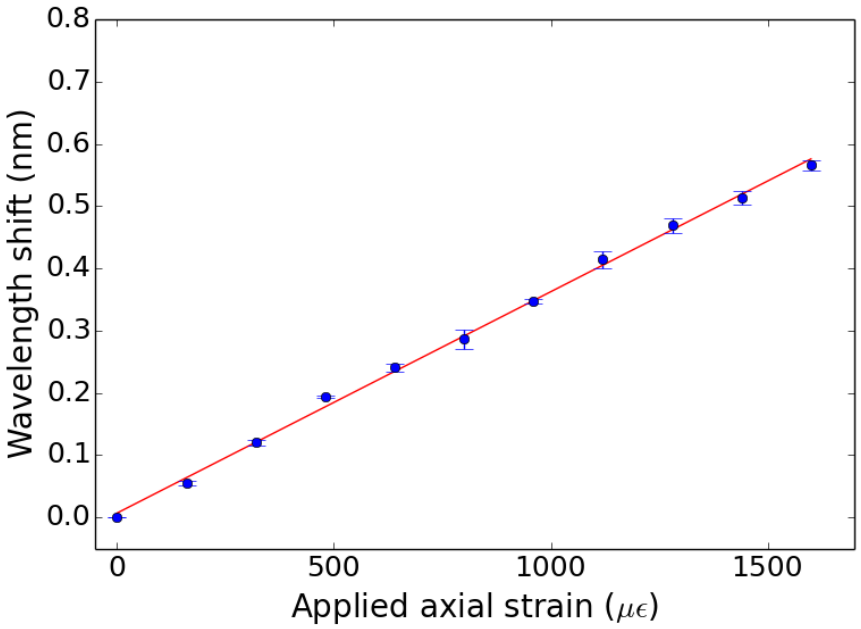

Figure 6.13: The wavelength shift of the beat interference of a 15 *cm* length of PM1550 as axial strain was applied to an 6 *cm* segment of its length. R-squared = 0.99.

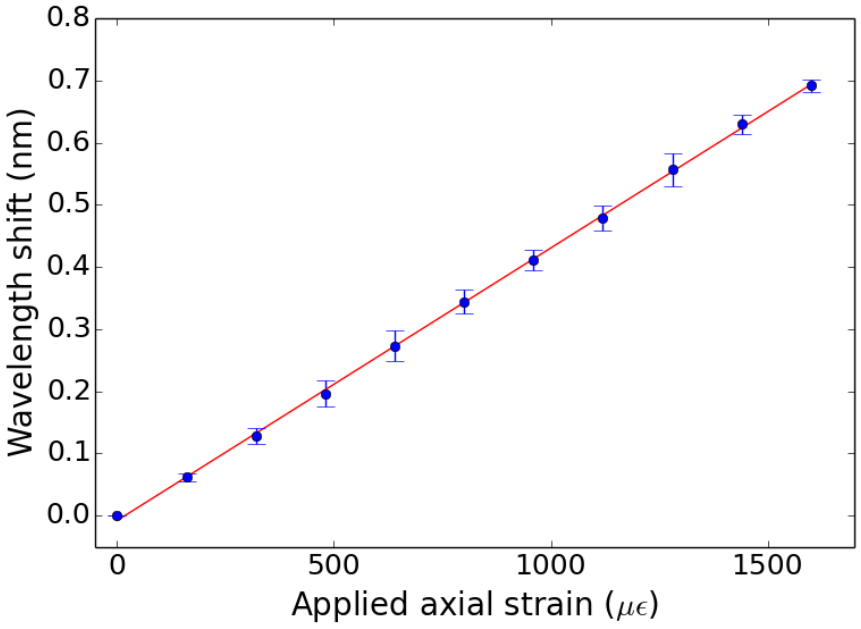

Figure 6.14: The wavelength shift of the beat interference of a 14 *cm* length of PM1550 as axial strain was applied to an 6 *cm* segment of its length. R-squared = 0.99.

While the PM1550 is birefringent, the rotational orientation of the fibre had no effect on its sensitivity to applied axial strain, since the strain was applied equally

to both orthogonal polarisation modes. The linear response to applied axial strain shows that the difference in phase between the two orthogonal polarisation modes propagating through the birefringent fibre, changes linearly as axial strain is applied along the length of the fibre. There was no change in the period of the beat frequency, which shows that the difference in refractive index between the two orthogonal polarisation modes remained constant as axial strain was applied to it.

There was a trend for shorter length sensor heads having greater sensitivity to applied axial strain. Figure 6.15 shows the sensitivity of a sensor head to applied axial strain as a function of its length. Equation 6.1 in Section 6.2 described the relationship between the change in the difference in phase, between the two orthogonal polarisation modes propagating in the birefringent fibre, as a function of wavelength. The equation implies that the sensitivity of the sensor head to applied axial strain should be inversely proportional to its length. It shows that the change in the difference in phase, across the wavelength range scanning the fibre, increases as the length of the birefringent fibre decreases. The sensitivity of the sensor head to applied axial strain increasing as its length decreases follows Equation 6.1. The sensitivity of the sensor head is proportional to the beat frequency, which is inversely proportional to the length of the fibre. An inversely proportional relationship between the length of the sensor head and its sensitivity to applied axial strain cannot be seen in Figure 6.15. There were errors introduced by the method used to account for the reduced length of the segment strain applied to both the 14 *cm* and 15 *cm* sensor heads. This is the most likely reason for the sensitivity of the 15 *cm* sensor head being so low. Due to time constraints the work on measuring the sensor head's sensitivity to applied axial strain could not be repeated. The next step would be to repeat the work, either starting with longer sensor heads, or measuring strain applied to a 6 *cm* segment for all the different length sensor heads.

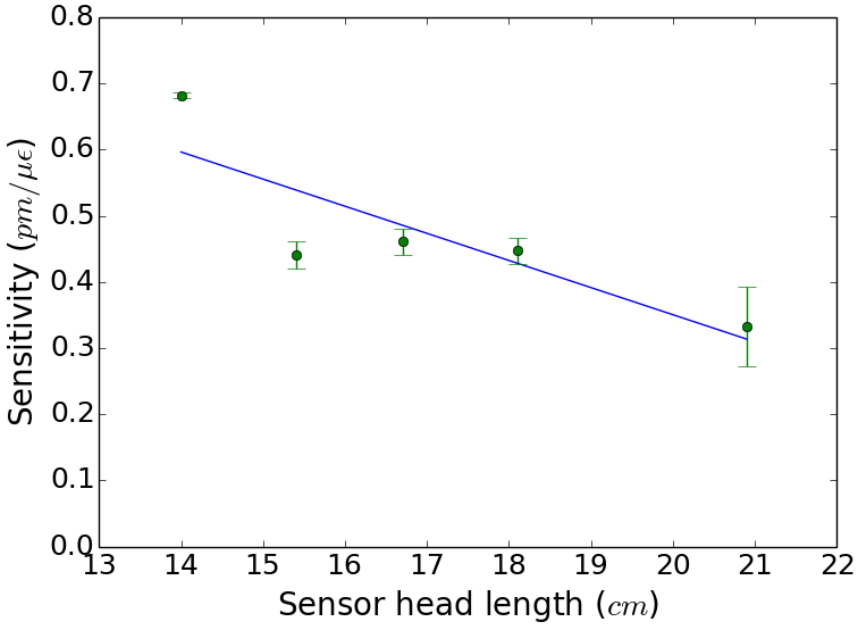

Figure 6.15: Relation between length of the sensor head and its sensitivity to applied axial strain. The error bars are the mean of the standard deviation of three sets of measurements, divided by the strain range the sensor head experienced. R-squared = 0.72.

Table 6.1 states the sensitivity of the different length sensor heads to applied axial strain, and the uncertainty in their sensitivity. The uncertainty of their sensitivity is taken to be the mean of the uncertainty for the series of three measurement sets taken, divided by the strain range applied to the sensor heads. The typical sensitivity of a fibre Bragg grating (FBG) written in SMF, a standard optical approach to measuring strain, to applied axial strain at 1550 nm is $1.225 \pm 0.006 pm/\ \mu\epsilon$ [12]. This implies that even the most sensitive sensor head, the 14 cm sensor head, is still half as sensitive as a standard FBG based axial strain measurement system. To make the sensor head competitive with FBG based axial strain sensor systems, the sensor head sensitivity would have to be enhanced, or provide a benefit not already provided by an FBG based system.

Table 6.1: The sensitivity of different lengths of PM-PCF to applied axial strain. The uncertainty is the standard deviation between the three sets of measurements done on each length.

Length (cm)	Sensitivity $pm/\mu\epsilon$	uncertainty $pm/\mu\epsilon$
14 (14.0)	0.682	0.004
15 (15.4)	0.441	0.02
17 (16.7)	0.461	0.02
18 (18.1)	0.447	0.02
21 (20.9)	0.332	0.06

Applied transverse load

As described in Section 6.2, the angular orientation of the birefringent fibre the sensor head is constructed from, affects its sensitivity to applied transverse load. Figure 6.16 shows the sensitivity of a $15cm$ long sensor head to applied transverse load, depending on which angle the fibre was orientated. The 0 degree orientation is parallel to the vector of the applied transverse load. Figure 6.16 shows that the orientation of the fibre has a significant effect on its sensitivity to applied transverse load; for angles 0 ± 5 degrees, 30 ± 5 degrees, 150 ± 5 degrees, and 180 ± 5 degrees there was a positive wavelength shift as transverse load was applied. For angles 60 ± 5 degrees, 90 ± 5 degrees, and 120 ± 5 degrees there was a negative wavelength shift as transverse load was applied.

When the transverse load was applied parallel to the fast axis of the fibre, the beat interference shifted to a longer wavelength. This was the same response for the sensor head to applied axial strain. When the transverse load was applied parallel to the slow axis of the fibre, the beat interference shifted to a shorter wavelength. This is the opposite response for the sensor head to applied axial strain. When strain is applied to an axis of the fibre, it retards the phase of the polarisation mode propagating through that axis [13]. This shifts the position of peaks of the beat interference. The direction of shift depends on which polarisation mode's phase is retarded.

This can be better understood if we consider the phase relationship between or-

thogonal modes. If the refractive index experienced by either orthogonal polarisation mode is changed, the difference in phase between the two orthogonal polarisation modes changes as given by the phase relationship $\phi = L\Delta\beta$. If the refractive index of the slow axis increases, the difference in refractive index $\Delta\beta$ will also increase. If the refractive index of the fast axis increases, the difference in refractive index $\Delta\beta$ will decrease.

This shows that depending on which polarisation axis experiences strain, the direction of the change in the phase difference between the axis will be different. When strain is applied to the fast axis the phase difference decreases, which implies that the peaks in the beat interference will shift to longer wavelengths. The range of orientations in Figure 6.16 is 180 degrees, this means that the same polarisation mode is encountered twice. This confirms the analysis since the response for 180 degrees was similar to the response at 0 degrees. Applications for this stem from the fact that the sensitivity of the sensor head can be tailored by changing its rotational orientation, with the possibility for an orientation with a sensitivity close to zero.

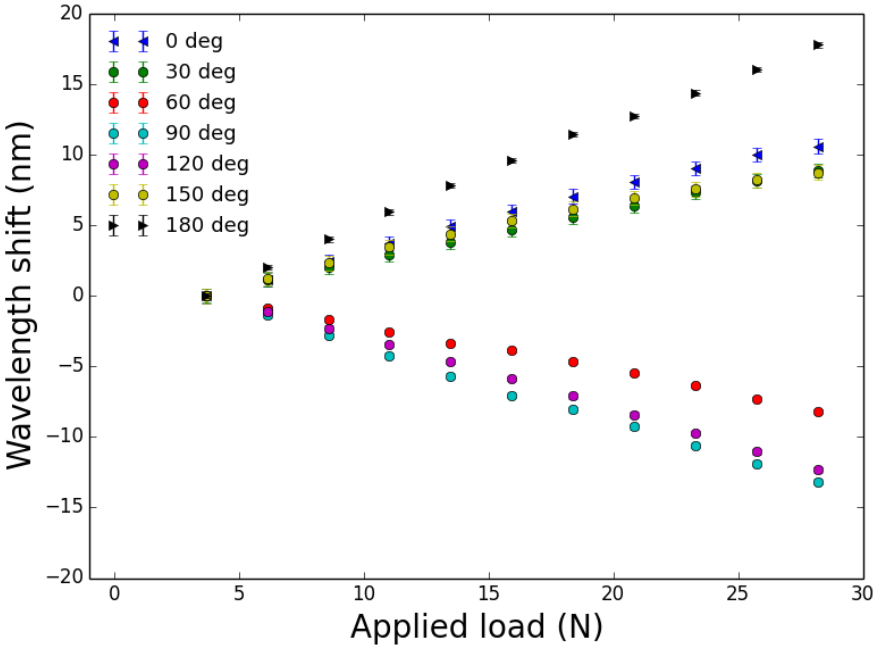

Figure 6.16: The wavelength shift as a function of applied transverse load, for different rotational orientations of a PM-PCF 15 *cm* sensor head.

To evaluate the effect of length of the sensor head on its sensitivity to applied transverse load, it was placed in four different rotational orientations. This was done using the fibre holders in the transverse load setup, as described in Chapter 4. They can rotate with a measured angle, rotating the fibre in the setup, but not when transverse load is being applied to it. The four orientations are; 0 degrees, 30 degrees, 60 degrees, and 90 degrees. The 0 degrees position was aligned with the fast axis of the fibre, the other angles were the fibre rotated along the fibre's propagation axis. These orientations were kept fixed even for different length of sensor head. This range of 90 degrees allowed the sensitivity of both polarisation modes to be assessed.

Chehura et al. [14] found that for FBGs written in non-PCF birefringent fibre there was a sinusoidal relationship between the sensitivity of the FBG to transverse load, and the alignment of either orthogonal polarisation modes with the axis to which the load was being applied. The sensitivity of the 14 *cm* sensor head to applied load as a function of its rotational orientation is shown in Figure 6.17. The error bars were calculated by dividing the mean of the standard deviation for the series of three measurement sets taken, by the range of applied transverse load the sensor head experienced. As already stated, unlike FBGs there can be a wavelength shift to shorter wavelengths in response to applied transverse load, when it is applied parallel to the slow axis. In the case of FBGs the sensitivity is either decreased, or increased depending on its rotational orientation, and does not produce a negative sensitivity [14]. The sensor head might have a sinusoidal sensitivity to applied load, but there needs to be smaller increments of angle to map this. Due to time constraints this was not undertaken, but a further expansion of this work would be to map the sensitivity of a sensor head in small angular increments.

There was a large variation between the four angular orientations, in the sensitivity of the sensor head to applied transverse load as a function of the length of the sensor head. Figure 6.18 shows the sensitivity of the different length sensor heads

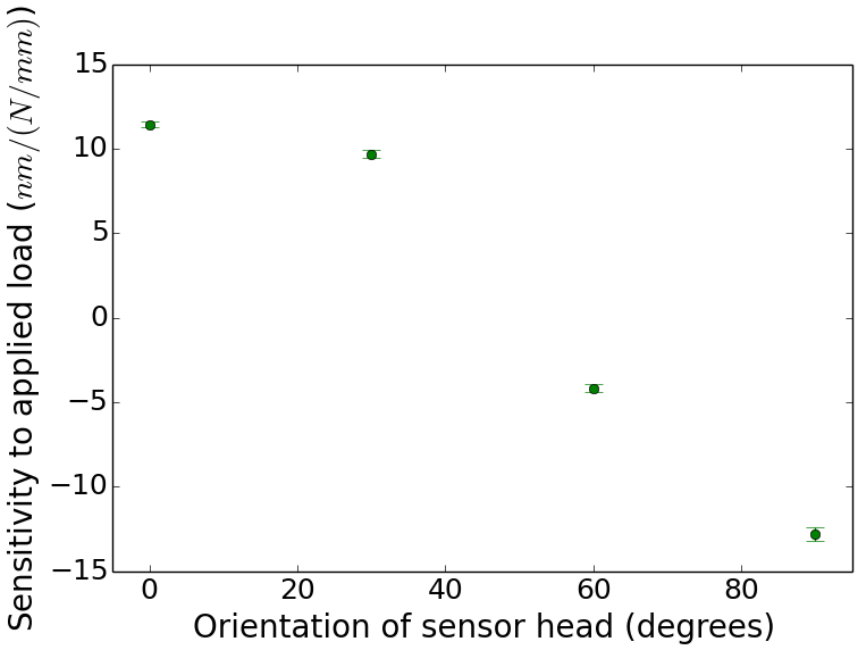

Figure 6.17: The sensitivity of the 14 *cm* sensor head as function of its rotational orientation.

to applied transverse load, while in the 0 degree orientation (parallel to the fast axis). There is no clear trend in the sensitivity, as already discussed in section 6.3.1, although Equation 6.1 implies that the sensitivity should be inversely proportional to the length of the fibre.

The trend expected by Equation 6.1 can be partially seen in the 90 degree orientation (parallel to the slow axis), shown in Figure 6.19. Due to its negative sensitivity to applied transverse strain, weaker sensitivity is less negative and closer to zero. The sensitivity curves, but it plateaus which is not a trait predicted by Equation 6.1.

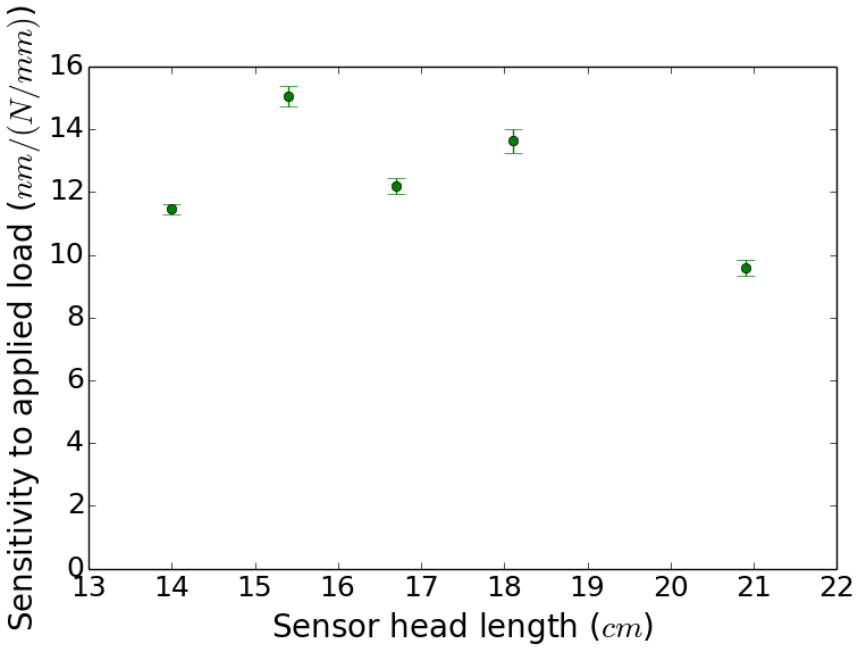

Figure 6.18: The sensitivity of the sensor head as function of its length, while load is applied parallel to the fast axis.

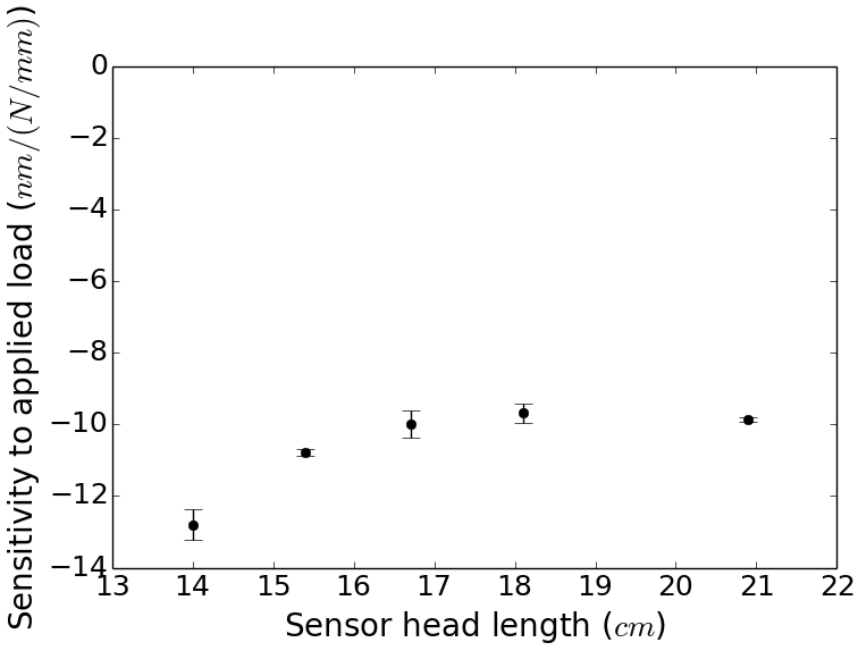

Figure 6.19: The sensitivity of the sensor head as function of its length, while load is applied parallel to the slow axis.

For the 30 degree and 60 degree orientations, the sensitivity between different length sensor heads varied significantly. Those orientations are close to the "zero"

orientation (45 degrees), where the fibre would be insensitive to applied transverse load. The accuracy of fibre orientation was ±5 degrees. If the sensitivity of sensor head is sinusoidal with regards to orientation, the largest change in sensitivity will be close to the 45 degree orientation. This means inaccuracy in rotational orientation will have a greater affect in orientations closer to 45 degrees. The fast axis (0 degree orientation) of the fibre was flagged with tape, where the tape was wrapped round it with the tail pointing in the direction parallel to the fast axis.

As discussed in Chapter 1 the hole structure of the fibre hides the birefringence inducing enlarged holes near the fibre core of PM1550. This means that side illumination does not reveal the different axes of the fibre, this was described in greater detail in Chapter 4. To find those, the fibre end was examined with a microscope, and the fast axis flagged with tape. When placing the new length sensor head into the transverse load setup, there was a source of error in aligning the flags with the 0 degree mark of the angle measuring fibre mounts. This was human error in aligning the flag with the zero mark. The cumulative inaccuracy between the flagged fibre axis and the fibre mounts meant that the angle was not consistent enough with the 30 degrees and 60 degrees to get an accurate measure of the change in sensitivity with regards to length.

A further investigation only into the sensitivity to transverse load could reduce these inaccuracies by using a 180 degree range of orientations, and changing them in steps of 15 degrees. Further the fibre would not be removed from its mounts, but shortened while in them. This would remove the error introduced by taking the fibre out and placing it back in again.

Table 6.2 lists the sensitivity of the sensor heads to applied transverse load, as a function of length and rotational orientation. The uncertainty in the sensitivities is the mean of the standard deviation for each data point divided by the range of transverse load applied to the sensor head. An FBG written into elliptically clad birefringent fibre can have a sensitivity to transverse load as high as 0.23 ±

$0.02nm/(N/mm)$ [14]. Depending on the orientation of the sensor head, it can have a sensitivity two orders of magnitude higher than this. This implies that roles currently occupied by FBG based sensor systems for the measurement of transverse load could be replaced by a sensor head.

Table 6.2: The sensitivity of PM-PCF sensor heads, of different lengths, at different rotational orientations, to applied transverse load. The uncertainty in the sensitivity is derived from the standard deviation of the three sets of measurements done.

	Sensitivity $nm/(N/mm)$			
Length (cm)	0 degrees	30 degrees	60 degrees	90 degrees
14 (14.0)	11.46 ± 0.16	9.71 ± 0.23	-4.16 ± 0.24	-12.80 ± 0.42
15 (15.4)	15.06 ± 0.34	12.49 ± 0.59	-11.29 ± 0.20	-10.78 ± 0.09
17 (16.7)	12.20 ± 0.25	1.78 ± 0.09	-3.90 ± 0.15	-9.99 ± 0.38
18 (18.1)	13.63 ± 0.37	12.12 ± 0.17	-3.69 ± 0.03	-9.68 ± 0.27
21 (20.9)	9.58 ± 0.26	6.24 ± 0.19	0.14 ± 0.16	-9.86 ± 0.05

Response to change in temperature

Table 6.3 shows that regardless of the length of the sensor head, it had weak sensitivity to temperature change. The uncertainty in the measurement of the sensitivity, the mean of the standard deviation of each point for the series of three measurements divided by the temperature range (25^0C to 125^0C), was almost always greater than the measured sensitivity. As discussed in Chapter 1 the photonic crystal fibre (PCF) uses a hole structure to guide light. This is composed of un-doped silica and air. The PCF structure is less sensitive to temperature change than SMF. For an FBG written in Panda, the slow axis has a sensitivity to temperature change of $15.6 \pm 0.1pmC^{-1}$, and for the fast axis $16.5 \pm 0.1pmC^{-1}$[14]. The sensor head's sensitivity to temperature change was at least an order of magnitude smaller than an FBG's. This means that for roles that require a low sensitivity to temperature change, a sensor head can replace an FBG based sensor system.

Table 6.3: The sensitivity of PM-PCF sensor heads, of different lengths, to applied temperature change. The uncertainty in the sensitivity is derived from the standard deviation of the three sets of measurements done.

Length (cm)	Sensitivity $pm/^0C$	uncertainty $pm/^0C$
14 (14.0)	-0.13	1.95
15 (15.4)	-0.20	0.51
17 (16.7)	0.08	0.85
18 (18.1)	-1.00	0.94
21 (20.85)	-1.20	1.17

6.3.2 Two sensor heads

As described in section 6.1, a quasi-distributed sensor system is a series of point sensors that are interrogated simultaneously, and monitor an extended region [1]. The two sensor head system was intended to show if the sensor head approach could be expanded to be a quasi-distributed sensor system. To assess this it needed to be known if the two sensor heads would exhibit cross-talk with regards to each other. Figure 6.7 in section 6.2 shows the arrangement of the two sensor head system. Sensor head B was the proximal sensor head to the OBR, and sensor head A was the distal sensor head to the OBR.

The response of both sensor head A and sensor head B, when axial strain is applied to an $8cm$ segment of sensor head A, is shown in Figure 6.20. From this it is clear that strain applied to sensor head A has little to no effect on the signal from sensor head B. There might be a slight shift of the response from sensor head B to shorter wavelengths, but this is at least orders of magnitude smaller than the response of sensor head A.

When axial strain is applied to a $8cm$ segment of sensor head B, shown in Figure 6.21, there is a strong response from sensor head A, and a clear sign of cross-talk between the sensor heads. Sensor head A's response to axial strain applied to sensor head B is not as strong as sensor head B's response, but it is of similar order of magnitude.

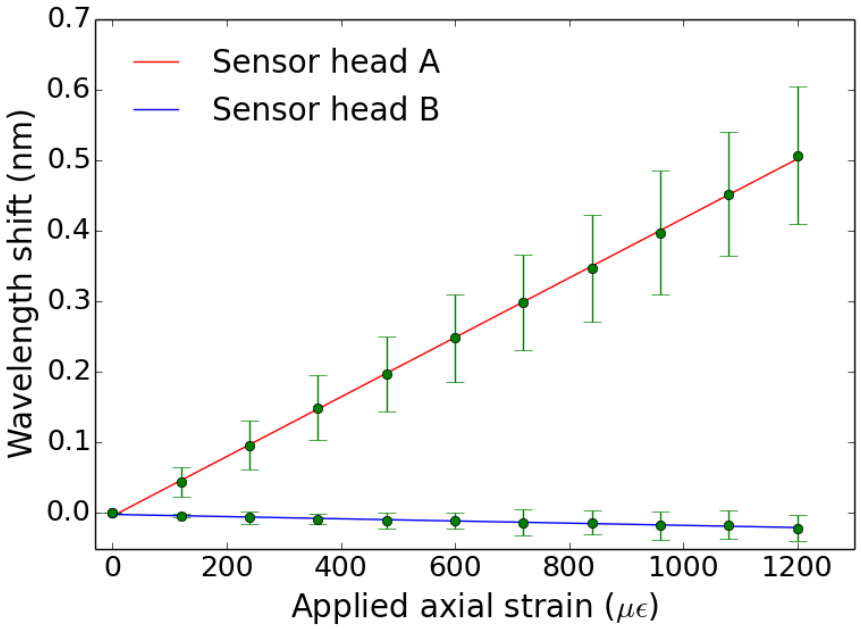

Figure 6.20: Shows the response of both sensor heads, as axial strain is applied to sensor head A. The error bars are the standard deviation of three sets of measurements.

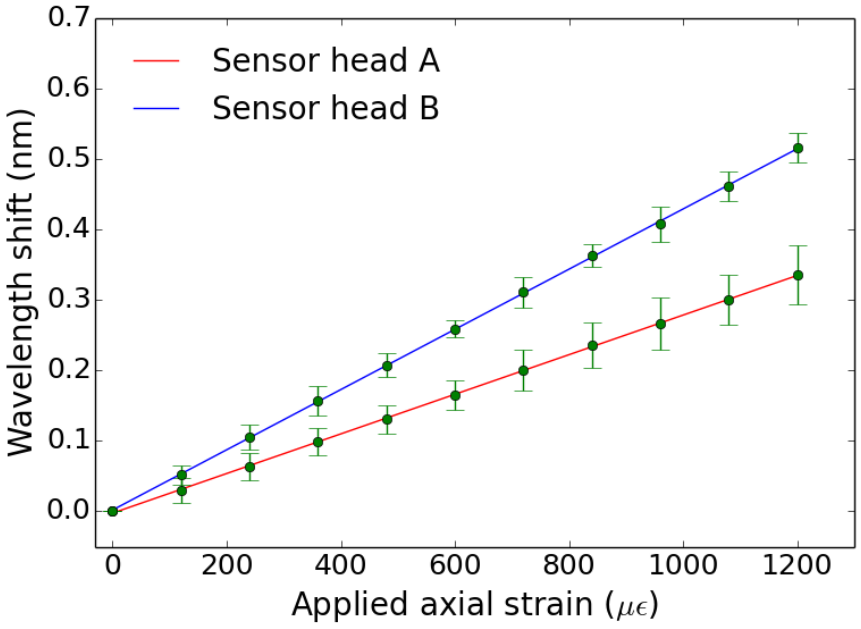

Figure 6.21: Shows the response of both sensor heads, as axial strain is applied to sensor head B. The error bars are the standard deviation of three sets of measurements.

This cross talk response is repeated even if the wavelength shift is to shorter wavelengths. Figure 6.22 shows the response of both sensor heads as transverse load

is applied to the slow axis of sensor head A. There might be a response from sensor head B to longer wavelengths, in the opposite direction to sensor head A's response, but it is orders of magnitude smaller.

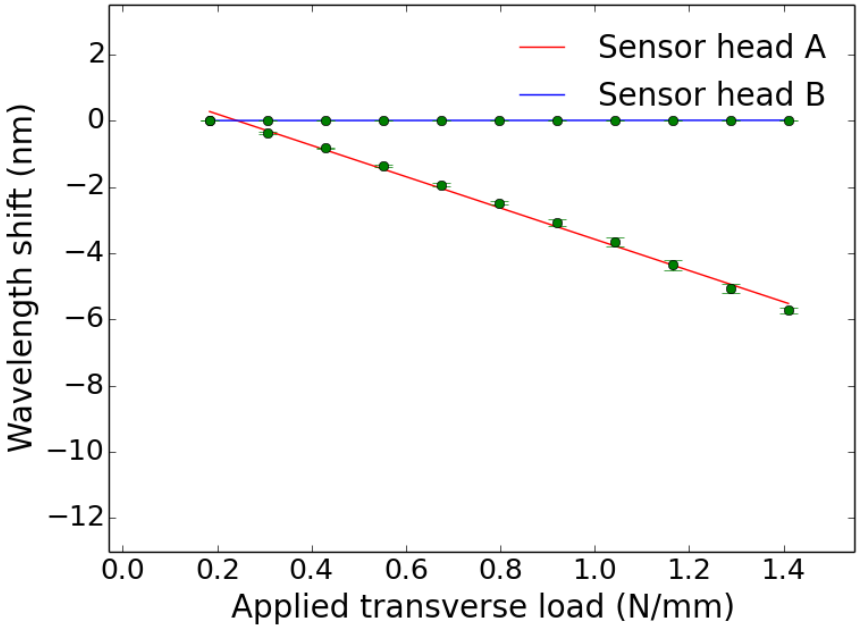

Figure 6.22: Shows the response of both sensor heads, as transverse load is applied to sensor head A. The error bars are the standard deviation of three sets of measurements.

When transverse load is applied to the slow axis of sensor head B, both sensor head A and sensor head B respond to it. Sensor head A's response is weaker, matching how it behaved when axial strain was applied to sensor head B, shown in Figure 6.21.

This problem can be better understood by looking at the path light takes from the sensor head to the OBR. Light leaves the OBR and propagates along the SMF to sensor head B, where some is reflected back towards the OBR. The transmitted light propagates through sensor head B and along the SMF until it reaches sensor head A. Light is reflected off sensor head A, propagates back along the SMF and through sensor head B, and through the last of the SMF to the OBR. The two orthogonal polarisation modes interfere at the detector in the OBR to register the change in relative phase.

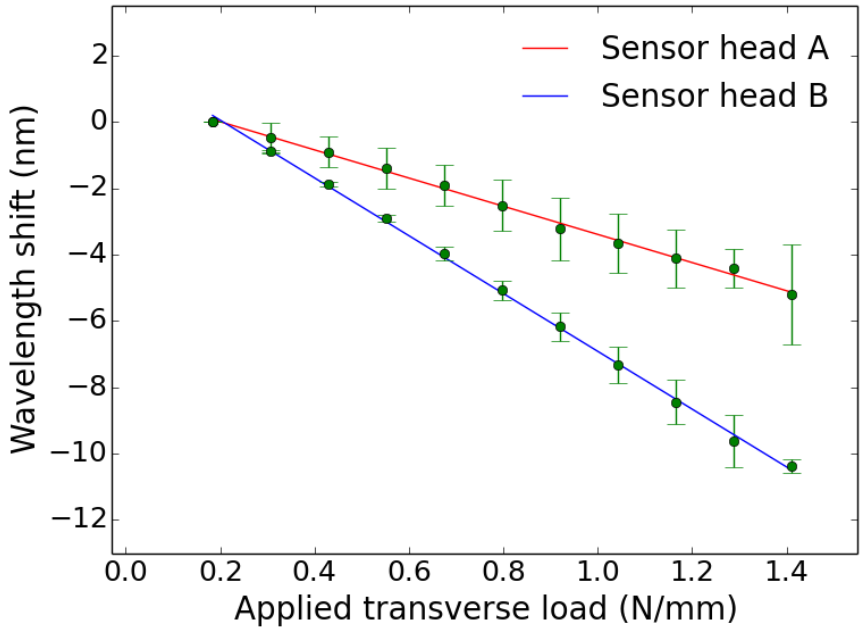

Figure 6.23: Shows the response of both sensor heads, as transverse load is applied to sensor head B. The error bars are the standard deviation of three sets of measurements.

Light from sensor head B reaches the OBR directly, as long as conditions for the SMF do not change, the phase of the light will be unmodified. Light from sensor head A reaches the OBR via sensor head B. Changing conditions on sensor head B modifies the phase of light propagating through it both to and from sensor head A. If the change in phase caused by conditions to sensor head B, is subtracted from the signal to the OBR, the change in phase caused by conditions to sensor head A can be extracted.

This is a limitation on the system because of how light propagates through the optical fibres. While the PCF used has a low sensitivity to temperature change, and therefore the change in its birefringence due to temperature change is low, the SMF used is sensitive to temperature change. While effort was taken to strap the SMF down to keep it from moving, any curls in the fibre (such as from being on a reel) induced small amounts of birefringence. This birefringence would have a temperature dependence, and changes in the lab temperature would have affected it, and therefore possibly affected the relative phase between the two orthogonal

polarisation modes. While the lab was a temperature controlled environment, this is still a limitation on the system being developed further as applications would be for environments not temperature controlled. A possible solution would be to use single mode PCF instead of the SMF, which would have a lower susceptibility to temperature effects.

It was already discussed in section 6.3.1 that shorter length sensor heads have greater sensitivity, because they have a larger wavelength shift in position of the beat interference. This is important for extracting the information on the amount that sensor head B is modifying the phase of light propagating through it. For the light that returns directly from sensor head B its effective length was $40cm$. This is twice its actual length, because the light propagates through it, reflects off the end and returns through the sensor head again.

Light that propagates to sensor head A and returns to the OBR also propagates through sensor head B experiencing an effective length of $40cm$ of sensor head B. This means that by measuring the response of sensor head B, that change in relative phase can be removed from the signal from sensor head A. There is still the issue that any birefringence in the SMF has not been accounted for. The birefringence in the SMF can potentially rotate the polarisation modes propagating from sensor head A into sensor head B, and this will have an effect on the change in the relative phase difference induced by sensor head B on the signal from sensor head A. The only way to account for this would be to use polarisation controllers to negate the birefringence in the SMF. However that would require a clearer measure of the birefringence in the SMF.

If the issue of birefringence in the SMF is resolved, the method of removing the phase caused by sensor head B will mitigate the effects of cross-talk between the sensor heads, and allow the work to progress to more than two sensor heads in series, subtracting the affect of each sensor head on the signal of the following sensor head in the series.

6.4 Chapter summary

In this chapter, a technique to measure axial strain and transverse load was presented. This is an expansion of Rota-Rodrigo et al. [5], who made a sensor head from a short length of birefringent photonic crystal fibre interrogated with an OBR, to measure applied axial strain. The expansion was to construct several sensor heads of different lengths, and compare their sensitivity to both applied axial strain and applied transverse load. Further a two sensor head system was constructed, that had the sensor heads in series and interrogated simultaneously by the OBR. The aim of this was to test an approach for a quasi-distributed sensor system for the measurement of strain, and to develop methods to mitigate the cross-talk between the multiple sensor heads. The sensor heads were short lengths of PM1550, between 14 cm and 21 cm in length, spliced to a much longer length of SMF (> 3 m). The OBR measured the beat interference of the sensor head as both orthogonal polarisation modes left it entering the SMF and interfering before reaching the OBR. The position of the minima of the beat interference was used to measure its wavelength shift. Sensitivity of the sensor head corresponds to the wavelength shift of the beat interference as strain is applied to it. Greater wavelength shift is equivalent to greater sensitivity.

It was found that there was a trend for shorter length sensor heads having greater sensitivity to both measurands. This was explained using Equation 6.1, which relates the change in phase difference between the two orthogonal polarisation modes across a wavelength range. For the same wavelength range, a shorter length fibre can measure a smaller change in phase difference. This meant that smaller fibre lengths were more sensitive to smaller phase changes caused by either axial strain or transverse load applied to the birefringent fibre. This trend was weak, and the effects of other factors were more dominant to the sensitivity of the sensor head. The sensor head had a linear response to axial strain, with the beat frequency remaining fixed. The beat frequency remaining constant shows the beat length was unaffected

across the strain range used, 0 $\mu\epsilon$ to 1500 $\mu\epsilon$. The sensitivity of the sensor head to applied axial strain, < 0.700 $pm/\mu\epsilon$, was an order of magnitude smaller than an equivalent FBG system, 1.225 ± 0.006 $pm/\mu\epsilon$ [12]. It would have to possess other benefits to replace an FBG sensor system for the measurement of strain

The sensitivity of the sensor head to transverse load was dependent on the rotational orientation of the birefringent fibre. Transverse load was applied to an axis of the fibre perpendicular to its propagation axis. If this was aligned with the fast axis of the fibre the beat interference shifted to longer wavelengths, matching its response to applied axial strain. If instead this was aligned with the slow axis of the fibre, the beat interference shifted to shorter wavelengths, the opposite to its response to applied axial strain. Transverse load applied to one polarisation axis of a fibre retards the phase of that polarisation [13]. If it retards the phase of the fast axis, it reduces the phase difference between the orthogonal polarisation modes when they interfere, shifting the beat interference to longer wavelengths. If it instead retards the phase of the slow axis, it increases the phase difference between the orthogonal polarisation modes, shifting the beat interference to shorter wavelengths. For specific orientations of the sensor head, it was found to have a sensitivity to applied transverse load > 12.0 $nm/(N/mm)$, this is two orders of magnitude greater than typical sensitivities of an FBG to applied transverse load, 0.23 ± 0.02 $nm/(N/mm)$ [14]. This implies that the sensor head could replace a FBG system for the measurement of transverse load.

It was found the sensor head was highly insensitive to change in temperature from 25 ^0C to 125 ^0C, regardless of the length of the sensor head. The sensor head sensitivity to temperature change with the largest magnitude was -1.20 ± 1.17 pm/C. For an FBG written in Panda, the slow axis has a sensitivity to temperature change of 15.6 ± 0.1 pm/C, and for the fast axis 16.5 ± 0.1 pm/C[14]. This implies that the sensor head has a sensitivity at least an order of magnitude lower to temperature change when compared to an FBG. Sensing roles that require a low sensitivity to

temperatures currently occupied by FBGs could instead use PM1550 sensor heads.

Overall when compared to FBG sensor systems, a sensor head had a much lower sensitivity to temperature change, a much higher sensitivity to applied transverse load, and lower sensitivity to applied axial strain. This means the sensor head could occupy roles that require high transverse load sensitivity, and low temperature sensitivity. The sensor head can also distinguish if transverse load is applied to its fast or slow axis, a novel property that deserves further exploration.

While shorter length sensor heads were more sensitive to both measurands, when progressing to the two sensor head system longer lengths were used for convenience. They were more convenient due to the limitations of the setups used to apply either axial strain or transverse load, and needing spare length in case of bad cleaves required reducing the fibre in length further.

The two sensor head system was two sensor heads spliced together via a long length ($\approx 3\ m$) of SMF, with sensor head B connected to the OBR via a long length ($\approx 3\ m$) of SMF, which was spliced to sensor head B. This arrangement allowed the OBR to interrogate both sensor heads simultaneously. There was cross talk between the sensor heads, which meant that strain applied to sensor head B gave a false signal from sensor head A. This is because strain applied to sensor head B modified the phase of light before it reached sensor head A. A further limitation was that any birefringence in the SMF could have affected the relative phase of the two orthogonal polarisation modes. This birefringence would have been temperature sensitive. The only approach to mitigate this would be to use polarisation controllers to control for this.

An expansion to this work would be utilising a method to monitor the birefringence in the SMF, and to use the polarisation controllers to mitigate this. With this in place, the method removing the phase change induced by 'upstream' sensor heads could be used to expand the system to a three sensor head system, with shorter length sensor heads. The shorter length sensor heads will possess greater

sensitivity but require the approach to applying strain to them to account for their shorter length. The three sensor head system will expand on the approach to remove the affect of cross talk. This will be done by first accounting for the influence of the proximal sensor head to the OBR on the phase of light passing through it to the other two sensor heads, and then accounting for the influence of the next sensor head on the phase of light propagating through it to the final sensor head. With success of this, a larger multiple sensor head system can be developed to reach the aim of developing a quasi-distributed sensor system for the measurement of strain.

Other configurations can also be used to limit cross talk. Rather than having the sensors in series, they could be placed in parallel. With the appropriate lengths to spatially separate them so they can be identified by the OBR, they could all be connected by a coupler. This would remove the cross-talk from sensor heads 'upstream', it would not remove issues from birefringence in the SMF. Both configuration approaches are vulnerable to this issue.

The approach described in this chapter lead to another sensor head like system, that used three fibre Bragg gratings (FBGs) to interrogate the phase changes along a length of birefringent fibre. This approach is described in Chapter 7.

References

[1] Y. Zhao and F. Ansari. Quasi-distributed fiber-optic strain sensor: Principle and experiment. *Applied Optics*, 40(19):3176–3181, 2001.

[2] A. D. Kersey, M. A. Davis, H. J. Patrick, M. LeBlanc, K. P. Koo, C. G. Askins, M. A. Putnam, and E. J. Friebele. Fiber Grating Sensors. *Journal of Lightwave Technology*, 15(8):1442–1463, 1997.

[3] A. J. Rogers, S. V. Shatalin, and S. E. Kanellopoulos. Optical-fibre Backscatter Polarimetry for the Distributed Measurement of Full Strain Fields. *Proc. of SPIE*, 6004:1–14, 2005.

[4] Z. Wang. *Intrinsic Fabry-Perot Interferometric Fiber Sensor Based on Ultra-Short Bragg Gratings for Quasi-Distributed Strain and Temperature Measurements*. PhD thesis, Virginia Polytechnic Institute and State Univesity, 2006.

[5] S. Rota-Rodrigo, M. Bravo, a. M. R. Pinto, and M. López-Amo. High-sensitivity PCF sensing head for strain measurement. *Proc. of SPIE*, 8421:842136–842136–4, 2012.

[6] B. Huttner, J. Reecht, N. Gisin, R. Passy, and J. P. Von Der Weid. Local birefringence measurements in single-mode fibers with coherent optical frequency-domain reflectometry. *IEEE Photonics Technology Letters*, 10(10):1458–1460, 1998.

[7] R. Calvani, R. Caponi, and F. Cisternin. Polarization Measurements on Single-Mode Fibers. *Journal of Lightwave Technology*, 7:1187–1196, 1989.

[8] W. H. Steel. *Interferometry.* Cambridge Studies in Modern Optics 1, Cambridge, 2nd edition, 1986.

[9] *Optical Backscatter Reflectometer 4400 User Guide.* Luna Technologies, 2009.

[10] W. Eickhoff and R. Ulrich. Optical frequency domain reflectometry in single-mode fiber. *Applied Physics Letters*, 39(9):693–695, 1981.

[11] A. F. Fercher. Optical coherence tomography. *Journal of Biomedical Optics*, 1 (2):157, 1996.

[12] J. Roths and F. Jülich. Determination of strain sensitivity of free fiber Bragg gratings. *Proc. of SPIE*, 7003:700307–700308, 2008.

[13] W. K. S. Chiu, J. M. Maguire, and M. J. Berliner. Phase sensitivity of conventional single-mode and holey optical fibers : a comparison study. *Optical Engineering*, 42:0–6, 2003.

[14] E. Chehura, C.-C. Ye, S. E. Staines, S. W. James, and R. P. Tatam. Characterization of the response of fibre Bragg gratings fabricated in stress and geometrically induced high birefringence fibres to temperature and transverse load. *Smart Mater. Struct.*, 13:888–895, 2004.

Chapter 7

Three wavelength interrogation using FBGs written in PMF

7.1 Introduction

In Chapter 6 a sensor head to measure strain was developed, by measuring the changes in the beat frequency of a short length of non-PCF birefringent fibre (Panda style). The sensor head was interrogated in reflection, using the cleaved end of the birefringent fibre as the source of reflection. There are other approaches to producing broadband reflection, however all that is needed is to sample the beat interference at a few wavelengths.

The work presented in this chapter is a continuation of the work in Chapter 6. A sensor head was constructed using three FBGs acting as the source of reflection. Figure 7.1 shows a short section of the beat interference of a sensor head used in Chapter 6. The beat interference can be sampled at three wavelengths to determine the position of the peak and to calculate the phase of the beat interference [1]. This sampling can be done with three FBGs written to have a small wavelength separation, shown in Figure 7.1. The intensity of reflection from each FBG can be used to determine the phase of the beat frequency using a process called phase

shifting interferometry, which is described in the following section.

To summarise, the aim of the work presented in this chapter was to use FBGs to measure the change in the difference in phase between two orthogonal polarisation modes propagating through the birefringent fibre. Unlike the rest of the work in this thesis this is not incorporating PCFs. The ambition was to use similar principles used in this work in a novel fashion. The sensor would have similar strain measurement applications, but would not require expensive fibre to operate.

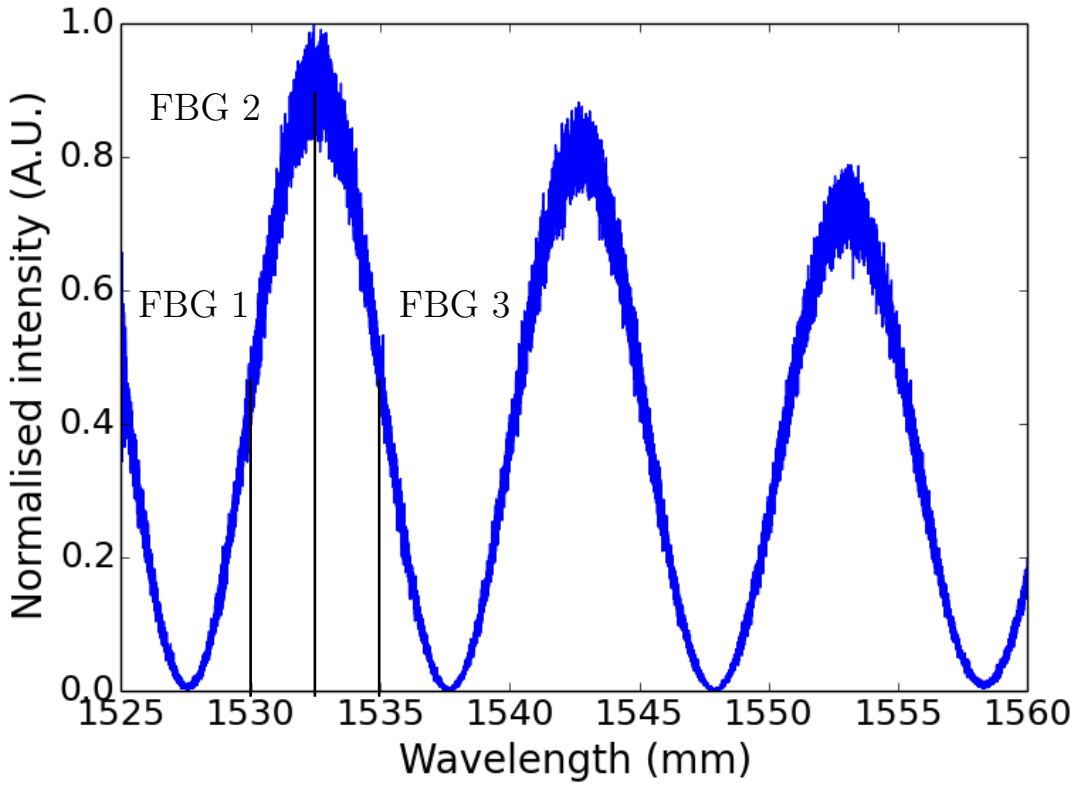

Figure 7.1: Beat interference of the birefringent fibre that the FBGs were embedded in. Three FBGs that could be used to determine the phase of the beat interference are shown.

7.2 Phase shifting interferometry

Phase shifting interferometry (PSI) is a phase stepping technique proposed by Carré [2] for interferometric measurements in 1966. PSI techniques use the interferomet-

rical beat of a reference beam with a beam reflecting at a test surface; a schematic of this is shown in Figure 7.2 [3]. The beam from a narrow wavelength coherent lightsource is split at a partially reflecting mirror into two beams; one illuminates the test surface, the other illuminates a reference mirror. The two beams reflect at the surfaces and recombine to form an interference pattern that can be detected. The intensity of beam at the detector is a function of the difference in the path length between the beam that intersects with the test surface, and the beam that intersects with the reference mirror. The position of the reference mirror oscillates along the axis parallel to the beam that reflects at the mirror. This oscillates the intensity of the beam at the detector. The intensity at the detector is sampled at a series of points along the oscillation cycle [4].

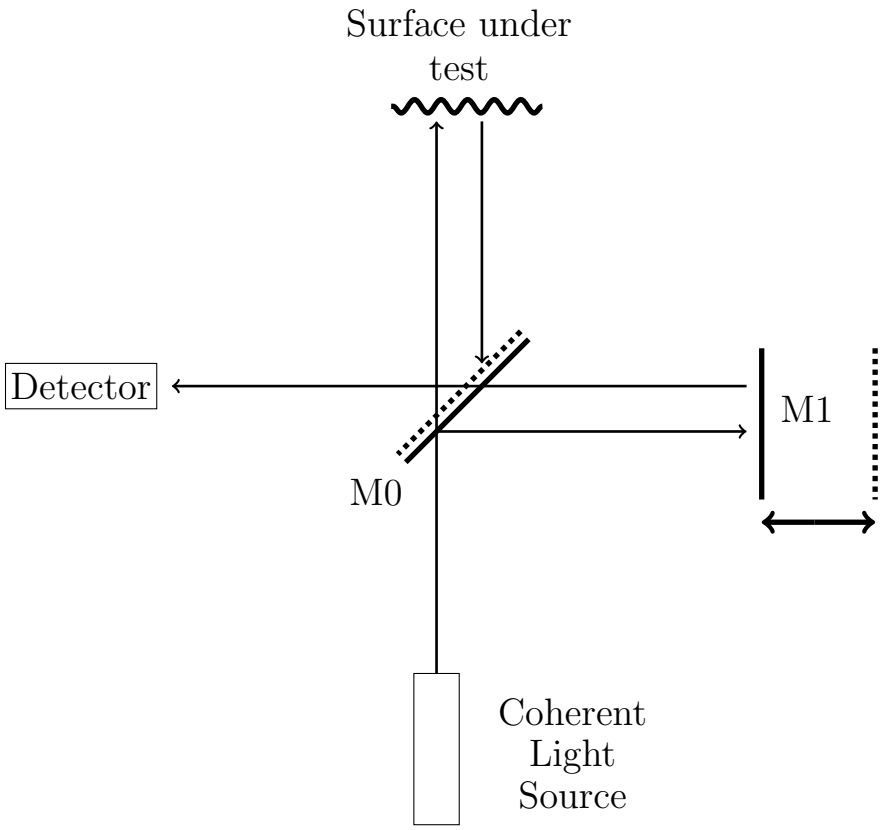

Figure 7.2: Schematic of a Michelson interferometer. M0 is a partially reflecting mirror. M1 is the reference mirror with an oscillating position [1, 5].

The intensity of the of the interference at each point of the cycle is given by

equation 7.1 [1]:

$$I = I_0(1 + VCos(\theta)) \tag{7.1}$$

where I_0 is the DC intensity, V is the fringe visibility, and θ is the phase difference between the two beams. These three quantities are generally unknown, and to solve them requires at least three equations, of the form of equation 7.1. Equations 7.2 to 7.4 are the three simaltaneous equations that can be used to directly measure the phase difference between the reference beam and the test beam.

$$I_1 = I_0(1 + VCos[\theta - \alpha]) \tag{7.2}$$

$$I_2 = I_0(1 + VCos[\theta]) \tag{7.3}$$

$$I_3 = I_0(1 + VCos[\theta + \alpha]) \tag{7.4}$$

where $I_{j(j=1,2,3)}$ are the detected intensities and α is the phase shift between adjacent intensity measurements. Equations 7.2 to 7.4 can be reorganised to make θ the subject, shown in equation 7.5;

$$\theta = Tan^{-1}\left(\frac{1 - Cos\alpha}{Sin\alpha}\frac{I_1 - I_3}{2I_2 - I_1 - I_3}\right) \tag{7.5}$$

If $\alpha = \pi/2$, it simplifies to equation 7.6;

$$\theta = Tan^{-1}\left(\frac{2I_2 - I_1 - I_3}{I_3 - I_1}\right) \tag{7.6}$$

These equations were initially formulated for a change in the phase difference between the reference beam and the test beam being produced by an oscillation in the position of the reference mirror. This change can also be produced by modulating the wavelength of the coherent light source. If a wavelength range is swept, the change in intensity would map the beat interference between the two paths. If the intensity of the interference at three different wavelengths is measured, the phase

can be determined using equation 7.6. This approach was used in this work to produce a strain sensor, and will be described in greater detail in the next section.

7.3 Interrogation of a birefringent fibre using PSI

It was discussed in Chapter 2 that birefringent fibre can act like a Mach-Zehnder interferometer. Birefringent fibre can also act like a Michelson interferometer if it is interrogated in reflection. By embedding three FBGs in close proximity to each other, in a short length of birefringent fibre, the changes in beat interference between the two orthogonal polarisation modes can be measured.

In this work a sensor head was constructed by using three FBGs embedded in a polarisation maintaining fibre (PMF) acting as a source of reflection. This is similar to the approach in Chapter 6, however in Chapter 6 a cleaved end was used as a source of reflection. Figure 7.3 shows the schematic of the sensor head. The sensor head is the region of the PMF to which strain is applied. It is between the splice and the three FBGs acting as a source of reflection.

The FBGs were written to have a wavelength spacing that corresponds to a phase difference between them of $\pi/2$. Equation 6.2 in Chapter 6 gives the wavelength range for a 2π phase difference, the wavelength range of $\pi/2$ is given by $\Delta\lambda = \lambda(L_B/8L_A)$ [6]. The wavelength spacing was chosen to be $5nm$ using this formula.

An optical backscatter reflectometer (OBR) was used to measure the intensity of the reflection from the three FBGs. The OBR was used in Chapter 6, and is described in greater detail in that chapter. In the work presented in this chapter, the OBR was used as a scanning laser source (centred $1500nm$) and detector to measure the intensities of reflection of the three FBGs. The scanning range used was $60nm$, as this is much greater than the beat frequency range of the PMF used.

A plot of the intensities measured by the OBR is in Figure 7.4. This is for both polarisation states, which is why each FBG has a double peak, one for each

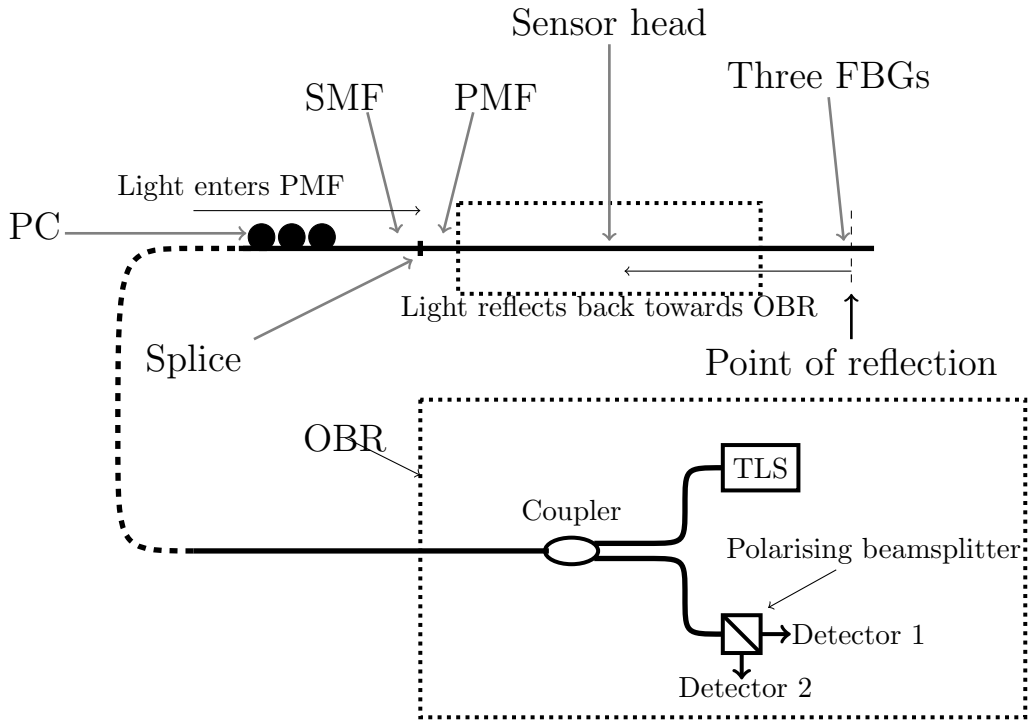

Figure 7.3: Schematic of the sensor head. The sensor head is the region of PMF between the splice and the three FBGs. The OBR is composed of a coupler, a tuneable laser source (TLS), a polarising beamsplitter, and two detectors. Light from the TLS leaves the OBR, passes through the polarisation controller (PC), crosses the SMF into the PMF (with the sensor head contained within the PMF), reflects off the three FBGs. It returns to the SMF where the two orthogonal polarisation modes propagate to OBR, and through the coupler in the OBR. The modes interfere with each other at the detector, with the detector measuring the intensity of each polarisation mode.

polarisation. This is due to the refractive index difference between the polarisation axes, which changes the Bragg condition and means each polarisation axis has a different wavelength peak [7]. A spectrometer and laser source could have been used in this work, however it was convenient to use the OBR as it was already being utilised for the work presented in Chapter 6.

The response of the sensor head to three conditions were measured; applied axial strain, applied transverse load, and temperature change. The intensities of the three FBGs recorded by the OBR, were put into equation 7.6 to determine the phase change to the different conditions. As discussed in Chapter 6 the beat interference for each of the polarisation states were out of phase with each other by π. This meant that as the sub-peak of one FBG increased in intensity as the phase of the

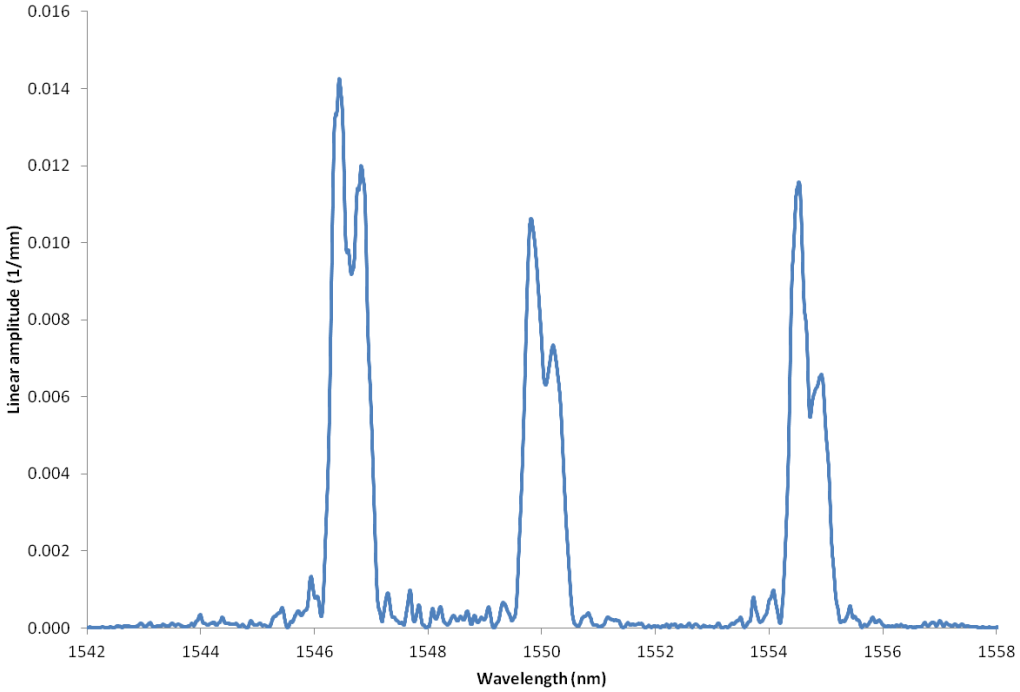

Figure 7.4: The OBR wavelength spectrum when interrogating the three FBGs.

beat interference changed, the other sub-peak decreased. Due to this, only one sub-peak was used for interrogating the phase of the beat interference. The different setups used to apply strain (or change temperature) to the sensor head presented in this chapter were the same as those presented in Chapter 6. The response of the sensor head is discussed in the following section.

7.4 Phase response of the sensor head

The PMF sensor head interrogated with three wavelengths was observed to be sensitive to all the measurands. Unlike the PMPCF sensor head presented in Chapter 6, it did not have linear change in phase to any of the measurands. The PMF used was Panda-style, it uses two stress lobes to induce birefringence by applying stress across the core of the fibre. Any strain applied to the sensor head modifies this innate stress, so the non-linear response is not unexpected.

7.4.1 Applied axial strain

Figure 7.5 shows the change in phase of light along PMF as axial strain was applied to a 15.3cm segment. There is a clear non-linear response, with an inflection at 4 $m\epsilon$. Unfortunately the phase did not uniquely identify the strain. The beat frequency measured is produced by the refractive index difference between the two orthogonal polarisation modes. This refractive index difference is induced in the PMF by stress lobes. As strain is applied to the PMF, it modifies the stress pre-existing in the fibre, which affects how the refractive index changes as strain is applied to the fibre. This produces the non-linear change in phase of the beat frequency as axial strain is applied.

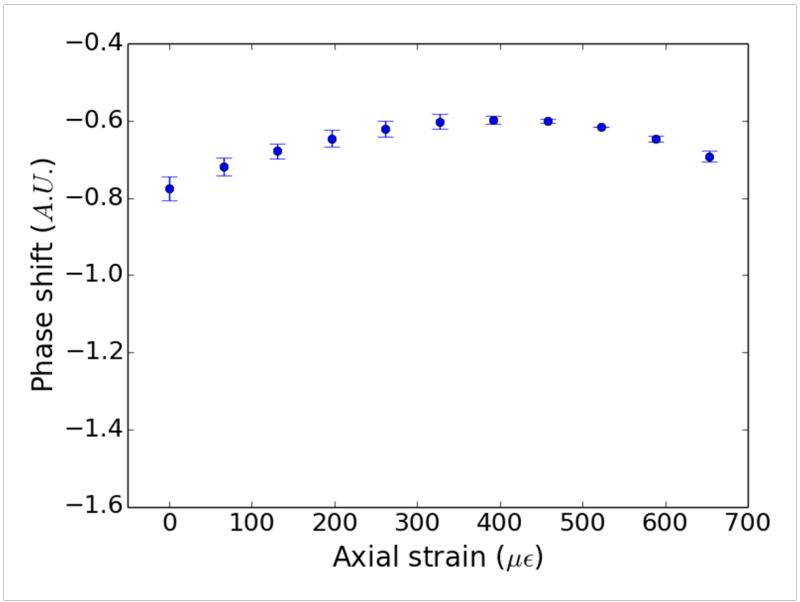

Figure 7.5: The absolute phase of light reflecting at FBGs in the PMF, as axial strain was applied to it.

7.4.2 Applied transverse load

Figure 7.6 shows the change in phase of the sensor head as transverse load was applied to a 2cm segment, for four different angular orientations; 0 degrees (aligned to the fast axis), 30 degrees, 60 degrees, and 90 degrees (aligned to the slow axis). All the responses are non-linear and there is a clear regime change between 30 degrees

and 60 degrees. Unfortunately the phase does not uniquely identify the applied transverse load for all the orientations other than for 0 degrees which was aligned with the fast axis of the fibre. As discussed above strain modifies the induced stress in the fibre. This implies that the sensor head should have a similar response to transverse load as it does for axial strain. However its 90 degree response, with multiple inflections, suggests that the beat frequency phase oscillates sinusoidally. The PSI technique used measures the change in the phase of the beat frequency. The beat frequency is a function of the phase difference between the two orthogonal polarisation modes, and therefore reducing the length of the PMF fibre will increase the size of the beat frequency and can potentially increase the strain range between inflections. An expansion of this work could observe the influence of the length of the sensor head or the range of strain it can measure with a unique phase.

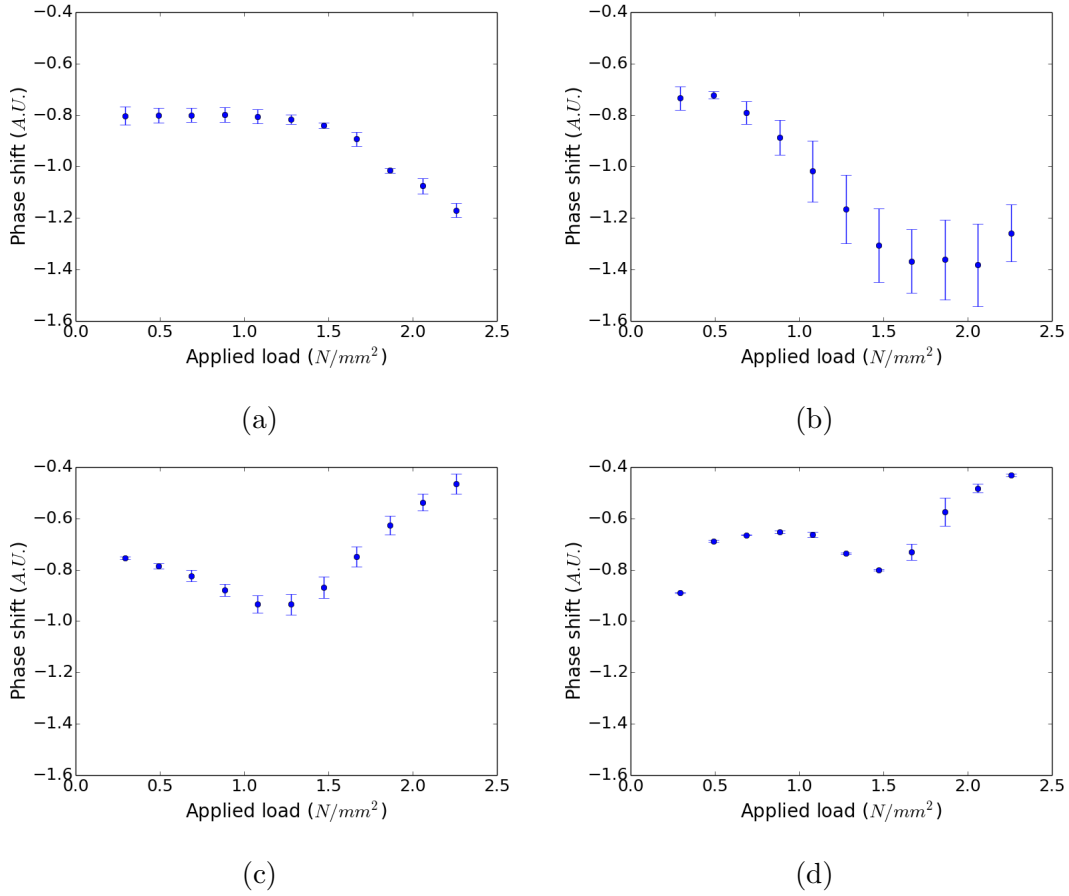

Figure 7.6: The absolute phase of the beat interference of the PMF sensor head, as transverse load was applied to it, using four different rotational orientations: (a) 0 degrees, (b) 30 degrees, (c) 60 degrees, (d) 90 degrees.

7.4.3 Temperature change

Figure 7.7 is a plot of the phase of the beat frequency of the sensor head for different temperatures. To reach these temperatures a $2cm$ segment was heated. There is a clear non-linear response, which is consistent with the sensor head's response to both applied axial strain and applied transverse load. Unlike for axial strain and transverse load, there was a unique phase for each temperature. However it can be observed that there is an inflection near the 75^0C. This could have been resolved by looking at higher temperatures, but due to time constraints higher temperatures were not explored.

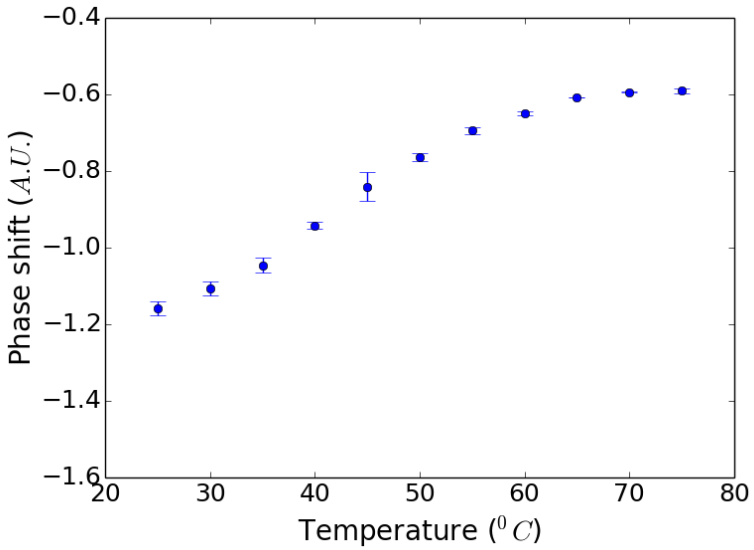

Figure 7.7: The absolute phase of light reflecting at FBGs in the PMF, as it was heated.

7.4.4 Limitations of the system

This system measures small changes in the relative phase difference between the two orthogonal polarisation modes propagating through the birefringent fibre. Since the interference happens at the detector (in this case within the OBR), it is sensitive to any birefringence in the SMF. Much like the case with the sensor head system presented in Chapter 6, curl or temperature variations across the SMF can induce birefringence and modify the relative phase difference. As such this requires the SMF to be under fixed environmental conditions. This requirement is not easily met in the fields in which this system would be used.

Further the formula used to calculate the phase based on the relative intensities of the FBGs, assumes they occupy the same position in the birefringent fibre. Due to practical limitations they were written with $1cm$ spacing from each other, and this could not be further reduced. This limits the applicability of this formula to make the calculation.

7.5 Chapter summary

A sensor head was constructed from a short length of PMF spliced to SMF. Embedded into the the PMF were three FBGs close in wavelength ($5nm$) from each other centred on $1550nm$. The three FBGs were used to interrogate the phase change in the fibre due to each of; applied axial strain, applied transverse load, or temperature change. Due to the birefringence of the fibre four different orientations were used; 0 degrees (aligned with the fast axis of the fibre), 30 degrees, 60 degrees, and 90 degrees (aligned with the slow axis of the fibre). It was found that while the sensor head was sensitive to all measurands, it did not have a linear response to any of them. Also the phase measured did not uniquely match the measurand for both applied axial strain and applied transverse load. In the case of temperature change the phase could cease to uniquely match temperature at higher temperatures.

As the system measured changes in phase between two orthogonal polarisation modes, it was sensitive to any changes in the birefringence in the SMF that connected the sensor head to OBR. This is a severe limit on the applications of this system. The method of measuring the change in phase used a formula that had limited validity, as it required the FBGs to be in the same position, however due to practical limitations they had $1cm$ spacing.

Using a shorter length of PMF could allow a larger strain range to be measured, before the phase no longer uniquely corresponds to a measured strain. This would increase the wavelength range of one period of the beat frequency, and require the FBGs to be written with a greater wavelength separation. An expansion to this work would be to measure how changing the length of the PMF between the splice and the FBGs could improve the sensor head's sensitivity, and increase the strain range that has a unique phase. This expansion does not resolve the fundamental issues with the system, and as such the work presented in this chapter does not warrant further exploration.

Overall this sensor head system is less convenient than the one presented in

Chapter 6. The sensor head in Chapter 6 had a low temperature response, and a linear response to both applied axial strain and applied transverse load. The sensor head presented in this chapter does not lend itself to being used in a quasi-distributed system.

A comparison of all the sensor types developed in this work with respect to each other will be covered in the following chapter.

References

[1] A. Ezbiri. *Passive signal processing techniques for miniature fibre Fabry-Perot interferometric sensors*. PhD thesis, Cranfield, 1996.

[2] P. Carré. Installation et utilisation du comparateur photoélectrique et interférentiel du Bureau International des Poids et Mesures. *Metrologia*, 2(1): 13–23, 1966.

[3] K. Creath. Phase-measurement interferometry techniques. *Progress in Optics*, 26:349–393, 1986.

[4] J. H. Bruning, D. R. Herriott, J. E. Gallagher, D. P. Rosenfeld, a. D. White, and D. J. Brangaccio. Digital wavefront measuring interferometer for testing optical surfaces and lenses. *Applied Optics*, 13(11):2693–2703, 1974.

[5] K. T. V. Grattan and T. Sun. Fiber optic sensor technology: An overview. *Sensors and Actuators, A: Physical*, 82(1):40–61, 2000.

[6] R. Calvani, R. Caponi, and F. Cisternin. Polarization Measurements on Single-Mode Fibers. *Journal of Lightwave Technology*, 7:1187–1196, 1989.

[7] E. Chehura, C.-C. Ye, S. E. Staines, S. W. James, and R. P. Tatam. Characterization of the response of fibre Bragg gratings fabricated in stress and geometrically induced high birefringence fibres to temperature and transverse load. *Smart Mater. Struct.*, 13:888–895, 2004.

Chapter 8

Summary and recommendations for future work

8.1 Introduction

The aim of this work was to develop strain sensors that are sensitive to applied axial strain and applied transverse load. Often photonic crystal fibres (PCFs) were incorporated into the sensors due to the numerous benefits this brings and these will be highlighted later in this chapter. To achieve this, splicing of PCFs was investigated, so that they could be included into fibre optic sensor systems. From the investigation into splicing PCFs, a microcavity based strain sensor, where a small air bubble formed from splicing PCF to SMF, was developed and enhanced by encapsulation within a resin cube. To develop a 'quasi-distributed' strain sensor system, a short length of polarisation maintaining photonic crystal fibre (PM-PCF) was spliced to SMF, and interrogated with an optical backscatter reflectometer (OBR) while axial strain or transverse strain was applied to it. To move to a 'quasi-distributed' system, two sensor heads were spliced together in tandem and interrogated simultaneously to measure the cross-talk between the sensor heads. As a comparison to the PM-PCF, a standard polarisation maintaining fibre (PCF) based sensor head was

developed, where three short length FBGs were embedded within it. The following section describes the conclusions from the work undertaken.

8.2 Conclusions

8.2.1 Photonic crystal fibre splicing

An investigation into improving PCF to SMF splices was undertaken and discussed in Chapter 4. This was to support the later work on utilising PCF in sensor systems by reducing loss in the intensity of light as it transmits across the interfaces of PCF to SMF components. It was shown that the length of the hole collapse of the PCF after a splice has a clear relationship with the loss across that splice. Reducing the length of the hole collapse incurred during splice formation, also reduced the loss of the resultant splice. It was found that the splices with the shortest length of hole collapse and lowest loss were produced with a lower main arc current and an arc offset during construction. For both PCF to SMF splices and PCF to PMF splices, a 120 μm arc offset was found to produce the shortest length of hole collapse. For PCF to SMF splices a main arc current of 14.3 mA was found to produce the shortest length of hole collapse, and the lowest loss. For PCF to PMF splices a main arc current of 12.9 mA was found to produce the shortest length of hole collapse, and the lowest loss. This is consistent with what was found by Zuoming et al. [1].

8.2.2 In-fibre Fabry-Perot microcavities

Expanding on the work of Favero et al. [2] in Chapter 5, a microcavity based strain sensor was developed. 'Microcavity' refers to a small bubble inside the fibre overlapping the core that acts like a Fabry-Perot cavity. This produces a sinusoidal pattern in reflection when illuminated with a broadband light source and interrogated with a spectrometer; this pattern shifts wavelength due to applied strain. The microcavities are constructed from splicing PCF to SMF. The PCF is internally pressurised

during splice formation, air is pushed towards the splice joint due to hole collapse, creating the air filled void or microcavity at the interface of the PCF to SMF. Favero et al. [2] developed this to measure applied axial strain, that is strain applied parallel to the axis of the fibre. In this work it was used to measure applied transverse load, pressure applied perpendicularly to the axis of the fibre, as well as applied axial strain. Axial strain was measured in this work to compare with the sensor's sensitivity to transverse load. This was an attempt to see if there was a correlation. The mean sensitivity of the microcavities produced in this work to applied axial strain is $0.286 nm/\mu\epsilon$, with a standard deviation of $0.002 nm/\mu\epsilon$. This is roughly half the sensitivity of an FBG to applied axial strain[3].

It was found that the microcavities were weakly sensitive to transverse load, with a mean sensitivity of $-0.018\ nm/(N/mm^2)$ and a standard deviation of $0.013\ nm/(N/mm^2)$. The microcavities were inconsistent between each other in their sensitivity, but since it is such a weak effect the variation in construction only needed to be minor to affect this. A key point is that the sinusoidal pattern shifts to longer wavelengths when axial strain is applied to the microcavity, but to shorter wavelengths when transverse load is applied. The periodicity was described by Equation 5.1, which showed that the periodicity was inversely proportional to the length of the cavity. The implication was that the wavelength shift to longer wavelengths was caused by the length of the cavity decreasing, and that the shift to shorter wavelengths was caused by the length of the microcavity increasing. The conclusion was that applying axial strain decreased the length of the microcavity, and applying transverse load increased the length of the microcavity.

Since this effect is weak, an FBG has a sensitivity of $0.15\ nm/(N/mm^2)$[3], it was investigated how encapsulating the microcavity in a resin cube could improve its sensitivity to transverse load. The resin cube was successful in transducing applied transverse load into applied axial strain, to which the microcavity was far more sensitive. This improved the sensitivity of the microcavities to applied transverse load

from $-0.018\ nm/(N/mm^2)$ to $0.71\ nm/(N/mm^2)$. Before being coated in a resin cube the microcavities had effectively no sensitivity to temperature change across the range of 25^0C to 125^0C, however when coated they had a mean sensitivity of $0.0126\ nm/^0C$ and a standard deviation of $0.0015\ nm/^0C$. The resin cube encapsulated microcavity transverse load sensor had a high sensitivity to transverse load while having a low temperature sensitivity.

8.2.3 Beat frequency interrogation using a short PM-PCF length for strain measurements

Chapter 6 discussed the construction of a sensor head from a short length of polarisation maintaining photonic crystal fibre (PM-PCF) spliced to a longer length of single mode fibre (SMF). The sensing region of the fibre was the length between the splice and the cleaved fibre end. The sensor head was interrogated with an optical backscatter reflectometer (OBR), while it experienced each of applied axial strain, applied transverse load, or temperature change.

The beat interference between the two polarisation axes of the PM-PCF was analysed, and the position of the peaks and troughs shifted wavelength as strain was applied to the sensor head. This was done in reflection using the well cleaved fibre end of the PM-PCF as a source of reflection. This was an expansion of the work of Rota-Rodrigo et al. [4], since they had only applied axial strain to the sensor head. How the length of the PM-PCF region affected the sensor head's sensitivity to any of the measurands was investigated and it was found there was an inconsistent trend for shorter lengths to be more sensitive to the measurands, while the same length segment of the PM-PCF had the axial strain applied to it.

It was found that for an 8 cm segment the sensitivity of the sensor head to applied axial strain was of order $0.5nm/\mu\epsilon$, approximately the same sensitivity as a standard FBG ($0.6nm/\mu\epsilon$)[3]. This is convenient since using a longer segment of PM-PCF experiencing applied axial strain was found to linearly improve the

sensitivity of the sensor head, so the sensitivity of an FBG can be reached. The sensor head was also found to have no sensitivity to temperature change in a range of 25^0C to 125^0C. The sensor head's sensitivity to applied transverse load was found to be highly dependent on its rotational orientation, due to it being birefringent it responded differently depending on which polarisation axis had the load applied to it. Applying transverse load to the fast axis of the PM-PCF moved the minima to longer wavelengths, whilst applying transverse load to the slow axis moved the minima to shorter wavelengths. This rotational orientation sensitivity meant that the sensitivity to applied transverse load was greater for some angles than for others. There was a potential orientation where the PM-PCF would be insensitive to applied transverse load, though this was impractical to use. When this was determined the work was expanded to have two sensor heads in tandem with each other.

The aim was to develop a precursor to a 'quasi-distributed' sensor system, that could interrogate multiple sensors simultaneously, and hopefully to both types of strain. It was found that the signal of the sensor heads were not independent, and applying either axial strain or transverse load to the sensor head closer to the OBR produced a false signal in the sensor head further away from the OBR. To compensate for this, the phase change measured in the proximal sensor head to the OBR, could be removed from the signal from the distal sensor head to interpret the actual strain the distal sensor head experienced.

A further limitation of the system was that any birefringence within the SMF would change the relative phase of the two orthogonal polarisation modes propagating through the optical fibre. To mitigate this would require knowing what phase shift that birefringence had provided, but this would have a thermal sensitivity, and any movement in the SMF would also change it. This limits further expansion of the system.

8.2.4 Three wavelength interrogation using FBGs written in PMF

As a comparison to the work developing a PM-PCF based sensor head, a similar approach was applied to regular polarisation maintaining fibre (PMF) in Chapter 7. Instead of using a well cleaved fibre end, three FBGs were embedded in the PMF. Using a phase shifting interrogation technique based on work by Ezbiri [5], the FBGs were used to sample the intensity of the beat interference at three different wavelengths. The intensity of reflection from the FBGs were used to measure the phase of the beat interference, and how it changed when the sensor head experienced: applied axial strain, applied transverse load, or temperature change.

The intensity of reflection at the FBGs was interrogated with an optical backscatter reflectometer (OBR), though unlike the work in Chapter 6, the OBR was just used as a narrow linewidth sweeping laser source, and a detector.

Unfortunately the PMF based sensor head did not show linear sensitivity to any of applied axial strain, applied transverse load, or temperature change. As was expected the transverse load sensitivity was dependent on which polarisation axis had transverse load applied to it, but there was no clear preferred orientation.

A limitation to this system, and the PCF birefringent sensor head work in Chapter 6, was that any induced birefringence in the SMF will change the relative phase between the two orthogonal polarisation modes. As discussed above, to mitigate this would require knowing what phase shift that birefringence had provided, but this would have a thermal sensitivity, and any movement in the SMF would also change it.

8.3 Recommendations for future work

8.3.1 Chapter 4

From the investigation into splicing PCF to SMF, and the investigation into the production of microcavities, it was found that by internally pressurising the PCF, the amount of hole collapse during splicing was reduced. This matches the outcome of Zhu et al. [6], who found that internally pressurizing the PCF could reduce loss during splicing. This was not utilised in this body of work, since pressurising the fibre would have been an added complication. However it is an avenue that could be explored if a further reduction in splice loss is needed. This could be achieved using the same setup used in the production of the microcavities. In that case the air from the hole collapse formed a bubble at the splice joint, so the settings used by the fusion splicer would have to be modified to minimise this.

Mode field diameter (MFD) mismatch was not explored in depth within this work. Others have explored this, using the hole collapse affect on the MFD to reduce mismatch between the PCF and the SMF [7, 8, 9]. While this experiment was aimed at reducing hole collapse overall, the results can be used to design the system to at least in part control the length of the hole collapse region. If a computer model was generated to describe how the hole collapse affects the mode field diameter of the PCF, a combination of choice of SMF and changing the length of the hole collapse could be used to minimise MFD mismatch. To generate the computer model the MFD of the fibre after hole collapse would have to be measured. This will most likely require cleaving the fibre at the joint, so that the MFD at the joint can be directly measured. This is a technically challenging task, requiring precision cleaving.

A small project that would be of interest would be measuring the backscatter constant of the PCF used in this work (PM1550-01). An optical backscatter reflectometer (OBR) was used to measure loss across the splice joint, however the difference in backscatter constant only allowed a relative change in loss to be mea-

sured, not an absolute measurement. An absolute measurement would be beneficial to future work.

8.3.2 Chapter 5

In Chapter 5, the microcavities were shown to be inconsistent in their response to the measurands. They were constructed using a fusion splice, a device shared in the lab, and this is the most likely source of the inconsistency. A benefit of the microcavities is that they could be produced with a commonly available device (to optical laboratories). Any future work would benefit from a dedicated machine, such that the internal conditions would remain consistent, or at least changes could be better understood.

Using a laser fusion splicer would allow better control, and allow further investigation into the conditions required to produce the most effective microcavities. With the current approach the differences in the microcavities could be catalogued, but greater control over their formation could help to study what properties enhance their sensitivity to different measurands. This could allow an exploration to assess if some construction methods produce microcavities more sensitive to axial strain rather than transverse load. The microcavity work suffered, like the splicing work, from the requirement of measuring the splicing conditions indirectly. The heat of the silica was taken to be given by the main arc current used for fusion. However a camera that could measure the temperature of the fibre during splicing would measure the heat distribution directly, rather than inferring it from the modelled heat distribution around the arc points. Further the internal pressure of PCF at the point of splicing was shown to be a function of the pressure provided by the Drucker pump, and the effect of the push distance. An accurate measure of the internal pressure at the splice joint would be invaluable.

While in this work the microcavities' sensitivity to transverse load was measured, their response to hydrostatic pressure was not. Fávero et al. [10] developed

a hydrostatic sensor incorporating birefringent PCF. This would be similar work, but with the benefit of reducing the amount of PCF needed. The birefringent fibre however works by pressure changing the relative refractive index between the two axes of the fibre, in the case of the microcavity it does not have a preferred axis, so it is unknown how it will respond to hydrostatic pressure.

The method of applying a resin cube to the microcavites limited the size of the resin cube to dimensions of at least $6mm$. The mould was made of silicone rubber, but there are potentially other materials from which the mould could be constructed, which could produce smaller resin cubes. Smaller resin cubes could produce less strain on the microcavities due to changes in temperature, which would decrease the large sensitivity of the microcavity to temperature change when coated. The relationship between the microcavities' sensitivity to axial strain, and sensitivity to temperature change when coated in a resin cube could be explored and determined.

An uncoated microcavity has much lower sensitivity to temperature change, but also a lower sensitivity to transverse load. However in a system that utilises a microcavity and an FBG, the microcavity could be used to compensate for temperature change. As such microcavities could be used in hybrid system to correct for temperature change, not just those using FBGs.

8.3.3 Chapter 6

It was found in the investigation of the PM-PCF based sensor heads that shorter length sensor heads had greater sensitivity to the measurands. This was because the interference of the two orthogonal polarisation modes had a larger wavelength period for shorter sensor heads. As such the limit on the minimum size of the sensor head was determined by the wavelength range of the OBR. If this wavelength range was increased, the sensor heads could be shorter in length and more sensitive. Shorter lengths would also improve the practicality of inserting the sensor head into different environments.

A more fundamental limitation is that any birefringence induced into the SMF causes issues in the system, as it introduces an unknown change in the phase difference between the two orthogonal polarisation modes. Single mode PCF would be less sensitive to induced birefringence from stress or temperature variation than the SMF used in the experiment. As such an expansion of the work that replaced the SMF with single mode PCF would help mitigate this issue. However this system will always be sensitive to this issue, and FBGs will always have an advantage over it in this regard.

The final step in the investigation of the PM-PCF based sensor heads is to expand to three or more sensor heads, and test the approach to remove the cross-talk from proximal sensor heads from the signal from distal sensor heads. This would lead into a fully developed 'quasi-distributed' system.

8.3.4 Chapter 7

The response of the PMF based sensor head could be analysed further by observing the influence of the length of the sensor head on its sensitivity to the measurands, and also to increase the strain regions that correspond to a unique measure of the phase of the beat interference. The response of the PMF based sensor head could be improved by moving to five wavelength interrogation, by utilising five FBGs embedded into the PMF. It is not clear if this would create regions of 'linear' response to applied conditions. As mentioned in Chapter 7, the formula used to interpolate the phase from the FBG intensity assumes the FBGs are all placed in the same location. This is an issue with this approximation for the three FBG system, the same issue would be compounded by an expansion to FBGs. Further this approximation would likely be no longer valid for shorter PMF lengths with five FBGs.

These approaches do not resolve the issue of any induced birefringence in the SMF, but like the PCF sensor head, that could be resolved by replacing the SMF with single mode PCF. This would greatly increase the cost of using the sensor head

system, as the PCF would be more expensive that the PMF (per unit meter as well as in total). As such this solution seems impractical for the PMF sensor head system.

Overall this thesis has described work on the development of interferometric point sensors, often incorporating photonic crystal fibre (PCF). The point sensors with PCF as a component often had weak, or no sensitivity to temperature change. An expansion of the work as a whole would be to develop other PCF based analogues of current fibre optic strain sensors, to have similar sensitivities to their measurands but the capability to ignore temperature changes in their environment. They could be paired with other sensors types to allow for the influence of temperature on those sensors to be accommodated.

References

[1] S. Zuoming, S. Ningfang, J. Jing, S. Jingming, and M. Pan. Low loss fusion splicing polarization-maintaining photonic crystal fiber and conventional polarization-maintaining fiber. *Optical Fiber Technology*, 18:452–456, 2012.

[2] F. C. Favero, G. Bouwmans, V. Finazzi, J. Villatoro, and V. Pruneri. Fabry Perot interferometers built by photonic crystal fiber pressurization during fusion splicing. *Optics Letters*, 36:4191–4193, 2011.

[3] J. Roths and F. Jülich. Determination of strain sensitivity of free fiber Bragg gratings. *Proc. of SPIE*, 7003:700307–700308, 2008.

[4] S. Rota-Rodrigo, M. Bravo, a. M. R. Pinto, and M. López-Amo. High-sensitivity PCF sensing head for strain measurement. *Proc. of SPIE*, 8421:842136–842136–4, 2012.

[5] A. Ezbiri. *Passive signal processing techniques for miniature fibre Fabry-Perot interferometric sensors*. PhD thesis, Cranfield, 1996.

[6] T. Zhu, F. Xiao, L. Xu, M. Liu, M. Deng, and K. S. Chiang. Pressure-assisted low-loss fusion splicing between photonic crystal fiber and single-mode fiber. *Optics Express*, 20:24465–24471, 2012.

[7] J. T. Lizier and G. E. Town. Splice losses in holey optical fibers. *IEEE Photonics Technology Letters*, 13(8):794–796, 2001.

[8] Y. L. Hoo, W. Jin, J. Ju, and H. L. Ho. Loss analysis of single-mode fiber/photonic-crystal fiber splice. *Microwave and Optical Technology Letters*, 40(5):378–380, 2004.

[9] K. Nakajima, K. Hogari, J. Zhou, K. Tajima, and I. Sankawa. Hole-Assisted Fiber Design for Small Bending and Splice Losses. *IEEE Photonics Technology Letters*, 15(12):1737–1739, 2003.

[10] F. C. Fávero, S. M. M. Quintero, C. Martelli, A. M. B. Braga, V. V. Silva, I. C. S. Carvalho, R. W. A. Llerena, and L. C. G. Valente. Hydrostatic pressure sensing with high birefringence photonic crystal fibers. *Sensors (Basel, Switzerland)*, 10(11):9698–711, 2010.

Appendix A

Reproduction of NL-1.5-670-02 technical report

Photonic Crystal Fibers by

blazephotonics

NL-1.5-670-02

Highly nonlinear PCF

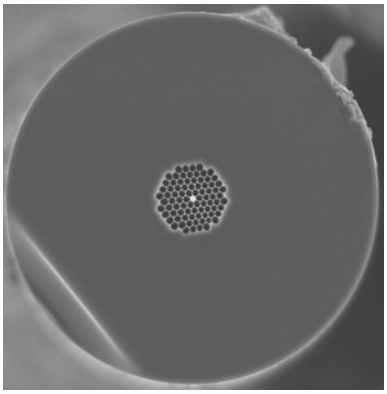

Our highly nonlinear photonic crystal fibers guide light in a small solid silica core, surrounded by a microstructured cladding formed by a periodic arrangement of air holes in silica. The optical properties of the core closely resemble those of a rod of glass suspended in air, resulting in strong confinement of the light and, correspondingly, a large nonlinear coefficient. By selecting the appropriate core diameter, the zero-dispersion wavelength can be chosen over a wide range in the visible and near infrared spectrum, making these fibers particularly suited to supercontinuum generation with Ti:Sapphire or diode-pumped Nd^{3+}-laser sources.

Nonlinearity: 190 W^{-1} km^{-1}
Zero dispersion λ=670nm
Single material
Spliceable

Unique properties of Highly nonlinear PCF

- Zero dispersion wavelengths from 670-880 nm available
- Nonlinear coefficients up to 190 $W^{-1}km^{-1}$ available (cf 1.1 $W^{-1}km^{-1}$ for SMF 28 at 1550 nm)
- Near-Gaussian mode profile

Applications

- Supercontinuum generation for frequency metrology, spectroscopy or optical coherence tomography
- Four-wave mixing and self-phase modulation for switching, pulse-forming and wavelength conversion applications
- Raman amplification

To contact BlazePhotonics, please visit our website www.blazephotonics.com or send an email message to info@blazephotonics.com

blazephotonics

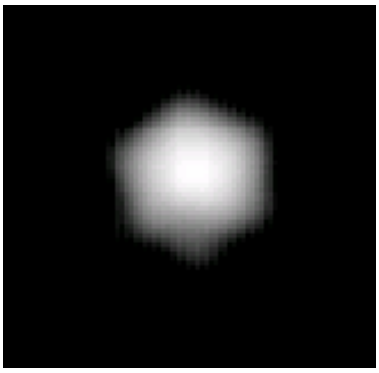

Typical measured near field profile (log scale)

Optical properties

• Zero dispersion wavelength (λ_0)		670±5 nm
• Dispersion slope at λ_0		1.4 ps·nm^{-2}·km^{-1}
• Attenuation	λ_0	< 90 dB/km
	1550 nm	< 25 dB/km
	1380 nm	< 300 dB/km
	1000 nm	< 60 dB/km
	600 nm	< 110 dB/km
• Mode field diameter[1] at λ_0		1.1±0.1 µm
• Numerical aperture[2] at λ_0		0.5
• Effective nonlinear area[3]		1.23 µm^2
• Nonlinear coefficient[4] at λ_0		190 W^{-1}·km^{-1}

Physical properties

• Core diameter (average)	1.5±0.1µm
• Pitch (distance between cladding holes)	1.9 µm
• Air Filling Fraction in the holey region	>90%
• Width of struts holding the core	70 nm
• Diameter of holey region	20 µm
• Diameter of outer silica cladding (OD)	106 µm
• Coating diameter (single layer acrylate)	220 µm
• Available length	up to 1 km

To contact BlazePhotonics, please visit our website www.blazephotonics.com
or send an email message to info@blazephotonics.com

Typical attenuation spectrum and chromatic dispersion

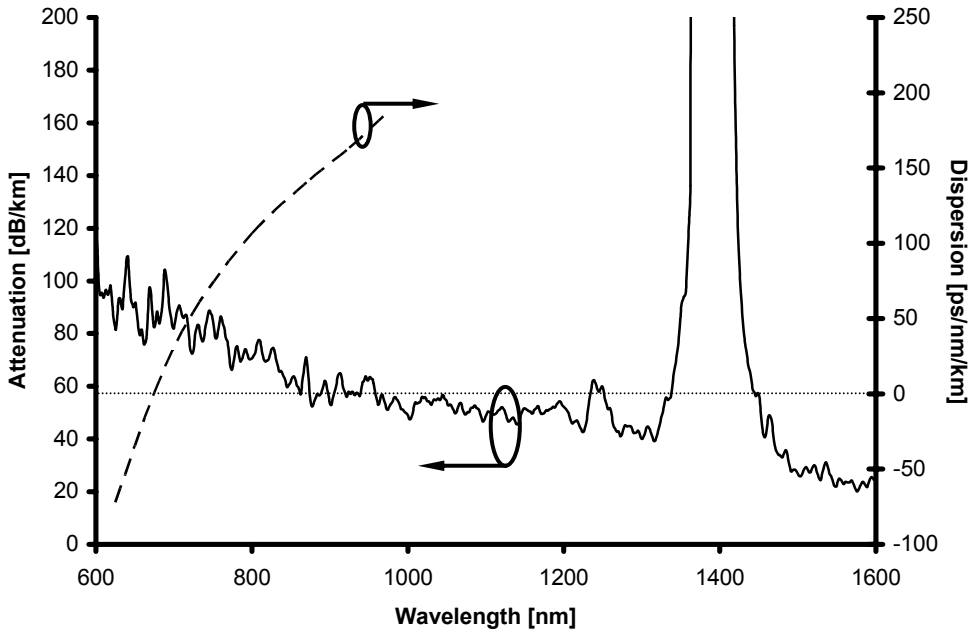

SEM image of PCF region and core

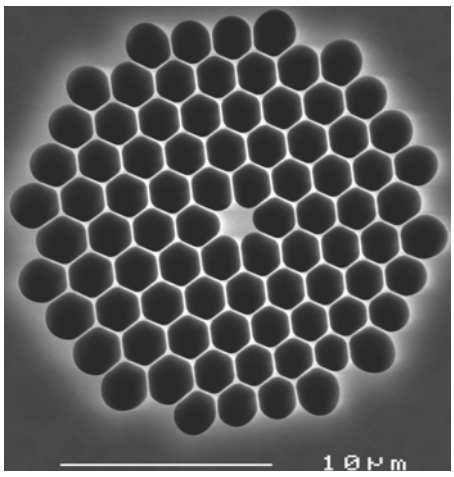

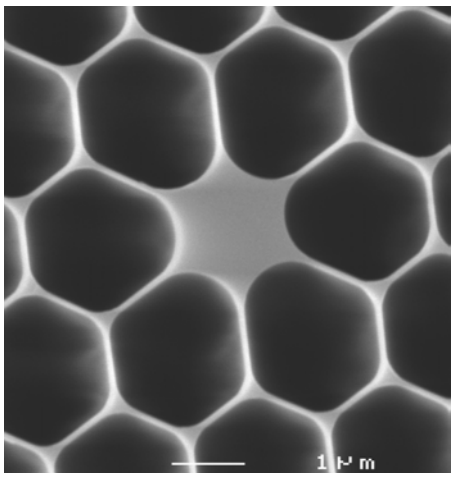

To contact BlazePhotonics, please visit our website www.blazephotonics.com
or send an email message to info@blazephotonics.com

Notes

1 Full 1/e-width of the near field intensity distribution

2 Sine of half angle at which a Gaussian fit to the far field intensity distribution has dropped to 1% of its peak value

3 $$A_{eff} = \frac{\left(\int_{\infty} |\mathbf{E}(\mathbf{r})|^2 d^2\mathbf{r} \right)^2}{\int_{silica} |\mathbf{E}(\mathbf{r})|^4 d^2\mathbf{r}}$$

4 $$\gamma = \frac{2\pi n_2}{A_{eff}\lambda}$$

$n_2 \approx 2.5 \times 10^{-20}$ m^2 W^{-1} for silica

Appendix B

Derivation of equation 6.1

The full derivation for equation 6.1 starts with the phase relationship $\phi = L\Delta\beta$. This describes the difference in phase (ϕ) between the two orthogonal polarisation modes which propagate in the birefringent fibre. L is the length of the birefringent fibre, and $\Delta\beta$ is the difference between the propagation values of the two orthogonal polarisation modes while within the birefringent fibre. This relationship is differentiated with respect to wavelength, leading to the relationship;

$$\frac{\delta\phi}{\delta\lambda} = \frac{\delta L}{\delta\lambda}\Delta\beta + \frac{\delta(\Delta\beta)}{\delta\lambda}L$$

$\frac{\delta L}{\delta\lambda}$ is equal to zero as the length of the fibre is independent of the wavelength of the modes propagating through it. $\Delta\beta$ is defined as $\frac{2\pi\Delta n}{\lambda}$, where Δn is the difference in refractive index experienced by the two orthogonal polarisation modes as they propagate through the birefringent fibre. λ is the wavelength of the two orthogonal polarisation modes propagating through the fibre. This leads to the next step;

$$\frac{\Delta\phi}{\Delta\lambda} = L\frac{\delta}{\delta\lambda}\Big(\frac{2\pi\Delta n}{\lambda}\Big)$$

$\frac{\delta\phi}{\delta\lambda}$ is replaced with $\frac{\Delta\phi}{\Delta\lambda}$ since the focus of the derivation is on a narrow wavelength range where Δn remains fixed with regards to wavelength. $\Delta\phi$ is the change in

the difference in phase between the two orthogonal polarisation modes propagating through the birefringent fibre, as the wavelength is changed by $\Delta\lambda$, centred on λ. Following through with the differentiation leads to;

$$\frac{\Delta\phi}{\Delta\lambda} = -\frac{2\pi\Delta nL}{\lambda^2}$$

The beat length, L_B, of the fibre is given by $\frac{\Delta n}{\lambda}$ and can be substituted in;

$$\frac{\Delta\phi}{\Delta\lambda} = -\frac{2\pi L}{\lambda L_B}$$

This can be rearranged to give the final form;

$$\Delta\phi = -(\Delta\lambda/\lambda)(2\pi L/L_B)$$

This gives the change in the difference in phase between the two orthogonal modes propagating through the birefringent fibre. In the case in Chapter 6, the fibre is interrogated in reflection, which means $L = 2L_A$, where L_A is the actual length of the birefringent fibre. The resulting form of the equation is;

$$\Delta\phi = -(\Delta\lambda/\lambda)(4\pi L_A/L_B)$$